
# Constitutive modelling of the strain hardening behaviour of metastable AISI 301LN austenitic stainless steel as a function of strain and temperature

By

**TULANI W. MUKARATI**

A dissertation submitted in fulfilment of the requirements for the degree of

**PhD (METALLURGY)**

Department of Materials Science and Metallurgical Engineering

FACULTY OF ENGINEERING BUILT ENVIRONMENT AND INFORMATION TECHNOLOGY, UNIVERSITY OF PRETORIA, SOUTH AFRICA

**September 2020**

UNIVERSITEIT VAN PRETORIA
UNIVERSITY OF PRETORIA
YUNIBESITHI YA PRETORIA

| | |
|---|---|
| TITLE | CONSTITUTIVE MODELLING OF THE STRAIN HARDENING BEHAVIOUR OF METASTABLE AISI 301LN AUSTENITIC STAINLESS STEEL AS A FUNCTION OF STRAIN AND TEMPERATURE |
| STUDENT | Tulani W. Mukarati |
| STUDENT NUMBER | 16378025 |
| DEGREE | PhD (METALLURGY) |
| DEPARTMENT | DEPARTMENT OF MATERIALS SCIENCE AND METALLURGICAL ENGINEERING |
| FACULTY | FACULTY OF ENGINEERING, BUILT ENVIRONMENT AND INFORMATION TECHNOLOGY |
| UNIVERSITY | UNIVERSITY OF PRETORIA |
| SUPERVISORS | Prof R.J. Mostert & Prof C. Siyasiya |

**DECLARATION**

I, Tulani W. Mukarati, do declare that, apart from referenced work, which have been duly acknowledged, this thesis is a product of my own work and efforts under the supervision of Professor Roelf J Mostert and Prof C Siyasiya in the department of Materials Science and Metallurgical Engineering, University of Pretoria. This work has neither in part nor in whole been presented elsewhere for other degrees.

**.....**

**Tulani W. Mukarati**

**Author/Researcher**

**.....**

**Date**

UNIVERSITEIT VAN PRETORIA
UNIVERSITY OF PRETORIA
YUNIBESITHI YA PRETORIA

**Constitutive modelling of the strain hardening behaviour of metastable AISI 301LN austenitic stainless steel**

by

Tulani W. Mukarati

Submitted to the department of Materials Science and Metallurgical Engineering,
in fulfilment of the requirements for the degree of
Doctor of Philosophy in Metallurgy

## ABSTRACT

The automotive industry currently demands materials with improved formability and crash performance. Austenitic stainless steels have been singled out for potential development of high strength steels to achieve exceptional combinations of strength and ductility due to their high strain hardening abilities. Austenitic 301LN stainless steel is the least alloyed and most metastable among the 300-series austenitic stainless steels. Plastic deformation at a temperature below $M_d$ transforms the metastable austenite phase to a thermodynamically more stable martensite phase accompanied with enhanced strain hardening. There are two different deformation mechanisms of austenitic stainless steels which are TRIP and TWIP effects. In this work, both mechanisms were observed at different deformation temperatures with both phase transformations and twin formations contributing towards the strain hardening.

This research work concentrated largely on the derivation of constitutive equations of both volume fraction of martensitic transformation and mechanical response of a metastable austenitic stainless steel alloy as a function of applied strain and temperature. The alloy investigated was a lean version of AISI 301LN. A calibration evaluation of the Ferritescope values was performed with the use of magnetizing tests (VSM), X-ray and neutron diffraction analyses to arrive at a reliable methodology for the determination of the martensite content during the tests. A calibration factor of 1.70 was obtained when tensile deformed samples were used (with analyses done using Vibrating Sample Magnetometer measurements, X-ray and Neutron diffraction techniques) and a calibration factor of 1.62 was obtained when cold rolled samples were used with analysis done using the neutron diffraction technique only. A series of interrupted uniaxial tensile tests at temperatures ranging between -60 and 180 °C at a constant

strain rate of 6.67 x $10^{-4}$ $s^{-1}$ were performed. A low strain rate and a small interruption interval were chosen to minimize the heating effect due to adiabatic heating. The strain hardening behavior of AISI 301LN metastable austenitic stainless steels was observed to be a complex process which is related not only to the generation of a dislocation structure but transformation and twinning hardening as well depending on the deformation temperature. Strain hardening curves were derived at different temperatures and were found to be following the same basic mathematical equation for the formation of the strain-induced martensitic transformation product as a function of true strain. Prior cold rolling was also done to different gauges ranging from 5% and 70% at ambient temperature, with small reduction passes applied to minimize adiabatic heating. A series of interrupted uniaxial tensile tests were done on the prior cold rolled samples at a low strain rate of 6.67 x $10^{-4}$ $s^{-1}$. All the derived strain hardening curves were extended up to the true strain levels of 1.0, to arrive at estimates of the strength coefficient, K. The strength coefficient, K was found to be in the range of 1500 MPa ~ 1780 MPa, as calculated from the convergence of sigmoidal hardening curves at a log stress of ~ 3.25 (at log true strain of 0).This was found to be in accordance with the tensile strength of 1715 MPa after a cold rolling of 63.2% (which is equivalent to the compressive true strain of 1.0). The calculated values of strain hardening and martensite formed, using the developed constitutive equations, agree well with the experimental results for a wide range of deformation temperatures and prior cold rolling percentages.

A linear variation of stress as a function of strain-induced martensite, observed at moderate martensite fraction levels, was explained as being due to the dispersion hardening effect. An abrupt change from a linear variation that occurred on exceeding a threshold value of martensite formed, was believed to be due to “percolation effect of martensite,” where clusters of martensite forms a continuous network linking up in 3D, adding more blockage to dislocation movement in the austenite phase. A percolation threshold of martensite was found to be in the range of 30 ~ 45%. This was found to be the percentage of martensite present when the rate of martensitic transformation reaches a maximum. At the percolation threshold of martensite, there is an interchange of roles of martensite and austenite, where martensite behaves as a matrix phase and austenite as dispersions embedded in the martensite phase. This results in higher strength as more stress is required to move the dislocations past the percolated martensite barriers which also reduces the plasticity of the austenite.

**Acknowledgements**

The following people and laboratories who made this work successful are fully acknowledged:

1. My supervisors: Prof Roelf Mostert and Prof Charles Siyasiya for their continued technical assistance and expertise for which this thesis would not have been a success. Special heartfelt gratitude to Prof Waldo Stumpf for his technical assistance in putting a proposal and help with designing some of the experiments. His personal counsel is equally appreciated.
2. The Stoneman X-Ray Analytical Facility at University of Pretoria together with great assistance from Wiebke Grote and Prof Johan de Villiers is much appreciated in the XRD work and Neutron diffraction data analysis.
3. Columbus Stainless (Pty) Ltd for financial support and stainless steel materials used. In particular, a special gratitude to Corne Theart, Mike Bolleurs and Dave Smith for their technical assistance.
4. Department of Science and Technology, S.A. Government, through their FMDN (Ferrous Metals Development Network) programme as administered by Mintek for their financial support.
5. The use of the NEP Physical Properties Measurements on Cryogenic Cryogen free Measurement System at UJ, obtained with the financial support from the SA NRF (Grant No: 88080) and the URC/FRC, University of Johannesburg (UJ), South Africa. In particular, I would like to acknowledge technical assistance from Prof Charles Sheppard and Prof Prinsloo Aletta.
6. Dr Andrew Venter and Zeldah Sentsho and use of the cryogenic Neutron Diffraction facility for bulk and depth dependent phase quantification measurements of deformed samples using neutron diffraction technique at NECSA (South Africa).
7. The use of the Instron tensile machine and the environmental chamber at Mintek, South Africa, in doing interrupted tensile tests at elevated and sub-ambient temperatures. At Mintek, I would like to express my heartfelt gratitude to Dr Jones Papo, Mr Joseph Moema, Dr Asimenye Kapito, Absalom Mabeba, Mbavhalelo Maumela and Lebedike Mampuru for their support and assistance in the laboratories.
8. Dr Johan Westraadt and the Centre for HRTEM at Nelson Mandela Metropolitan University for TEM work.

9. Engineer Ronald Koenis at MEGCHEM laboratory for assistance with use of the theta dilatometer in determining the martensite start temperature of the steel investigated.
10. The Laboratory for Microscopy and Microanalysis at University of Pretoria and great assistance from Mr Andrea Botha, Erna van Wilpe and their whole team.
11. Carel Coetzee, Rorisang and Lwazi at IMMRI, University of Pretoria for the use of GDOES, Gleeble 1500 Thermomechanical Simulator and EBSD system.
12. The Department of Materials Science and Metallurgical Engineering. In addition to the people mentioned before, I would like to acknowledge technical assistance received from Prof Pieter Pistorius, Dr Robert Cromarty, Mr Vinod Kurup, Mr Sibusiso Mahlalela, Dr Kofi Annan, Mr Mfesane Tshazi and Mr Joel Matea. I would like to express my appreciation to my colleagues Tresor Mapoli, Patrick Kambilinya, Rutendo Matengaifa, Helena Rossouw and Kedibone Lekganyane for their support and assistance in the laboratories. Special gratitude to Ms Gabi Ngema for her assistance with all the administration issues.
13. Special gratitude to my entire family especially my mom and my wife, Namatirai for support, encouragement and prayers. My utmost thanks are to the **Lord Almighty**, for anything could have happened but I had your guidance.

**Table of Contents**

**List of Figures**

**List of Tables**

## LIST OF ACRONYMS

| | | |
|---|---|---|
| MASS | - | Metastable Austenitic Stainless Steel |
| AHSS | - | Advanced High Strength Steels |
| AISI 301LN | - | Austenitic stainless-steel grade 301 |
| $M_d$ temperature | - | temperature beyond which no martensite is formed upon straining in metastable austenitic steels (°C) |
| $M_d$ (30/50) | - | temperature at which 50% of α′-martensite is obtained in a tension test for a true deformation of 0.3 (°C) |
| $M_d$ (x/y) | - | temperature at which y% of α′-martensite is obtained in a tension test for a true deformation of x (°C) |
| $M_s$ | - | martensite start temperature |
| $M_s^{\sigma}$ | - | is the temperature above which martensitic transformation can occur due to plastic deformation only (°C) |
| α′ | - | body centered tetragonal (bct)/body centered cubic (bcc) martensite |
| SIM | - | strain-induced martensite |
| SIMT | - | strain-Induced Martensitic Transformation |
| γ | - | face centered cubic (fcc) austenite |
| ε martensite | - | hexagonal compact epsilon martensite (hcp) |
| σ | - | true stress, flow stress (MPa) |
| ε | - | hexagonal compact epsilon martensite/true strain |
| dσ/dε | - | work hardening rate |
| $A_{50}$ | - | Elongation to fracture on a 50 mm gauge length |
| $R_{p(0.2)}$ | - | yield strength, MPa |
| $R_m$/UTS | - | tensile strength/Ultimate Tensile Strength, MPa |
| $R_{p(0.2)}/R_m$ | - | Ratio of yield strength to tensile strength |
| CR | - | Cold rolling |
| CW/AP | - | Cold Work/Annealing and Pickling |
| CW/RA | - | Cold Work/Reversion Annealing |
| XRD | - | X-ray Diffraction |
| EBSD | - | Electron Back Scattered Diffraction |
| SEM | - | Scanning Electron Microscopy |

| | | |
|---|---|---|
| $\gamma_{SFE}$/SFE | - | Stacking Fault Energy (mJ/m$^2$) |
| TRIP | - | Transformation Induced Plasticity |
| TWIP | - | Twinning Induced Plasticity |
| TEM | - | Transmission Electron Microscopy |
| VSM | - | Vibrating Sample Magnetometer |
| GDOES | - | Glow-discharge optical emission spectroscopy |
| $MS_c$ | - | specific saturation magnetization |
| $\Delta G^{\gamma\rightarrow\alpha'}$ | - | Chemical Gibbs free-energy difference between austenite and α′-martensite phases (J/m$^3$) |
| $\Delta G^{\gamma\rightarrow\alpha'}{}_{Ms}$ | - | Chemical Gibbs free-energy difference between austenite and α′-martensite phases at a martensite start temperature (J/m$^3$) |
| $\Delta G^{\gamma\rightarrow\alpha'}{}_{T1}$ | - | Chemical Gibbs free-energy difference between austenite and α′-martensite phases at a given temperature, $T_1$ (J/m$^3$) |
| $\Delta G_{MECH}$ | - | Mechanical Gibbs free energy |
| $\Delta G_{CHEM}$ | - | Chemical Gibbs free energy |
| n | - | Hollomon strain hardening exponent |
| $n_i$ | - | instantaneous strain hardening exponent at a given applied strain |
| $\sigma_{\alpha'}$ | - | stress level in α′-martensite |
| $\sigma_\gamma$ | - | stress level in γ-austenite |
| K | - | Strength coefficient |
| $\alpha_s$ | - | maximum strain sensitivity which corresponds to the log true strain value where there is a maximum slope of the log-log plot of the true stress-true strain curve |
| $\alpha_m$ | - | true strain which corresponds to maximum rate of martensitic transformation |
| $\beta_s$ | - | a constant derived from the nature of the log-log plots of the true stress-strain curves. The numerical value is given by, $\beta = (A - B)(4 \times n_{ipeak})^{-1}$ |
| $\beta_m$ | - | a constant derived from the nature of the percentage of martensite as a function of strain. The numerical value is given by, $\beta = (V_{\alpha's})(4 \times$ maximum slope of the rate of martensitic transformation$)^{-1}$. |

| | | |
|---|---|---|
| $V_{\alpha'}$ | - | percentage of strain-induced martensite formed within uniform elongation of tensile sample at a given temperature |
| $V_{\alpha's}$ | - | saturation value of $V_{\alpha'}$, that is, the maximum amount of martensite that could be attained in the material at a given temperature |
| A | - | maximum log of true stress ($\log \sigma_{max}$) when the sigmoidal function levels off after the martensitic transformation reaches saturation point |
| B | - | minimum log of true stress ($\log \sigma_{min}$) at the beginning of the sigmoidal curve, before any significant martensitic transformation |
| $n_{ipeak}$ | - | the peak instantaneous strain hardening exponent |
| $R^2$ | - | coefficient of determination |

**PUBLISHED JOURNAL AND CONFERENCE PAPERS**

1. Mukarati, T. W, R. J. Mostert, and C. W. Siyasiya. "The direct observation of surface martensite formation upon cooling to temperatures close to ambient in a heat treated AISI 301 stainless steel." In *IOP Conference Series: Materials Science and Engineering*, vol. 430, no. 1, p. 012042. IOP Publishing, 2018.
2. Mukarati, T. W, R. J. Mostert, and C. W. Siyasiya. "Development of a mathematical equation describing the strain hardening behaviour of metastable AISI 301 austenitic stainless steel." In *IOP Conference Series: Materials Science and Engineering*, vol. 655, no. 1, p. 012008. IOP Publishing, 2019.
3. Mukarati, Tulani W., Roelf J. Mostert, and Charles W. Siyasiya. "The sigmoidal strain hardening behaviour of a metastable AISI 301LN austenitic stainless steel as a function of temperature." *Materials Science and Engineering: A* (2020): 139741.

**Novel ideas**

A single sigmoidal mathematical equation to adequately describe the austenite to martensitic transformation as a function of applied strain for a specific lean variant of the metastable austenitic steel AISI 301LN, applicable at various deformation temperatures was derived. The same form of the sigmoidal equation was used to describe the strain hardening behavior of this steel at various temperatures showing a direct relation between the rate of martensitic transformation and strain-hardening. The strain hardening sigmoidal curve fitted led to the estimation of strength coefficient at various tensile deformation temperatures. The estimated strength coefficient at 30 °C during tensile deformation was found to be the same as the strength coefficient values found even after prior cold rolling at room temperature followed with tensile deformation at 30 °C. This was also in accordance with the tensile strength obtained after a high degree of prior cold rolling, (at least 63.2% thickness reduction which is equivalent to a compressive true strain of 1). This behavior was shown to be due to strain hardening response decreasing as the degree of prior cold rolling increased, due to increased martensitic transformation. At a high degree of cold rolling (above 63.2%), no further tensile strain hardening was observed, and tensile strength was found to correlate very well with the estimated strength coefficients determined at 30 °C, thus validating the sigmoidal equations developed.

The developed constitutive sigmoidal model was modified to describe the strain hardening response of prior cold rolled samples. Satisfactory results were obtained.

## Chapter 1: Introduction

Crash worthiness has recently attracted a continuous development of Advanced High Strength Steels (AHSS) from both industry and academia, particularly for structural applications in the automotive industry. The bulk of conventional steels lie inside a classical "banana" curve as shown in Figure 1.1. A second generation of steels with high manganese content have been developed with high strength-elongation ratio which include high manganese austenitic stainless steels such as twinning induced plasticity steels and aluminium added lightweight steels with induced plasticity (L-IP) [1]. A new third generation of steels is under development with significant potential of reduction in costs through reduced alloying elements, improved weldability, high corrosion resistance, improved mechanical properties such as toughness, fatigue resistance, high energy absorption capabilities and outstanding combinations of strength, ductility and formability [2], [3]. The third generation of AHSS offer a great lightweighting potential for automotive applications with improved occupant safety in crash events as well as significant reduction in fuel and energy consumption [1], [4], [5]. The development of third generation AHSS requires optimization of complex microstructures to achieve the desired mechanical properties. AHSS are considered composite materials based on multi-phase microstructures, hence the rule of mixtures could be applied in predicting the overall strength as a function of the volume fractions of the individual constituent with the same austenitic grain size [6]. Martensite is a critical phase which is required in significant amounts towards the strength (both initial yield strength and ultimate strength) whilst austenite contributes towards the strain hardening and ductility.

This thesis aims to develop a set of constitutive equations of linking microstructural constituents (volume fraction, size and distribution of second phase), with flow parameters such as strain, tensile strength, strain hardening and elongation for a specific metastable austenitic steel grade, with a certain defined chemistry. The equations were developed by quantifying the influence of process variables such as temperature, strain, strain rate, degree of cold rolling, initial austenitic grain size and annealing on the mechanical properties of such a third generation of AHSS.

The research is of high scientific and technical interest which focusses on lean alloyed AISI 301LN metastable austenitic stainless steel. AISI 301LN has tensile strength in the range of 600 ~ 800 MPa and total elongation to fracture of 45 ~ 60% [7], [8] which places it well above

the first generation steels in Figure 1.1. However, annealed austenitic stainless steels have low yield strength making them unsuitable for structural applications [9].

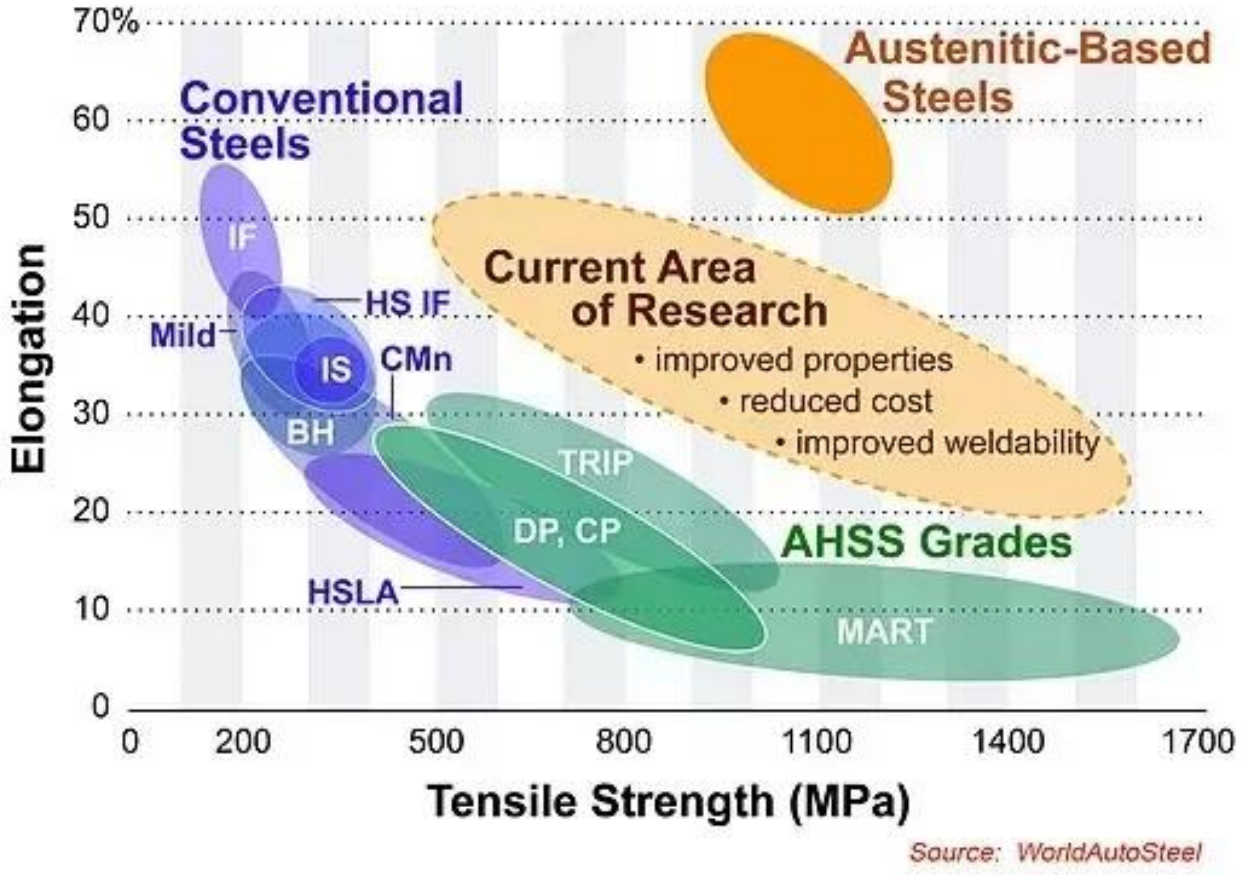


**Figure 1.1: The range of mechanical properties of various steel grades [10].**

## 1.1 Background of study

Columbus Stainless Steel Company manufactures AISI 301 austenitic stainless steel to various tempers using Sendzimir Z-high mills. The cold rolled stainless steel coils are produced in a wide range of thicknesses and different tempers which are namely, deadlight temper (DLT), light temper (LT), standard/special temper (ST), medium temper (MT), and high/heavy temper (HT) through coordinated cold rolling processes and annealing cycles. The austenitic grade AISI 301 stainless steel is of a specific chemistry for use in temper rolling to optimize the work hardening rate by the formation of Strain Induced Martensite (SIM) as dictated by the $M_d$ temperature. The specification of AISI 301 stainless steel is relatively wide and is provided in the 301, 301 L and 301 LN grades. Over time, a specific variant of AISI 301LN steel has been developed at plant level which shows promise for further development in order to use it in the transport sector as a “third generation AHSS” material. This variant of the AISI 301 LN

metastable austenitic employs a low level of carbon content (C ~ 0.02 %) and a moderately high level of nitrogen (C ~0.11%), together with low levels of nickel (Ni ~ 6.5 %).

The intermediate annealing and pickling (AP1 and AP2) cycles are done in all the tempers to attain required properties except in high temper where reversion annealing can be done at the end of the process and/or the product is produced in as-cold rolled condition. The process and product control on the "dead light", "light", "special", and "medium" tempers within the manufacturing process is easily achieved but not so with the "heavy" tempers of more than 30% cold deformation. This is because the effect of variables such as chemistry of the steel, the exact degree of cold work, the strain rate of the cold work and the temperature of the cold work (adiabatic self-heating during deformation) are still largely unclear which makes the achievement of required properties challenging. A fundamental understanding of the interplay of these variables is decisive in the development of comprehensive constitutive predictive equations for the material behavior during material processing and in predicting the material behavior during crash performance, for the specific variant of AISI 301 LN mentioned.

The heavy tempered 301 steel is intended for the bodywork casing of railway coaches and a paramount requirement is a high work hardening rate in the event of a collision to provide a high degree of protection to all the people onboard. The outstanding combination of properties which are therefore required in high temper for coil thickness of 4/4.5 mm as per established specification for Metro Coach manufacture are as shown in Table 1.1[11].

**Table 1.1: Hypothesized limits for mechanical properties required for crash relevant AISI 301LN steel**

| Mechanical property | Hypothesized Limits |
|---|---|
| 1. Yield strength, $R_{p(0.2)}$ | 750 ~ 920 MPa |
| 2. Tensile strength, $R_m$ | 1000 ~ 1150 MPa |
| 3. Elongation to fracture, $A_{50}$ | At least 22% |
| 4. Hardness ($H_{RC}$) | Approximately 36 HRC |
| 5. Ratio ($R_{p(0.2)}/R_m$) | Less than 0.8 |

The required strength levels and ductility are classified in the design manuals for structural stainless steels for Metro coach manufacturing [8]. Most stainless-steel companies

have only managed to attain a UTS of 970MPa in this grade and additional deformation resulted in severely impairing of both ductility (< 22% requirement) and hardness (> 36 HRC requirement) which will be both outside the hypothesized/stipulated limits for the high temper grade [8]. Although annealed austenitic stainless steels have excellent combinations of high strength, high ductility and high formability, the yield strength is quite low, approximately 350 ~ 380 MPa [7], [11], [12], [13].

Hence one aim of this research was to understand the correlation between the processing variables of the specific lean variant of AISI 301LN stainless steel and its mechanical properties in order to improve/develop a suitable processing technique to produce coils with the established specifications for manufacturing of Metro Coaches.

The established experience in the stainless-steel industry is using the standardized Cold Work/Annealing Process (CW/AP) for High Temper 301 on line AP1 where annealed hot coil 301 from the Steckel mill of different hot band gauges, is given several passes of cold work on the Sendzimir Z-high mills, an intermediate annealing step, and a final cold work again on the Sendzimir Z-high mills. An alternative process called the Cold Work/Reversion Annealing or CW/RA process has been suggested. This consists of heavy temper rolling of an approximately 50% cold work of the annealed hot band from the Steckel to form heavy martensite and annealing followed by a skin pass. This leads to a very fine austenite grain size but with less than 10% untransformed martensite for strength but is difficult to manufacture using the existing mill equipment at the steel mill concerned.

### 1.2 Problem Statement

One of the current uncertainties in the current process for heavy temper lean-alloyed 301LN is related to the influence of Stacking Fault Energy (SFE). The alloy SFE value dictates the deformation mechanism, whether the TRIP effect or the TWIP effect dominates. Most stainless steel companies measure the degree of martensite formation by Ferritescope instrument which gives an indication of the BCC form of SIM $\alpha'$ martensite but not of the HCP form known as $\varepsilon$ martensite. The correlation between the Ferritescope measurements and the volume fraction of actual austenite decomposition products for this alloy is largely unknown. This problem regarding the material characteristics would be characterized and quantified by SEM EBSD and Neutron Diffraction in this project and its effects on the YS/UTS, the % elongation as dictated by the chemical composition and the degree of cold work would be established.

Secondly, the cold reduction required to attain the required mechanical properties on the heavy tempers is not easily predicted using existing plant-based correlations, and the material often fails to reach the required elongation requirements. One of the possibilities for this unpredictability is the rate of formation of SIM α′ and ε martensite, as a function of strain and temperature. The plant-based stress strain curves indicate the start of martensite transformation and strain hardening at around 7.5% to 10% strain for ambient conditions, but significant uncertainty exists regarding the microstructural behavior for this grade. This project would, therefore, consider the change in mechanical properties with the application of strain together with the rate of formation of α′ and ε martensite during deformation at various temperatures and strains.

### 1.3 Justification

For the lean alloyed 301 LN metastable stainless steel in question, the cold working process results in strain-induced martensite (SIM) formation from the metastable austenite (TRIP effect). Further cold working results in the creation of lattice defects in strain-induced martensite which become nucleation sites for austenite transformation during reversion annealing [14]. High density of crystal defects will in turn result in ultra-fine grains upon reversion annealing [15]. This grain size refinement is a practical approach in increasing strength and hardness without significant reduction in plasticity [16], [17], [18], [19], [20]. Thermo-mechanically controlled processing (TMCP) is one of the ways for grain size refinement [21]. Strain hardening (resulting from increased dislocation density, twins, stacking faults, the Suzuki locking or martensitic transformation) has potential in increasing the strength of material with enhanced plasticity [7].

Crashworthiness (crash performance) is directly proportional to the strength of a material and is related to the amount of crash energy absorbed to withstand intrusion, hence the amount of mechanical energy absorbed before failure needs to be determined. This is related to the percentage of cold working and volume fraction of α′ induced during deformation. The stability of the austenite phase controls the rate and volume fraction of α′ martensite formation during deformation making it critical in tailoring the mechanical properties [22].

For the variant of the AISI 301 LN metastable austenitic steel which employs a low level of carbon content (C ~ 0.02 %), a moderately high level of nitrogen (N ~ 0.11%), together with low levels of nickel (Ni ~ 6.5 %), a thorough understanding of the isolated individual influence of process and crash variables on resulting microstructures and corresponding mechanical

properties forms basic fundamentals for metal forming operations and crash-related performances [23], needs to be established.

### 1.4 Research aims and objectives

The current research work is therefore aimed at developing fundamental relationships required to exploit the specific lean AISI 301LN metastable austenitic stainless steel alloys for the design and manufacturing of crash-relevant parts of bodywork casing of metro coaches. This steel grade exhibits TRIP effects largely due to lean alloying elements giving it a potential for extremely high work-hardening capacity and strength among the austenitic 300 series, making the material attractive in terms of crashworthiness, occupant safety, and cost. The aims include derivation of constitutive equations of interrelationships of required tensile properties of yield strength, tensile strength, ratio of yield strength to tensile strength, uniform and total elongation to fracture as a function of degree of applied strain at various temperatures and evolution of microstructural constituents. Constitutive equations required development to describe the influence of process variables such as temperature of deformation, degree of plastic deformation, strain rate, alloy chemistry composition within the current alloy limits, initial microstructure and morphology on the strain hardening strengthening mechanism. Derivation of instantaneous strain hardening exponents, strength coefficients to describe the strain hardening behavior of AISI 301LN, was part of the objectives. The deformation microstructural mechanisms causing the observed strain hardening behavior were studied and explained. Constitutive equations have the potential of resulting in good control of mechanical properties during production of steel and finished components from this grade. In addition, such equations can be utilized during numerical simulations of materials behavior during collisions, studying passenger safety. This will result in a thorough understanding of the process-product relationships in the CW/AP process with the potential of improvement in the process design and control of mechanical properties of the lean alloyed AISI 301LN steel and associated finished components.

The overall objective of the research is therefore to develop comprehensive constitutive predictive equations for material behaviour during the application of strain during processing and collisions, incorporating the process and collision variables. The developed model could also be used to select the most viable processing methodology to produce lean alloyed AISI 301LN coils with the required mechanical properties for bodywork casing of metro coaches.

## 1.5 Research hypothesis

It is hypothesized that a set of constitutive equations can be developed that will describe the strain hardening behaviour and martensitic transformation kinetics of this grade as a function of applied strain and temperature, for the specific lean AISI 301 LN alloy (low carbon and nickel, medium - high nitrogen) in question. These constitutive equations will facilitate the development of processes and products that can be regarded as pertaining to the “third generation AHSS” products.

# Chapter 2: Literature Review

A review of existing literature that was done to chronicle the past research efforts in developing improved AISI 301LN stainless steel coils with enhanced mechanical properties for the manufacture of bodywork casing of railway carriages. The review focusses on the AHSS strengthening mechanisms of AISI 301LN. Steels are iron based metals alloyed by carbon. Steels are currently an essential class of materials used in wide range of applications, ranging from kitchen cutlery to spacecraft due to superior mechanical properties such as high strength, good formability, versatility and durability. Steels can be roughly classified as carbon steels, alloy steels, tool steels and stainless steels. 90 % of the total world steel productions are carbon steels and they contain the basic alloying elements of iron and carbon [24]. Low alloy steels are designed to exhibit superior mechanical properties to plain carbon steels with precise additions of alloying elements such as chromium, nickel and molybdenum. Tool steels contain tungsten, molybdenum, cobalt, and vanadium to increase heat resistance and durability making excellent cutting and drilling equipment [24].

## 2.1 Stainless steels

Stainless Steels contain chromium content of at least 10.5% by mass. Nickel can be added for special applications that demand both good corrosion resistance and good mechanical properties such as increased strength, weldability, ductility and toughness.

Stainless steel can be further classified into 5 groups based on microstructure at room temperature, specific properties and basic grade or “type”. The classes are: austenitic stainless steels (stable and metastable), ferritic stainless steels, martensitic stainless steels, duplex stainless steels and precipitation-hardenable stainless steels. The chemistry of the steel can be varied within limits to modify mechanical properties such as weldability, strength, machinability, work hardening and formability under different conditions and temperatures [24].

### 2.1.1 Austenitic Stainless Steel

Austenitic stainless steels constitute the largest group of stainless steel and can be classified as either stable austenitic stainless steels or metastable austenitic stainless steels. The austenitic microstructure in the solution annealed condition is non-magnetic. The microstructure is face-centred-cubic (FCC) lattice which is like that of pure iron at high temperatures of 912 - 1495 °C. Due to the FCC microstructure, austenitic stainless steels possess excellent ductility, formability and toughness. The austenitic grades are weldable and have excellent corrosion

resistance due to the high content of chromium and molybdenum. The strength can be increased through cold working; with some grades supplied in temper rolled condition which makes it magnetic because of presence of strain-induced martensite. Interstitial elements of carbon and nitrogen, in addition to nickel stabilizes the austenitic structure. The austenitic phase in this class of stainless steel can be classified as stable or metastable with respect to the deformation temperature. Austenitic stainless steel can be further sub-divided into five sub-groups which are Cr-Ni grades (300 series), Cr-Ni-Mo grades, Cr-Mn grades (200 series), high temperature austenitic grades and high-performance austenitic grades.

**I. Cr-Ni grades**

Also known as 18-8 type or 300 series of stainless steels, indicating the approximate amount of chromium and nickel respectively with no molybdenum added. Nitrogen and Sulphur improves the strength and machinability, respectively. The amount of nickel is generally lower in this grade of austenitic steels compensated by higher additions of nitrogen to maintain the stability of the austenitic structure. In low nickel alloys, manganese up to 2% is added to improve the solubility of nitrogen in the austenitic structure, preventing the martensitic transformation and increasing strength. The typical tensile yield strength of Cr-Ni alloys after annealing is around 200~275MPa, which is lower compared to that of the high nitrogen Cr-Ni alloys which is around 500MPa. Titanium and niobium are added to increase the mechanical properties by the formation of precipitates [25]. The commonly known and widely researched alloy is AISI 304. This research focusses on AISI 301LN, which is lean alloyed and metastable.

**II. Cr-Ni-Mo grades**

This grade has a chromium content of around 17%, nickel content of 10~13% and 2~3% molybdenum. It is also known as “general purpose grades”, and sometimes called “acid-proof” type of stainless steel due to increased corrosion resistance because of molybdenum additions. Nitrogen and Sulphur could be added to improve strength and machinability respectively. Titanium and niobium could be added in stabilized grades to increase the mechanical and weldability properties by the formation of precipitates at high temperatures [25].

**III. Cr-Mn grades**

This grade is known as “200-series” grades according to AISI/ASTM standards. It has lower nickel content with the austenitic microstructure stabilized by manganese and nitrogen [25], [9].

**IV. High temperature austenitic grades**

This grade has high chromium (17–25 %), high nickel (8–20 %) content with no molybdenum. It is designed to be used at high temperatures above 550 °C for long service life where creep strength is important. In dry gases, it has good oxidation resistance in addition to aqueous corrosion resistance. Silicon and cerium are added to increase oxidation resistance. Nitrogen is added in some grades to increase creep strength [25].

**V. High performance austenitic grades**

This grade has high alloying content with chromium content varying between 17~25%, nickel content varying between 14 ~ 25% and molybdenum varying between 3 ~ 7%. This type of grade is designed for very demanding environments. Nitrogen could be added to further increase the corrosion resistance and strength. Copper is added in some grades to increase the resistance to certain acids [25].

### 2.1.2 Ferritic Stainless Steel

This is the simplest type of stainless steel alloyed with 11.2~19% chromium, with no to very small amounts of nickel (for economic purposes as the nickel price is volatile). Other alloying elements that can be added include molybdenum for corrosion resistance and niobium and/or titanium to improve weldability. The ferritic microstructure is body-centered-cubic and magnetic. This type of steel is commonly used in making washing machine drums due to their corrosion and oxidation resistance nature [25].

### 2.1.3 Martensitic Stainless Steel

This type of stainless steel has higher carbon content as compared to other types of steels for strength and hardenability. This class of steel can be hardened by quenching and tempering to increase ductility and toughness. The crystallographic structure is body-centered-tetragonal (BCT). Little to no nickel is added to this type of steel, and molybdenum is sometimes added for improved ductility and corrosion resistance. Due to the high carbon content, the weldability of this type of steel is poor. Adding some nickel and reducing the carbon content results in the

improvement in the weldability of martensitic steel. This type of steel is magnetic and hardenable [25].

### 2.1.4 Duplex Stainless Steel

This type of steel has a phase balance of approximately 50% austenite and 50% ferrite; hence have a ferritic-austenitic microstructure. It was designed to combine the beneficial properties of ferritic as well as of austenitic stainless steel. The duplex microstructure gives rise to high strength and high resistance to stress corrosion which in turn is largely because of the characteristic composition of the duplex stainless steels which have higher chromium content (20.1-25.4%), lower nickel content (1.4-7%) as compared to the austenitic grades. The yield strength of an annealed duplex steel is around 2 times the yield strength of each individual phase alone, in the range of 550 ~ 690 MPa. Corrosion resistance can be improved by molybdenum (0.3-4%) and nitrogen additions, which balance the microstructure. The lower nickel content makes the duplex grades more price stable as compared to austenitic grades and as a partial replacement of nickel, manganese is added in some grades. Manganese increases the solubility of nitrogen into the material thereby increasing the strength as well. Due to the ferrite content, this type of steel is magnetic [25].

### 2.1.5 Precipitation-hardened (PH) Stainless Steel

The formation of fine intermetallic precipitates within the microstructure results in high strength and good fracture toughness [26]. This type of steel is magnetic [25]. The microstructure consists of martensite and metastable austenite or a mixture of the two phases. Metastable austenite transforms to strain-induced martensite if deformed at a temperature below $M_d$ (30/50). The $M_d$(30/50) temperature as defined by Angel [27], is the temperature at which 50% martensite will form at 30% true strain deformation. Formability and work hardening of precipitation-hardened stainless steels are greatly enhanced by the strain-induced martensitic transformation [26]. The precipitation hardenable stainless steels can attain a high tensile strength of up to 1700 MPa, which is similar to martensitic steels. This grade is used in specialized applications where high strength and corrosion resistance are required.

## 2.2 The effects of alloying elements in stainless steels

The microstructure and mechanical-property inter-relationships of steel are due to the combined effect of the alloying elements coupled with heat treatments and impurities present. A

desired microstructure is obtained by a careful balancing of the different alloying elements during processing. Some alloying elements have stronger effect on the microstructure than others [25]. Some elements such as V, Nb and Ti are added for grain size refinement in metastable austenitic stainless steels [12]. The alloying elements can be divided into either ferrite-stabilisers or austenite-stabilisers [25].

### 2.2.1 Ferrite stabilisers

i. Chromium (Cr)

It gives basic corrosion resistance by formation of a surface passive film of chromium oxide, resistance to oxidation at elevated temperatures and promotes ferritic microstructure [25].

ii. Silicon (Si)

It improves oxidation resistance at high temperatures and in strongly oxidizing solutions at lower temperatures. It promotes a ferritic microstructure and increases strength [25].

iii. Molybdenum (Mo)

Molybdenum promotes ferritic microstructure and increases the mechanical strength. Molybdenum increases strength at elevated temperatures, creep resistance, uniform and localized corrosion resistance by increasing the pitting potential of the potentiometric curve. Molybdenum increases hardness in martensitic steels at higher tempering temperatures due to carbide precipitation. However, in ferritic, duplex and austenitic steels care should be taken regarding the level of molybdenum as molybdenum promotes formation of secondary phases [25].

iv. Titanium (Ti)

Titanium promotes a ferritic microstructure. It improves toughness, formability and corrosion resistance in ferritic stainless steels. It lowers the martensite hardness in martensitic steels through formation of carbides and thereby increases tempering resistance. It forms intermetallic compounds in precipitation hardening steels thereby resulting in increase in strength. It increases weldability, intergranular corrosion resistance and mechanical properties at high temperatures in stabilized grades of austenitic steels by combining with carbon [25].

v. Niobium (Nb)

Niobium (formally known as columbium) promotes a ferritic microstructure and increases mechanical properties at high temperatures. This element can be added as grain refiner.

It improves weldability and intergranular corrosion resistance by improving resistance in sensitization in stabilized grades of austenitic and ferritic steels by combining with carbon. It lowers the martensite hardness in martensitic steels through formation of carbides thereby increases tempering resistance [25].

vi. Aluminium (Al)

Aluminium improves oxidation resistance. It increases strength in the aged condition by formation of intermetallic compounds in precipitation hardening steels. It is a strong ferrite former which lowers the hardenability of stainless steels [25].

vii. Vanadium (V)

Vanadium promotes ferritic microstructure. It increases the hardness in martensitic steels through formation of carbides and it increases tempering resistance and toughness. It can only be added in hardenable stainless steels [25].

### 2.2.2 Austenite stabilizers

i. Nickel (Ni)

It stabilizes the austenitic microstructure resulting in increased ductility and toughness. It also reduces the corrosion rate in the active state and hence is advantageous in acid environments such as industrial atmospheres, chemical and textile processing industries. In precipitation hardening steels, nickel is used to form intermetallic compounds that are used to increase strength. In martensitic grades, nickel addition combined with lowered carbon content improves weldability [25].

ii. Manganese (Mn)

It improves hot ductility. Its effect on the ferrite/austenite balance varies with temperature: at low temperature manganese is an austenite stabilizer but at high temperatures it is a ferrite stabilizer. Manganese increases the solubility of nitrogen and is used to obtain high nitrogen contents in duplex and austenitic stainless steels. Manganese, as an austenite former, can partially replace nickel in the 200 series stainless steel [25].

iii. Carbon (C)

Carbon is a strong austenite former that significantly increases the mechanical strength of the alloy. However, it increases susceptibility to intergranular corrosion by carbide formation of

the form $M_{23}C_6$ where M is chromium, which was a problem in the early stainless steels. The modern grades do not suffer from intergranular corrosion due to the low carbon content. Low carbon versions, designated as "L" are preferred so as to guarantee corrosion resistance of the weld seam as good as of the base metal [28], [29]. Carbon will strongly reduce both toughness and corrosion resistance in ferritic stainless steels whilst in martensitic steels, it increases hardness and strength but impairs toughness [25].

iv. Nitrogen (N)

It improves the mechanical properties in both strength and hardness, and further increase localized corrosion resistance. However, increased nitrogen content may cause hot ductility problems [7]. Nitrogen reduces the toughness in both ferritic and martensitic stainless steels leading to severe material embrittlement due to nitride precipitation [30]. Nitrogen influences the solid solution strength and strain-induced martensitic transformation in austenitic stainless steels. Nitrogen is a strong austenite stabilizer and hence retards the strain-induced martensitic transformation and promotes twinning in austenitic stainless steels upon cold deformation [31].

v. Copper (Cu)

Copper promotes austenitic microstructure, hence improves formability and corrosion resistance in certain acids. It improves machinability by decreasing work hardening [25].

### 2.3 Strengthening mechanisms in stainless steels

There is a wide range of methods that can be used to strengthen austenitic stainless steels which include: strain – induced martensitic transformation strengthening, solid solute strengthening, precipitation hardening, alloying, work (strain) hardening and grain size refinement [12], [32]. Strengthening is associated with increase in hardness, strength, toughness and fatigue resistance. The work hardening rate depends on the composition of alloys. Lean chemical composition and hence low stacking fault energy results in increased work hardening during cold deformation leading to higher flow strength. AISI 301LN is a lean alloyed and has been proposed to have the highest work hardening rate among the 300-series austenitic steels. The AISI 301LN is described as metastable due to low stacking fault energy values at room temperature. During cold deformation, austenite transforms to strain-induced martensite resulting in increase in strength [33].

### 2.3.1 Grain size refinement

In metastable austenitic stainless steels, grain size refinement is an effective method to increase the yield strength but at the expense of strain-hardening rate [7]. This is achieved through an advanced thermomechanical process which involves alternate steps of heavy cold rolling to induce large amount of martensite followed by an intermediate/reversion annealing treatment to form ultra/fine-grained austenitic microstructure [2], [16]. A typical thermomechanical treatment consisting of cold rolling with a total reduction ranging from 50 to 90% has been found to have increased yield strength from 250–350 MPa to 1200–1600 MPa [34]. High density of grain boundaries serves as barriers to dislocation movement. A higher amount of stress is thus required to cause plastic deformation. In metastable austenitic stainless steels, plastic deformation produces small lattice defects which act as embryos for the nucleation of the martensitic phase. The martensitic phase nucleates at the intersections of microscopic shear bands which comprise of dense bundles of overlapping stacking faults which acts as precursors for mechanical twins and/or ε-martensite [35], [36], [37]. The saturated amount of martensite is dependent on processing variables such as temperature of deformation (including that due to adiabatic heating), rate of deformation (strain rate), alloy chemistry and initial austenitic grain size. Further deformation results in the crushing of martensite which leads to fragmentation of martensite laths forming a high density of defects which in turn provides nucleation sites for austenite on the reverse martensitic transformation giving rise to control of microstructure and grain refinement during annealing. The nano- or ultrafine-grained microstructure has improved combination of strength and ductility [17]. Grain size refinement maintains anisotropy in mechanical properties [9]. Grain sizes in the order of 2μm are reported to have been obtained for AISI 301 in the literature [7]. A lower stacking fault energy leads to a better grain refinement with enhanced strength [38].

### 2.3.2 Dislocation strengthening

The ability of dislocations to move, slip, cross-slip, climb or glide during deformation has an influence on the mechanical properties of austenitic steels. The dislocations in austenitic steels with low stacking fault energy dissociate to partial Shockley dislocations with wider stacking faults during deformation [39]. A stacking fault binds the dissociated partial dislocations making them move as a unit along the slip plane [7].

### 2.3.3 Strain hardening

Unlike martensitic steels where quench and partitioning could result in hardening of steels, austenitic, duplex and precipitation hardened stainless steels can be hardened by strain (work) hardening Cold plastic deformation causes generation of dislocations. The concentration of dislocations increases with further plastic deformation resulting in entangling of each other inhibiting further dislocation motion thereby increasing the metallic strength. It has been reported in the literature that the maximum UTS attained through cold rolling of AISI 301LN is 970MPa which is lower than the required 1000 ~ 1150 MPa for manufacture of railway carriage [11]. Severe cold rolling impairs ductility and hardness beyond tolerable limits. The disadvantage of strengthening by cold rolling is the introduction of anisotropy of mechanical properties. The strength becomes different relative to the direction of testing. The strength in tension and compression is different [9]. Temper rolling results in strain-induced martensitic formation in addition to strain hardening resulting in increase in strength [40]. The strength levels are matched to the design requirement for structural stainless steel through temper rolling.

### 2.3.4 Solid solution strengthening

This involves the dissolving of alloying elements such as interstitial elements of carbon and nitrogen or substitutional elements. The differences in size of atoms creates strain fields which with dislocation movement. The atoms of solute element distort the crystal lattice, for example carbon atoms distorts the bcc structure of martensite to bct. The distortion of crystal lattice results in increased resistance to the mobility of dislocations resulting in increased strength. Interstitial elements are more effective in solid solution hardening as compared to the substitutional elements [41], [42].

### 2.3.5 Dispersion strengthening

This involves the strengthening of a soft ductile matrix with fine hard particles in significant amounts such as in composite materials. In metastable austenitic stainless steels, the second hardening effect due to martensitic transformation results in increased inhibition of dislocation movement leading to increase in strength of the material. The increase in strength is directly proportional to the volume fraction and distribution of the second hardening phase [43].

### 2.3.6 Precipitation (age hardening) strengthening

This involves the precipitation of a second phase of fine precipitates from a supersaturated solid solution. The fine precipitates act as pinning points in a similar manner to solutes, though the particles are not necessarily single atoms. This results in increased resistance to dislocation movements during deformation leading to increased strength. The degree of strengthening is not only dependent upon the size but also on the volume fraction of the particles [42].

### 2.3.7 Transformation strengthening

In metastable austenitic stainless steels, plastic deformation induces solid-state austenite to strain-induced martensitic transformation. The dislocation density is high in the martensite phase as compared to the austenite phase. The increased dislocation density further hinders dislocation movement during cold working leading to increase in strength [44].

## 2.4 Thermodynamics behind martensitic phase transformation

Thermodynamic modelling provides a powerful tool in manipulating thermo-mechanical treatment processes to achieve a desired property in the material. It enables the calculation of Gibbs free energies of phases and chemical driving force for martensitic transformation during deformation at given conditions of alloying content and temperature [45].

The athermal martensitic transformation can only take place if the difference in chemical free energy of austenite and martensite reaches a critical value of $\Delta G^{\gamma\rightarrow\alpha'}{}_{Ms}$ as indicated in Figure 2.1, which shows the variation of Gibbs free energy of martensite, annealed and deformed austenite as a function of temperature. The temperature corresponding to the critical Gibbs free energy value of $\Delta G^{\gamma\rightarrow\alpha'}{}_{Ms}$ is the martensite start ($M_s$) temperature. However, this transformation can take place at a higher temperature ($T_1$) if sufficient stress is applied [46]. The Gibbs free energy for austenite to martensite transformation is then given by the sum of chemical and mechanical components as shown below [47]:

$\Delta G^{\gamma\rightarrow\alpha'}{}_{T1} + \Delta G_{MECH} \rightarrow \Delta G^{\gamma\rightarrow\alpha'}{}_{Ms}$ (with $T_1 > M_S$), where $\Delta G_{MECH}$ is zero if no stress is applied during transformation [47].

$\Delta G_{MECH}$ required for $\gamma\rightarrow\alpha'$ transformation decreases with undercooling below the critical temperature, $T_0$.

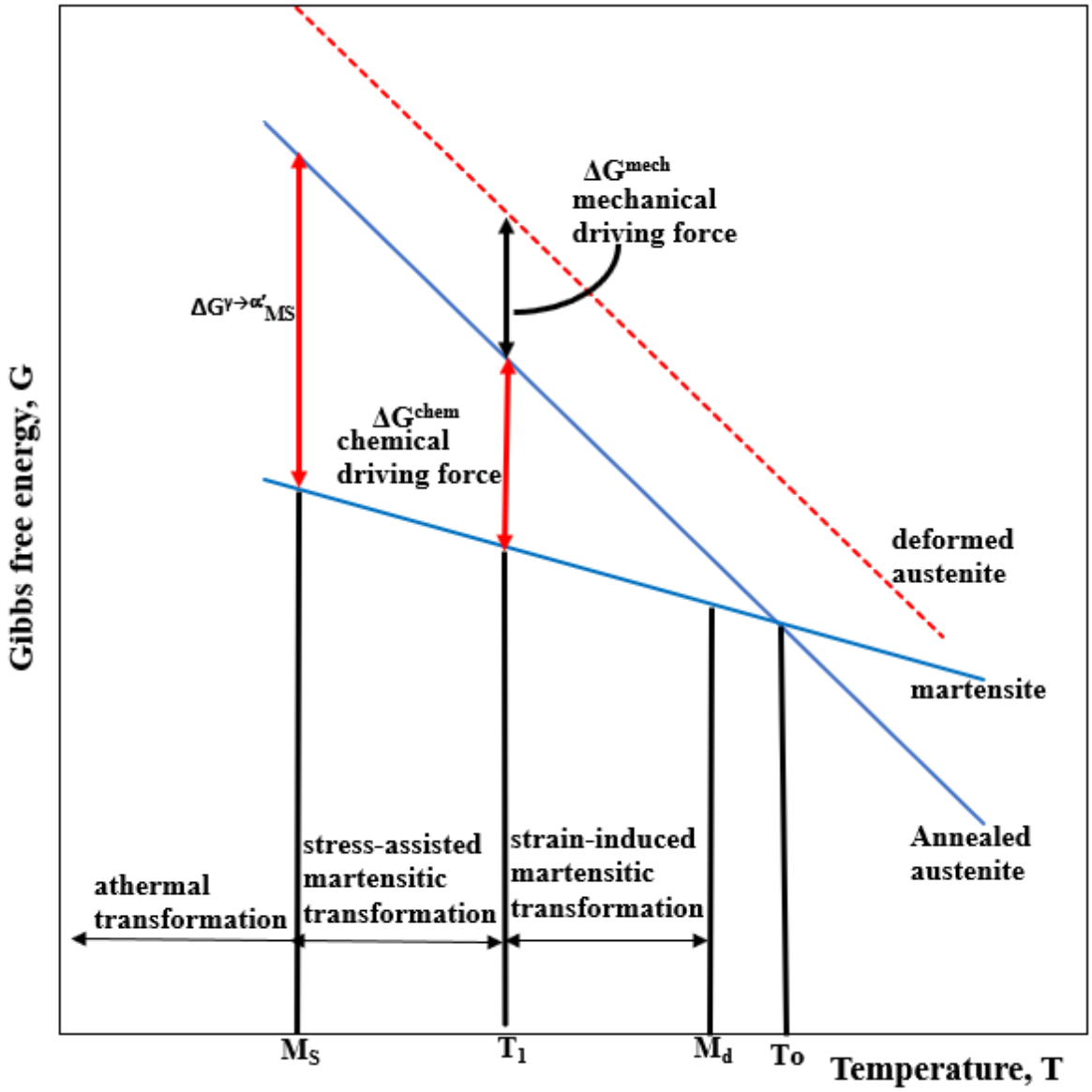


**Figure 2.1 Gibbs free energy diagram for martensite, annealed and deformed austenite as a function of temperature [48], [49], [50], [51]**

AISI 301LN austenitic stainless steels are thermodynamically metastable steel which undergo martensitic transformation upon cold deformation leading to the Transformation Induced Plasticity (TRIP) effect. The TRIP effect is the deformation mechanism of metastable austenitic stainless steels which is accompanied by martensitic phase transformation leading to increased strain hardening. The thermodynamics that underlie such phase transformation, particularly the role of Gibbs free energy and its components, such as the driving force needs to be understood. It is particularly the interplay between the Gibbs free energy, driving force and various retarding forces that determines the outcome of the microstructure in any phase

transformation. The critical Gibbs energy for martensitic transformation needs to be determined at the $M_s$ temperature of the alloy. The variation of Gibbs free energy of martensite and austenite phases as well as the influence of deformation on Gibbs free energy of austenite as a function of temperature [48]. The thermodynamics of strain-induced transformation is as illustrated in Figure 2.1. The chemical driving force for the martensitic transformation at a particular temperature is given by the difference of Gibbs free energy of austenite and martensite phases.

**2.5 Stacking Fault energy (SFE)**

Stacking fault energy (SFE) plays a key role in the deformation behavior of austenitic stainless steels. SFE measurements can be done by Transmission Electron Microscopy (TEM), X-Ray diffraction (XRD) or neutron diffraction. During plastic deformation, the work-hardening rate, and the deformation mode (whether homogeneous slip, cross slip or twinning) are all correlated with the stacking fault energy (SFE) of the material [52], [39]. The lower the value of the stacking fault energy the more metastable the austenitic stainless steel becomes, leading to a large degree of dislocation dissociation into partials which strongly hinders the cross slip.

Figure 2.2 shows the deformation mechanisms as a function of testing temperature in correlation with the SFE and the mechanical properties of a CrMnNi TRIP/TWIP steel. The $M_d$ temperature is the temperature beyond which no strain-induced martensite forms upon plastic deformation [43], [53], [54]. Therefore, $M_s$ and $M_d$ temperatures are the lower and upper limit for the SIM transformation from the thermodynamically metastable austenite upon deformation. The smaller the difference between the $M_s$ and $M_d$ temperatures, the higher the stability of austenite against strain-induced martensitic transformation. [45], [55]. Similarly, Remy and Pineau defined $E_s$ and $E_d$ temperatures. $E_s$ is the temperature for spontaneous $\gamma \rightarrow \varepsilon$ martensitic transformation and $E_d$ is the maximum temperature beyond which no $\gamma \rightarrow \varepsilon$ martensitic transformation can be induced upon plastic deformation [56]. $T_s$ and $T_d$ could be defined in the same manner with respect to the temperature at which twinning starts forming during deformation and a temperature beyond which no twinning forms. The deformation mechanism will be just through dislocation glide (refer to Figure 2.2). The austenite stability indicators are all correlated with the SFE of the alloy.

Accordingly, the austenite to martensite transformation could occur at temperatures even higher than the $M_s$ temperature during deformation [7], [57]. The deformation mechanism shifts from dislocation glide and formation of ε-martensite to dislocation glide and mechanical

twinning and then to pure dislocation glide/slip as the SFE increases [52], [58]. The following transformation sequences with increasing cold work, have been reported in literature: γ (face-centred cubic [fcc]) → dislocations → stacking faults → mechanical twinning (γ′) → ε-martensite (hexagonal close packed [hcp]) → α′-martensite (body-centred cubic [bcc]) and γ → dislocations → α′-martensite [7], [52], [57], [59], [60], [61], [62], [63], [64], [65], [66], [67], [68], [69], [70], [71], [72].

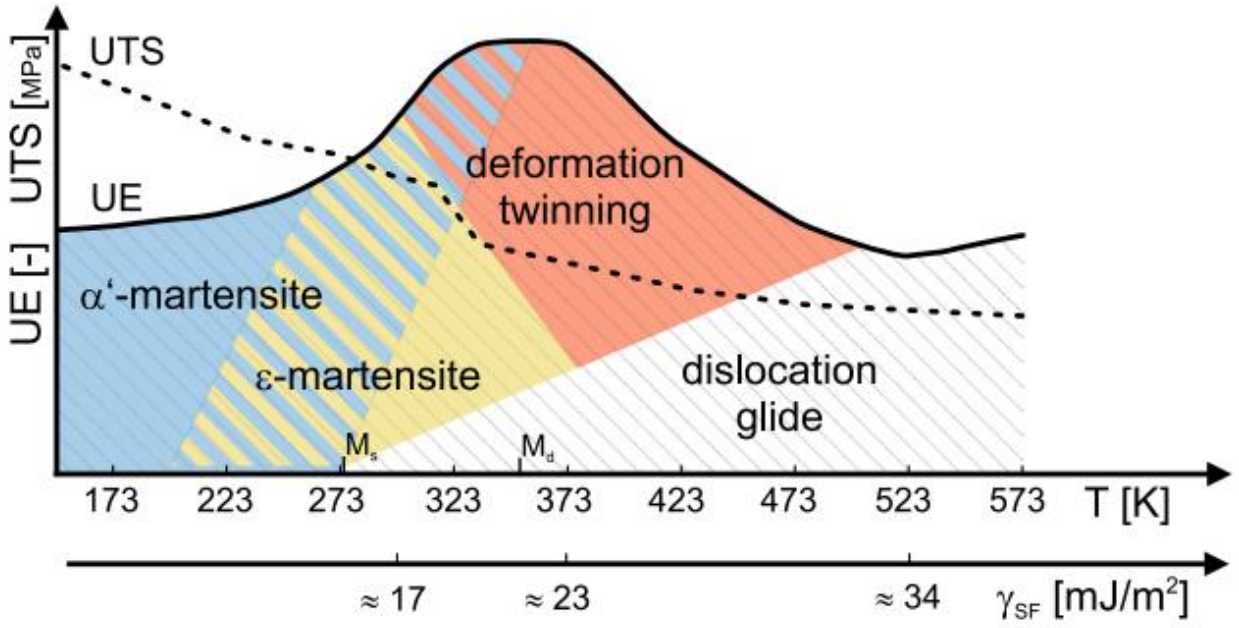


**Figure 2.2: Overview of the deformation mechanisms as a function of testing temperature in correlation with the SFE and the mechanical properties of a CrMnNi TRIP/TWIP steel [73].**

AISI 301LN is a very lean alloyed stainless steel, hence it has the lowest SFE among the 300-series austenitic stainless steels. The lower SFE of metastable austenitic stainless steels makes them amenable to strain-induced martensitic transformation upon deformation and this results in grain refinement upon reversion annealing for higher strength without much sacrifice in ductility [55], [74]. The SFE, however, is not only a function of chemistry (composition-sensitive parameter) but also a function of the deformation temperature (including that due to adiabatic heating) [52], [59], [75], [76], [77], [78]. The formation of planar lattice defects such as stacking faults, deformation twins and ε-martensite particularly depends on the value of the stacking fault energy [79], [80], [81]. The adiabatic heating results in an increase in SFE and high values of the SFE can result in twinning and cross slip without the formation of ε-martensite [82], [60]. Typical SFE values for austenite (γ) to ε- and/or α′-martensitic transformation have

been reported to be below 20 $mJm^{-2}$, whereas mechanical twinning is promoted if the SFE lies in the range between 15 and 30 $mJm^{-2}$ [83], [84]. This is confirmed in Figure 2.2 where formation of ε- martensite is shown up to SFE of 20 $mJm^{-2}$ with mechanical twinning shown to be dominating from SFE in the range between 15 ~ 30 $mJm^{-2}$. A mixture of ε-martensite and mechanical twins has been reported in literature rather than purely ε-martensite or purely mechanical twins [52]. Mechanical twinning and ε-martensite act as intermediate phases in the transformation of austenite to α′-martensite. The formation of ε-martensite and mechanical twins during plastic deformation strongly depend on the SFE and deformation temperature [85].

Figure 2.3 shows deformation mechanism as a function of SFE. Different values of upper limit of SFE for which the deformation mechanism changes from TRIP effect to TWIP effect has been reported in the literature ranging from 18 to 20 $mJm^{-2}$. Slight variation is attributed to the chemical composition of the studied alloys, grain size, accuracy of the method of SFE measurement used, density and configuration of dislocations [86]. A decrease in SFE, on the other hand, leads to an increase in stored energy during cold deformation as cross slipping becomes more difficult to achieve and this leads to, inter alia, reduction in the recrystallization start temperature during annealing [13]. Yonezawa et al. have showed that different heat treatment conditions have effects on SFE values of austenitic stainless steels [87].

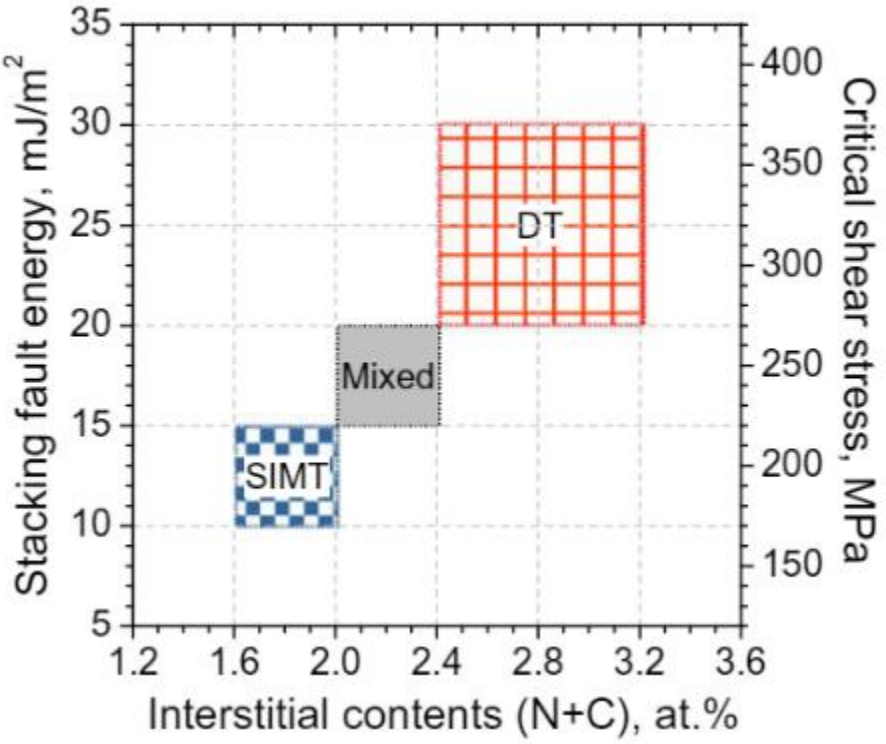


**Figure 2.3: Deformation mechanism as a function of SFE [88]**

Talonen et al. observed the presence of ε-martensite in steels with SFE < 18 $mJm^{-2}$ [39]. The formation of ε-martensite is not necessarily a precursor for α′-martensite formation especially if either the chemical composition, strain rate and/or temperature had been altered giving a high SFE [7], [89], [39]. Simultaneous mechanical twinning and α′-martensitic transformation has been reported in literature if the SFE lies between 15 and 20 $mJm^{-2}$ due to similar deformation mechanisms for formation and evolution of twins and ε-martensite [36], [52], [90], [91]. For higher stacking fault energies, plasticity and strain hardening are controlled exclusively by dislocation glide processes [77], [75]. The theoretical temperature dependence of SFE, $d\gamma/dT$ for 18-8 stainless steel has been approximated as 0.1 $mJm^{-2}K^{-1}$ [39], [92], [93].

Mahato et al. reported an increase of SFE during deformation of TWIP steels from 19.9 $mJ/m^2$ at 2% strain, 23.4 $mJ/m^2$ at 5% strain to over 40 $mJ/m^2$ at 46% [94]. This explains why ε-martensite is formed in the early stages of the deformation in TRIP steels with low SFE and the transformation mechanisms changes to solely, γ → dislocations → α′-martensite with increase in plastic deformation. The formation of ε-martensite is suppressed with increase in SFE and deformation temperature and, conversely the formation of mechanical twins is promoted with an increase in SFE and deformation temperature [52], [63].

Table 2.1 shows the most widely used equations to estimate the SFE of Fe-Ni-Cr-based alloys [95]. It is important to note that most of the equations do not include the effect of the nitrogen content, which is inconsistency with the results shown in Figure 2.4, which shows marked difference of volume fraction of strain-induced martensite as a function of strain with slight variation in nitrogen content. Moreover, the equations have been determined by multiple regression analysis by considering only a limited number of alloying elements. This makes the applicability of the equations to limited chemical compositions [96]. Vitos et al. demonstrated that the effect of alloying elements is dependent on the host composition. The same alloying element may cause a different change on the SFE depending on the host composition. This means that there is no universal composition-based equations to calculate SFE [97]. The derived SFE values for the tested alloys in this thesis range from 4.7 $mJ/m^2$ to 29.4 $mJ/m^2$. Talonen and Hanninen [39] determined the SFE of AISI 301LN using X-ray diffraction and obtained an average value of approximately 14.7 ± 0.8 $mJ/m^2$. This value is very close to 15.3 $mJ/m^2$, as derived using both Brofman and Ansell equation, and Pickering equation.

**Table 2.1: Equations to estimate the SFE of Fe-Ni-Cr-based alloys**

| Authors | Equation | Calculated range, for tested AISI 301LN, mJ/m$^2$ | Alloys used | References |
|---|---|---|---|---|
| Schramm and Reed | –53 + 6.2(%Ni) + 0.7(%Cr) + 3.2(%Mn) + 9.3(%Mo) | 4.66 ~ 6.58 | | [7], [13], [57], [98], [99], [100] |
| Brofman and Ansell | 16.7 + 2.1(%Ni) -0.9(%Cr) + 26(%C) | 15.3 ~ 15.4 | 9 ~ 20% Cr, 5 ~ 20% Ni, ≤ 0.29% C < 0.1% other elements. | [7], [101] |
| Rhodes and Thompson | 1.2 + 1.4(%Ni) + 0.6(%Cr) + 17.7(%Mn) – 44.7(%Si) | 26.2 ~ 29.4 | AISI 310 | [102] |
| Pickering | 25.7 + 2(%Ni) + 410(%C) - 0.9(%Cr) – 77(%N) – 13(%Si) – 1.2(%Mn) | 15.3 ~ 16.9 | ~ 16% Cr, ~ 7% Mn ~ 6% Ni | [103] |
| Qi-Xun et al. | $39 + 1.59(\%Ni) – 1.34(\%Mn) + 0.06(\%Mn)^2 -1.75(\%Cr) + 0.01(\%Cr)^2 + 15.21(\%Mo) – 5.59(\%Si) – 60.69(\%C + 1.2\%N)^{0.5} + 26.27(\%C + 1.2\%N)(\%Cr + \%Mn + \%Mo)^{0.5} + 0.61[\%Ni(\%Cr + \%Mn)]^{0.5}$ | 19.2 ~ 20.9 | ~ 40% Mn, ~ 25% Cr, ~ 23% Ni, ~ 2% Mo, ~ 4% Si, ~ 0.045% (C and N) with a total amount of alloying elements ≤ 45% | [104] |
| Ojima et al. | 5.53 + 1.4(%Ni) - 0.16(%Cr) + 17.1(%N) | 13.8 ~ 13.9 | 10 ~ 25%Cr, 4 ~ 25% Ni, < 1.3% Mn, < 1% N | [105]. |
| Yonezawa et al. | -7.1 + 2.8(%Ni) + 0.49(%Cr) + 2.0(%Mo) – 2.0(%Si) + 0.75(%Mn) – 5.7(%C) - 24(%N) | 17.2 ~ 17.8 | 10 ~ 16%Ni, 13 ~ 18%Cr, 0 ~ 3% Mo, 0 ~ 2% Si, 0 ~ 4% Mn, 0 ~ 0.08% C. 0 ~ 0.1% N | [87] |

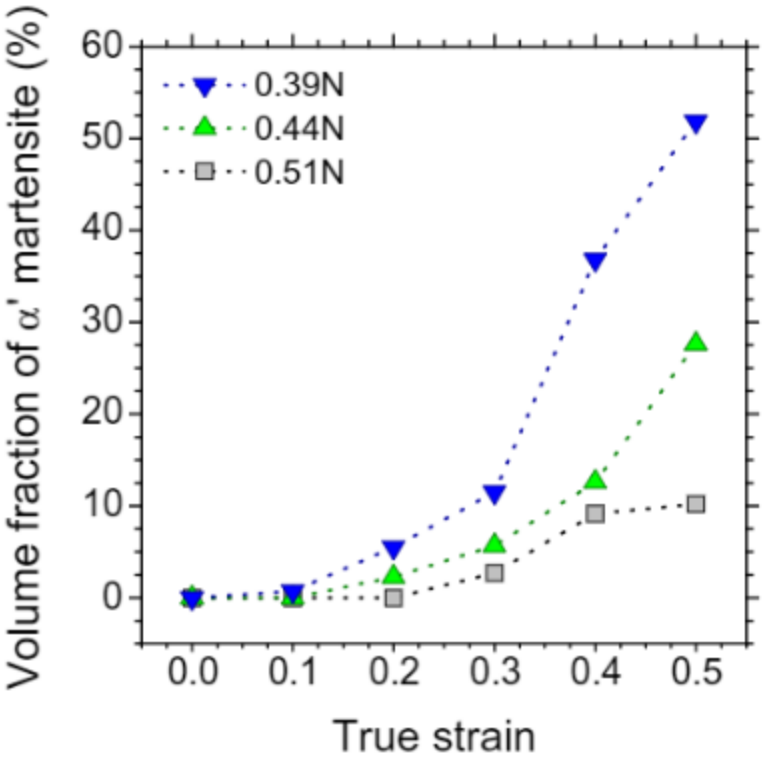


**Figure 2.4: Influence of nitrogen on SIMT [88]**

Table 2.2 shows some empirical equations that have been proposed to estimate the $M_d$ (30/50) temperature in determining the influence of chemistry on the martensitic transformation of Fe-Ni-Cr-based alloys. Based on chemistry, $M_d$ (30/50) parameter can be used as the austenite stability indicator. In some of the classic literature regarding martensite formation, including the equations in Table 2.2, carbon and nitrogen are assigned similar potencies regarding austenite stabilization. For example, the Eichelman and Hull equation to calculate the Martensite start temperature ($M_s$), Gladman equation, and the Angel equation as well as the Nohara et al. modification to calculate the $M_d$ (30/50) temperature for 18-8 stainless steel [106] uses the same constant for both the carbon and nitrogen content. However, more recent research work by Masumura et al. had shown that nitrogen has a stronger austenite stabilization effect compared to carbon [107], [108]. The Sjöberg equation [17], takes the independent effects of carbon and nitrogen into account. There is a strong relationship between the $M_d$ (30/50) temperature and chemical composition of the alloy. Stable austenitic steels such as AISI 309, AISI 316 and AISI 321 have very low $M_d$ temperatures, hence do not present strong martensitic transformation when deformed at room temperature [57].

**Table 2.2: Empirical equations to estimate the $M_d$ (30/50) temperature of Fe-Ni-Cr-based alloys**

| Authors | Equation | Calculated range, for tested AISI 301LN, °C | References |
|---|---|---|---|
| Angel | 413 – 13.7(%Cr) – 9.5(%Ni) - 8.1(%Mn) - 18.5(%Mo) - 9.2(%Si) - 462(%[C+N]) | 29.8 ~ 34.4 | [13], [57], [109] |
| Nohara | 552 – 13.7(%Cr) – 29(%[Ni+Cu]) - 8.1(%Mn) - 18.5(%Mo) - 9.2(%Si) - 68(%Nb) - 462(%[C+N]) - 1.42(GS-8) where GS is ASTM grain size number | 37.0 ~ 45.5 | [110], [111], [112] |
| Sjoberg | 608 – 515(%C) – 821(%N) – 7.8(%Si) - 12(%Mn) - 13(%Cr) - 34(%Ni) -6.5(%Mo) | 30.1 ~ 35.3 | [17] |
| Gladman | 497 – 462(%C + %N) – 9.2(%Si) – 8.1(%Mn) – 13.7(%Cr) – 20(%Ni) – 18.5(%Mo) | 44.5 ~ 49.9 | [113] |

## 2.6 Phase Transformation

Microstructural evolution holds an important key in understanding the austenitic stainless steels (A.S.S) material's behavior during forming operations [35]. The strain-induced martensitic transformation occurs between the martensitic start ($M_s$) temperature and the $M_d$ temperature. The $M_d$ temperature is a critical temperature above which austenite is stable and no martensitic transformation takes place upon deformation [65].

### 2.6.1 Austenite

In metastable austenitic stainless steels (MASS), the austenite phase is stable at a higher temperature as compared to the martensite phase. The phase is described as metastable if it transforms to martensite upon deformation at room temperature thereby increasing the mechanical strength of the material [79].

### 2.6.2 Martensite

There are two distinct types of martensite which can be formed, α′(bcc/bct) and ε(hcp) martensite, during cold deformation below the $M_d$ temperature [57], [114]. The crystallography of these two types of martensite differs distinctly.

#### 2.6.2.1 Epsilon (ε) martensite

This form of martensite can be formed through cooling and/or deformation (strain induced) [39]. The ε-martensite (hexagonal) is highly metastable with a low Gibbs free energy

slightly less than that of the austenite (fcc) structure [115]. There is a strong dependence of the volume fraction of ε-martensite on deformation temperature [116]. This was observed in austenitic TRIP steels with less than 13 mJ/m$^2$.

The ε-martensite phase is formed by overlapping stacking faults which are formed in the early stages of deformation (at strains lower than 0.15) hence it is considered as an intermediate phase in the transformation of austenite to α′-martensite [117], [118].

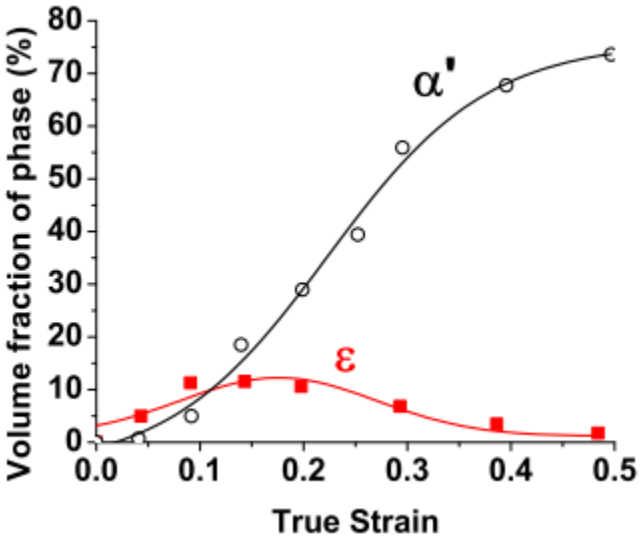


**Figure 2.5: Percentages of α′ and ε martensites as a function of tensile strain at room-temperature tensile of grade 301 as measured by X-ray diffraction [119]**

The decrease in ε-martensite after reaching the peak in all steels as a function of percentage of cold rolling in Figure 2.6 indicates that ε-martensite transforms to α′-martensite with further cold rolling [107].

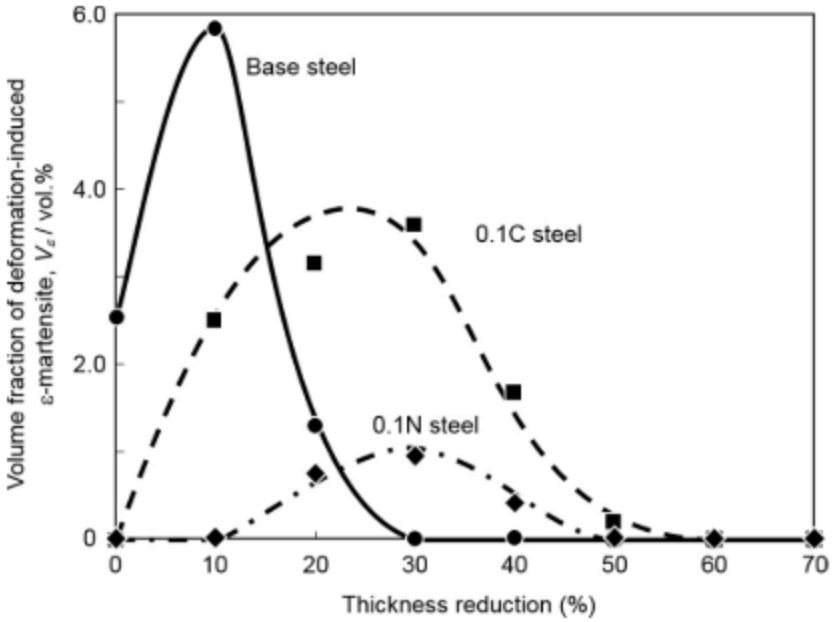


**Figure 2.6: Variation of volume fraction of deformation-induced ε martensite as a function of thickness reduction by cold rolling in different steels [107]**

### 2.6.2.2 α′-Martensite

The crystallographic structure of α′-martensite is body-centred cubic/body centred tetragonal depending with the amount of carbon. With very low carbon content, it is body-centred cubic. The martensitic transformation can be either thermally induced or strain-induced or stress-induced [45]. Athermal martensite was found to be nucleating preferably at ε-martensite, annealing twins and grain boundaries [120]. An empirical equation for the $M_s$ temperature by Eichelmann and Hull [106] for 18-8 austenitic stainless steels, is given in equation (2.1):

$$M_s\,(°C) = 41.7*(14.6-Cr) + 5.6*(8.9-Ni) + 33.3*(1.33-Mn) + 27.8*(0.47-Si) +$$

$$1666.7*(0.068-C-N) - 17.8 \quad \text{Equation 2.1}$$

For all 300-series of austenitic stainless steel, the $M_s$ temperature falls into the cryogenic range below 0 °C [57].

#### 2.6.2.2.1 Strain-induced (α′) martensite

The intersection of shear bands and ε-martensite are the favorable nucleation sites for α′-martensite formation [7], [39], [120], [121]. Plastic deformation produces small lattice defects which act as embryos for the nucleation of martensitic phase. The martensitic phase nucleates as embryos that forms at the intersections of microscopic shear bands which comprise of bundles of

overlapping stacking faults, mechanical twins and ε-martensite [122]. The formation of shear bands are necessary precursors for strain-induced martensitic transformation [7], [39]. As the plastic deformation increases, and/or cryogenic temperature lowered, the α′-martensite grows by consuming of ε-martensite, mechanical twins and austenite phases [123], [86]. The α′-martensite formed is lath-like in terms of morphology [32], [35], [46], [89]. The phase transformation leads to an increase in strength in metastable austenitic stainless steels (MASSs) during cold rolling. The martensite phase has higher strength than austenite of the same chemical composition. The formation of strain-induced martensite accommodates additional strain, hence the phase transformation leads to an increase in strain hardening rate, resulting in excellent combinations of strength, toughness and ductility at low cost [32], [36], [52], [79], [53]. There is no strain-induced martensitic transformation for highly stable austenitic steels with no much increase in the strength through strain hardening [33].

Figure 2.7 shows different mechanisms for martensitic transformation in metastable austenitic stainless steels as a function of deformation temperature.

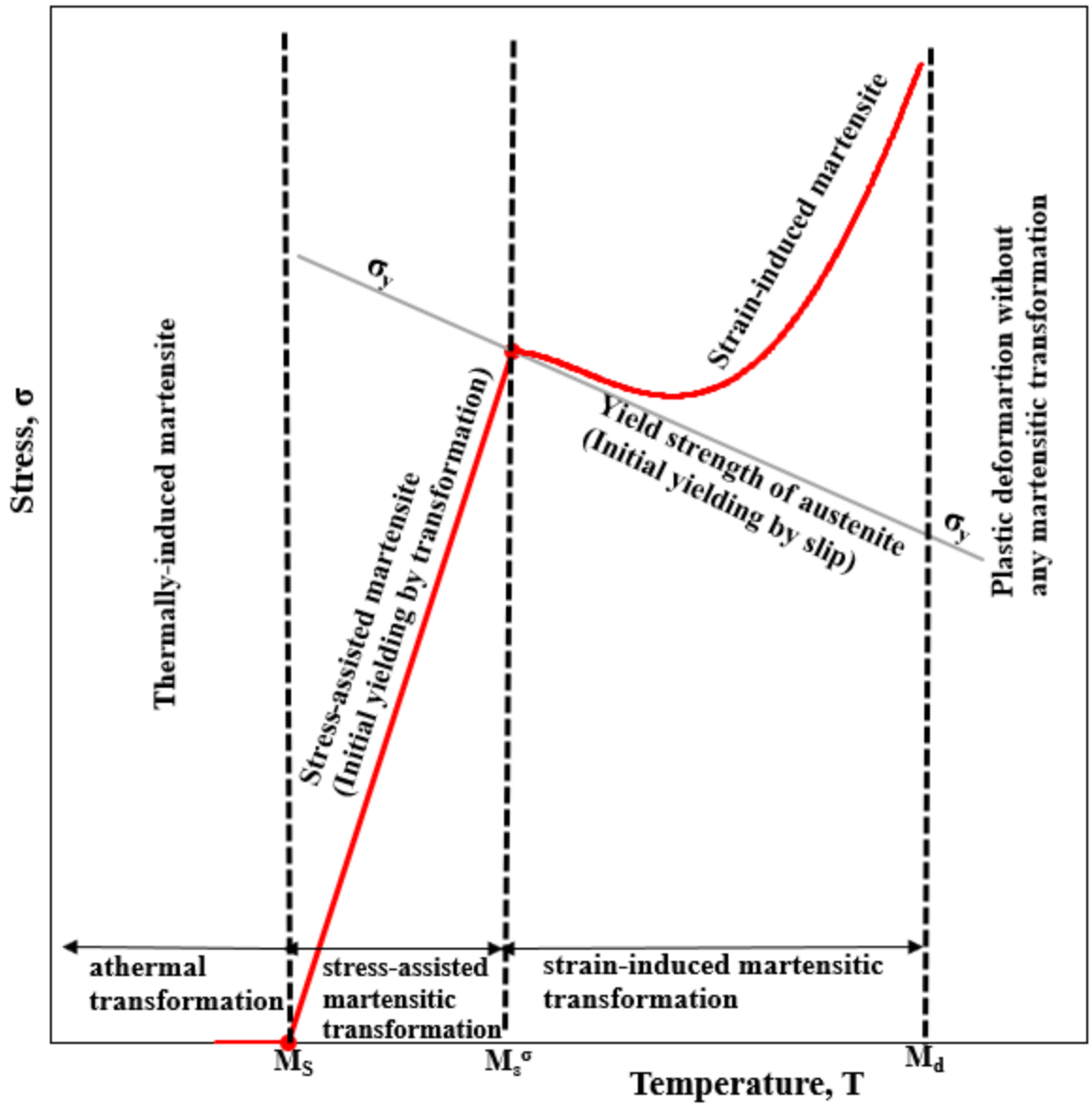


**Figure 2.7. Different mechanisms for martensitic transformation in metastable austenitic stainless steels [79], [124]**

$M_s^{\sigma}$ is a corresponding $M_s$ temperature at the yield strength of the austenite and is the highest temperature for the transformation to be induced by elastic stress. The temperature lies above the normal $M_s$ temperature in which yielding is initiated by the onset of martensitic transformation under applied stress. The yielding is initiated by regular slip processes in the austenitic phase at a temperature above the $M_s^{\sigma}$ temperature. The variation of yield strength as a function of temperature is negative above the $M_s^{\sigma}$ temperature and positive below the $M_s^{\sigma}$ temperature. The amount of stress required to induce martensite decreases to zero as temperature

decreases below the $M_s^{\sigma}$ temperature. At the martensitic start temperature, $M_s$, no stress is required to induce martensite [79].

Below the $M_s^{\sigma}$ temperature, martensitic transformation is possible below the yield strength of the austenite. This is referred to as stress-assisted martensitic transformation. Above the $M_s^{\sigma}$ temperature, martensitic transformation can only be initiated above the yield strength of the material. As temperature of deformation increases, the initiating stress to induce martensitic transformation increases until the $M_d$ temperature limit is reached beyond which no strain-induced transformation will occur [79].

#### 2.6.2.2.2 Stress-assisted transformation

Applied stress aids the thermodynamic driving force and hence, the embryos are identical to those that activate thermally induced martensite. The morphology of martensite is plate-like or lenticular. The martensitic transformation occurs before the onset of plastic deformation. The transformation is caused by dislocation multiplication and twinning [35]. The critical stress required to assist the transformation increases linearly with temperature below the yield strength of austenite as shown in Figure 2.7 [124].

## 2.7 Process Variables

A constitutive model for material behavior during cold rolling requires information about the material's response as a function of strain, strain rate (rate of deformation), strain state, stress state, annealing, exact degree of cold work, exact temperature of cold work, stacking fault energy (SFE), initial austenitic grain size and exact alloy chemistry [82], [53]. A plant-based predictive model is needed to achieve the required mechanical properties in terms of $R_{p0.2}$, $R_m$, ratio of $R_{p0.2}/R_m$, $A_{50}$ and a certain hardness, hence a thorough understanding of the role of each variable is important. The nature of the applied stress, whether the deformation mode was tension or compression was found to have slight influence on crystallographic orientation at high strains [7].

### 2.7.1 Degree of cold working

The volume fraction of SIM increases as the strain increases until a 'saturating strain' is reached where the formation of martensite becomes supersaturated. Further deformation results in crushing of martensite, which forms a high density of defects which in turn provides nucleation sites for austenite on the reverse transformation during annealing. A high density of crushed martensite can be increased by decreasing the supersaturating strain, and/or by cold deformation

at very low temperatures. This results in a nano- or ultrafine-grained microstructure with improved combination of strength and ductility. This in a way corresponds to the decrease in SFE thereby increasing the chemical driving force for the martensitic transformation [14]. Heavily cold-deformed martensite has a potential of resulting in highly refined austenite grain size (ultrafine (nano- or submicron) grained structure) upon reversion annealing. A double cold-deformation with intermediate annealing cycle has been reported to have achieved a good combination of strength and ductility in 10Cr-5Ni-8Mn alloy [8]. Severe cold rolling has potential in achieving final improvements in strength, ductility and fatigue resistance [2].

### 2.7.2 Temperature of cold working

Most metallurgical transformations are influenced by temperature variations [28]. The formation of strain-induced martensite is affected by the stacking fault energy (SFE) and chemical driving force, which all are temperature dependent. The SFE value determines the austenite stability, controls the formation of shear bands during cold working, and hence, thereby controls the formation of nucleation sites for α′-martensite [39], [46]. The austenite stability is critical in tailoring the resulting mechanical properties [125]. As the temperature of deformation increases the thermodynamic driving force for martensitic transformation decreases. A temperature decrease lowers the SFE which enhances the tendency for martensitic transformation [79].

### 2.7.3 Effect of initial austenitic grain size

Austenite stability increases with the decrease in austenite grain size as the $M_d$ temperature is lowered [53]. Finer grained austenitic steels could show lower martensite kinetics during cold deformation as the martensite formed in the fine austenite grains hinders the growth of the newly nucleated martensite laths. The critical chemical energy required for the formation of martensite decreases with increase in initial austenitic grain size. Thus finer grained austenitic microstructures result in improved austenite stability [90], [46]. The grain size has been reported to also have an influence on the deformation mechanism with grain size refinement changes TRIP effect to TWIP effect in accommodating additional strain [90].

### 2.7.4 Strain rate

Materials processing and automotive crash events are subjected to medium to high strain rates. The effect of strain rates can be classified as direct strain rate effects or indirect effects. The indirect effects of strain rates include the self-heating of the material during deformation as the

strain rate increases. Adverse increase in adiabatic heating during deformation at high strain rates consequently causes temperature increases (higher than the initial deformation temperature) resulting in reduced thermodynamic driving force for the austenite → martensitic transformation and increase in the SFE leading to an increased austenite stability [46], [126].

This results in strain rate having the same influence as that of the temperature of deformation [126]. High strain rates therefore inhibit the α′ martensite transformation due to increased adiabatic heating [8]. With continuous increase in SFE, the deformation mode changes from transformation induced plasticity (TRIP) effect to twinning induced plasticity (TWIP) effect and then to slip [127]. Lower strain rates hence keep the SFE low which favors the transformation induced plasticity effect. However, there is a need to optimize the mechanical properties at high strain rates since the forming process and crash-worthiness occur at high strain rates/velocities [128]. As the amount of strain-induced martensite decreases with increase in strain rate, the UTS decreases with increasing strain rate. The yield stress increases with increasing strain rate [126]. The 300-series metastable austenitic stainless steels have been reported in literature to have low sensitivity to strain rate [22]. The effect of increased strain rate in suppression of austenite → martensitic transformation was observed at strains greater than 0.25 in AISI 304 [35]. There is a remarkable increase in temperature resulting from the adiabatic heating at high strains. Without temperature increase, increase in strain rate has been found to be enhancing martensitic transformation [79].

### 2.7.5 Alloy chemistry

The stacking fault energy (SFE) is a function of chemistry. In principle, the mechanical properties and work hardening rate could be tailor-made by the control of chemistry to get the desired properties [7]. The manganese content in metastable austenitic steels can also influence the transformation path during cold rolling. In high manganese steels typically (15~30 wt% Mn), the γ → ε transformation path occurs whereas γ → ε → α′ is the transformation path in medium manganese steels (5~12 wt% Mn) [129]. In metastable austenitic steels, there are two transformation sequences which are: γ → ε → α′ and γ → α′.

### 2.7.6 Annealing and pickling

An intermediate heat treatment is necessary to recover and to recrystallize the cold deformed microstructure. The intermediate or controlled annealing process makes the material amenable for subsequent forming operations by restoring formability. Upon heating, both ε- and

α′-martensites transform back to austenite leading to grain refinement [116]. Recrystallization has been reported to be occurring at 100 $^{O}$C above the strain-induced martensitic reversion temperature [64]. A thermo-mechanical process which consists of severe cold rolling followed by intermediate annealing of ASSs results in nano/submicron grained structure with high strength, high hardness and good ductility [2], [32].

When the reverted austenite partially or fully transforms to martensite, this leads to increased final strength. Inappropriate heat treatment, service at high temperatures or welding can, however, lead to the formation of other phases. These may be thermodynamically stable or kinetically favored in lower temperature regimes and can have a major influence on mechanical properties and corrosion resistance. The transformation rate is dependent on the percentage of martensite which directly relates to the degree of prior cold-rolling deformation. Annealing is done over a narrow temperature range to achieve the desired mechanical properties, avoiding grain growth, secondary recrystallization and sensitization. An excellent combination of strength and ductility has been reported to be achieved through partial/controlled annealing for AISI 304 steel [8].

### 2.7.7 Skin pass rolling

To give a shiny surface quality, coils are given a very light cold rolling treatment, around 0.5~1% reduction in the final forming step after annealing and pickling. This gives high surface flatness and low surface roughness.

## 2.8 Strain-hardening behavior

Austenitic stainless steels possess unique characteristics which can be utilized to develop high strength steels due to their high strain hardening abilities with strain hardening exponents of around 0.35 compared to 0.16 ~ 0.26 of low carbon steels [112]. This increased strain hardening results in increased crashworthiness during collision events. Metastable austenitic stainless steels offer extreme high combinations of strength, strain hardening and elongation, making this class of steels most attractive candidates for this application.

The strain hardening and the tensile flow stress behavior of automobile steel have been the subject of continued scientific and technical interest in order to ensure the appropriate conditions during material processing and performance [130], [131]. This fact has attracted continuous development of advanced high strength steels with increased levels of ductility and strength [132]. A quantification of the flow properties including the strain hardening exponents

of metastable austenitic steels, as a function of strain and temperature, is however required to evaluate the benefits offered by it. Constitutive equations to correlate true stress and true plastic strain have been proposed in literature with the view of predicting the performance of the material during service [133], [134]. In order to study the work hardening behavior of AISI 301LN, different equations and models were applied, and relative appropriateness tested and compared.

### 2.8.1 Hollomon power law

The work-hardening behaviour of many engineering materials have been sufficiently described by the Hollomon power law [135], [136], [137], [138]:

$$\sigma = K\varepsilon^n \quad \text{Equation 2.2}$$

where:

σ is the true stress;

K is the strength coefficient,

ε is true plastic strain,

n is the strain hardening exponent.

A log-log plot should give a straight line with the slope as strain hardening exponent, n and the intercept at ε = 1 as the strength coefficient, K. A second phase transformation in 18-8 metastable austenitic steels exhibits a deviation from the classical Hollomon law [139].

### 2.8.2 Ludwik model

The Ludwik model has an additional stress factor ($\sigma_o$) for materials which show a varied yield strength with similar strain hardening [135], [136].

$$\sigma = \sigma_o + K\varepsilon^n \quad \text{Equation 2.3}$$

### 2.8.3 Swift model

An equation with an additional strain term, $\varepsilon_o$, which accounts for pre-strain was proposed by Swift, for materials which show similar yield strength with varied strain hardening behaviour [135], [136].

$$\sigma = K(\varepsilon_o + \varepsilon)^n \quad \text{Equation 2.4}$$

### 2.8.4 Ludwigson model

For stable austenitic stainless steels, although the Hollomon or Ludwik equations can describe the plastic flow behaviour at high strain levels, the models were found to be insufficient in describing the plastic flow behaviour and work hardening at low strain values [42], [135]. A modified Ludwik model was then proposed by Ludwigson to consider the deviation [30], [135]. An assumption made was a continuous evolution of strain induced martensite as a function of strain and macroscopic flow stress as estimated by the contribution of strength of all individual phases present.

$$\sigma = K\varepsilon^n + \Delta \quad \text{..... Equation 2.5}$$

where:

the deviation $\Delta = \exp(K_1)\exp(n_1\varepsilon)$,

K and n have the same meaning as in the Hollomon equation

$\exp(K_1) \approx$ proportional limit

$n_1$ is the slope of the deviation of stress from the Hollomon equation plotted against true strain, $\varepsilon$ [135].

The Ludwigson modification has earlier been found to be adequate in describing the tensile flow and work hardening behaviour of ferritic stainless steels. There was no information which was found in literature about applicability of the Ludwigson equation in describing the work hardening behaviour of metastable austenitic stainless steels which undergo a phase transformation during deformation.

### 2.8.5 Voce model

The Voce stress relationship is usually applicable only at high temperatures where dynamic recovery cancels out the work hardening effect during the test. The Voce flow stress relationship for materials which show saturation stress at high stress/strain levels can be represented as follows [135]:

$$\sigma = \sigma_s - (\sigma_s - \sigma_1)\exp[-(\varepsilon - \varepsilon_1)/\varepsilon_c] \quad \text{.....Equation 2.6}$$

where:

$\sigma_s$, is the saturation stress,

$\sigma_1$ and $\varepsilon_1$ are the true stress and true plastic strain values at the onset of plastic deformation, respectively, and

$\varepsilon_c$ is a constant.

**2.9 Modelling kinetics of strain-induced martensitic transformation**

The control of strain-induced martensite in the metal forming processes and annealing process is important in the simulation and development of process model to produce AISI 301LN steel with the required mechanical requirements. A process model captured the effects of measurable process variables such as given in 2.10 above.

Several equations have been reported in literature to model the behavior of the $\gamma \rightarrow \alpha'$ transformation. These include Olson and Cohen model [121], Gompertz model [140], and Guimaraes model [28]. For the kinetic model to describe the $\gamma \rightarrow \alpha'$ transformation, the parameters and constants should be correlated to the measurable physical processes and should be applied over a wide range of temperature and applied strain, rather than just a single set of experimental data. The transformation kinetic laws describe the volume fraction of martensite in the material at a given strain and temperature [114].

The transformed volume fraction of martensite at a given applied strain is given as, $f_{\alpha'}$. The saturation value for the percentage of martensite has been found out to be always less than 100% with some retained austenite. Hence the volume fraction of the strain-induced martensite has been calculated using, $f_s$ instead of 1 since $f_s \leq 1$. Factors that affect saturation value and the rate of approach to saturation value for volume fraction of strain-induced martensite include initial austenitic grain size, stacking fault energy, alloy chemistry, the nature of applied strain, strain rate and deformation temperature [121], [140].

The incremental formation of strain-induced martensite as the function of strain, that is, the differential change of volume fraction of martensite per unit strain allows good simulation and predictive percentage of martensite even if process variables such as temperature and strain rate changes [79].

There is a need to develop a model that combine both the thermodynamics effects and thermomechanical equations [28]. These include the kinetics of strain-induced transformation, the flow stress (mechanical) equations describing the strain hardening behavior of microstructures containing both austenite and strain-induced martensite and any thermal

equations describing the latent heat generated during strain-induced martensitic transformation, and the plastic work done transforming into heat and thermal expansion [28].

### 2.9.1 Olson and Cohen model

Olson and Cohen (1974) fitted a sigmoidal model on the data obtained by Angel (in 1954) [27] for strain-induced martensite as a function of strain at various temperatures. The isotropic transformation equation is described as below:

$$f_{\alpha'} = 1 - \exp\left(-\beta_O\left(1 - \exp\left(-\alpha\varepsilon\right)\right)^n\right) \quad \text{Equation 2.7}$$

where:

$f_{\alpha'}$ is the volume fraction of strain-induced martensite.

$\varepsilon$ is the applied strain.

$\alpha$ is a strain-independent constant which indicates the rate of shear-band formation and is dependent on the stacking fault energy, strain rate and temperature of deformation.

$\beta$ is a temperature dependent constant.

n is an exponent which is usually set equal to 4.5 for AISI 304 as it gives the best agreement between the experimental results and the proposed model

The model considers the nucleation and growth of strain induced martensite as controlled by $\alpha$ and $\beta$ parameters. It has been reported that $\beta$ is governed by the thermodynamic driving force for the martensitic transformation, $\Delta G$ and could be influenced by the stress state of the material.

#### 2.9.1.1 Limitations of Olson and Cohen model

1. The model does not predict the saturation volume fraction of strain-induced martensite at a given temperature.
2. The parameters $\alpha$ and $\beta$ were given as constants during the process at a given temperature. This makes them suitable for simulation of isothermal forming processes only.
3. The parameter n was arbitrarily fixed to 4.5 which was based on single data fit. There is no well-defined behavior of the parameter as a function of temperature and/or applied strain.

4. The β constant is not well defined in the equation. It was set as a constant for a wide temperature range and decreases to zero around $M_d$ temperature of AISI 304 material.

### 2.9.2 Gompertz model

The Gompertz model is a sigmoidal function to describe the formation of strain-induced martensite in AISI 304 as a function of applied strain [140].

$$f_{\alpha'} = f_s \exp[-\exp(-\beta(\varepsilon - \varepsilon_m))] \quad \text{Equation 2.8}$$

where:

$f_{\alpha'}$ is the volume fraction of strain-induced martensite.

$f_s$ is the saturation volume fraction of $f_{\alpha'}$.

β is a temperature dependent constant associated with the rate of transformation.

ε is the applied strain.

$\varepsilon_m$ is the amount of applied strain required to achieve $f_s/e$ where e is natural logarithm approximately equal to 2.72.

### 2.9.3 Matsumura equation

Matsumura et al. proposed the following equation to calculate the volume fraction of strain-induced martensite [141], [142].

$$V_{\alpha'} = 1 - V_{\gamma o}/(1 + (k/q) * V_{\gamma o} * \varepsilon^q) \quad \text{Equation 2.9}$$

where:

$V_{\alpha'}$ is the percentage of strain-induced martensite.

$V_{\gamma o}$ is the initial percentage of austenite before deformation.

ε is the applied plastic strain.

k and q are constants.

The estimated $V_{\alpha'}$ from the above equation is always below 100% as in agreement with past studies depending on the deformation conditions. To take into consideration the saturation value of less than 100%, Tsuchida et al. modified the above equation to [141]:

$$V_{\alpha'} = V_{\alpha s}[1 - V_{\gamma o}/(1 + (k/q) * V_{\gamma o} * \varepsilon^q)] \quad \text{Equation 2.10}$$

where: $V_{\alpha s}$ is the saturation percentage of strain-induced martensite.

### 2.9.4 Guimaraes model

The model was developed using an isothermal tensile test with the percentage of martensite estimated using the saturated magnetism from small discs cut from the tensile specimens.

$$V_{\alpha'}(\varepsilon_{eq}, T) = V_{\alpha'}^{max}(T) \cdot (1-\exp(-(D\varepsilon_{eq})^n)) \quad \text{..... Equation 2.11}$$

where:

$\varepsilon_{eq}$ = square root $[2/3(\varepsilon_I^2 + \varepsilon_{II}^2 + \varepsilon_{III}^2)]$,

$V_{\alpha'}(\varepsilon_{eq}, T)$ is the volume fraction of martensite

D is the stability parameter of the kinetics of martensitic transformation

n is the deformation mode parameter of the kinetics of martensitic transformation

$V_{\alpha'}^{max}(T)$ is the saturation volume fraction of martensite at a given temperature T which is defined as 0 at a temperature above $M_d$ and 100% at a temperature below or equal to $T_1$.

The saturation volume fraction of strain-induced martensite, $f_s$, varies as a function of temperature with the following equation proposed by Santacreu et al.

$$V_{\alpha'}^{max}(T) = V_o f(M_d - T) \quad \text{..... Equation 2.12}$$

## 2.10 Modelling flow stress of a phase mixture

An attempt to formulate hardening laws has been reported in the literature with several constants which do not have a direct physical interpretation. The martensitic transformation from a fully austenitic microstructure makes metastable austenitic stainless steels a “composite” like in nature making the strain-hardening rate determined by the rate of phase transformation [48]. An approach which considers the microstructural changes (such as changes in volume fraction of phases, dislocation density (dislocation formation rate and dislocation annihilation rate during dynamic recovery at high temperature) and grain sizes) during deformation in calculating the mechanical behavior of metastable austenitic stainless steels with the use of experimentally determined stress-strain curves at a certain range of temperature is more acceptable [114].

New constitutive equations for flow stress and volume fraction of martensite as a function of strain will make it suitable for an online control of metal forming process with little computational capacity using any work hardening model.

Talonen determined the true stress-strain response of austenite and strain-induced martensite separately and combined using XRD stress measurements as shown in Figure 2.8 [96]. The stress analysis indicates a non-homogeneous distribution of stress between austenite and strain-induced martensite phases. The mechanical response is difficult to predict due to quite several parameters involved. Due to martensitic transformation, a classical Hollomon equation is generally not satisfactory in fitting the tensile curve [28].

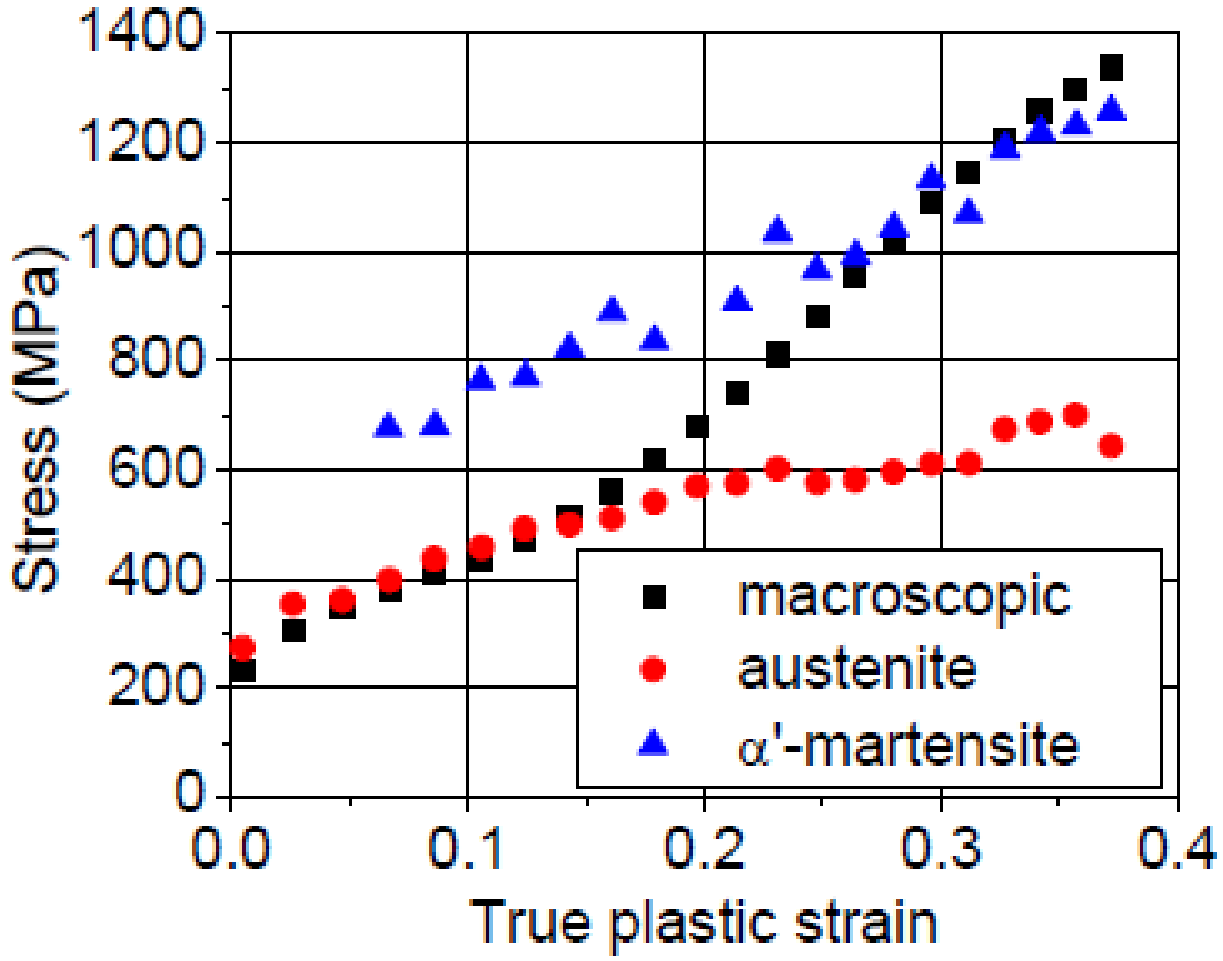


**Figure 2.8: True stress levels in the microstructural constituents with applied strain in a MASS as measured by *in situ* XRD. The "macroscopic" data points refer to strain gauge results [96]**

Figure 2.9 show the variation of stress of the phases during deformation as a function of strain-induced martensitic microstructural evolution.

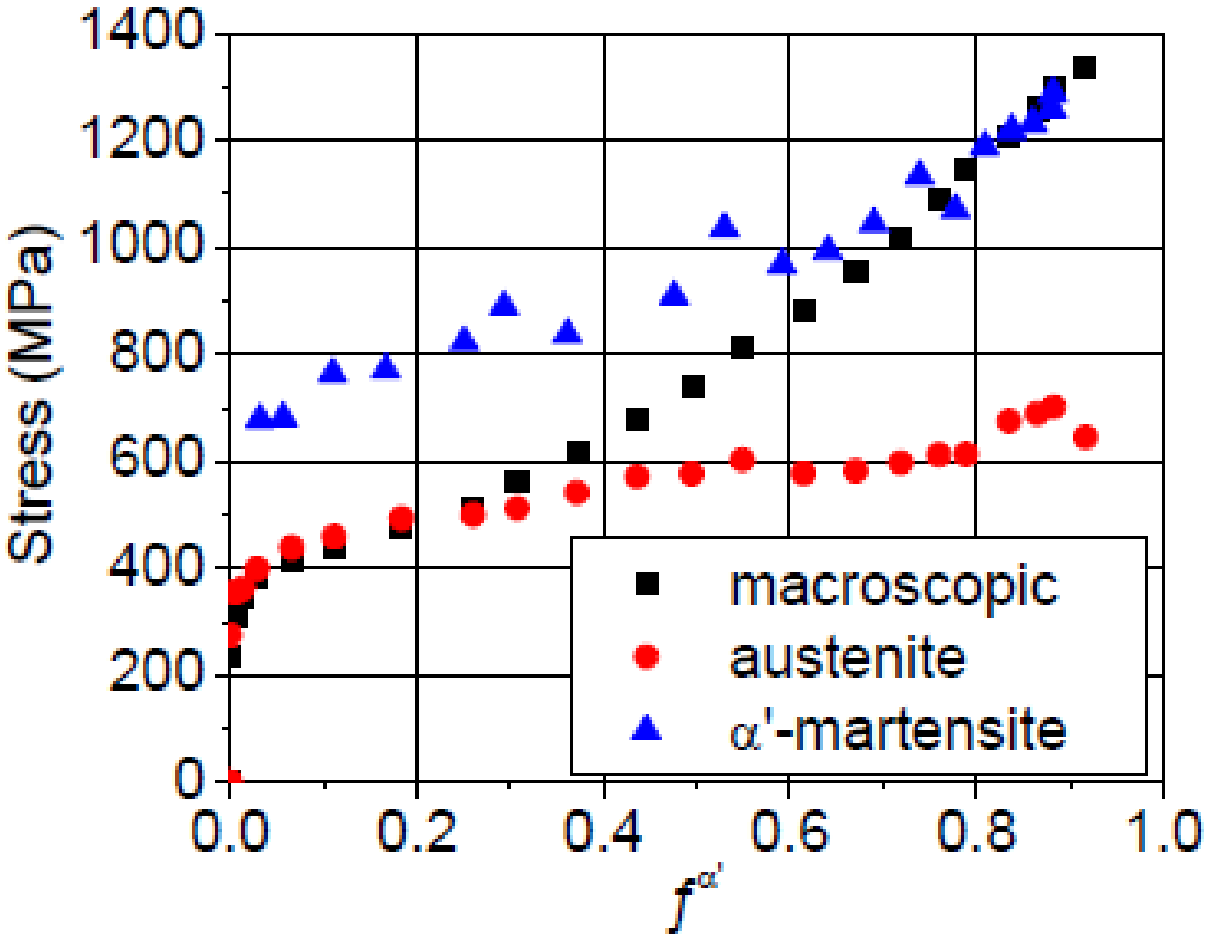


**Figure 2.9: True stress levels in the microstructural constituents as a function of volume fraction of α′-martensite in a MASS as measured by *in situ* XRD. The "macroscopic" data points refer to strain gauge results [96]**

The strength and hardness contribution from martensite is higher than the strength and hardness contribution from austenite due to higher dislocation density as shown in Figure 2.10 [44].

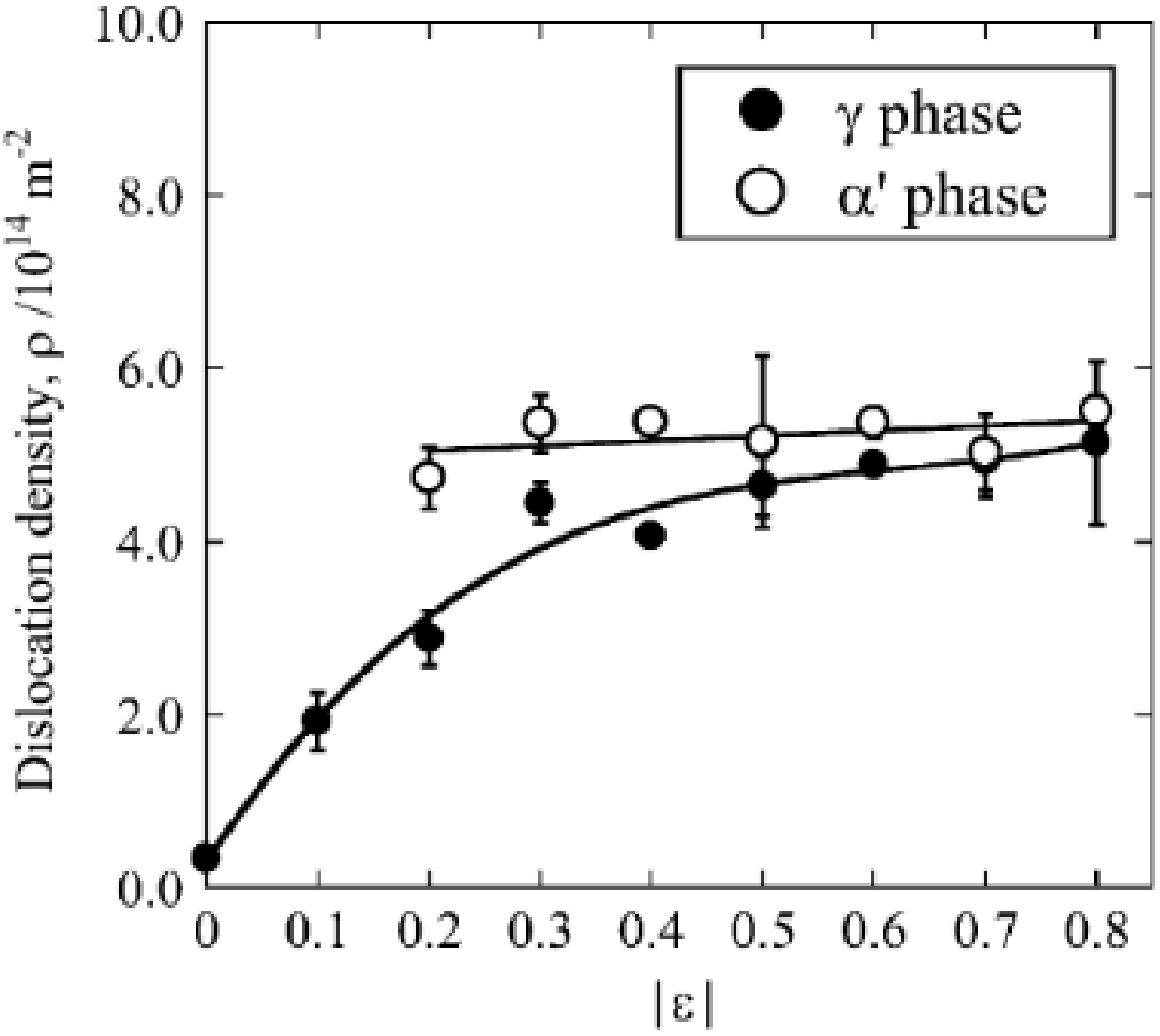


**Figure 2.10: The variation of dislocation density as a function of strain in both austenite and martensite phases in cold rolled SUS304 steel at room temperature [44]**

The increase in volume fraction as a function of strain and/or temperature, result in the gradual increase in strength of the steel. The hardening contribution from dislocations could be estimated using the following equation [4], [143]:

$$\sigma_{disl} = \alpha M G b \rho^{1/2} \quad \text{..... Equation 2.13}$$

where:

α is a constant

M is the average Taylor factor,

G is the shear modulus,

b is the magnitude of the Burger's vector,

ρ is the dislocation density.

The typical values for Fe are: α = 0.3, M = 3, G = 64 GPa and b = 0.25 mm. TEM is used to determine the density of dislocations, ρ to estimate the dislocation hardening contribution [143].

### 2.10.1 Rule of mixture

The total strength of metastable austenitic stainless steel can be calculated using a classical rule of mixtures between the mechanical behavior of austenite (including dislocations as a function of strain) and that of a steel alloy containing a constant volume fraction of martensite embedded in an austenitic phase matrix [4], [29]:

$$\sigma_{total} = \sigma_{\gamma} \cdot V_{\gamma} + \sigma_{M} \cdot V_{M} \quad \text{Equation 2.14}$$

where:

$\sigma_{\gamma}$ and $V_{\gamma}$ are the strength and volume fraction of untransformed austenite

$\sigma_{M}$ and $V_{M}$ are the strength and volume fraction of strain-induced martensite

Equation 2.14 reduces to

$$\sigma_{total} = \sigma_{\gamma} \cdot (1 - V_{M}) + \sigma_{M} \cdot V_{M} \quad \text{Equation 2. 15}$$

### 2.10.2 Hansel approach

The approach uses Hockett-Sherby description of the flow stress behavior of a phase mixture [79]. The total strength can be calculated as follows:

$$\sigma_{total} = \sigma_{\gamma}.V_{\gamma} + \sigma_{\gamma}.V_{M} + \Delta\sigma_{\gamma \rightarrow \alpha'}.V_{M} \quad \text{Equation 2.16}$$

where:

$\sigma_{\gamma}$ flow stress of the austenite phase

$\sigma_{total}$ is the flow stress of all the phases in the mixture

$V_{\gamma}$ and $V_{M}$ are volume fractions of austenite and martensite phases

$\Delta\sigma_{\gamma \rightarrow \alpha'}$ is a constant strength increase associated with martensitic transformation.

## Chapter 3: Materials, Techniques and Experimental Procedure

This chapter describes the materials, experiments, equipment, and characterization techniques that were used in the study of strain-induced martensitic transformations in AISI 301LN metastable austenitic stainless steel as a function of process variables. The test material used in this study was industrial material sampled after hot rolling, annealing and pickling process, designated as AP1 from here onwards. Different heats (to be designated as alloy A, alloy B and alloy C) with slightly different chemistry within AISI 301LN grade, as shown in Table 3.1 as received from Columbus Stainless steel (Pty) Ltd were studied. The test materials were received with thickness between 4 and 6 mm. Unless stated otherwise, the experiments were carried out using alloy A.

**Table 3.1: Chemical composition (spectrographic analysis) of annealed and pickled AISI 301LN as supplied (%wt)**

Steel A (initial gauge thickness of 4.05 mm).

| C | Mn | P | S | Si | Cr | Ni | N | Co |
|---|---|---|---|---|---|---|---|---|
| 0.02 | 1.54 | 0.026 | 0.003 | 0.42 | 17.49 | 6.6 | 0.1133 | 0.08 |
| Cu | Mo | Sn | Ti | Al | Nb | O | B | Fe |
| 0.15 | 0.16 | 0.009 | 0.008 | 0.005 | 0.003 | 0.0091 | 0.0018 | balance |

Steel B (initial gauge thickness of 4.44 mm).

| C | Mn | P | S | Si | Cr | Ni | N | Co |
|---|---|---|---|---|---|---|---|---|
| 0.02 | 1.35 | 0.026 | 0.004 | 0.42 | 17.6 | 6.63 | 0.1123 | 0.1 |
| Cu | Mo | Sn | Ti | Al | Nb | O | B | Fe |
| 0.15 | 0.16 | 0.008 | 0.008 | 0.005 | 0.002 | 0.0083 | 0.0016 | balance |

Steel C (initial gauge thickness of 5.61 mm).

| C | Mn | P | S | Si | Cr | Ni | N | Co |
|---|---|---|---|---|---|---|---|---|
| 0.023 | 1.48 | 0.022 | 0.003 | 0.4 | 17.33 | 6.52 | 0.113 | 0.16 |
| Cu | Mo | Sn | Ti | Al | Nb | O | B | Fe |
| 0.07 | 0.04 | 0.009 | 0.007 | 0.005 | 0.002 | 0.0068 | 0.0014 | balance |

## 3.1 Measurement and Characterization Techniques

Due to annealing and pickling done on the as-received materials, there was no strain induced martensite present in the microstructure prior to laboratory cold working as determined by Ferritescope measurements. To accurately define modelling of kinetics strain-induced martensitic transformation as a function of strain, a variety of complementary techniques for characterization and quantifying the volume fraction of austenite and martensite phases in stainless steels have been utilized which include x-ray diffraction, neutron diffraction, magnetic measurements with use of Ferritescope instrument (local magnetic permeability), VSM measurements (bulk magnetic induction), optical metallography, scanning electron microscopy (SEM) and Electron Backscatter diffraction (EBSD) analysis. Although x-ray and neutron diffraction analyses are considered reliable techniques in the measurement of martensite and austenite phases, the effect of texture remains a difficult challenge. VSM, Ferritescope and hardness measurements corroborated the phase fraction estimates that were used in the development of a calibration factor. The standard deviation was calculated to ascertain the uncertainty of measurements such as Ferritescope readings, hardness measurements.

### 3.1.1 X-ray Diffraction analysis

The X-ray diffraction experiments were carried out to identify the phases present and the Rietveld analysis was done for quantification purposes. The X-ray results were used to develop a calibration curve for correction of Ferritescope measurements to determine the true α′-martensite content. The samples for X-ray diffraction were lightly ground and electropolished using a Struers Lectropol-5 equipment and A3 electrolyte at an operating voltage of 35 V at room temperature for 50 s. To reduce the effect of texture during X-ray diffraction analysis, a rotating sample holder was used. The XRD characterisation for volume fraction of α′ martensite and γ-austenite were done on the surfaces. Quantification using X-ray is considered accurate for samples which were deformed through tensile straining due to homogeneous distribution of strain during deformation. It has been reported that the quantification of α′-martensite for deformation below 20% reduction in thickness by cold rolling is not reliable [144], [82].

### 3.1.2 Neutron Diffraction analysis

Neutron diffraction technique has a much greater penetration depth as compared to X-ray diffraction which only gives the volume fraction of α′ martensite on the surface. Neutron

diffraction analysis together with X-ray diffraction analysis were used to develop calibration curve for correction of Ferritescope measurements to determine the true α′-martensite content. The volume fractions of phases were accurately determined in the deeper body of the sample using neutron diffraction method. Samples for neutron diffraction analysis were wire cut and no further sample preparation was done to avoid further formation of strain-induced martensite during the process.

### 3.1.3 Ferritescope measurements

The magnetic induction test is an isotropic property and the Ferritescope measurements utilize the ferromagnetic properties of α′-martensite whilst ε-martensite and γ-austenite are paramagnetic [145], [146]. Changes in the magnetic properties of austenitic steel during deformation is attributed to α′-martensite which could be quantified using the magnetic induction method. The non-destructive incremental in-situ monitoring of α′-martensite content during the tests was done by local magnetic permeability measurements [114], using the portable Ferritescope instrument, (Helmut Fisher GmbH, model MP3B) a device that is normally used to measure the $\delta$-ferrite content of austenitic stainless-steel weldments [147]. The Ferritescope probe allows for in situ measurements during testing. The operational principle of the Ferritescope is based on the determination of the magnetic permeability of the material. This causes an error in the measured values of martensite fractions because the magnetic permeability of α′-martensite is apparently dissimilar to that of delta ferrite. Therefore, results obtained with a Ferritescope instrument were converted to actual α′-martensite contents by using a calibration curve which was developed by using different measurement techniques which could be accurate such as x-ray diffraction, neutron diffraction and magnetization measurements. A detailed study of strain-induced martensite measurement [147] had shown that the calibration factor can be accurately used for Ferritescope readings below 50. Instrument linearity and calibration becomes difficult at very high α′-martensite contents of above 85% [148].

The starting material is annealed and pickled with at least 99% γ-austenite giving a Ferritescope reading of less than 0.8. An increase in the Ferritescope readings was purely due to strain-induced martensitic transformation. When the probe is placed on a material, the excitation coil generates a low frequency alternating magnetic field which then interacts with the magnetic portions of the specimen. The changes in the magnetic field induces a voltage which is a direct measure of magnetic α′-martensite [126], [149]. The device has a penetration depth of

approximately 2 mm making it even better than the x-ray diffraction analysis. The measurements were made after deformation hence a precise measure of the magnetic permeability as a function of strain was acquired. The possible systematic measurement errors include changes in sample geometry such as thickness and area of the surface. Ferritescope measurements were done on samples which were at least 2 mm thick and 10 mm wide, with no need for geometry correction on the values obtained.

The Ferritescope measurements were taken on both stressed and unstressed (load removed) tensile samples. The magneto mechanical (Villari) effect of tensile stress and plastic strain on the Ferritescope readings was observed. The magnetic permeability measurements decrease with increasing elastic strain. The increase in Ferritescope readings taken at during unloading of the tensile sample does not indicate any martensitic transformation nor the decrease in Ferritescope readings during the elastic loading indicate any reversible phase transformations [114]. The presence of elastic stress hence influences the magnetic permeability of the material. The actual true Ferritescope measurement therefore is the one taken when the elastic strain is completely removed in an unstressed condition

### 3.1.4 VSM Measurements

Accurate measurements of austenite-to-martensite transformation is of paramount importance in quantifying the phase volume fractions as a function of process variables. The measurement of magnetic saturation can be used to quantify the volume fraction of strain-induced martensite. This is a bulk magnetic measurement which is more accurate compared to other techniques where the analysis is done on localized areas [40]. Unlike diffraction analysis, Ferritescope and VSM measurements are not affected by texture from plastic deformation. The magnetic response of a material increases linearly with an increase in the magnetic field and it eventually saturates. Reversing the magnetic effect, the magnetic response decreases to zero passing through the linear region to negative magnetic saturation. Temperature, crystal structure of the phase and chemistry have influence on the magnetic saturation of the material. The austenite phase is paramagnetic and thus non-magnetizing with no response to applied magnetic fields. In cold deformed austenitic stainless steels, the magnetic response is entirely due to strain-induced martensite. The magnetic saturation is defined as the maximum magnetic response of a material under applied magnetic field. If magnetic saturation of purely martensitic sample is known, the volume fraction of martensite can be calculated by the ratio:

$$V_{\alpha'} = MS_{\alpha'}/MS_c,$$

where: $MS_{\alpha'}$ is the saturation magnetization per unit mass of a given sample with unknown percentage of martensite, and

$MS_c$ is the specific saturation magnetization per unit mass of a of purely martensitic sample with an ideal 100% $\alpha'$-martensite.

This is only possible provided there are no other phases with the same magnetic properties as martensite such as ferrite. In literature, different values of $MS_c$ have been reported for different alloys. These include: 160.4 by Mangonon and Thomas for AISI 304 [64], a range between 154 and 175 by Hecker et al. for AISI 304 [35], 154 by Mumtaz et al. for AISI 201 [150] and 140 by Tavares et al. for modified AISI 201 [150], [151].

As applied magnetic field is increased, the magnetic orientation of the domains gets oriented in the direction of the field in a ferromagnetic material. When all the domains get oriented, the magnetic saturation will then be reached. Magnetic saturation measurements are normally determined using a vibrating sample magnetometer (VSM). The VSM magnetometer creates a large, variable and uniform magnetic field. The sample is vibrated perpendicular to the applied field. The applied magnetic field and the magnetic moment created by the magnetized sample are measured. The magnetic response of the material under a high magnetic field is used to determine the magnetic saturation [152].

Magnetization saturation was measured at University of Johannesburg, South Africa in a Cryogenic cryogen free physical properties measurement system from Cryogenic Pty Ltd (London) using the vibrating sample magnetometer (VSM) insert. The arbitrary units of emu/g for magnetization were used. The operational principle of VSM is similar to that of Ferritescope instruments [153].

Magnetization as function of temperature, M(T), measurements were done in a temperature range from 4 K to 300 K, at a rate of 0.5 K/min using zero field cooled (ZFC) and field cooled (FC) protocols. In the ZFC protocol the sample was cooled down to 4 K with no applied magnetic field, at 4 K the magnetic field was switched on to 0.5T and then measurements were taken upon heating in this field. For the FC protocol the sample was cooled to 4 K in an applied magnetic field of 0.5 T. At 4 K the measurements were taken upon heating to 300 K in an applied magnetic field of 0.5 T.

Magnetization as function of applied magnetic field ($\mu_0 H$) (measured in Tesla) were done at fixed temperatures using a ZFC protocol (as described above). Samples were measured at a rate of 0.2 T/minute to maximum fields of ±4 T and ±12 T (for an as-received sample which showed no magnetization saturation with applied magnetic field up to ±4 T).

Discs of 5mm diameter and less than 2 mm thickness were prepared by electro-discharge machining (EDM) from the uniform section of the gauge length of specimen. Samples were etched in boiling HCl to get rid of any contamination from EDM procedure and weighed, shortly before placing in a polymer straw for magnetic measurements. The measurements were done as follows: M vs Z was done to obtain the precise position relative to measurement coils. The magnet was then demagnetized so that the sample/magnet could be cooled in zero field (ZFC) to base temperature. At base temperature, the measurement field was switched. A few seconds was given for the field to stabilize. The M-T for samples were done while heating to 300K. At 300K, the sample was cooled to base temperature in the same field as was used for ZFC heating. This is known as field cooling (FC). The FC M-T results were collected in same field as ZFC field. The percentage of retained austenite was calculated by subtracting the percentage of strain-induced martensite from 100%.

### 3.1.5 Tensile tests

Single specimen uniaxial tensile tests were carried out using a hydraulic Instron-type tensile testing machine (1175 model) with a 50 mm gauge contact extensometer (Instron-type model 2630-112) to determine the elongation of the samples upon deformation. The contact extensometer was not removed until the end of the test to accurately measure uniform and total elongations. The Instron tensile machine was equipped with a 100kN load cell. The cross-head speed was set at 2 mm/minute, which produced a nominal initial strain rate of $6.67 \times 10^{-4}\ s^{-1}$ over the gauge length. Unless stated otherwise, this initial strain rate of $6.67 \times 10^{-4}\ s^{-1}$ was used in all tensile deformation tests in this work. The aim was to minimize the adiabatic heating effect from high strain rates. The experimental scatter of experimental values was included in all graphs and to some degree could have been caused by interruption during tensile deformation. A computer software interface was used to record the output of the load cell and extensometer. Gleeble 1500 Thermomechanical Simulator was used for studying the influence of strain rate on deformation behavior and martensitic transformation of AISI 301LN TRIP steel. Tensile samples were machined according to ASTM standards, A370 and E-8M. The sub-sized standard samples were

machined according to Barba's law for Gleeble tensile testing due to limitation of size on using Gleeble 1500 Thermomechanical Simulator. Changing the dimensions of the test samples has a negligible effect on the yield strength, tensile strength, elongation and reduction of area values provided the ratio (Barba's law), is maintained constant according to E – 8M, ASTM standard.

$$L_o/(A_o)^{1/2}$$

where:

$L_o$ is the original gauge length of the sample, and

$A_o$ is the original cross-sectional area of the sample.

The diameter of the probe of Ferritescope instrument was determined as 9 mm. Therefore, the sub-sized tensile samples had a width 10 mm, which was big enough for accurate measurement of martensite without using dimensional correlation factors. The gauge length was adjusted according to Barba's law.

Engineering stress – strain curves are convenient and easy measurements of engineering data on the strength of materials. The measurements are entirely based on the original dimensions of the samples whereas true stress – strain curves are instantaneous at every point of tensile test and hence the reduction in cross-section is taken into consideration. A true stress strain curve is known as the flow curve of the material as it is based on the actual plastic flow properties of the material. The true stress, $\sigma_{true}$ and true strain $\varepsilon_{true}$ were determined from the engineering stress – engineering strain curve using the following equations:

$$\sigma_{true} = F/A_o(e+1) = s(e+1) \quad \text{....Equation 3.1}$$

and

$$\varepsilon_{true} = \ln(e+1) \quad \text{....Equation 3.2}$$

where:

F is the applied force,

$A_o$ is the initial cross-sectional area of the sample,

e is the engineering strain and

s is the engineering stress.

The equations are only valid within the uniform elongation, that is, until the point of necking. Beyond the point of necking, the strain becomes inhomogeneous. An indication of the percentage of α′-martensite of all the specimens was initially determined using a Ferritescope (Helmut Fisher GmbH, model MP3B) under unloaded conditions at 5% engineering strain intervals. Readings were always taken in the uniform elongation section of the tensile samples. The device was calibrated using standard $\delta$-ferrite samples supplied with it. Seven readings were taken on each sample at different points within the gauge length on the surface. The mean and standard deviations were calculated.

The mechanical energy ($MJ/m^3$) absorbed in the uniform straining region was calculated by integration of true stress-strain curve obtained from tensile testing. The variation of mechanical energy absorbed as a function of strain at a specific temperature was worked out. This had made the calculations of martensitic transformation as a function of mechanical energy absorbed possible.

### 3.1.5.1 Effect of Deformation Temperature

The effect of deformation temperature on the martensitic transformation during cold working of AISI 301LN stainless steel was studied by performing tensile tests in the range of -60 $^{o}$C and +105 $^{o}$C at 15 $^{o}$C interval. The tests were conducted at Mintek in Randburg, South Africa at a low strain rate of $6.67 \times 10^{-4}\ s^{-1}$ to eliminate the effect of adiabatic heating to maintain a constant temperature. The temperature range is typical to temperatures during sheet processing and impact events. The sub-ambient test temperatures were achieved using carbon dioxide and above-ambient temperatures were achieved through the heating of elements in the walls and floor of the environmental chamber. The environmental temperature was air controlled.

### 3.1.5.2 Effect of strain rates

The effect of an increased strain rate on the martensitic transformation during cold working of AISI 301LN stainless steel was investigated by performing tensile tests at a limited range of strain rates between $6.67 \times 10^{-4}\ s^{-1}$ and $1.7\ s^{-1}$ at 30 $^{o}$C using Gleeble 1500 Thermomechanical Simulator. Temperature increases during and after deformation because of adiabatic heating at high strain rates were observed. The increase in temperature is regarded as high enough to cause practically adiabatic condition as the tests were interrupted at 5% strain intervals. The thermocouples were spot welded on the gauge section of the tensile sample.

### 3.1.6 Hardness measurements

Hardness measurements are considered simple, quick, cheaper and non-destructive tests to ascertain the mechanical properties of a material during inspection and control. However, the hardness number or value is not a fundamental property of a material and can only be defined in relation to the technique used to determine the value. The hardness value obtained in a particular test serves only as a comparison between materials or treatments. Hardness has no intrinsic significance as compared to other mechanical properties such as yield strength which can be utilized directly in the design. Hardness values have been used in estimating other mechanical properties such as tensile strength in special cases where a reliable basis for the approximate conversions has been obtained by comparison tests as stated in ASTM E92 – 82 (2003) standard test method for Vickers Hardness of metallic materials. For crash-resistant steel, a maximum hardness of HRc 36 has been called for.

Hardness is related to the elastic and plastic properties. Heat treatment or cold working results in changes in the hardness of the material. The hardness tests may be categorized into three classes which are elastic hardness, resistance to cutting or abrasion and resistance to indentation. An indenter of fixed and known geometry is depressed into the test material resting on a rigid platform under a known static load applied either directly or by means of a lever system. The hardness is expressed by a number that is either inversely proportional to the depth of indentation for a specified load and indenter or proportional to the average load over the area of indentation, depending on the type of test used.

In this thesis, Vickers Hardness technique was used. The instrument uses a square-based diamond-pyramid indenter with an included angle of 136$^{o}$ between opposite faces. The load range is usually between 1 and 120 kg. As a result of the latitude in applied loads, the Vickers tester is applicable to measuring the hardness of very thin sheets as well as heavy sections. Due to microstructural variations in the deformed AISI 301LN austenitic stainless-steel material, the larger the impression area the more accurate the average hardness reading. It was necessary to take many readings for heavily deformed AISI 301LN due to small impression area to obtain a true average hardness of the material.

Macro hardness tests using Vickers hardness testing machines were done on all the samples. The measurements were performed on the plane perpendicular to the rolling direction (longitudinal cross-sectional area) using 10 kg load with a dwell time of 10 s. At least 3 measurements were taken on each sample after a sample preparation which involved a lightly

ground, electropolishing using a Struers Lectropol-5 equipment and A3 electrolyte at an operating voltage of 35 V at room temperature for 50 s. Macro hardness measures the contribution of both martensites and austenite phases. In this thesis, a variation of Vickers hardness as a function of degree of cold rolling and as a function of percentage of strain induced martensite has been demonstrated. A correlation relationship between average hardness and tensile strength was deduced. In addition, the limiting percentage cold rolling to avoid exceeding the maximum hardness of HRc 36 was established.

### 3.1.7 Microstructural observations

All the samples were mechanically ground to 1200 grit size and electropolished using a Struers Lectropol-5 equipment and A3 electrolyte at operating voltage of 35 V at room temperature for 50 s before any microstructural analysis. Electropolishing was done to obtain a deformation-free surface which could be due to manual grinding and polishing. Electro-etching was done for light optical microscopical analysis. The microstructure of deformed metastable AISI 301LN is composed of a matrix of austenite reinforced by a certain percentage of islands of martensite depending with the degree and temperature of deformation. Understanding the microstructure aids in the modelling of the mechanical properties. This leads to multi-phase modelling in the designing of new steels: (constituent volume fractions, constituent properties, austenite stability). The microstructural evolution as a function of percentage of rolling and tensile strain has been observed and characterised using EBSD system.

#### 3.1.7.1 Electron back-scatter diffraction Electron (EBSD)

EBSD analysis was carried out using EBSD Oxford instrument at an accelerating voltage of 20kV and a working distance of 10 mm. The γ-austenite, α′-martensite and ε-martensite phases were clearly distinguished using EBSD and have subsequently been quantified. Heavily deformed material resulted in poor EBSD images due to poor Kikuchi patterns because of high levels of dislocations. EBSD Kikuchi quality maps of strained samples were added.

#### 3.1.7.2 Transmission Electron Microscope (TEM)

Microstructures of cold rolled and tensile strained materials were examined using transmission electron microscope (JEOL 2100). Thin TEM samples were first mechanically thinned and subsequently jet-polished with twin-jet equipment at 120 kV at room temperature using Struers A2 electrolyte.

### 3.1.8 Austenite stability indicators

Austenite stability indicators are a powerful way to gain insight into austenite metastability of a given chemical composition at a specific deformation temperature, for instance, metastable austenitic stainless steels of low SFE (below 20 mJ/m$^2$) in the AISI 300 series have shown a strong hardening phenomenon which is caused by the formation of strain-induced martensite [154]. Stability of metastable austenitic steels is chiefly influenced by the chemical composition [148]. The austenitic stability indicators are calculated based on chemical composition and/or deformation temperature. Table 3.2 shows the calculated $M_d$ (30/50) and derived SFE values for the different tested AISI 301LN heats. Several equations were formulated for estimation of stacking-fault energy (SFE). The Brofman and Ansell composition-based equation was used to determine the SFE of AISI 301LN austenitic stainless-steel heats to predict the austenitic stability of three different heats as illustrated in Table 3.1. The SFE of all the alloys testes was found to be similar as shown in Table 3.2. In this table, the $M_d$ (30/50) temperature and SFE values of three heats employed in this study are compared to that of alloy compositions which are at the maximum limits of the AISI 301 specifications.

Livitsanos and Thompson [155], defined the Maximum Elongation Temperature (M.E.T) as the temperature at which the major principal strain is maximum as determined from uniaxial tensile testing. The M.E.T was determined in this work on the plot of maximum uniform elongation as a function of deformation temperature. The $M_d$ (30/50) temperature was determined from tensile and volume fraction of martensite test results.

**Table 3.2: Calculated $M_d$ (30/50) and SFE for different tested AISI 301LN heats, as compared to steels of other compositions within the AISI 301 specification**

| AISI 301LN heats | *$M_d$ (30/50) temperature (°C) | **Stacking Fault Energy (mJ/m$^2$) |
|---|---|---|
| A | 29.8 | 15.3 |
| B | 30.0 | 15.3 |
| C | 34.4 | 15.4 |
| Max of 301 specification | -4.1 | 18.8 |
| Max of 301L specification | 5.1 | 15.7 |
| Min of 301LN specification | 5.1 | 18.1 |
| Max of 301LN specification | 65.2 | 15.7 |

* Calculated using Angel's equation [27]. ** Calculated using Brofman and Ansell equation [101].

Table 3.2 demonstrates that the austenite stability of the three alloys selected for the current study, compared to the maximum limits of the AISI 301 specification. The specification demonstrates that the three alloys have very similar levels of austenite stability. Furthermore, the composition of the three alloys have been selected in such a way that martensite formation can be readily achieved at ambient conditions, at relatively low alloying cost (low nickel content).

A lower carbon 301 grade designated as **301L** indicates a lower austenitic stability by a slightly higher $M_d$ (30/50) temperature and lower stacking fault energy. Grade **301LN** has higher nitrogen content so as to compensate for the lower carbon content. A much higher $M_d$ (30/50) temperature indicates a further reduced stability of austenite. The austenite stability index of the tested alloys in terms of $M_d$ (30/50) temperature and SFE places them with the 301LN grade.

## 3.2 Influence of process variables

### 3.2.1 Temperature and extent of strain application

A series of interrupted elevated and low temperature uniaxial tensile testing at 5% engineering strain intervals were conducted at various temperatures ranging from -60 to 180 °C using an Instron-type machine (1175 model) fitted with an environmental chamber (3110 model) with an initial strain rate of $6.67 \times 10^{-4}$ $s^{-1}$. A low strain rate was meant to avoid/minimize increase in temperature from adiabatic heating. An indication of the percentage of α′-martensite of all the specimens was initially determined using a Ferritescope at 5% engineering strain intervals. The device was calibrated using standard $\delta$-ferrite samples supplied with it. Seven readings were taken on each sample at different points within the uniform gauge length on the surface. In-situ magnetic measurements using a Ferritescope instrument were corrected to actual α′-martensite content by a correlation factor of 1.70, as was found from calibration curve [147]. The calibration curve was developed from tensile strained samples since tensile forces result in uniform distribution of strain and hence uniform distribution of α′-martensite as compared to cold rolling where friction-induced redundant strain results in more deformation near the surface than the centre. Non-uniform distribution of strain in cold rolling results in non-uniform distribution of α′-martensite across thickness. The magnetic measurements on the specimens were taken at different strains under loaded and unloaded conditions to show the magneto-mechanical (Villari) effect [156].

$M_d$ (30/50) is the temperature at which 50% of the austenite transforms to martensite after 30% true strain. The $M_d$ (30/50) was estimated from the sigmoidal curves showing the variation

of percentage of martensite as a function of straining temperature. $M_d$ temperature is temperature at which no martensite forms regardless of the amount of strain applied. These temperatures were determined experimentally from the tensile and Ferritescope (calibrated) measurements.

### 3.2.2 Influence of degree of prior cold rolling

The effect of temper rolling on tensile properties and hardness values has been investigated for the alloy concerned. The interrelationship equations between temper rolling reductions and tensile properties such as yield strength, ultimate tensile strength, uniform and total elongations, ratio of yield strength to tensile strength, and work hardening exponents have been investigated by others [157]. This has led to prediction of plastic deformation behaviour and mechanical (tensile and hardness) properties of steels during temper rolling.

Hot rolled, annealed and pickled (AP1) AISI 301LN stainless steel sheets with initial thickness ranging from 4 mm to 6 mm were cold rolled to different gauges employing cold rolling reductions ranging from 5%~70% at room temperature. Thickness reduction of ~ 0.8 % and less per pass was used to avoid significant adiabatic heating during cold rolling. Characterization of the material was then done using electron back scattered diffraction (for low deformed samples), X-ray diffraction (for high deformed samples), Ferritescope measurements and tensile testing. The microstructures were examined in two orientations, longitudinal cross sections and surface of AP1, and 5% to 65% cold rolled samples. Tensile samples were machined in the rolling direction from the cold rolled sheets. The cold rolled samples were not machined to the same thickness to avoid excessive formation of strain-induced martensite in the process. Tensile tests of the cold rolled samples were interrupted at 5% engineering strain for Ferritescope measurements and minimizing adiabatic heating.

### 3.2.3 Strain rate

A series of interrupted tensile tests were done in a Gleeble 1500 Thermomechanical Simulator at a fixed temperature of 30 °C at varying strain rates. An indication of the percentage of α′-martensite was determined using a Ferritescope instrument (Helmut Fisher GmbH, model MP3B) at 5% strain intervals. The magnetic measurements on the specimens were taken at different strains under unloaded conditions.

## 3.3 Development of calibration functions

Ferritescope readings do not provide the volume fraction of martensite but is directly correlated to it. Calibration functions were therefore developed both for samples strained in tension (section 3.3.1) and compression (section 3.3.2) using three test techniques

### 3.3.1 Calibration of Ferritescope measurements for tensile straining

Figure 3.1 shows the magnetization curves of samples with varying amounts of strain-induced martensite after tensile deformation using alloy A. The percentage of strain-induced martensite was calculated using $V_{\alpha'}$ = (MS/136), where MS is saturation magnetization per unit mass. This was estimated using a saturation magnetization of 123.5 emu/g which was obtained using a sample with known volume fraction of α′-martensite. The specific magnetization saturation value of 136 emu/g would be for a microstructure which contains ideally 100% α′-martensite. The magnetization saturation increases with increase in deformation at lower temperatures and was in good agreement with the results obtained through Ferritescope readings, X-ray and neutron diffraction analyses.

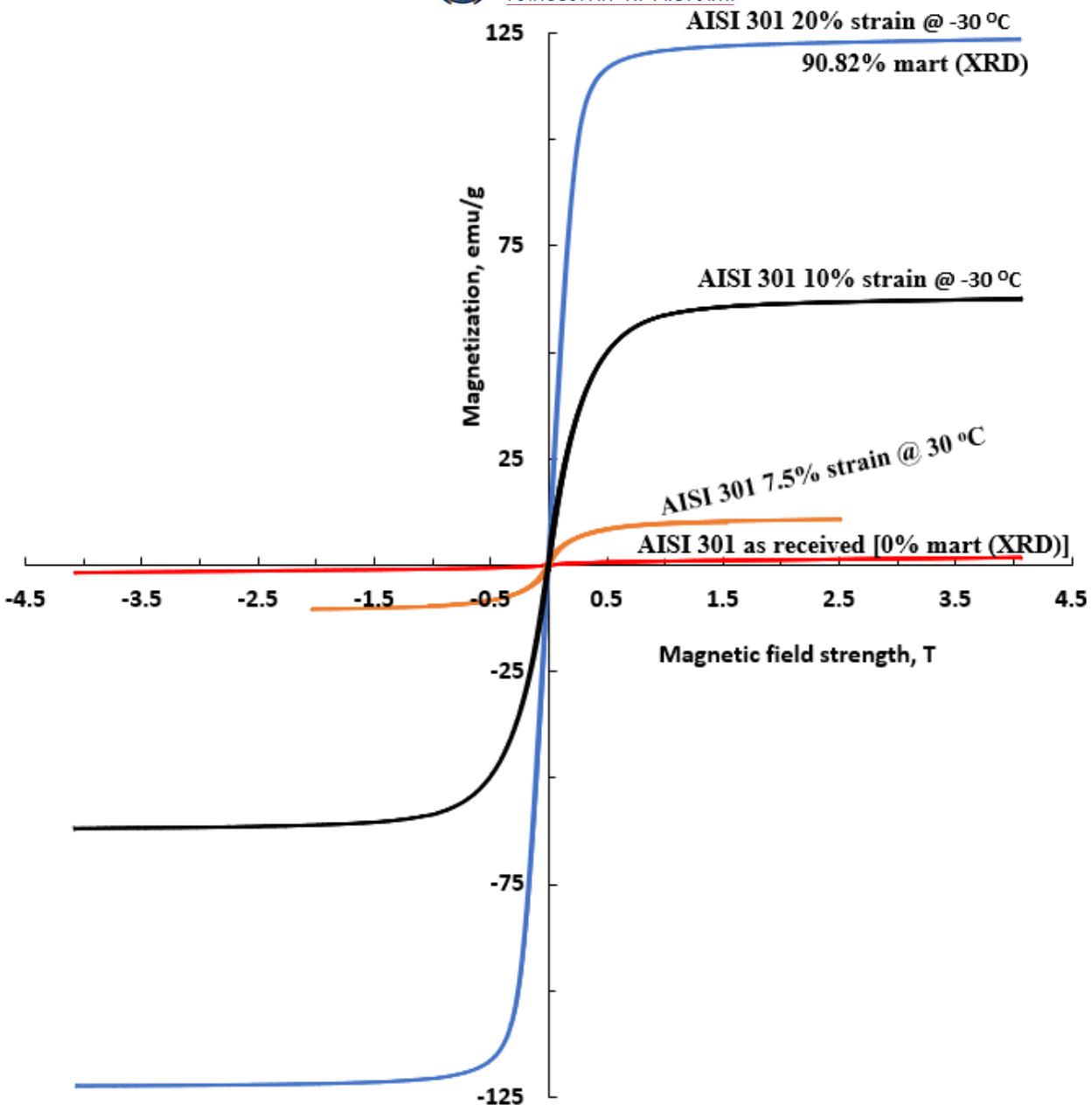


**Figure 3.1: Magnetization curves of samples with varying amounts of martensite**

A calibration curve (shown in Figure 3.2) was subsequently developed using VSM measurements, X-ray and neutron diffraction to determine the actual percentage of α′-martensite as a function of the Ferritescope measurements, which gave rise to equation (3.3) [158]. A calibration factor of 1.70 was obtained which is in good agreement with what was reported in literature [114], [147]. The calibration factor was done on unstressed sample. There was no need for thickness correction as the thickness of the samples were all greater than 2 mm. The relationship between Ferritescope readings and measured α′-martensite contents (using x-ray and

neutron diffraction techniques) was found to be linear with good coefficient of determination for Ferritescope readings below 50 (which corresponds to the α′-martensite content of 85%). This was however done using x-ray and neutron diffraction techniques which are both influenced by preferred orientation during plastic deformation, an effect known as texture. Partial randomization was done to minimize the effect of texture by spinning the samples in neutron diffraction measurements and rotation of the sample holder in x-ray diffraction analysis. The techniques are expensive, and time consuming, hence limited number of samples were analysed. Talonen et al. found the linearity up to the Ferritescope reading of 55 which corresponds to the α′-martensite of 90%). Talonen et al. and Besse et al. have used magnetic measurements and texture influence was not reported. With the determined correlation factor of 1.70, non-destructive in-situ measurements of α′-martensite content using Ferritescope instrument during interrupted tensile testing at various temperatures was possible.

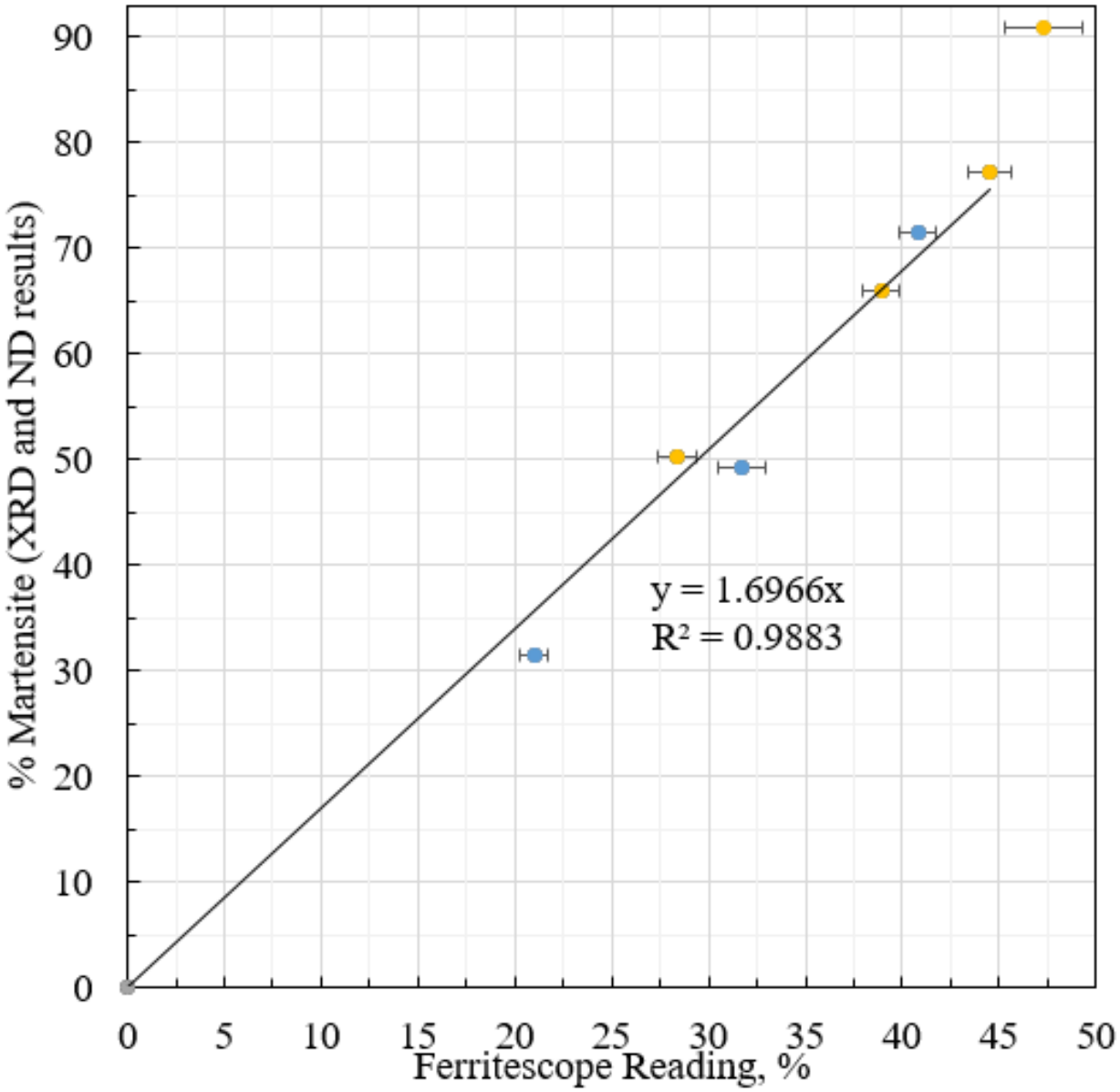


**Figure 3.2: Calibration curve between percentage of martensite measurements with X-ray and Neutron diffraction analyses and Ferritescope readings**

**$\alpha'$-Martensite content = 1.70 x Ferritescope reading ….....Equation 3.3**

### 3.3.2 Calibration of Ferritescope measurements for compressive straining

The prior cold rolling had resulted in a certain amount of martensitic transformation. The percentage of martensite was initially determined using the Ferritescope instrument and the readings were corrected by a multiplication factor of 1.62. A calibration factor of 1.62 for cold rolled samples was evaluated using neutron diffraction technique as shown in Figure 3.3 and was

found to be different from 1.70 shown in Figure 3.2 which was obtained using tensile samples. There is uniform distribution of strain during tensile deformation and hence uniform distribution of α′-martensite. The friction-induced redundant strain during cold rolling results in more deformation near the surface than the center hence slightly higher amounts of α′ martensite near the surface in the early stages of deformation. Non-uniform distribution of strain in cold rolling results in non-uniform distribution of α′-martensite across the thickness.

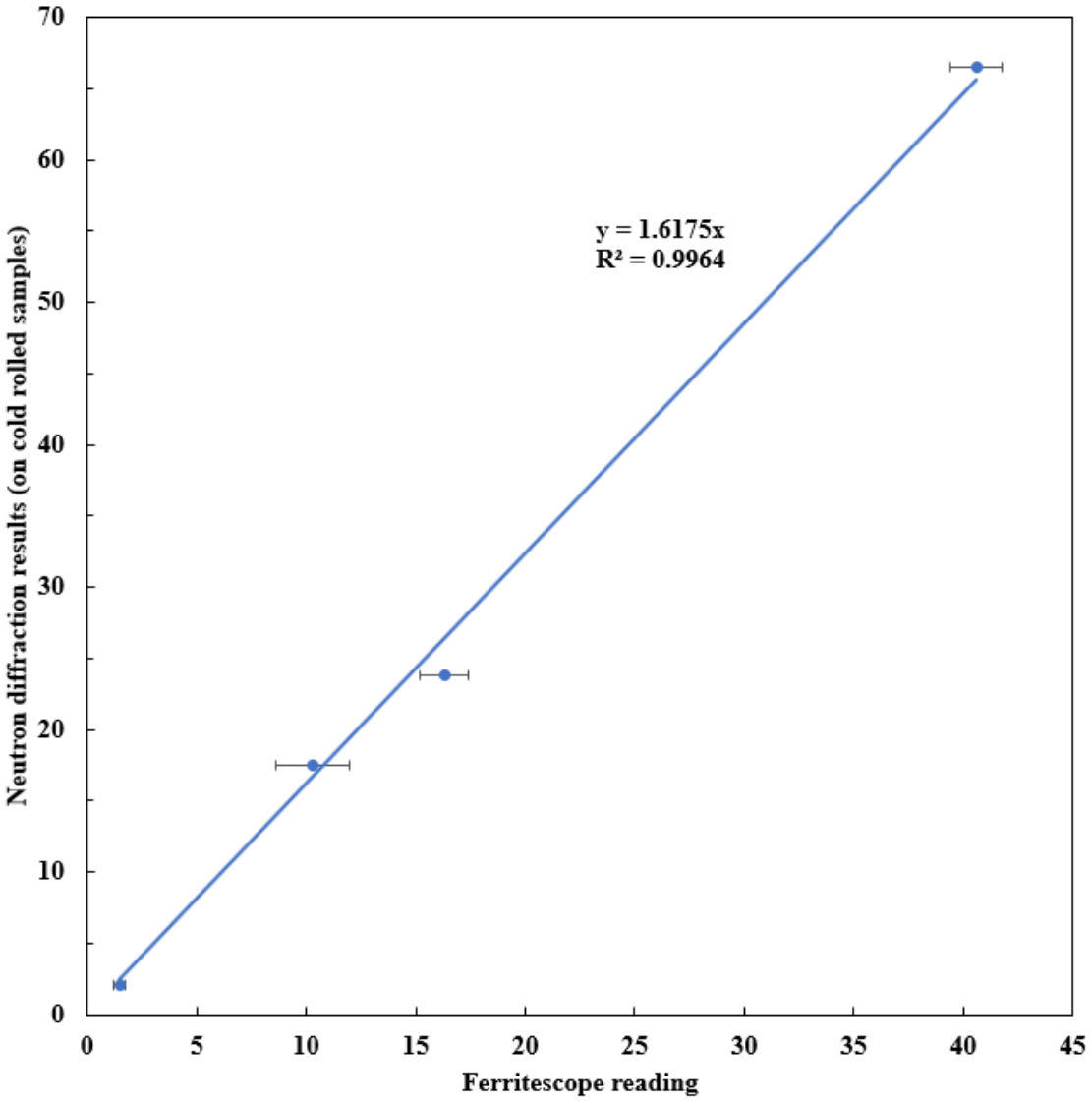


**Figure 3.3: Calibration curve between percentage of martensite measurements (Neutron diffraction analyses and Ferritescope readings) using alloy B cold rolled samples**

Figure 3.4 and Figure 3.5 show corrected (a calibration factor of 1.7) Ferritescope measurements taken under load (with load maintained) and after unloading (unstressed)

conditions during interrupted tensile tests at 5% engineering strain intervals at an initial strain rate of 6.67 x $10^{-4}$ $s^{-1}$ for alloy A and alloy B, respectively. Seven readings were taken on each sample at different points within the gauge length on the surface. The mean and standard deviations were calculated.

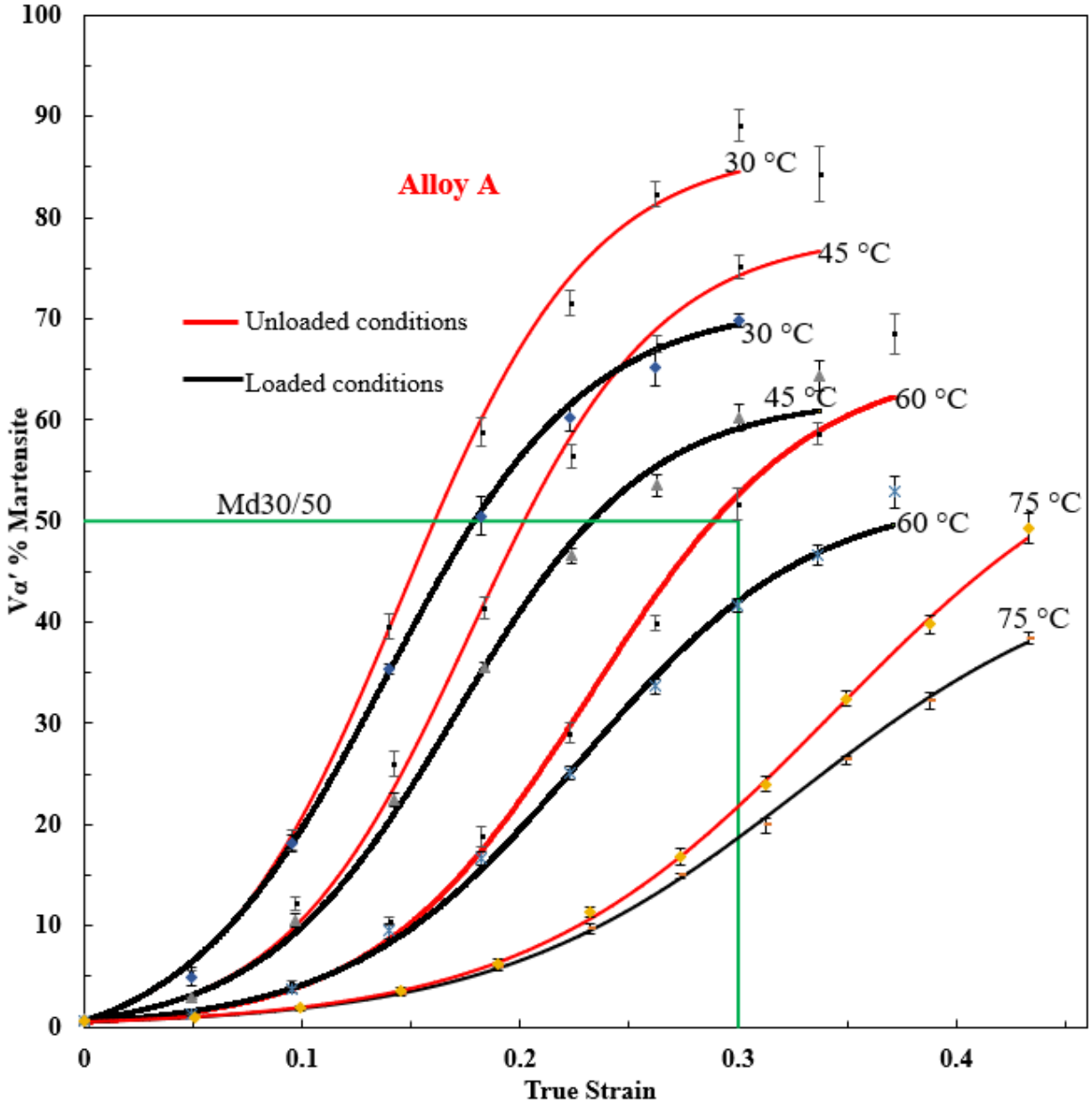


**Figure 3.4: Percentage of α′-martensite induced as a function of true strain at various deformation temperatures through tensile for alloy A with measurements performed under load (black line) and after unloading (red line) tested at an initial strain rate of 6.67 x $10^{-4}$ $s^{-1}$**

As the degree of deformation increases above a true strain of 0.1, an increasing deviation between the measurements performed under load and after unloading is observed in both alloys and at all temperatures. This shows a change in the magnetic response of the material due to applied tensile stress. At higher strain, the atoms are not in their equilibrium positions resulting in change of magnetic properties. The true measurements were taken under no applied stress with atoms in their equilibrium positions.

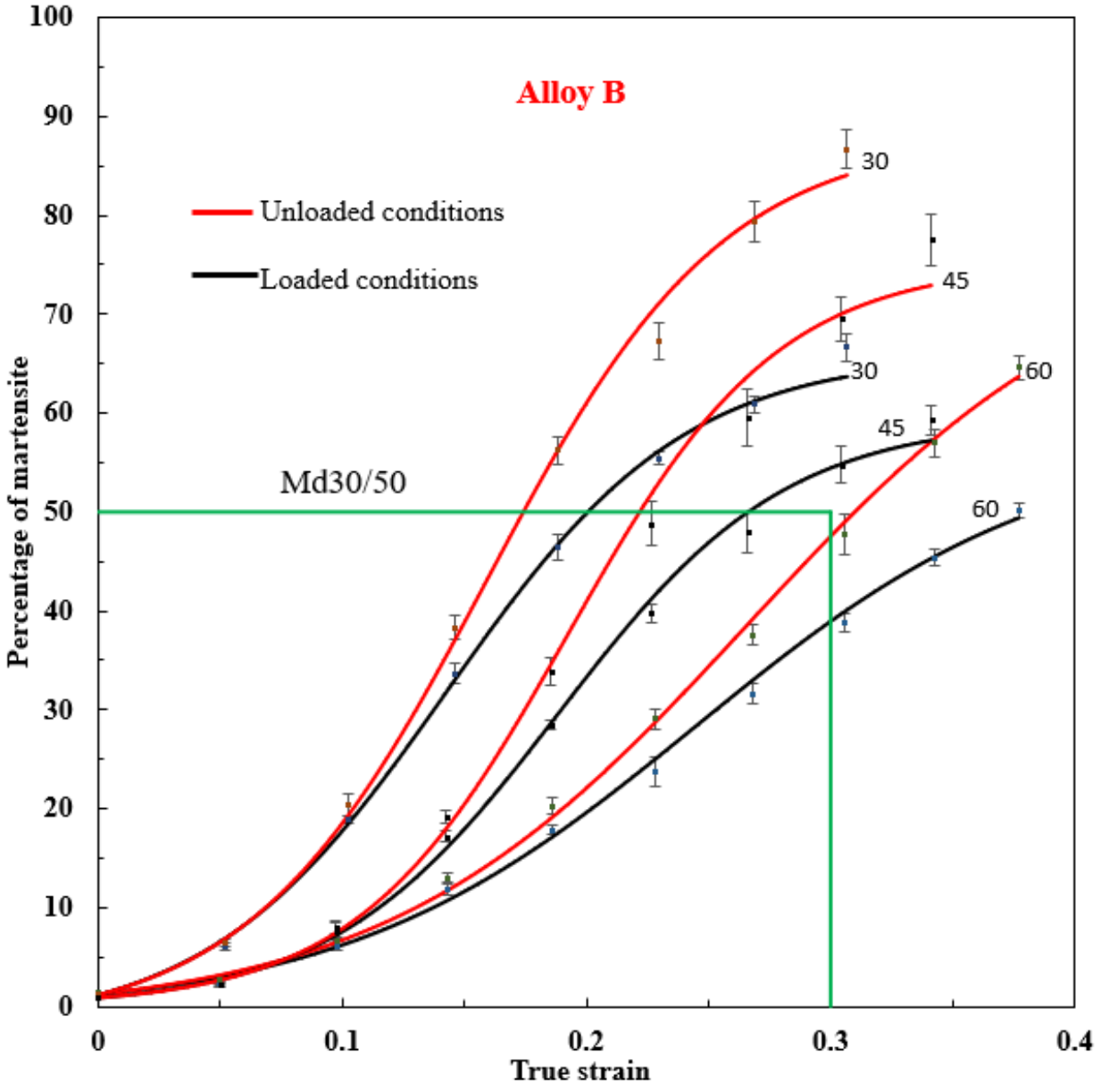


**Figure 3.5: Percentage of α′-martensite induced as a function of true strain at various deformation temperatures through tensile for alloy B with measurements performed under load (black line) and after unloading (red line) tested at an initial strain rate of 6.67 x $10^{-4}$ $s^{-1}$**

# Chapter 4: Results and Analysis

The results of the influence of simulated process variables on austenite to strain-induced martensitic microstructural transformation and the resulting mechanical properties of the specific lean- alloyed, medium nitrogen version of AISI 301LN investigations are outlined in this chapter. The general approach used here was that of establishing the influence of the plant processing variables on the austenite to martensite transformation by simulating the application of strain under controlled conditions. Tensile straining was used in many cases, and the influence of adiabatic heating was avoided in the laboratory by performing interrupted tensile straining, in relatively small strain increments. The influence of applied elastic strain on magnetic response was eliminated by relaxing the tensile samples after strain application.

The assumption at the outset was made that, because it has been shown that sigmoidal equations can be used to describe the transformation to martensite as a function of applied strain and temperature in austenitic steels, that constitutive equations that describe the plastic flow behaviour could be developed as well for the alloy in question, using the same sigmoidal format. In this way, a set of equations would be developed that would lead to an accurate calculation of the flow properties as a function of temperature and strain. Insight into the fundamentals of the flow behaviour would be gained by the preceding study of the dependence of the volume fraction of martensite on the applied strain and temperature, aided by imaging and analytical techniques such as electron microscopy, including EBSD, as well as neutron and X-ray diffraction. The influence of prior cold rolling on martensite content and tensile flow properties, would similarly be studied by eliminating adiabatic heating as far as possible.

Plant-based users of the equations to be developed, would need to factor in the influence of adiabatic heating on plant level by establishing the temperature changes during cold rolling, and compensating for that by using the temperature terms in the equations.

## 4.1 Influence of deformation temperature and strain (alloy A)

Alloy A was used in this section. As described earlier, the alloys evaluated here were selected due to plant experience indicating that a lean alloyed 301 LN steel, using low carbon and medium-to-high nitrogen levels, but low nickel content, showed promise as far as a combination of low cost to good mechanical properties are concerned. A comparison of the austenite stability of the alloy evaluated here, to that of the maximum and minimum of the AISI 301 LN specification, is shown in Table 4.1.

**Table 4.1: Calculated $M_s$, $M_d$ (30/50) temperatures and SFE for the tested alloy A, as compared to minimum and maximum compositions within the AISI 301LN specification**

| AISI 301LN heats | *$M_s$ temperature (°C) | **$M_d$ (30/50) temperature (°C) | **Stacking Fault Energy ($mJ/m^2$) |
|---|---|---|---|
| A | -240 | 29.8 | 15.3 |
| Min of 301LN specification | -366 | 5 | 18.1 |
| Max of 301LN specification | -150 | 65.2 | 15.7 |

*Calculated using Eichelmann and Hull [106]. ** Calculated using Angel's equation [27].

*** Calculated using Brofman and Ansell equation [101].

The comparison demonstrates that the alloy selected (A) is midway within the AISI 301 LN grade. The comparison to other AISI 301 specifications reported on in Table 3.2, indicates that the 301LN grade has the lowest austenite stability of the 301 grades, facilitating martensite formation at ambient temperature. Preliminary work was done to establish the $M_s$ temperature of the tested alloy A. Figure 4.1 shows the Neutron diffraction spectra before and after cooling the as-received sample A to -270 °C in a cryogenic neutron diffraction facility, showing no observed crystallographic changes due to the cooling.

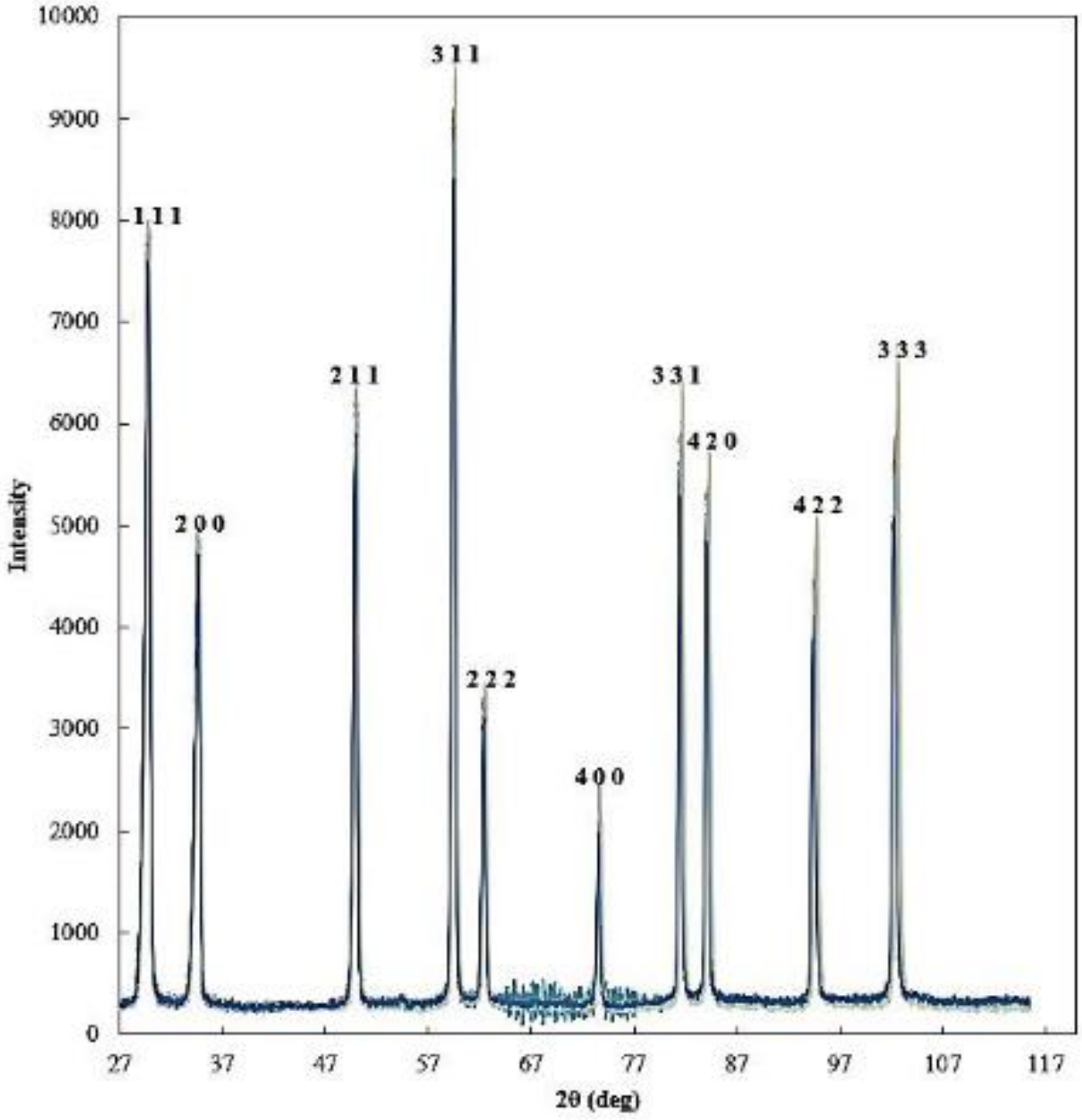


**Figure 4.1: Neutron diffraction analysis of steel A in 'as-received' condition at 27 °C, -23 °C, -28 °C, -31 °C, -35 °C, -38 °C, -43 °C, -46 °C, -49 °C, -53 °C, -73 °C, -123 °C, -173 °C, -270 °C and 27 °C again, with the diffraction spectra remain unchanged throughout the temperature range.**

The interrupted in-situ neutron diffraction results observed between 27 °C and -270 °C did not identify any transformation of the austenite of the as-received sample. All the diffraction spectra taken throughout the temperature range lie on top of each other as shown Figure 4.1. The calculated $M_s$ temperature of this steel is -240 °C using the Eichelman and Hull equation as shown in Table 4.1. However, Cryogenic Neutron Diffraction testing performed on the steel

showed no thermal martensitic formation even at temperatures approaching absolute zero Kelvin (-273 °C).

### 4.1.1 Effect of temperature on martensitic transformation

Figure 4.2 shows the α′-martensite transformation as a function of temperature and strain using alloy A. Interrupted tensile tests at an initial strain rate of 6.67 x $10^{-4}$ $s^{-1}$ were done at 5% engineering strain intervals allowing Ferritescope readings to be taken. Seven readings were taken on each sample at different points within the gauge length on the surface. The mean and standard deviations were calculated. A calibration factor of 1.70 was used to convert Ferritescope readings to actual martensite content as described in Chapter 3.3. The Ferritescope readings were taken under unloaded (unstressed) conditions. The relationship of percentage of strain-induced martensite as a function of strain indicates the effects of deformation temperature, that is, a transition from sigmoidal curve at low deformation temperatures to smooth (parabolic) curve at high deformation temperatures. The formation of strain-induced martensite is dependent on the deformation temperature, and greatly increases with decrease in temperature. The sigmoidal curve fitted, for temperatures between -60 °C to 60 °C, at all true strain levels could be accurately described by the following equation:

$$\mathbf{V_{\alpha'} = V_{\alpha's} - (V_{\alpha's})[1 + \exp(\varepsilon - \alpha_m)(\beta_m)^{-1}]]^{-1}} \quad \textbf{..... Equation 4.1}$$

with $R^2 \geq 0.991$, for all temperatures.

Where:

$V_{\alpha'}$ is the percentage of strain-induced martensite formed within uniform elongation of tensile sample at a given temperature, after correction by the "calibration curve" in Figure 3.2

$V_{\alpha's}$ is the saturation value of $V_{\alpha'}$, that is, the maximum amount of martensite that could be attained in the material at a given temperature. This value is reached when the sigmoidal function levels off and/or 100% for lower temperatures.

$\varepsilon$ is the true strain.

$\alpha_m$ is the true strain which corresponds to maximum rate of martensitic transformation.

$\beta_m$ is a constant derived from the nature of the percentage of martensite as a function of strain. The numerical value is given by, $\beta = (V_{\alpha's})$(4 x maximum slope of the rate of martensitic transformation)$^{-1}$.

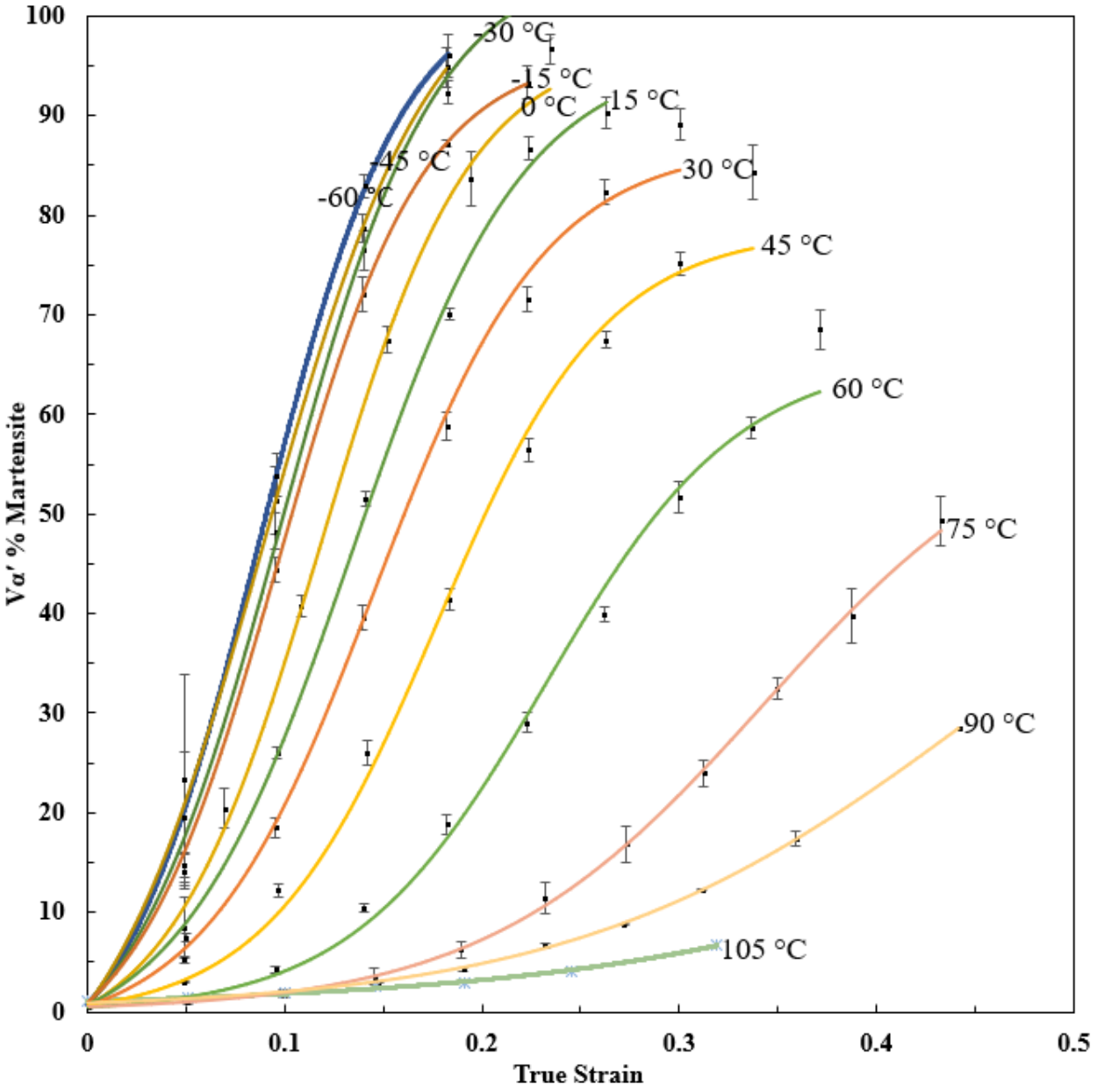


**Figure 4.2: Percentage of α′-martensite induced as a function of strain for alloy A at an initial strain rate of 6.67 x $10^{-4}$ $s^{-1}$ at various deformation temperatures (fitted sigmoidal curves).**

Martensitic transformation is enhanced at low temperatures hence the onset of strain-induced martensite occurred more readily with decrease in temperature. It has been observed that as temperature increases, the austenitic stabilization increases or the α′-martensite transformation is delayed. With increased austenitic stabilization with temperature, the critical amount of dislocations for α′-martensitic nucleation requires higher amount of plastic strain and mechanical energy accompanied by reduction in chemical energy for phase transformation at high

temperature. This shows that there is reduction in driving force for martensitic transformation as temperature increases.

Table 4.2 shows the values of $\alpha_m$ and $\beta_m$ as fitted in the derived constitutive equation (4.1). The values of $\alpha_m$ and $\beta_m$ varies as deformation temperature increases and this results in transition of the mathematical equation from a sigmoidal curve at low deformation temperatures to smooth curve at high deformation temperatures with a high coefficient of determination, $R^2$ observed in the whole temperature range tested.

**Table 4.2: The strain sensitivity, ($\alpha_m$) and $\beta_m$ for temperatures ranging between -60 °C and 105 °C for the AISI 301LN alloy investigated**

| Temperature, (°C) | strain sensitivity, $\alpha_m$ | $\beta_m$ | $R^2$ |
|---|---|---|---|
| -60 °C | 0.0876 | 0.0360 | 1.00 |
| -45 °C | 0.0898 | 0.0422 | 1.00 |
| -30 °C | 0.0980 | 0.0394 | 1.00 |
| -15 °C | 0.0968 | 0.0368 | 1.00 |
| 0 °C | 0.118 | 0.0383 | 0.999 |
| 15 °C | 0.134 | 0.0438 | 0.999 |
| 30 °C | 0.145 | 0.0434 | 0.999 |
| 45 °C | 0.177 | 0.0430 | 0.996 |
| 60 °C | 0.232 | 0.0492 | 0.993 |
| 75 °C | 0.343 | 0.0708 | 0.999 |
| 90 °C | 0.452 | 0.102 | 0.999 |
| 105 °C | 1.36 | 0.152 | 0.991 |

Figure 4.3 shows the rate of $\gamma \rightarrow \alpha'$ strain–induced martensitic transformation per unit strain ($dV\alpha'/d\varepsilon$). These values denote the slopes of the curves in Figure 4.2 as a function of strain. The instantaneous gradient increased to a maximum and thereafter decreases to zero martensitic transformation as martensitic saturation value at a given temperature is achieved. The maximum $\alpha'$-martensite transformation per unit strain applied decreased as deformation temperature increases.

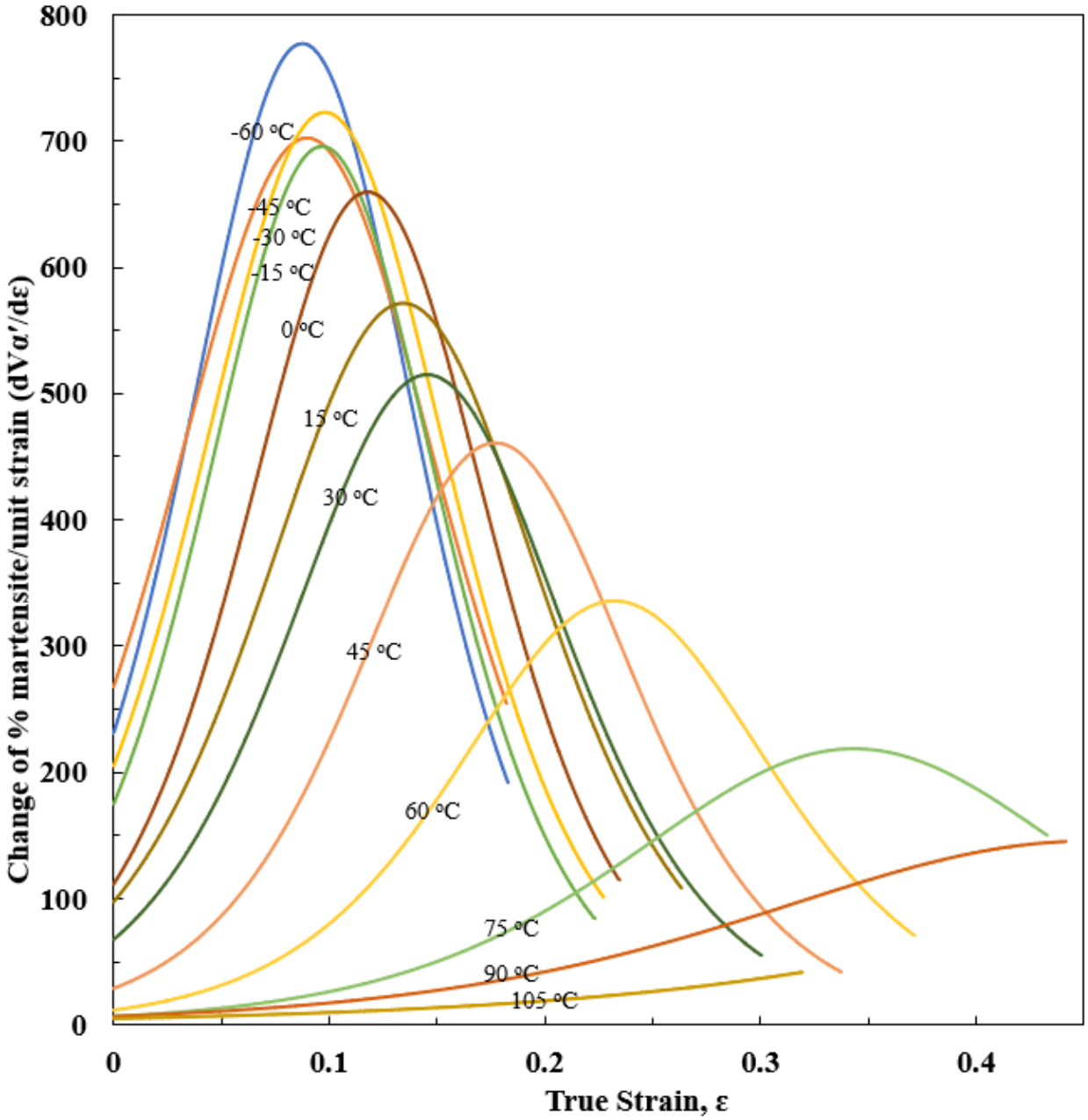


**Figure 4.3: Rate of α′-Martensite transformation as a function of strain for alloy A at an initial strain rate of 6.67 x $10^{-4}$ $s^{-1}$ in the temperature ranging from -60 °C to 105 °C**

Figure 4.4 was obtained by plotting applied strain, $\alpha_m$ at which maximum dVα′/dε occurs, which corresponds to the strain at which martensitic transformation rate is at a maximum. For temperatures, 90 °C and 105 °C, there is no specific strain which corresponds to maximum martensitic transformation due to a change of fit from sigmoidal to polynomial. For 105 °C, there is an initial austenitic stabilization at lower strain which required higher strain for significant martensitic transformation. The strain associated with for maximum martensite transformation

increases with temperature due to increased stabilization of austenite in the early stages of deformation.

Figure 4.5 shows the variation of $\beta_m$ constants as a function of temperature in the developed sigmoidal function for martensitic transformation as a function of applied strain. The curves in Figure 4.4 and Figure 4.5 represent equations giving the values of the sigmoidal function constants ($\alpha_m$ and $\beta_m$) as a function of temperature in the range -60 to 75 °C. The equations are:

$$\alpha_m = 1.36362 - (1.27402)/(1 + \exp((T-115.3718)/27.81226)) \quad \text{Equation 4.2}$$

With $R^2 = 0.99437$.

Where:

$\alpha_m$ is a constant in the sigmoidal function in equation (4.1). The variation of $\alpha_m$ as a function of deformation temperature is sigmoidal as represented by equation (4.2).

T is temperature in °C.

$$\beta_m = 4E\text{-}12*T^5 + 3E\text{-}10*T^4 + 2E\text{-}8*T^3 + 4E\text{-}7*T^2 - 4E\text{-}6*T + 0.0398 \quad \text{Equation 4.3}$$

With $R^2 = 0.9953$.

Where:

$\beta_m$ is a constant in the sigmoidal function in equation (4.1).

T is temperature in °C.

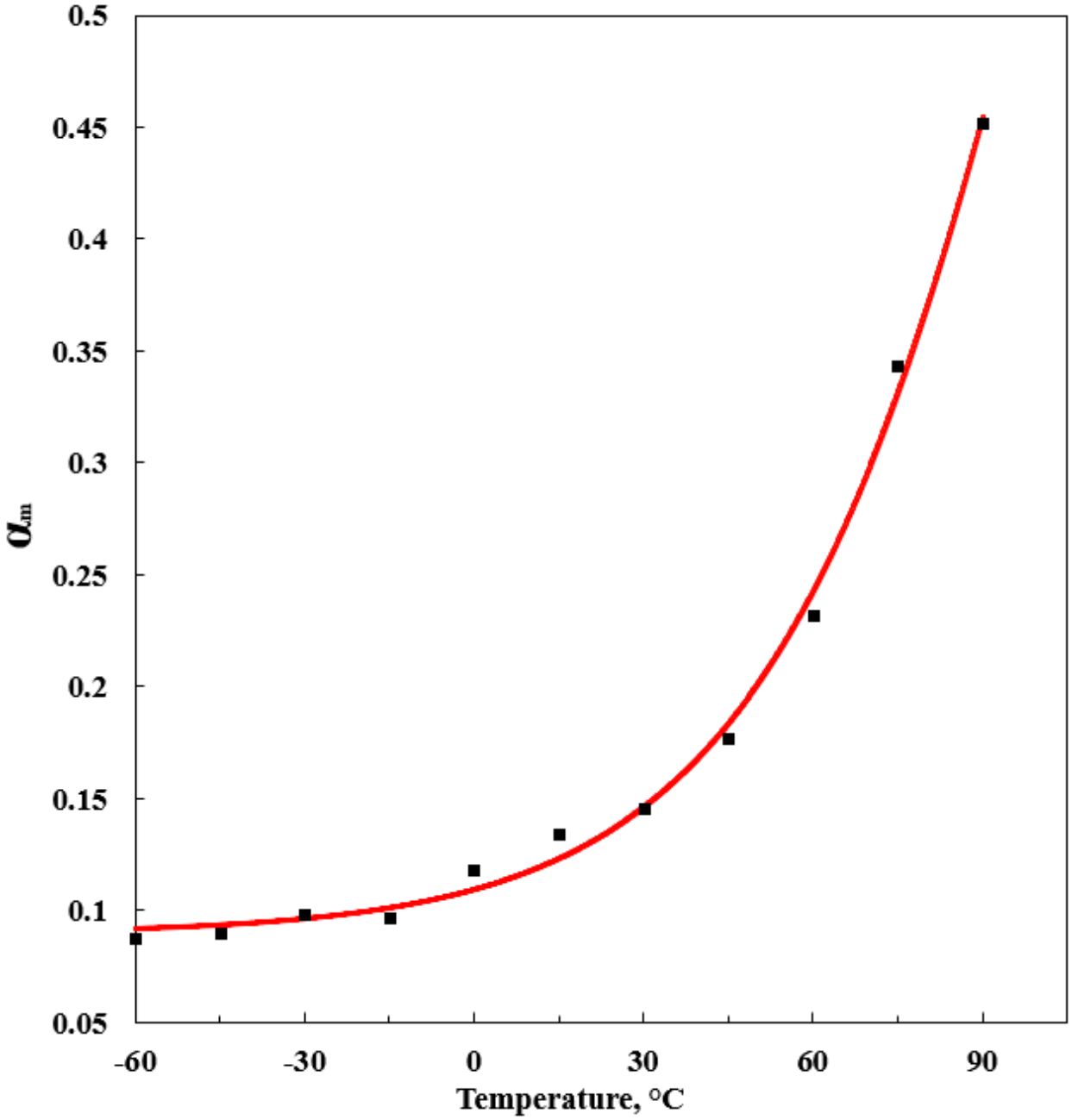


**Figure 4.4: Strain for maximum martensite transformation, $\alpha_m$ (strain sensitivity) as a function of deformation temperature for alloy A.**

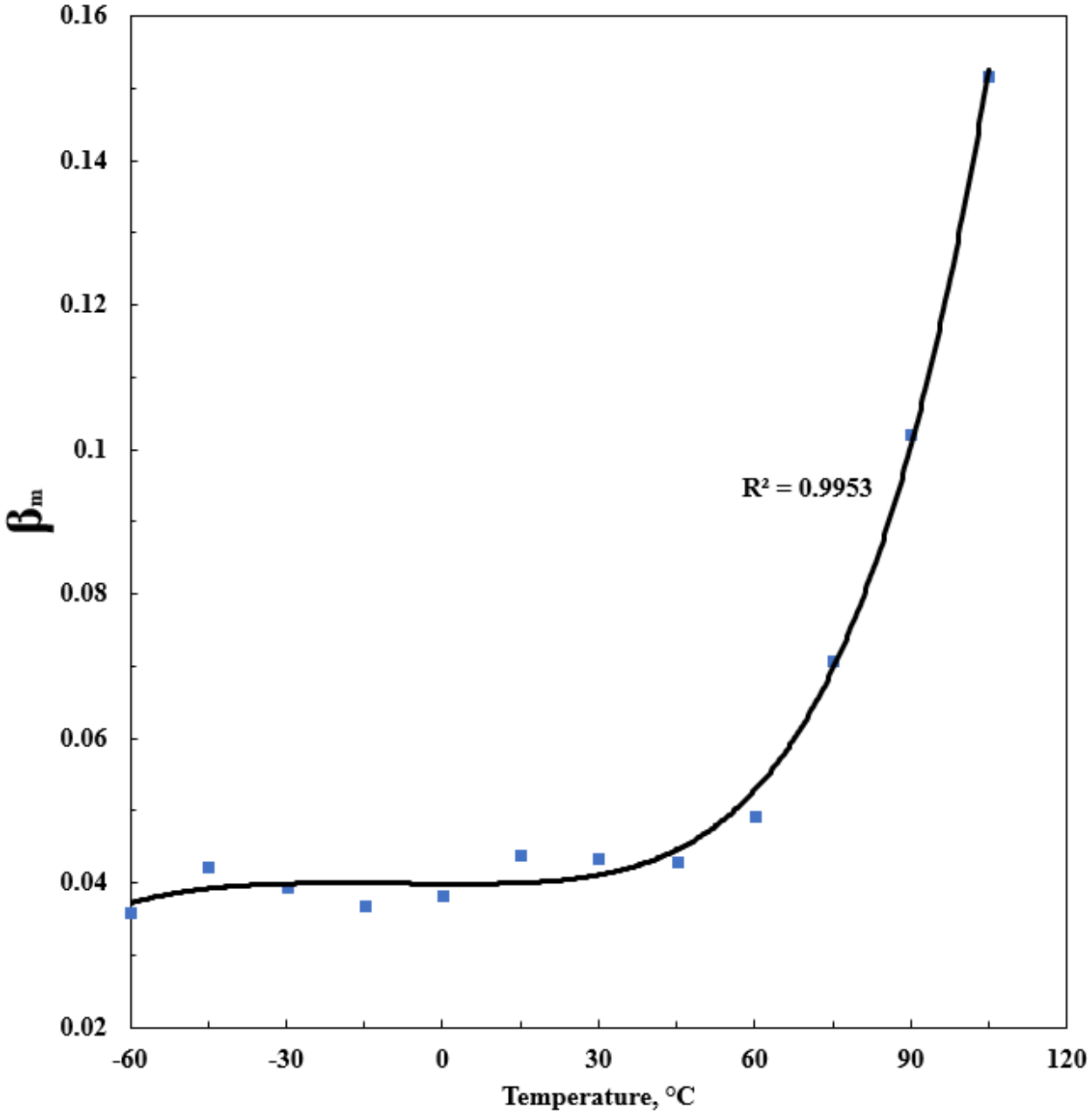


**Figure 4.5: Variation of $\beta_m$ as a function of deformation temperature for alloy A.**

The peak instantaneous martensitic transformation rate, as shown in Figure 4.6 was found to be decreasing as deformation temperature increases. For deformation temperatures of 90 °C and above, the mathematical function to describe the percentage of martensite induced as a function of strain changes to polynomial giving no clear applied strain as a turning point on the slopes of the curves. The mathematical relationship shown in Figure 4.6 can be represented by the following equation:

**Peak martensitic transformation rate = $-0.0284*T^2 - 3.4237*T + 645.85$ ..... Equation 4.4**

with $R^2 = 0.9876$.

Where:

T is the deformation temperature in °C.

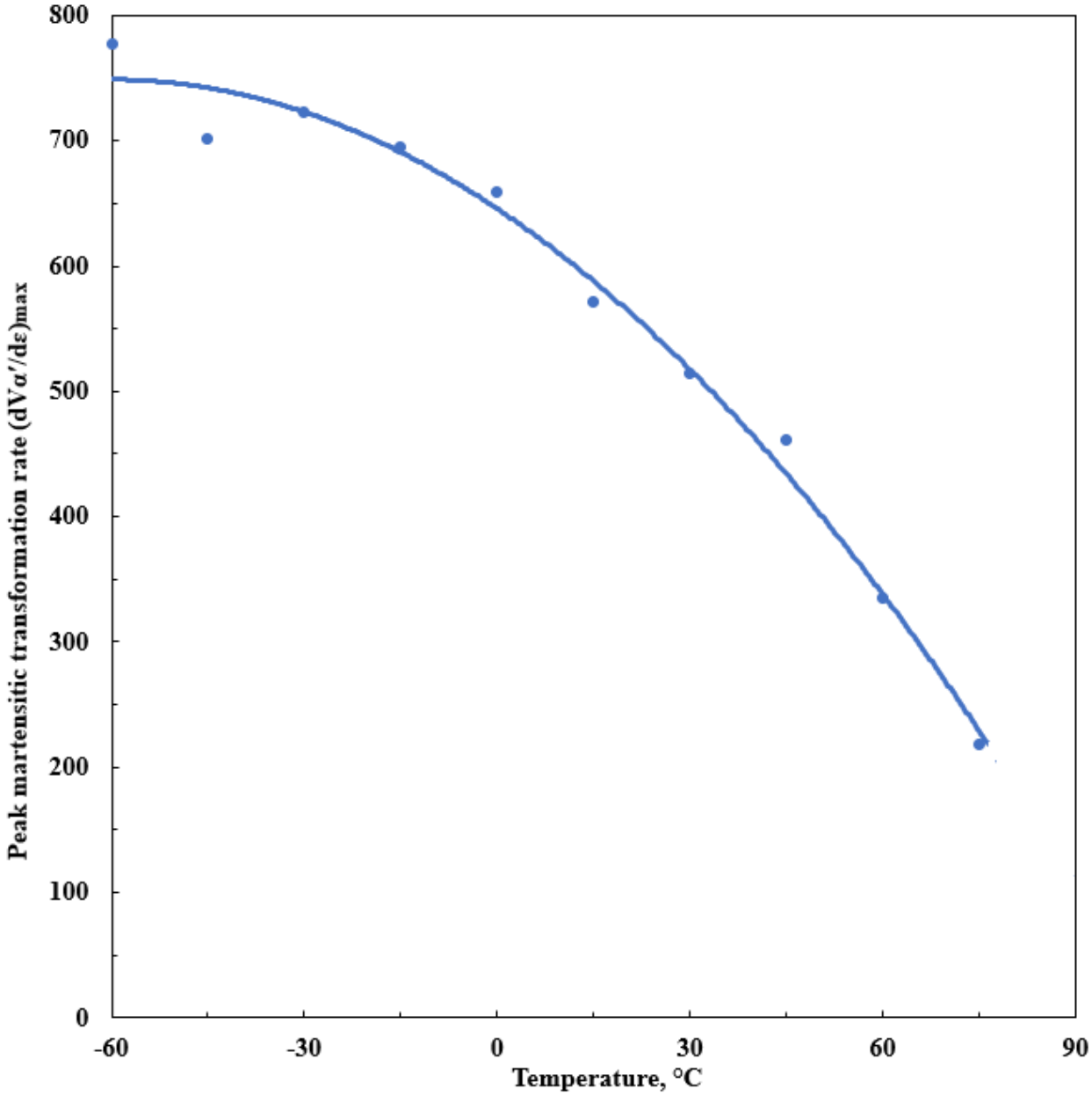


**Figure 4.6: Peak instantaneous martensitic transformation rate as a function of deformation temperature for alloy A**

$M_{dx/y}$ temperatures where x is strain and y is the percentage of martensite induced were determined and plotted as shown in Figure 4.7. The graph was developed by plotting the percentage of martensite induced, (y) at a given strain, (x) within the tested deformation temperatures. Strains of 0.05, 0.08, 0.1, 0.14, 0.18, 0.3 and 0.4 were randomly chosen with corresponding percentage of martensite taken from Figure 4.2 and plotted as a function of deformation temperature as shown in Figure 4.7. The $M_d$ (30/50) as extrapolated in Figure 4.7 was found to be 61 °C. The absolute $M_d$ temperature has been extrapolated as 117 °C as shown in the Figure 4.7. In addition to $M_d$ (30/50) and absolute $M_d$, constitutive equations for $M_{dx/y}$ temperatures where x is strain and y is percentage of strain-induced martensite could be derived.

The percentage of martensite induced at the same true strain, ε increased with decreasing deformation temperature. The mathematical relationship shown in Figure 4.7 can be all described by sigmoidal function as a function of temperature at a given applied strain:

$$\mathbf{V_{\alpha'}/(\varepsilon, T) = (V_{\alpha's/\varepsilon})[1 + \exp(T - T_m)(k_m)^{-1}]]^{-1}} \quad \textbf{…….. Equation 4.5}$$

With $R^2 \geq 0.991$, at all applied strains represented Figure 4.7.

Where:

$V_{\alpha'}/(\varepsilon, T)$ is the percentage of martensite induced at a given temperature and strain. The function fits the data points at various deformation temperature in the range -60 and 105 °C, at a given same applied strain. The variation of $V_{\alpha'}$/(at a given ε) as a function of deformation temperature was found to be sigmoidal as represented by equation (4.5).

$V_{\alpha's/\varepsilon}$ is the maximum percentage of martensite that can be formed at a given strain at the lowest deformation temperature tested (-60 °C).

T is temperature in °C.

$T_m$ is temperature which corresponds to 50% of $V_{\alpha's/\varepsilon}$ is induced.

$k_m$ is a constant derived from the nature of the percentage of martensite as a function of deformation temperature.

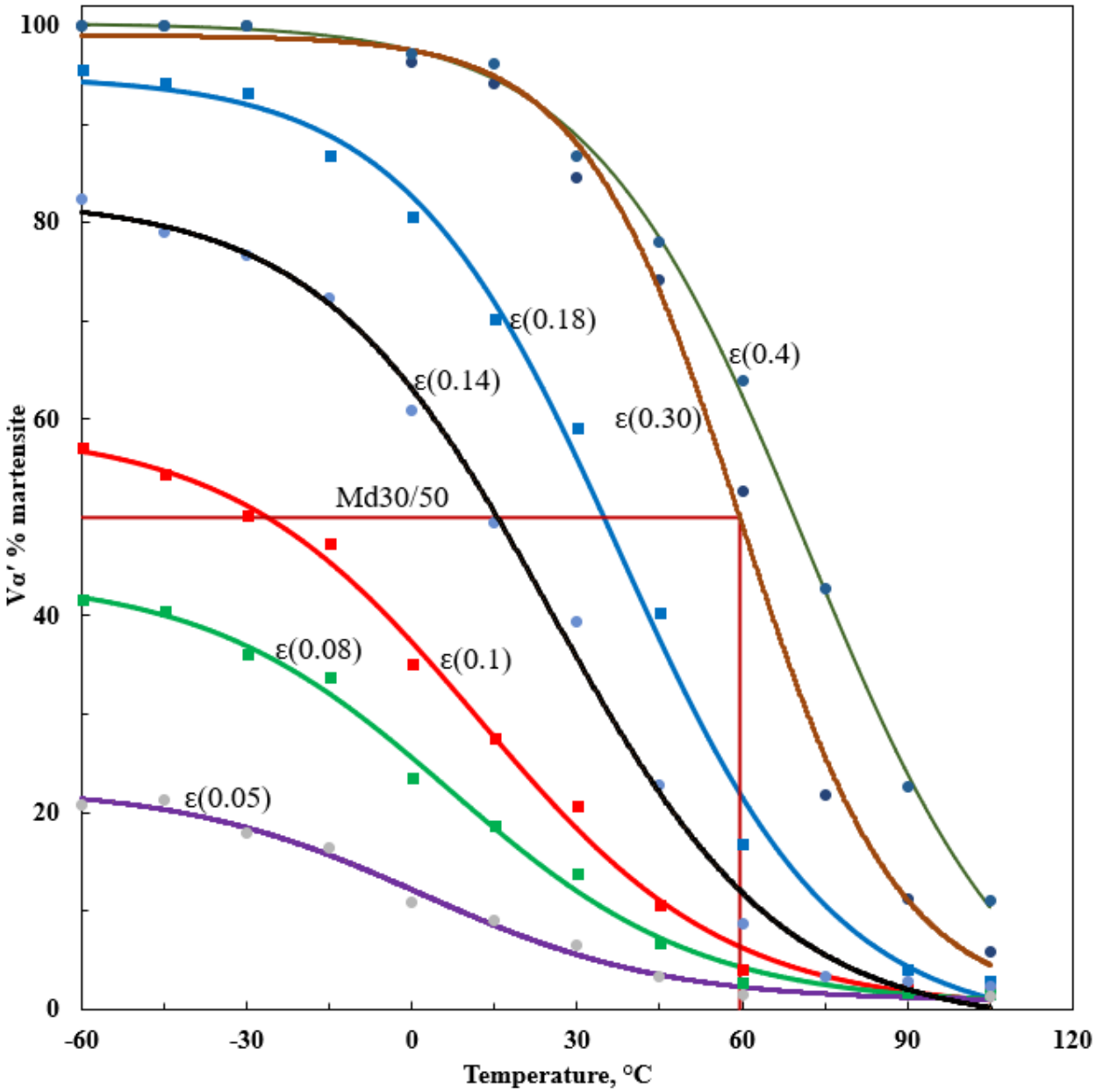


**Figure 4.7: Variation of percentage of martensite with tensile test temperature at various true strains for alloy A at an initial strain rate of 6.67 x $10^{-4}$ $s^{-1}$**

### 4.1.2 Effect of temperature on tensile behavior

The effects of deformation temperature on the engineering and true stress-true strain curves are shown in Figure 4.8 and Figure 4.9, respectively. In both cases, a transition of stress – strain behavior from smooth (parabolic) behavior at high deformation temperatures to sigmoidal behavior at low deformation temperatures was observed with corresponding changes in yield strength, tensile strength and elongation to fracture. The deformation behavior is largely

governed by the combined effect of strain hardening of the austenitic phase (due to dislocations and twinning) and formation of strain-induced martensite (SIM).

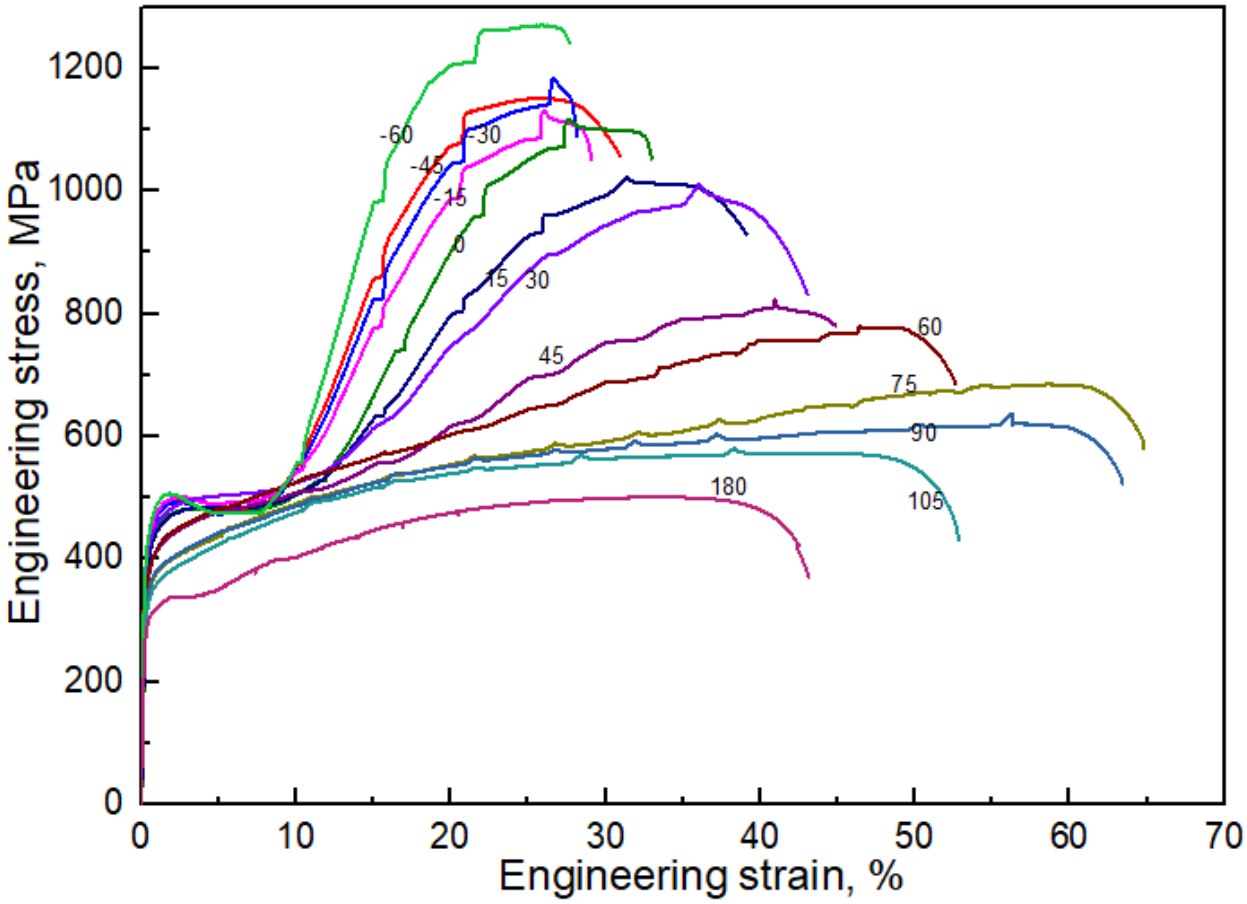


**Figure 4.8: Engineering stress-strain curves for alloy A at an initial strain rate of 6.67 x $10^{-4}$ $s^{-1}$ in the temperature range between -60 and 180 ºC**

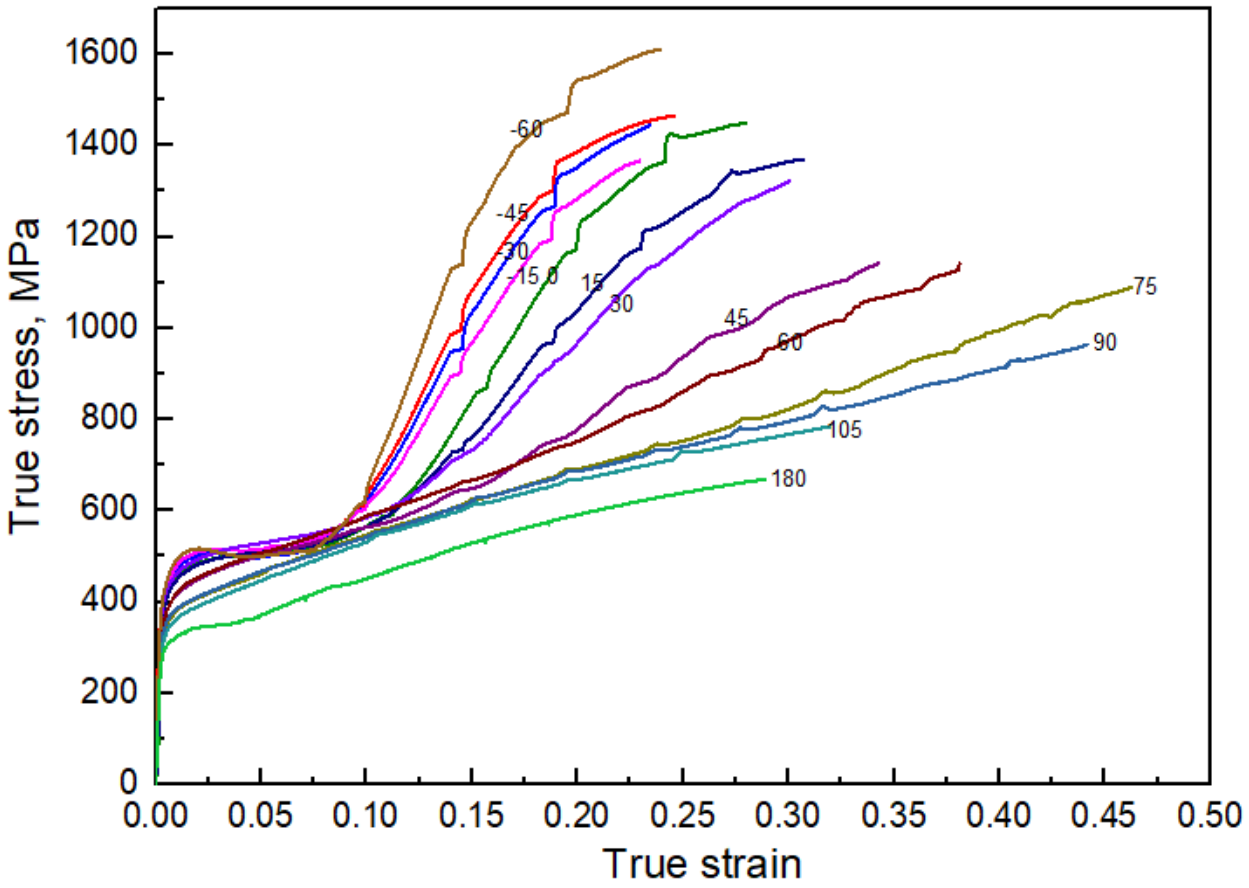


**Figure 4.9: True stress-true strain curves for alloy A at an initial strain rate of 6.67 x $10^{-4}$ $s^{-1}$ in the temperature range between -60 and 180 ºC (within uniform elongation region only)**

A very low strain rate of 6.67 x $10^{-4}$ $s^{-1}$ was chosen to minimize the adiabatic heating during deformation. In addition to a low strain rate during tensile deformation, interruption was done at 5% engineering strain and load removed. Enough time was given to a material to achieve the test temperature before the tensile deformation is resumed. Figure 4.10 shows engineering stress – strain curves for uninterrupted tensile test at an initial deformation temperature of 30 ºC and interrupted tensile test at 5% engineering strain at 30 ºC and 45 ºC. A temperature increase of 8 ºC was observed during uninterrupted tensile test. An adiabatic heating during uninterrupted test had lowered the stress -strain curve but still above the stress – strain curve of the test carried out at 45 ºC. Figure 4.11 shows the true stress-true strain curves for uninterrupted tensile test at an initial deformation temperature of 30 ºC and interrupted tensile test at 5% engineering strain intervals at 30 ºC and 45 ºC. The stress – strain curve which corresponds to the uninterrupted test carried out at an initial deformation temperature of 30 ºC lies in the middle of stress – strain

curves corresponding to interrupted tensile test at 5% engineering strain intervals at 30 $^{o}$C and 45 $^{o}$C, as adiabatic heating causes a temperature increase of 8 $^{o}$C.

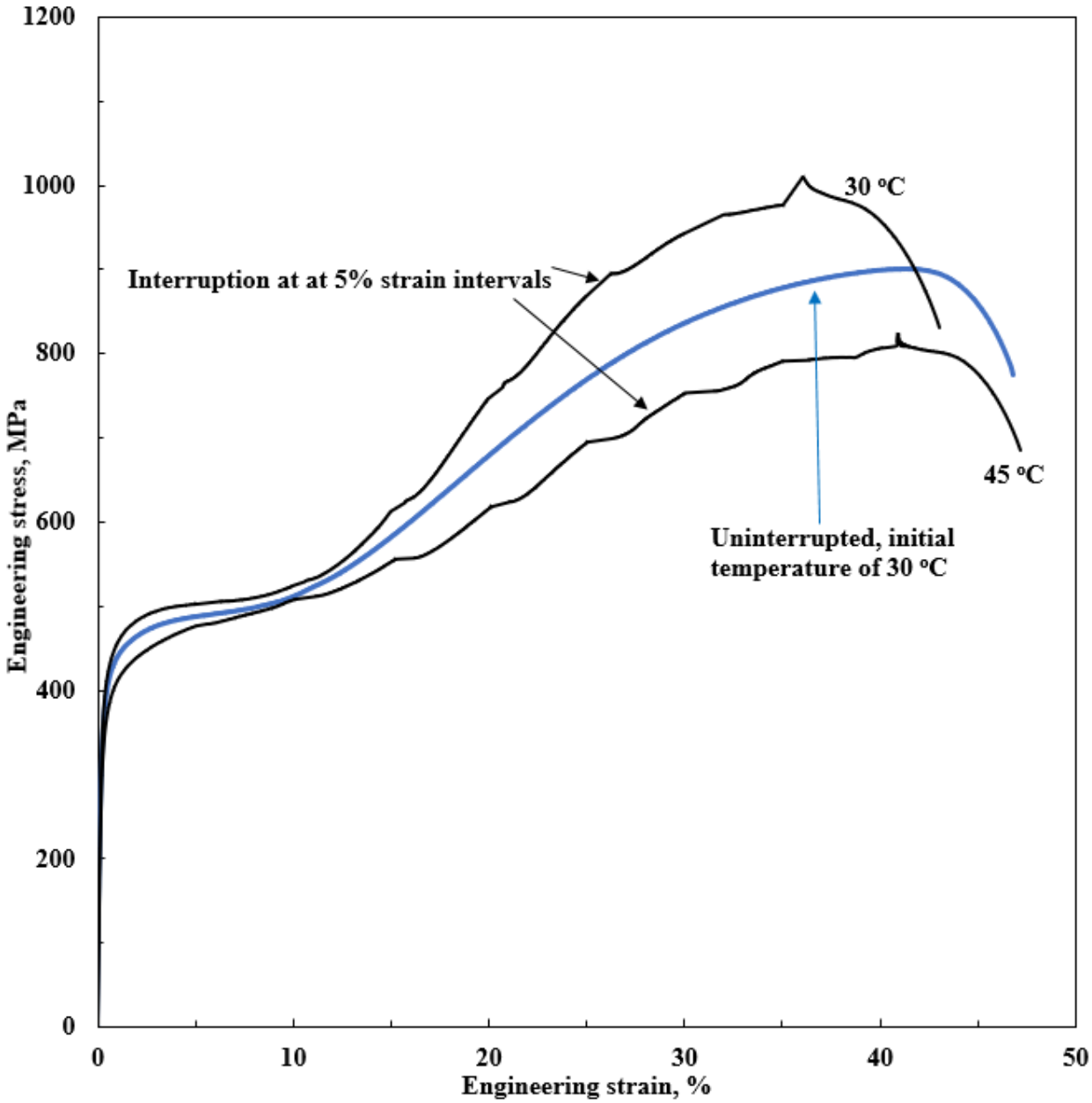


**Figure 4.10: Engineering stress – strain curves for uninterrupted tensile test at an initial deformation temperature of 30 $^{o}$C and interrupted tensile test at 30 $^{o}$C and 45 $^{o}$C for alloy A at an initial strain rate of 6.67 x $10^{-4}$ $s^{-1}$**

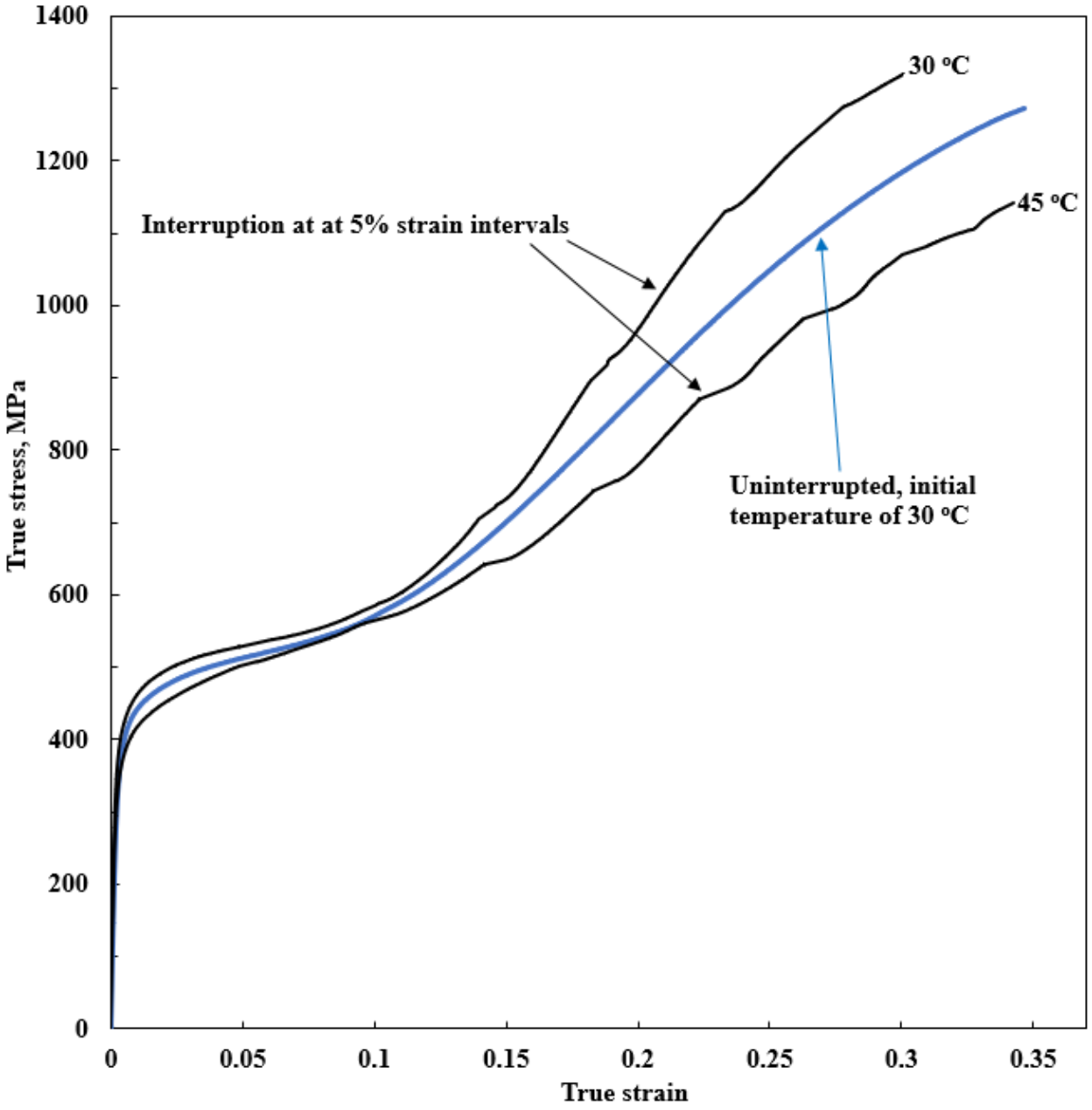


**Figure 4.11: True stress-true strain curves for uninterrupted tensile test at an initial deformation temperature of 30 °C and interrupted tensile test at 30 °C and 45 °C for alloy A at an initial strain rate of 6.67 x $10^{-4}$ $s^{-1}$**

Figure 4.12 shows the variation of yield strength as a function of deformation temperature. The yield strengths were extrapolated at 0.2% strain offset. The yield strength gradually deteriorates as the deformation temperature increases. Figure 4.13 shows the variation of UTS and uniform elongation as a function of deformation temperature. The α′-martensitic transformation and deformation temperature, both have influences on the tensile strength and

uniform elongation. There is a marked change of gradient of the uniform elongation at temperatures below 0 °C which could be attributed to early saturation of martensitic transformation. The uniform elongation curve exhibits a peak value at maximum elongation temperature (M.E.T) which was approximated as 75 °C. The curve shows a strong uniform elongation dependence on the deformation temperature. The α′-martensitic transformation governs the uniform elongation through its influence on the work-hardening rate. Elongation is not only dependent on the total amount of α′-martensite content formed but on the rate of α′-martensitic transformation and point at which the onset of α′-martensite transformation starts. The early and high rate of α′-martensitic transformation at low temperatures decreases the uniform elongation. The delayed onset of strain-induced martensitic transformation to higher strain levels with increasing deformation temperatures shifts the intersection of the work hardening rate curve with true stress-strain curve to higher strains showing delayed necking. Maximum uniform elongation is achieved when maximum rate of α′-martensite transformation and the associated peak of work hardening rate occurs at high strain levels. At 75 °C (Figure 4.2), there is a good balance between delayed strain for onset of strain-induced martensitic transformation and rate of transformation which resulted in peak elongation. The uniform elongation is strongly dependent on the deformation temperature and in accordance with Talonen [96], the lowest uniform elongation was obtained at lowest deformation temperatures tested. This was attributed to rapidly increasing and decreasing work hardening rate at lower deformation temperatures. At deformation temperatures higher than 75 °C, the total amount of α′-martensite decreases gradually as well as the rate of strain-induced martensitic transformation.

There was no martensitic transformation upon deformation at 180 °C. A slight increase in strength from 180 to 120 °C as shown by the fitted line of best fit suggests that the increase was due to twinning and thermal contribution (due to temperature drop) as there was no martensitic transformation within the temperature range. There is a slight increase tensile strength as the deformation temperature drops. The variation of tensile strength and yield strength as a function of deformation temperature were found to be both sigmoidal as shown in Figure 4.12 and Figure 4.13 in the deformation temperature range of -60 to 180 °C, respectively. The corresponding mathematical relationships can be represented by equation (4.6) and (4.7) as below:

**Yield strength = 293 + (132)/(1 + exp((T-59.1)/30.1)) ……..……..…… Equation 4.6**

**Tensile strength = 477 – (787)/(1 + exp((T-37.5)/36.3)) ……..……..…… Equation 4.7**

With $R^2 = 0.9853$ for variation of tensile strength and $R^2 = 0.9838$ for variation of yield strength.

Where:

T is deformation temperature in °C.

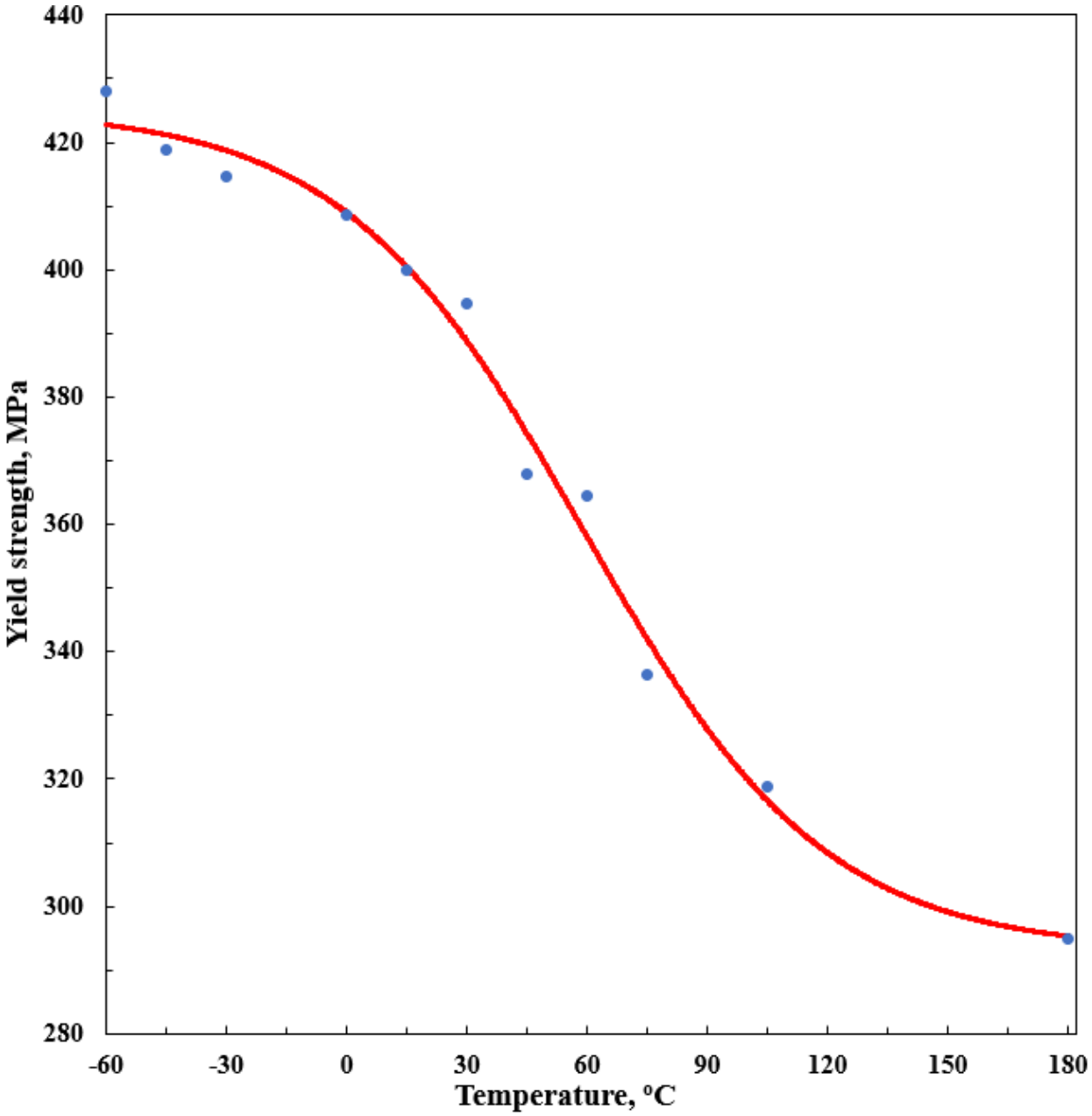


**Figure 4.12 Yield strength as a function of deformation temperature for alloy A tested at an initial strain rate of 6.67 x $10^{-4}$ $s^{-1}$**

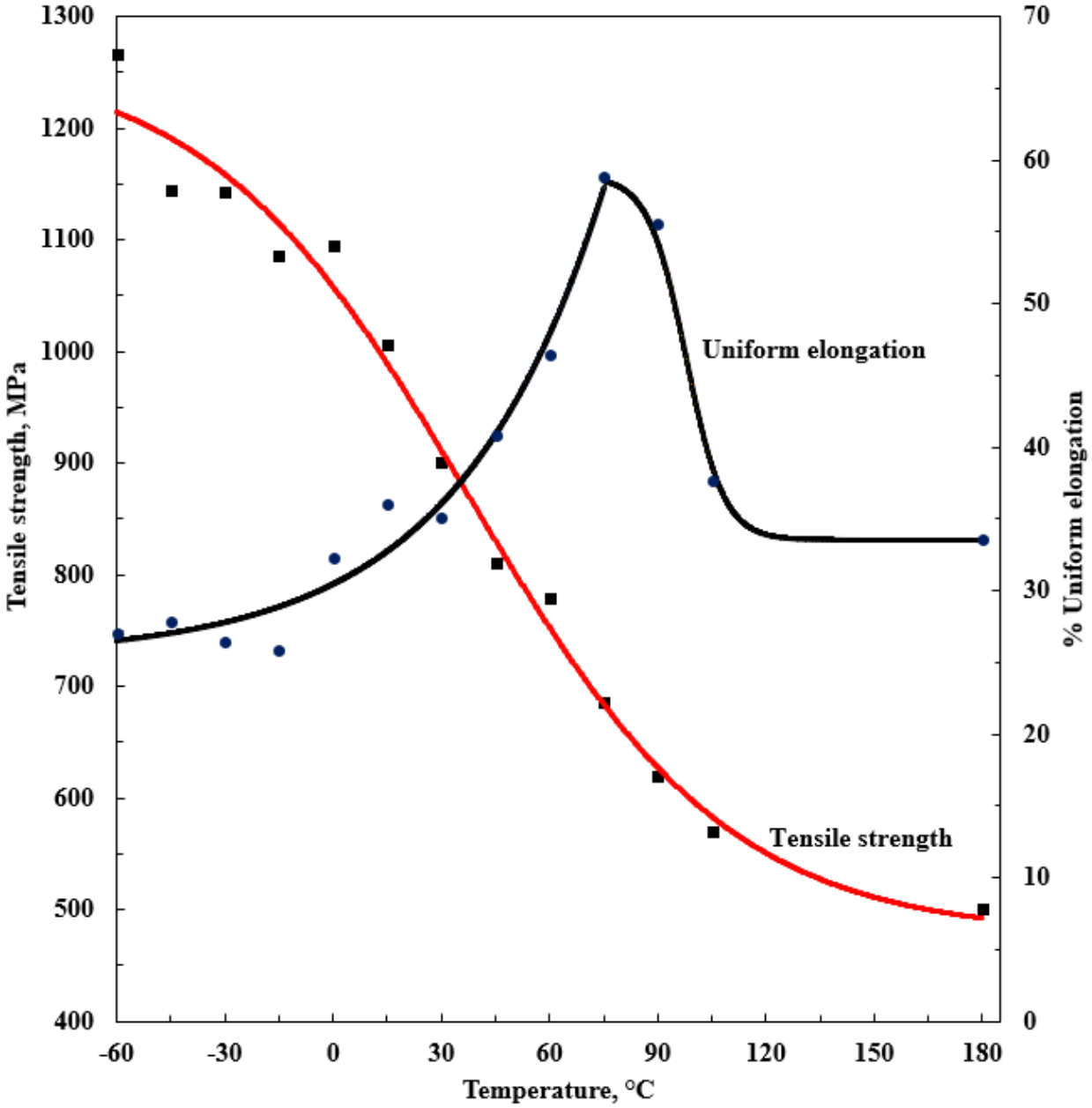


**Figure 4.13 Tensile strength and uniform elongation as a function of deformation temperature for alloy A tested at an initial strain rate of 6.67 x $10^{-4}$ $s^{-1}$**

There is a need to find a balance on the tensile strength and uniform elongation. Figure 4.14 shows the product of tensile strength and uniform elongation as a function of deformation temperature. A gradual decrease in tensile strength in the deformation temperature range between 30 °C and 75 °C is compensated by an increase in uniform elongation to the peak as shown in Figure 4.13. The peak was exhibited at 75 °C displaying the highest uniform elongation at this temperature. For deformation temperatures above 75 °C, both uniform elongation and

tensile strength decreases resulting in decrease in the product of tensile strength and uniform elongation. Therefore, deformation temperature below 75 °C, would be ideal in order to obtain a good balance of tensile strength and uniform elongation with deformation at 75 °C offering remarkable combinations of these properties.

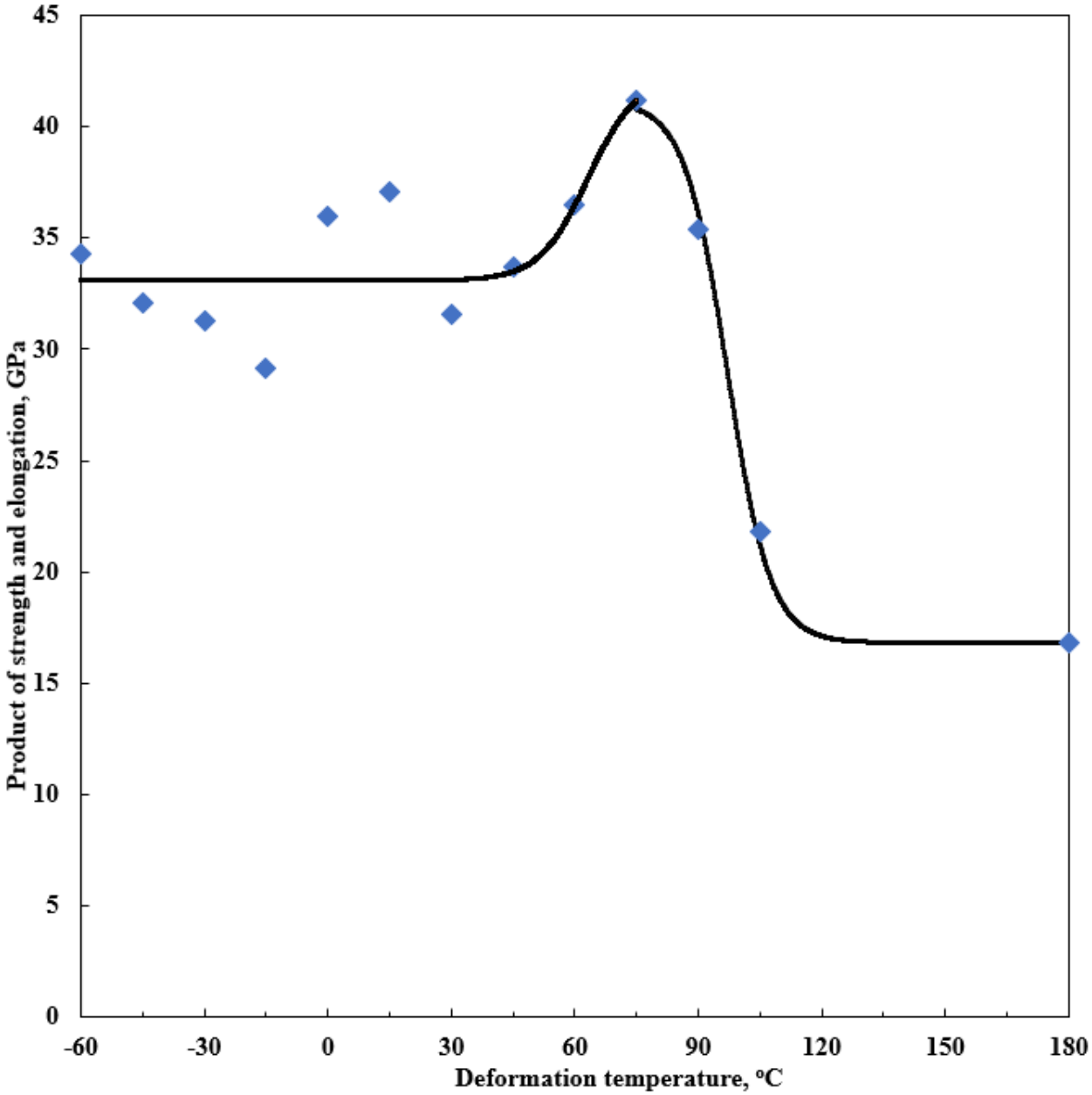


**Figure 4.14: Product of strength and elongation as a function of deformation temperature for alloy A tested at an initial strain rate of 6.67 x $10^{-4}$ $s^{-1}$**

Figure 4.15 shows the log-log plots of the true stress-true strain experimental data at 30 °C with an attempt to fit several existing flow stress equations. The figure demonstrates that

the existing flow equations do not adequately describe the flow behaviour of this steel. The Ludwigson equation adequately describes the behaviour at moderate strain levels but overestimates the stress values at high strains. The Hollomon and Ludwik equations result in deviations observed at both low and high strains. A deviation at high strains tends to overestimate the strength coefficient, K of the material. The calculated strength coefficient using the experimental data and the Hollomon and Ludwigson curves are found to be 4150 MPa and 3370 MPa respectively, which are clearly much higher than the published super full hard tensile strength of 1860 MPa for AISI 301 at room temperature, for this alloy [159]. The published strength coefficients for a higher carbon AISI 301 steel range from 2130 ~ 2872 MPa [61]. Figure 4.15 therefore illustrates the need for the development of new quantitative relationships for metastable austenitic steels.

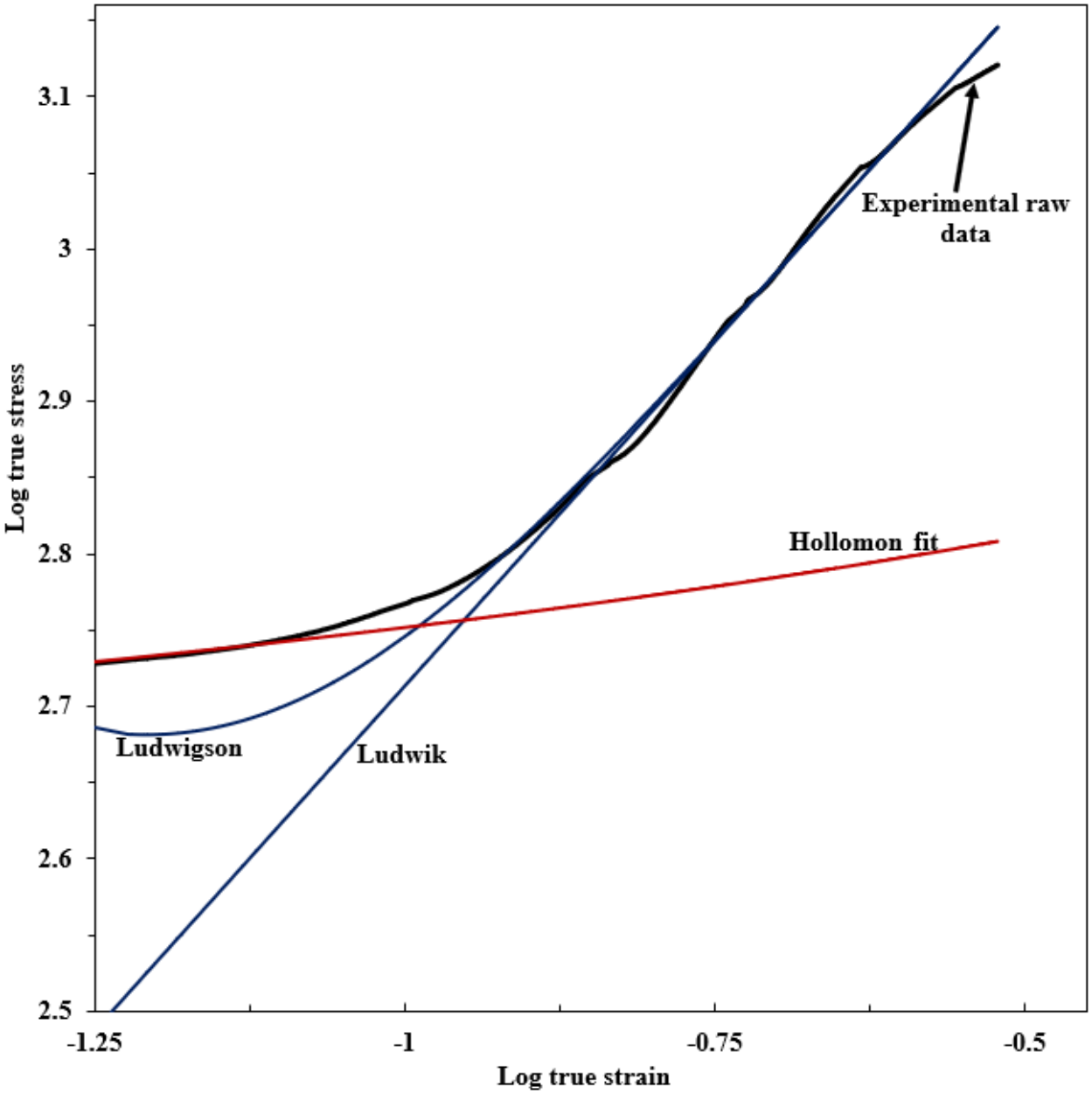


**Figure 4.15: Log-log plots of the true stress-strain curve at 30 °C with an attempt to fit several existing flow stress models for alloy A tested at an initial strain rate of 6.67 x $10^{-4}$ $s^{-1}$**

Figure 4.16 represents the plastic flow log-log plots of true stress and true strain obtained from the Figure 4.9 data. This Figure 4.16 demonstrates that, for temperatures of 75 °C and lower, there is a deviation of flow stress relationship from a classical Hollomon-type because of a second hardening phenomenon which is caused by the strain-induced martensitic transformation (SIMT). The deviation from the Hollomon power law is distinct in the range between ≈ 5 % (log ε = -1.3) to 8 % (log ε = -1.1) true strain for most temperatures below and

equal to 75 °C. This observation is in accordance with the results reported by other authors. Xing Li et al. [91], for TRIP steels, observed a so-called "critical strain", above which rapid work hardening was observed. This was explained by formation of significant amount of strain-induced martensite at ≈ 5 % (log ε = -1.3) to cause a second phase hardening behaviour. The beneficial effects of SIMT in austenitic steels includes enhanced strain hardening rate which results in delayed local necking and thereby improving ductility and formability [160]. The "critical strain" for the formation of significant amount of strain-induced martensite and/or combined with the amount of twinning slightly increases up to 8% (log ε = -1.1) as deformation temperature increases. The creation of twin boundaries act as very effective obstacles to dislocation glide by a dynamic Hall-Petch effect whereby twinning subdivide the grains causing the deviation of strain hardening from a classical Hollomon power law even at 180 °C [75], [66]. The deviation of the strain hardening behaviour from the Hollomon power law increases as deformation temperature decreases. The Hollomon strain hardening exponent, n for strain below the critical strain was found to be approximately 0.12, irrespective of deformation temperature. At temperatures above 75 °C, the strain hardening can be described by bi-linear Hollomon-type equations. At these elevated temperatures, the value of the strain hardening exponent increases for strain values above 8 % (log ε = -1.1). A non-constant strain hardening exponent makes the curve fitting with classical Hollomon power law and Ludwig model invalid.

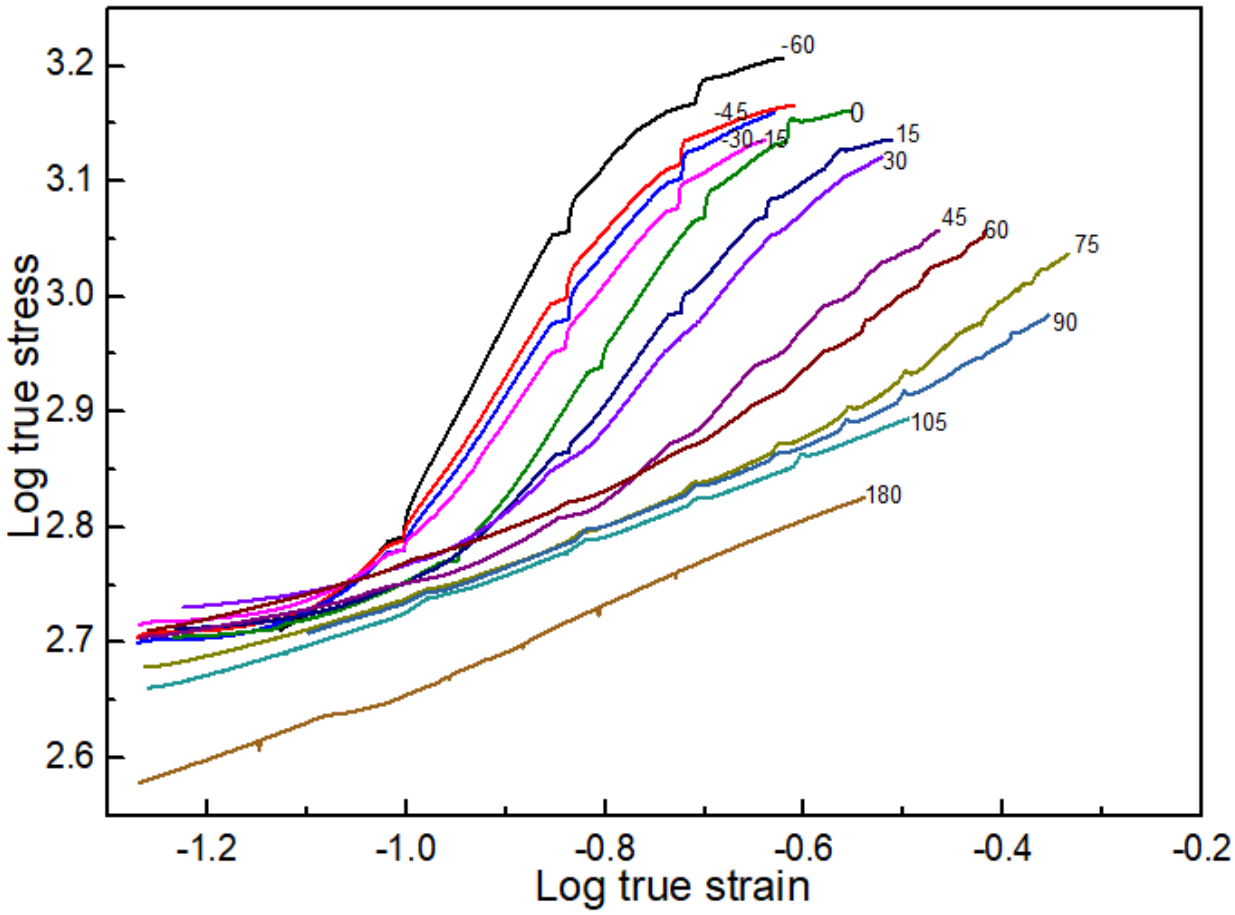


**Figure 4.16: The plastic flow log-log plot of true stress and true strain at all temperatures between -60 and 180 °C for true strain values greater than 5% for alloy A tested at an initial strain rate of 6.67 x $10^{-4}$ $s^{-1}$ (critical strain for pronounced work hardening)**

Figure 4.17 shows the result of sigmoidal fits to the experimental tensile data on a log-log plot of true stress-strain at all temperatures, for true strain values greater than 5%. Early work done on the strain hardening behaviour of AISI Type 301 steels, using cold rolled sheet with true strain values up to 0.95 at room temperature showed flow curves with sigmoidal shapes [61]. Furthermore, research done on the present alloy [158] showed that plots of the percentage of martensite as a function of true strain showed full sigmoidal behaviour for temperatures of 75 °C and lower (see Figure 4.17). A martensite saturation volume fraction of 0.85 was reached at true strain of 0.3, at 30 °C. It is therefore reasonable to fit sigmoidal curves through the experimental data and to extend the curves up to the true strain levels of 1.0, to arrive at estimates of the strength coefficient, K as shown in Figure 4.17 for temperatures up to and including 75 °C (see Figure 4.20 for the K-values as a function of temperature). The accuracy of such estimations

needs to be verified by compression or cold rolling testing at high strains and was done in the latter part of this thesis. The K-values were found to vary strongly with deformation temperature.

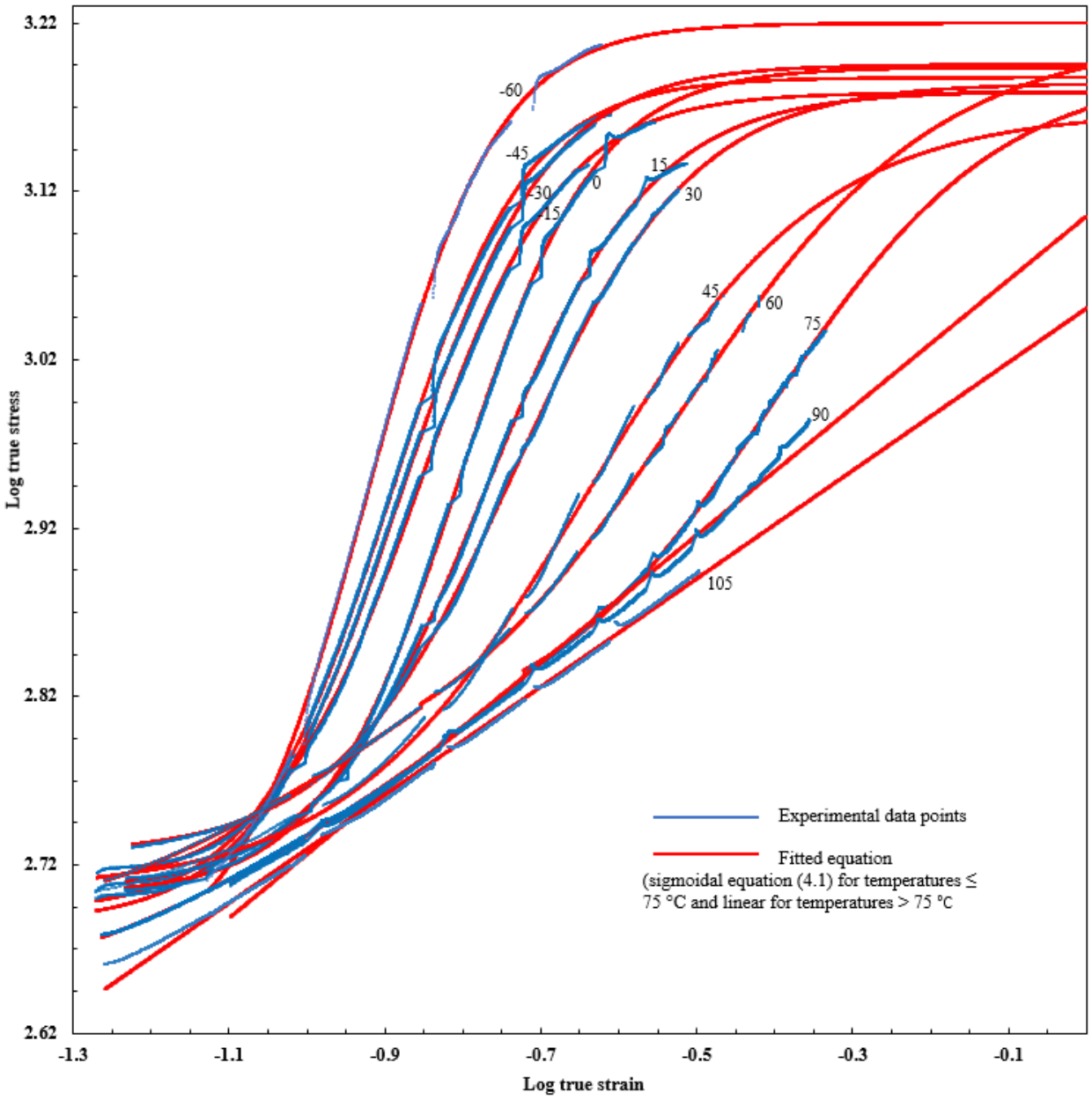


**Figure 4.17: The log-log plot of true stress-strain at all temperatures (given in °C), for true strain values greater than 5% (critical strain for pronounced work hardening) for alloy A tested at an initial strain rate of 6.67 x $10^{-4}$ $s^{-1}$, showing sigmoidal flow stress behavior.**

The blue line in Figure 4.17 represents the raw data from tensile testing whilst the red line represents the constitutive equation which was fitted. The curves were extrapolated to log true strain of zero to estimate the strength coefficient, K of the material at the given temperature.

The experimental strain hardening curves, from -60 °C to 75 °C, for a true strain ≥ 0.05, could be accurately described by the following single sigmoidal equation:

$$\log \sigma = A + (B - A)[1 + \exp(\log \varepsilon - \alpha_s)(\beta_s)^{-1}]]^{-1} \quad \text{Equation 4.8}$$

with $R^2 \geq 0.999$, for all deformation temperatures.

Where:

$\sigma$ is the true stress in MPa,

A is the maximum log of true stress ($\log \sigma_{max}$) when the sigmoidal function levels off after the martensitic transformation reaches saturation point.

B is the minimum log of true stress ($\log \sigma_{min}$) at the beginning of the sigmoidal curve, before any significant martensitic transformation.

$\varepsilon$ is the true strain.

$\alpha_s$ is the maximum strain sensitivity which corresponds to the log true strain value where there is a maximum slope of the log-log plot of the true stress-true strain curve.

$\beta_s$ is a constant derived from the nature of the log-log plots of the true stress-strain curves. The numerical value is given by, $\beta = (A - B)(4 \times n_{ipeak})^{-1}$, where $n_{ipeak}$ is the peak instantaneous strain hardening exponent, which is the instantaneous derivative of the sigmoidal function as given in equation (4.8) (see also Figure 4.21).

Table 4.3 summarizes the $\alpha_s$, $\beta_s$, A and B constants of equation (4.8) at temperatures up to 75 °C for the sigmoidal fit in Figure 4.17. For the higher temperatures of 90 °C and above, the sigmoidal function was found not to fit the experimental behaviour well. Rather, it was found that a bi-linear (Hollomon) function resulted in good correlations, with a relatively low strain hardening exponent found up to a true strain value of 8 %, and high values at strains larger than 8 %. Table 4.4 summarizes the Hollomon strain hardening exponents and strength coefficients after deformation at temperatures of 90 °C and above.

**Table 4.3: Constants α, β, $\alpha_s$ and $\beta_s$ in equation (4.8) as a function of temperature in the AISI 301LN steel**

| Temperature, (°C) | $\alpha_s$ | $\beta_s$ | A | B | $R^2$ |
|---|---|---|---|---|---|
| -60 °C | -0.922 | 0.0829 | 3.22 | 2.66 | 1.00 |
| -45 °C | -0.892 | 0.0867 | 3.19 | 2.69 | 1.00 |
| -30 °C | -0.879 | 0.0939 | 3.20 | 2.68 | 1.00 |
| -15 °C | -0.858 | 0.0919 | 3.18 | 2.71 | 1.00 |
| 0 °C | -0.805 | 0.0881 | 3.19 | 2.70 | 1.00 |
| 15 °C | -0.771 | 0.106 | 3.18 | 2.70 | 1.00 |
| 30 °C | -0.732 | 0.114 | 3.18 | 2.73 | 1.00 |
| 45 °C | -0.646 | 0.152 | 3.17 | 2.70 | 0.999 |
| *60 °C | -0.523 | 0.166 | 3.21 | 2.76 | 0.999 |
| *75 °C | -0.403 | 0.147 | 3.20 | 2.79 | 0.999 |

*For 60 °C and 75 °C, the critical strains for the start of the sigmoidal behaviour were 0.14 and 0.28 respectively due to increased stability of austenite at the high temperature (refer to Figure 4.16 and Figure 4.17).

**Table 4.4: The work hardening exponent (n) and the strength coefficient (K) at deformation temperatures of 90 °C and above for the AISI 301LN steel, determined using a Hollomon fit.**

| Temperature, (°C) | n | | K, MPa | *$R^2$ |
|---|---|---|---|---|
| | 0.2% offset < ε < 8% | ε > 8% | | |
| 90 °C | 0.12 | 0.379 | 1274 | 0.993 |
| 105 °C | 0.12 | 0.321 | 1123 | 0.998 |
| 180 °C | 0.10 | 0.352 | 1070 | 0.998 |

*The correlation coefficient given is for the strain range exceeding 8 %.

Figure 4.18 and Figure 4.19 show the variation of the alpha and beta constants as a function of temperature in the developed sigmoidal function given equation (4.8). The curves in

Figure 4.18 and Figure 4.19 represent equations giving the values of the sigmoidal function constants ($\alpha_s$ and $\beta_s$) as a function of temperature in the range –60 to 75 °C. The equations are:

$$\alpha_s = -0.959 + 0.139*\exp(0.0186*T) \quad \text{Equation 4.9}$$

With $R^2 = 1.00$.

Where:

$\alpha_s$ is a constant in the sigmoidal function in equation [4.8].

T is temperature in °C.

$$\beta_s = 0.177 - (0.0887)*[1 + \exp((T - 36.7)*(11.2)^{-1})]^{-1} \quad \text{Equation 4.10}$$

With $R^2 = 0.962$.

Where:

$\beta_s$ is a constant in the sigmoidal function in equation [4.8].

T is temperature in °C.

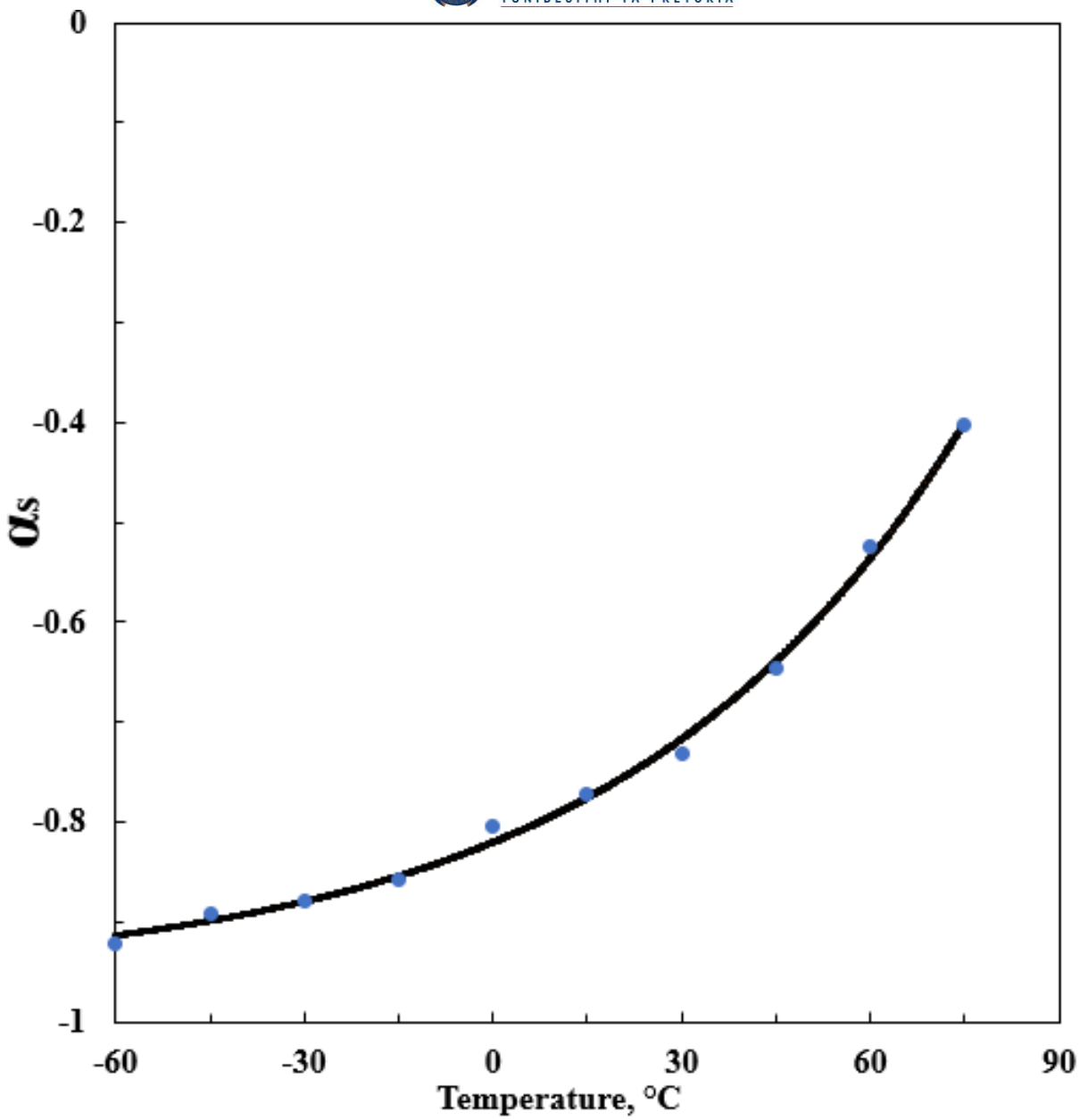


**Figure 4.18: Variation of the $\alpha_s$ constant as a function of deformation temperature for alloy A**

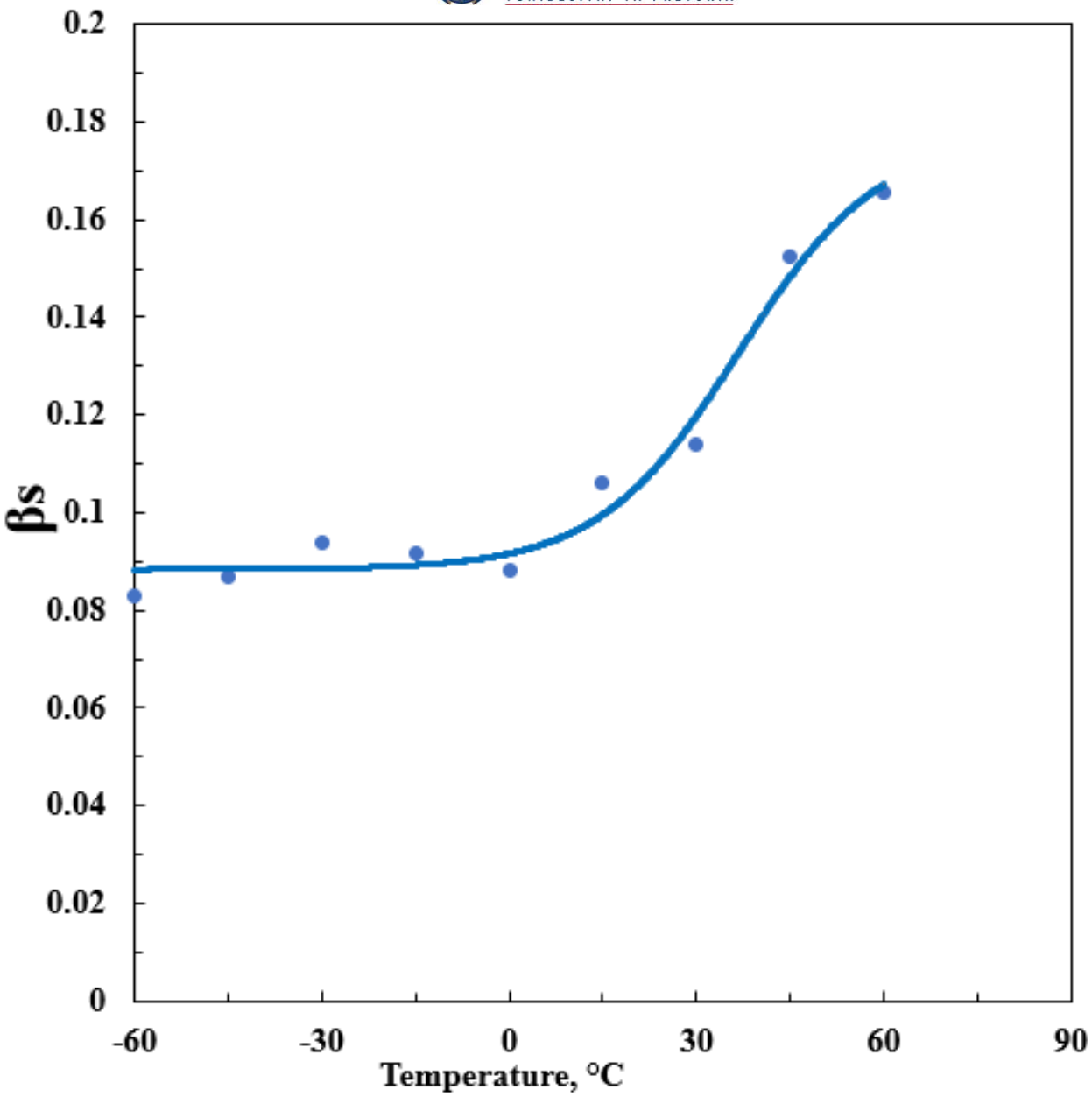


**Figure 4.19: Variation of the $\beta_s$ constant as a function of deformation temperature for alloy A**

Figure 4.20 shows variation of strength coefficient, K as a function of temperature determined from the developed equations (4.1) at a log true strain value of 0 ($\varepsilon$ = 1). The relatively high K-values found are in accordance with the K-values reported earlier for higher-carbon AISI Type 301 steels, tested at room temperature [61]. In that work, for the fully martensitic alloy, a K-value of 2870 MPa is implied in the experimental plot. If the influence of carbon content on martensitic hardness is accounted for, the strength coefficient translates to the value of 1890 MPa for a carbon content of 0.02 percent (at 100 percent martensite). This value

agrees with the magnitude of the K-values obtained in the present study at 100 percent of martensite. The variation of the strength coefficient, K, as a function of temperature in the range -60 to 105 °C in Figure 4.20 can be represented by the following equation:

$$\textbf{Strength coefficient, } K = 1070 + (470)*[1 + \exp((T - 88.0)*(7.43)^{-1})]^{-1} \text{…..... Equation 4.11}$$

with $R^2 = 0.909$.

Where:

T is the temperature in °C.

The strength coefficient was therefore found to be above 1500 MPa for temperatures below 45 °C and then decreases at higher temperatures. The high value of strength at the lower temperatures is attributed to the high saturation levels of percentage of transformed martensite, above 80% at temperatures of 30 °C (see Figure 4.2). The decrease of the strength coefficient at higher temperatures is due to lower saturation values of strain-induced martensite.

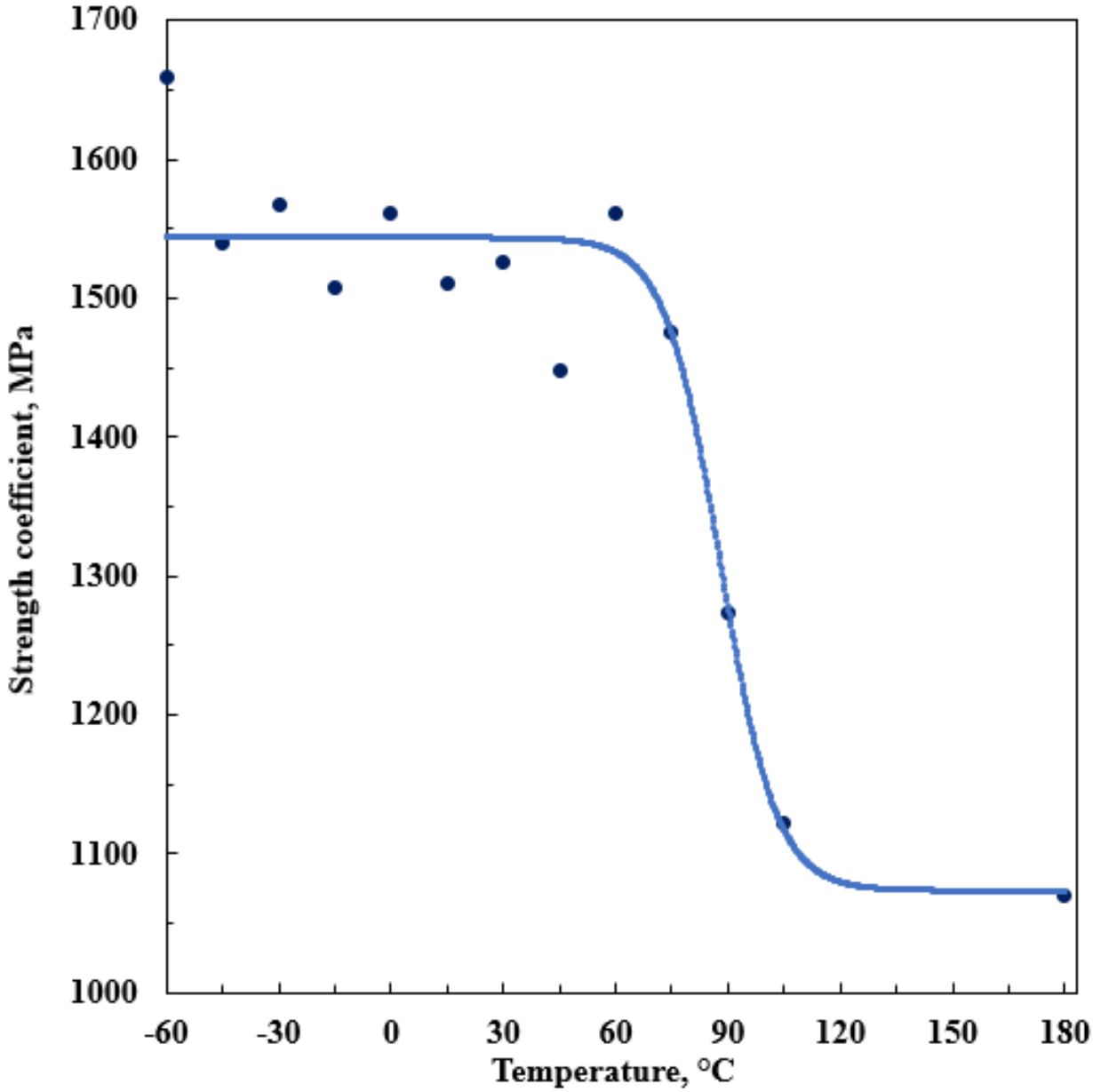


**Figure 4.20: Variation of the strength coefficient, K, as a function of temperature for alloy A.**

Figure 4.21 shows the variation of the instantaneous strain hardening exponent, $n_i$ as a function of true strain (in the sigmoidal behaviour region, typically above 5% strain) and the deformation temperature. The instantaneous strain hardening exponent, $n_i$ [135], [161], [162] is derived by calculating the instantaneous derivative of the log-log plot of equation (4.8), which was used to describe the mathematical relationship of the data shown in Figure 4.17.

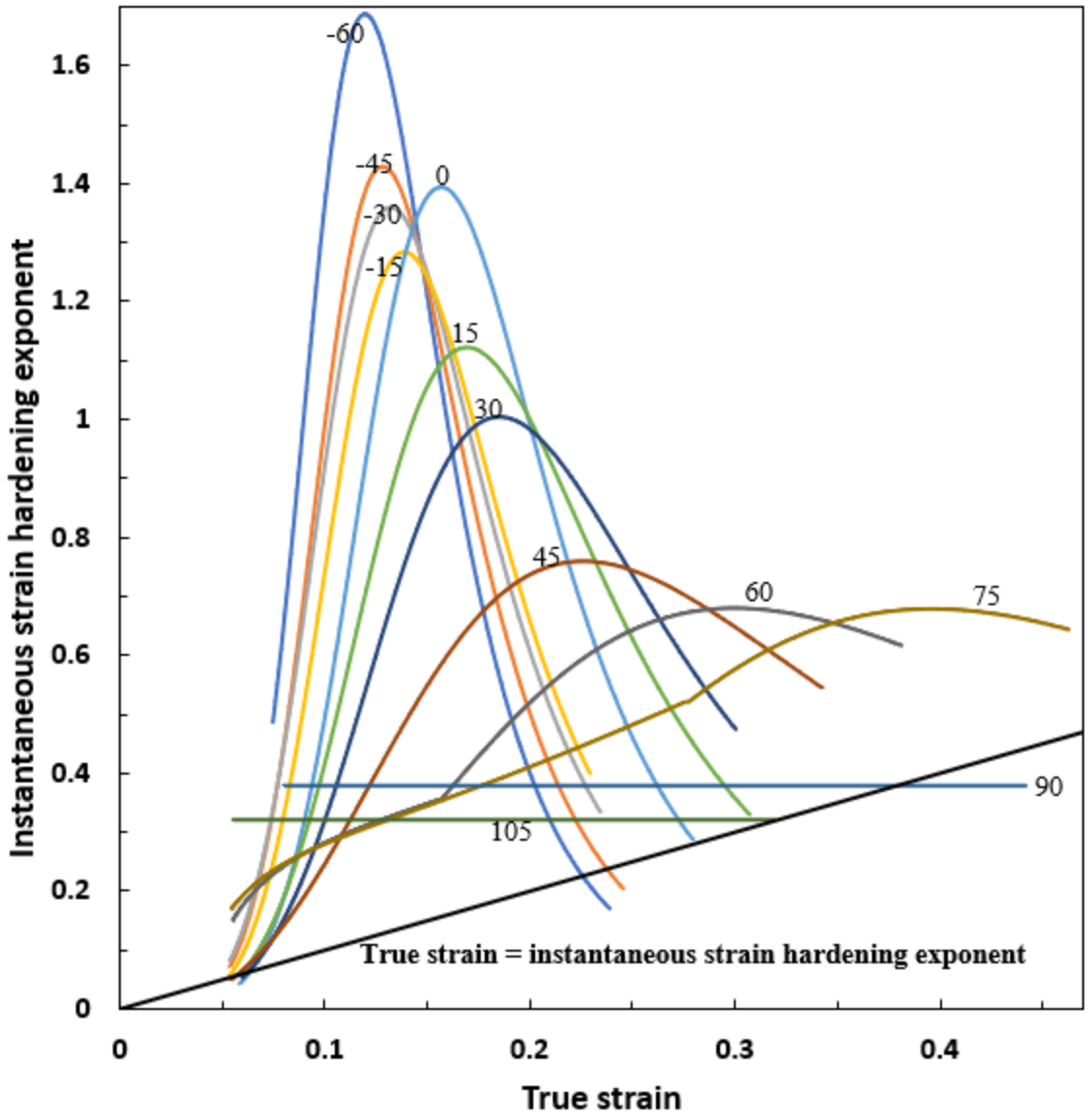


**Figure 4.21: Variation of instantaneous strain hardening exponent, $n_i$ as a function of true strain (above 5%) and deformation temperature (°C) for alloy A tested at an initial strain rate of 6.67 x $10^{-4}$ $s^{-1}$**

At low strains and deformation temperature, for temperatures of 45 °C and below, the instantaneous strain hardening exponent increases rapidly with increasing strain up to a peak value, after which it again decreases rapidly, in a fashion similar to the instantaneous gradient of martensitic transformation as a function of strain ($dV\alpha'/d\varepsilon$) (see Figure 4.3), which increased to a maximum rapidly and thereafter decreases to zero martensitic transformation. The rapid decrease in strain hardening rate after reaching a peak is attributed to suppressed martensitic transformation as the saturation value of martensite content is approached during deformation. It

is evident that not only the rate of martensitic transformation is high at low deformation temperatures, but also the level of strain hardening as well.

The straight line $n_i = \varepsilon$ which corresponds to the Considère criterion was drawn in Figure 4.21 showing that the strain corresponding to the maximum uniform elongation, $\varepsilon_u$, is equal to instantaneous strain hardening exponent, $n_i$, at the point of instability thereby satisfying the Considère's criterion, for temperatures of 15 °C and lower. Considère criterion is fulfilled when necking occurs where $n_i = \varepsilon$ at higher strains after neglecting the elastic strain. At a true strain of ~ 5 %, the curve apparently registers a first instability. However, the hardening continues until the occurrence of the second and final instability which leads to fracture. Munoz et al. had shown that the first instability does not distribute evenly over the gauge length [163]. In this work, fracture of tensile samples before the Considère criterion is fulfilled could be attributed to the interruptions done during tensile deformation at 5% strain increments.

The peak $n_i$ – values were found to generally increase with decreasing deformation temperatures due to the significant strain-induced martensitic transformation (SIMT), observed at these temperatures (see Figure 4.2). Comparing Figure 4.3 and Figure 4.21, the peak value for martensitic transformation was reached at lower strains than the peak values of the instantaneous work hardening rate. The results clearly indicate that the work hardening behaviour of AISI 301LN steel is controlled by the formation of strain induced α′-martensite [128].

Figure 4.22 shows the interaction of the work hardening rate ($d\sigma/d\varepsilon$) as a function of strain at various temperatures up to the maximum uniform strain. The curves were obtained by differentiating the flow stress-strain curves shown in Figure 4.16. The distinct peaks correspond to the strain at which the maximum instantaneous work hardening rate occurs, during plastic deformation.

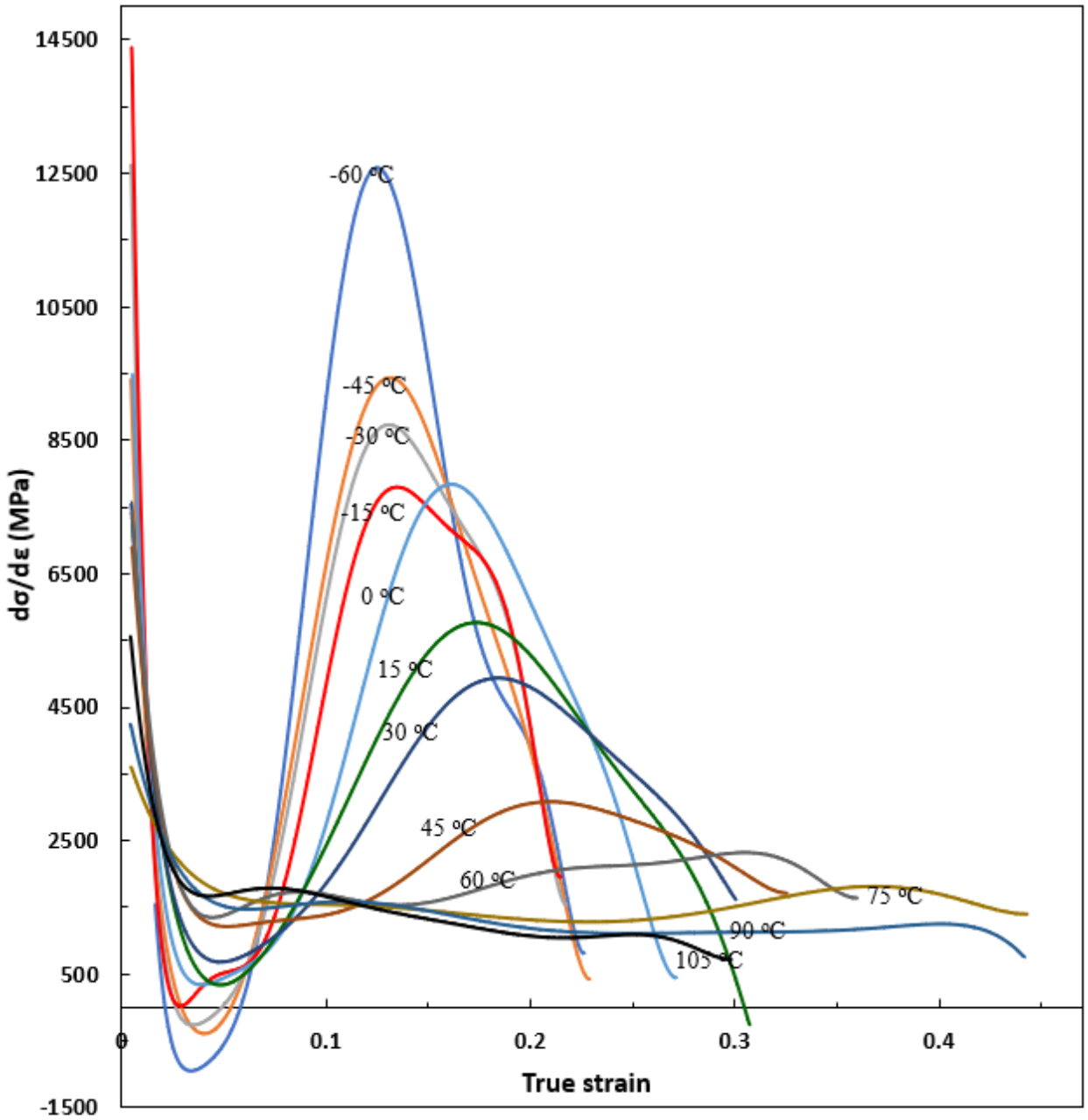


**Figure 4.22: The variation of the work hardening rate as a function of temperature for alloy A tested at an initial strain rate of 6.67 x $10^{-4}$ $s^{-1}$**

The work hardening rate decreases continually as a function of strain at a given deformation temperature. This is attributed to the decrease in α′-martensitic transformation rate. At higher deformation temperatures with decreased α′-martensitic transformation the distinct peaks were shifted to the higher strain values and becomes smaller till they eventually disappear with increasing temperature. Figure 4.23 shows the work hardening curves as a function of true stress obtained under uniaxial tensile tests at different deformation temperatures.

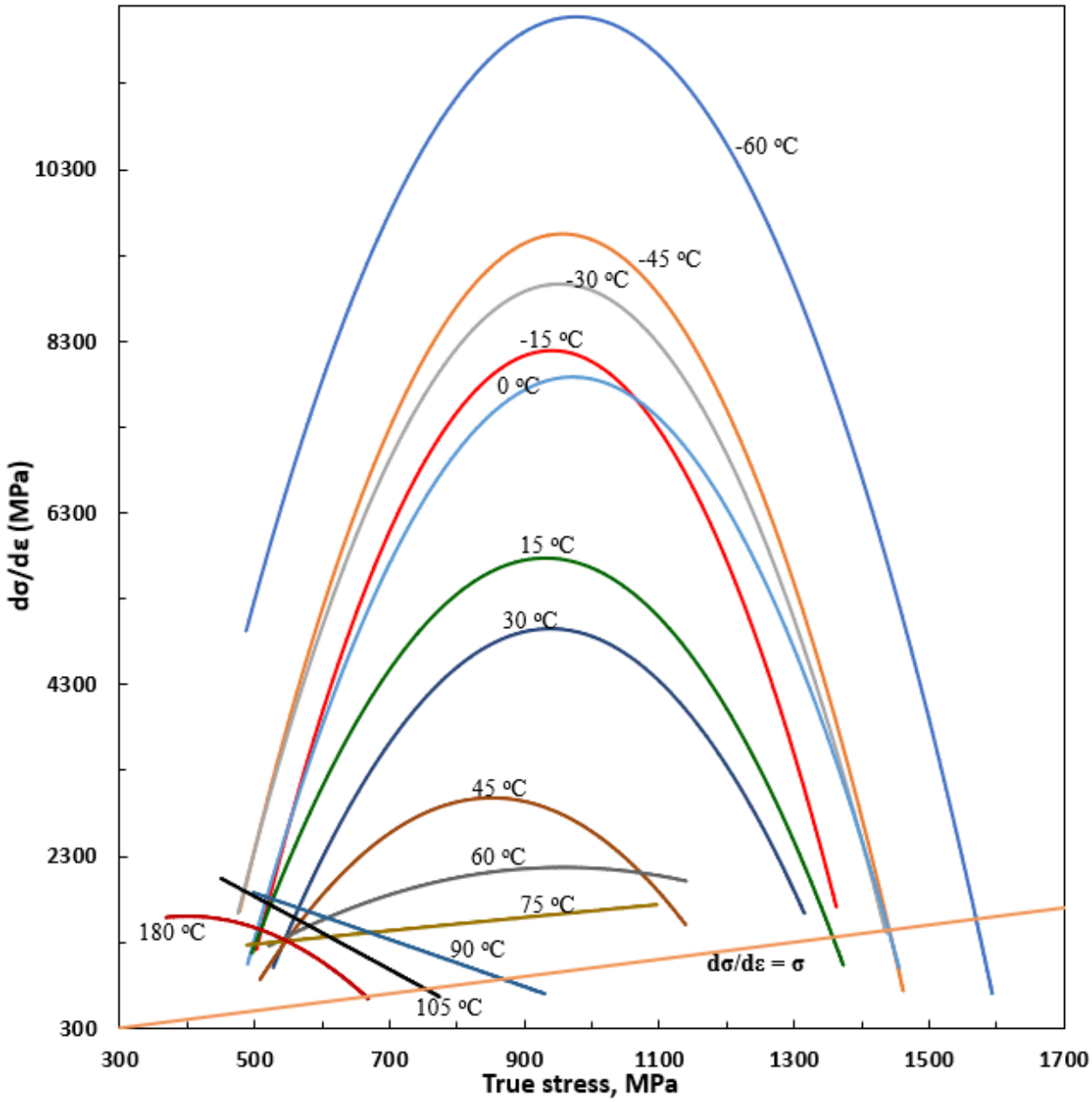


**Figure 4.23: Work hardening rate as a function of true stress at different deformation temperatures**

The straight line $(\partial\sigma/\partial\varepsilon) = \sigma$, which corresponds to the Considère criterion was drawn in Figure 4.23 showing the point of instability. Considère's plastic criterion is fulfilled when necking occurs where $(\partial\sigma/\partial\varepsilon) \leq \sigma$ after neglecting the elastic region. Figure 4.24 shows true stress and work hardening rate as a function of true strain at different deformation temperatures (for clarity, only selected deformation temperatures are shown).

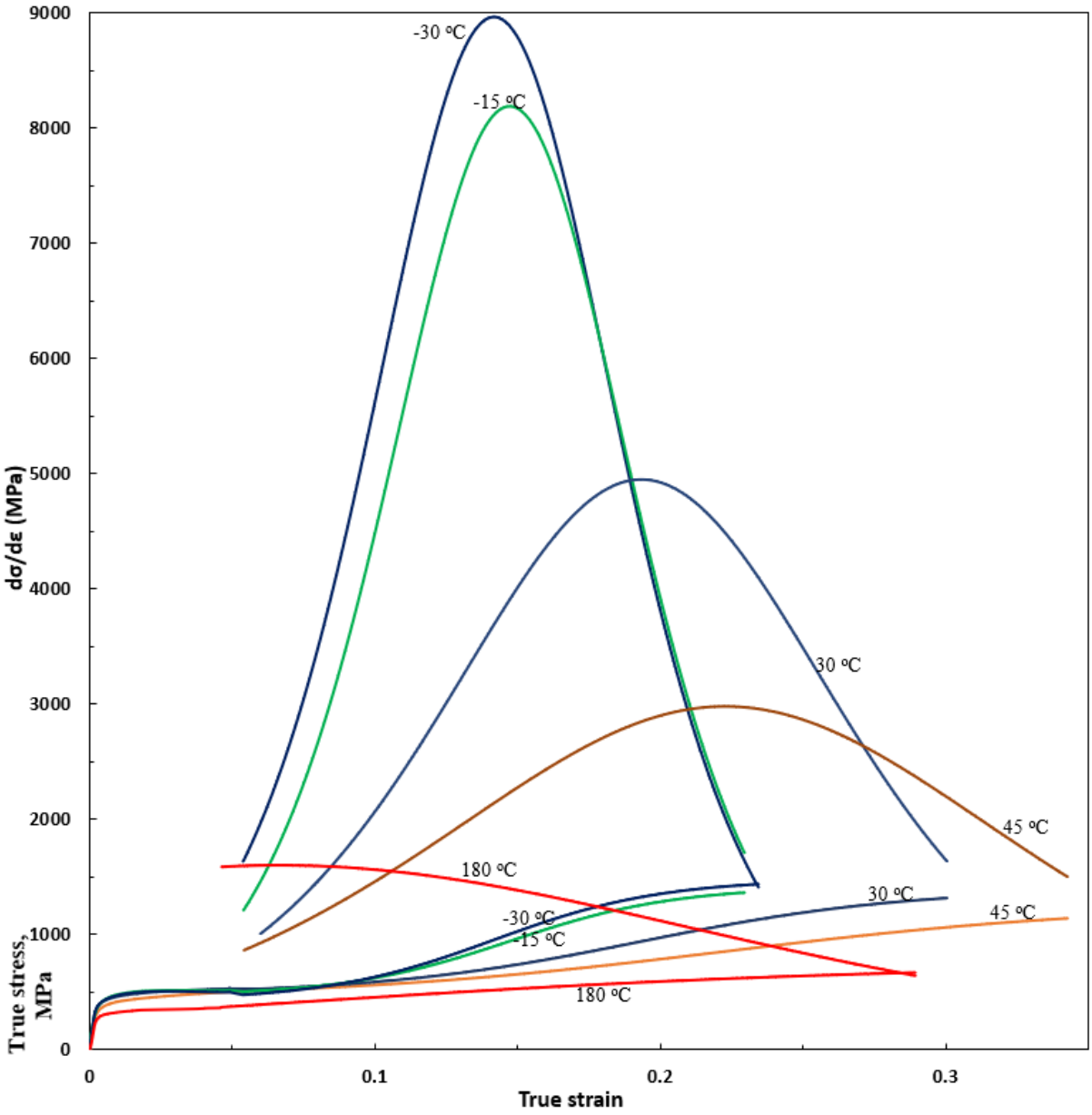


**Figure 4.24: True stress and work hardening rate as a function of true strain at different deformation temperatures (for clarity, only selected deformation temperatures are shown)**

Regardless of the temperature dependence of flow stress of metastable austenitic stainless steel, the Considère's criterion of plastic instability was successfully observed during tensile deformation. The remarkable increase in flow stress due to strain – induced martensite at lower temperatures forces the point of intersection between the two curves, true stress-strain curve and work hardening rate as a function of true strain to occur at lower strain values as temperature decreases as shown in Figure 4.24.

In the temperature range where SIMT is intense, the peak instantaneous strain hardening exponent was found to decrease from a value of 1.69 at a strain of 0.12 at -60 °C to 0.68 at 75 °C (see Figure 4.25). For the lower temperatures, however, the $n_i$-values rapidly increases with increasing strain, up to a peak $n_i$-value. As the strain corresponding to the peak $n_i$-value is exceeded, the $n_i$-values decrease sharply. The observed value is to be expected where sigmoidal behaviour is observed, as dictated by the mathematics inherent to equation (4.8).

As the deformation temperatures were increased, the sigmoidal strain hardening behaviour was less pronounced and at temperatures evaluated above 90 °C, the function describing the strain hardening behaviour of metastable austenitic AISI 301LN steel, changes to a linear (Hollomon-type) function in a log-log plot of true stress-strain curve. The mathematical relationships shown in Figure 4.25, can be represented by the following equation in the temperature range between -60 to 75 °C:

$$\mathbf{n_{i(peak)} = 0.281 + 1.33*[1 + \exp((T - 33.0)*(31.1)^{-1})]^{-1}} \quad \textbf{..... Equation 4.12}$$

with $R^2 = 0.949$.

Where:

$n_{i(peak)}$ is peak instantaneous strain hardening exponent.

T is the temperature in °C.

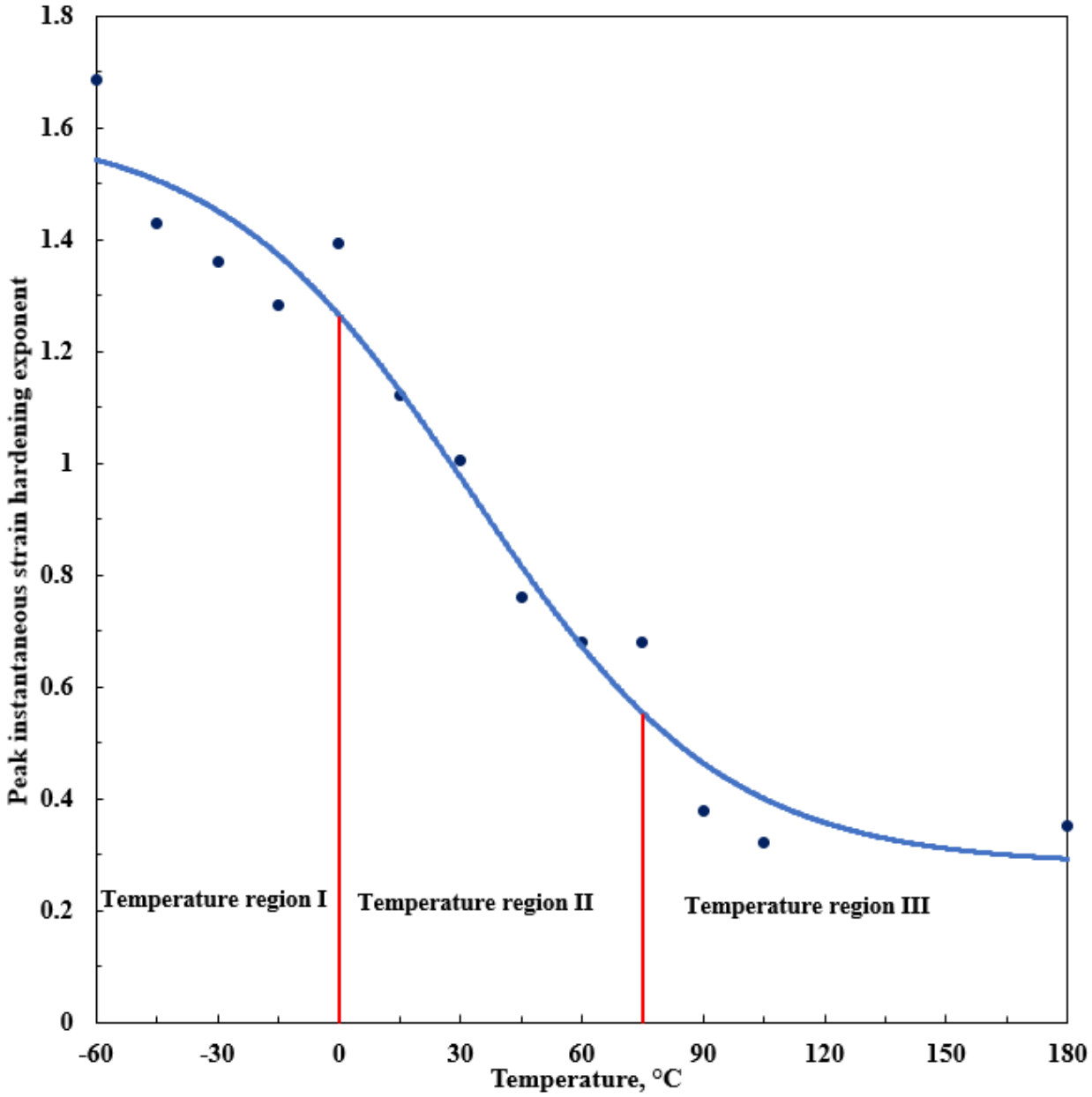


**Figure 4.25: Peak instantaneous strain hardening exponent ($n_i$)as a function of deformation temperature for alloy A**

The percentage of martensite present at the peak martensitic transformation was calculated by obtaining the corresponding strain to the peak martensitic transformation from Figure 4.3. This corresponding strain to the peak martensitic transformation at a given deformation temperature was then substituted in the derived constitutive equation (4.1) to estimate the percentage of martensite. The percentage of martensite present at the peak martensitic transformation was plotted as a function of deformation temperature as shown in

Figure 4.26. In a similar fashion, the percentage of martensite present at the peak instantaneous strain hardening exponent, $n_{ipeak}$, was calculated by obtaining the corresponding strain to the peak strain hardening from Figure 4.21. This corresponding strain to the peak instantaneous strain hardening exponent at a given deformation temperature was substituted in the derived constitutive equation (4.1) as before to estimate the percentage of martensite. The percentage of martensite present at the peak instantaneous strain hardening exponent was plotted as a function of deformation temperature in Figure 4.26 as well.

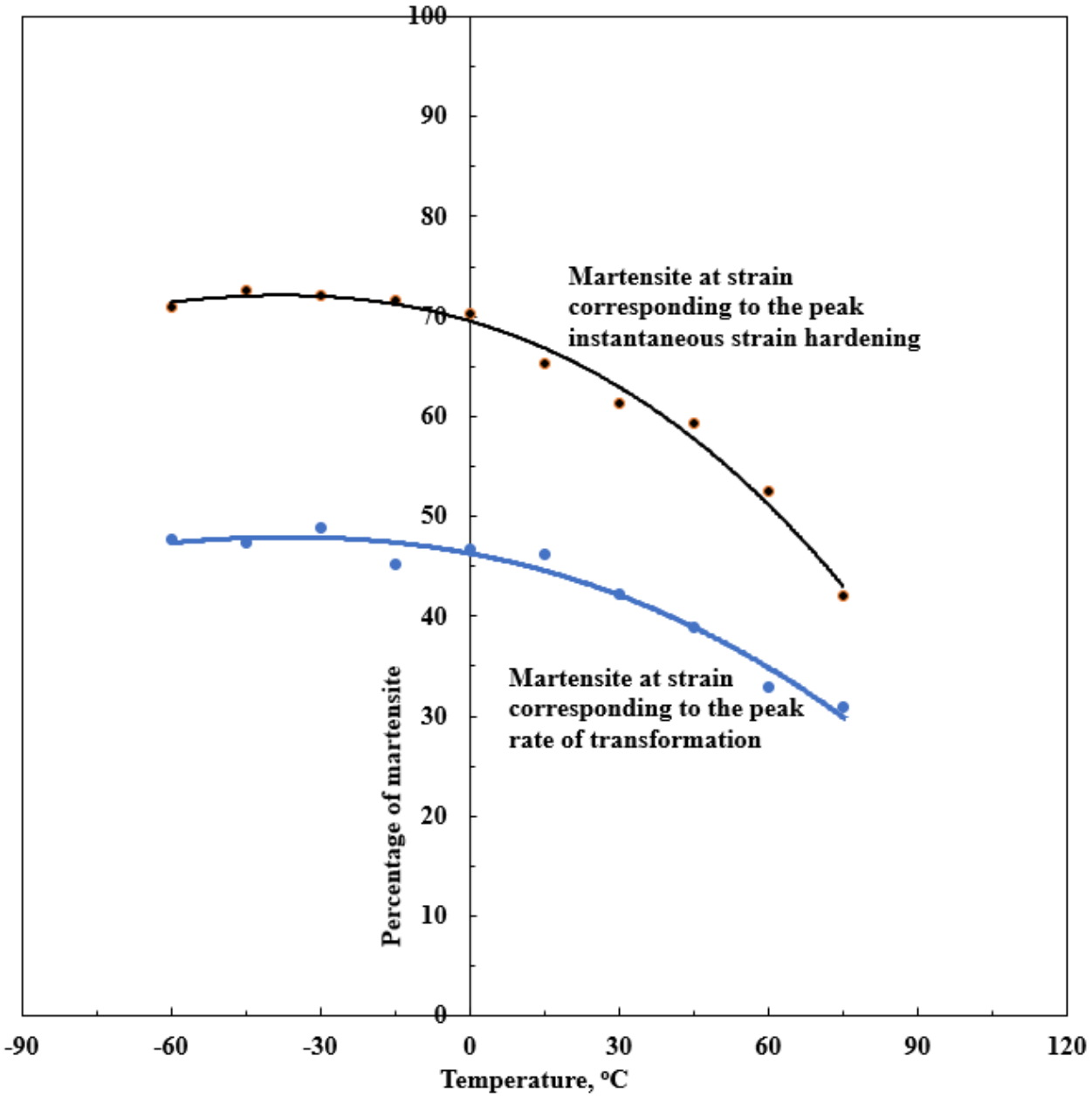


**Figure 4.26: Percentage of martensite present at strain value corresponding to the peak instantaneous strain hardening ($n_i$)-value as a function of deformation temperature for alloy A**

The mathematical relationships shown in Figure 4.26 can be represented by the following equations in the temperature range between -60 to 75 °C:

$$\mathbf{V_{\alpha'}(\text{at peak } n_i) = -7E\text{-}6*T^3 - 0.0023*T^2 - 0.1452*T + 69.553} \quad \textbf{..... Equation 4.13}$$

$$\mathbf{V_{\alpha'}[\text{at peak } (dV_{\alpha'}/d\varepsilon)] = -3E\text{-}6*T^3 - 0.0014*T^2 - 0.0931*T + 46.299} \quad \textbf{..... Equation 4.14}$$

with $R^2 = 0.9873$ for equation (4.13) and $R^2 = 0.9617$ for equation (4.14).

Where: T is deformation temperature.

### 4.1.3 Mechanical energy required to induce martensitic transformation at various temperatures

The mechanical energy values associated with the strain hardening were calculated by establishing the area below the tensile curves. Figure 4.27 shows the energy absorption of the AISI 301 steel at all temperatures during deformation. Figure 4.27 shows a proportional relationship between the applied strain and the mechanical energy absorbed during tensile testing at various temperatures in the range between -60 and 180 °C. The gradient is steeper at lower temperatures indicating higher energy absorption capability per given strain above true strain of 0.1 due to higher amount of martensitic transformation as shown in the earlier results. The higher amount of stress results in higher amount of energy absorption resulting in steeper gradient. However, ultimate toughness is lower at low temperatures due to low strain to fracture. As elongation to fracture increases at higher temperatures, the overall toughness increases up to a maximum at 75 °C and then decreases. The decrease is attributed to less amount of strain-induced martensitic transformed. The contribution of stress from martensite formation is higher compared to the contribution from deformation of austenite.

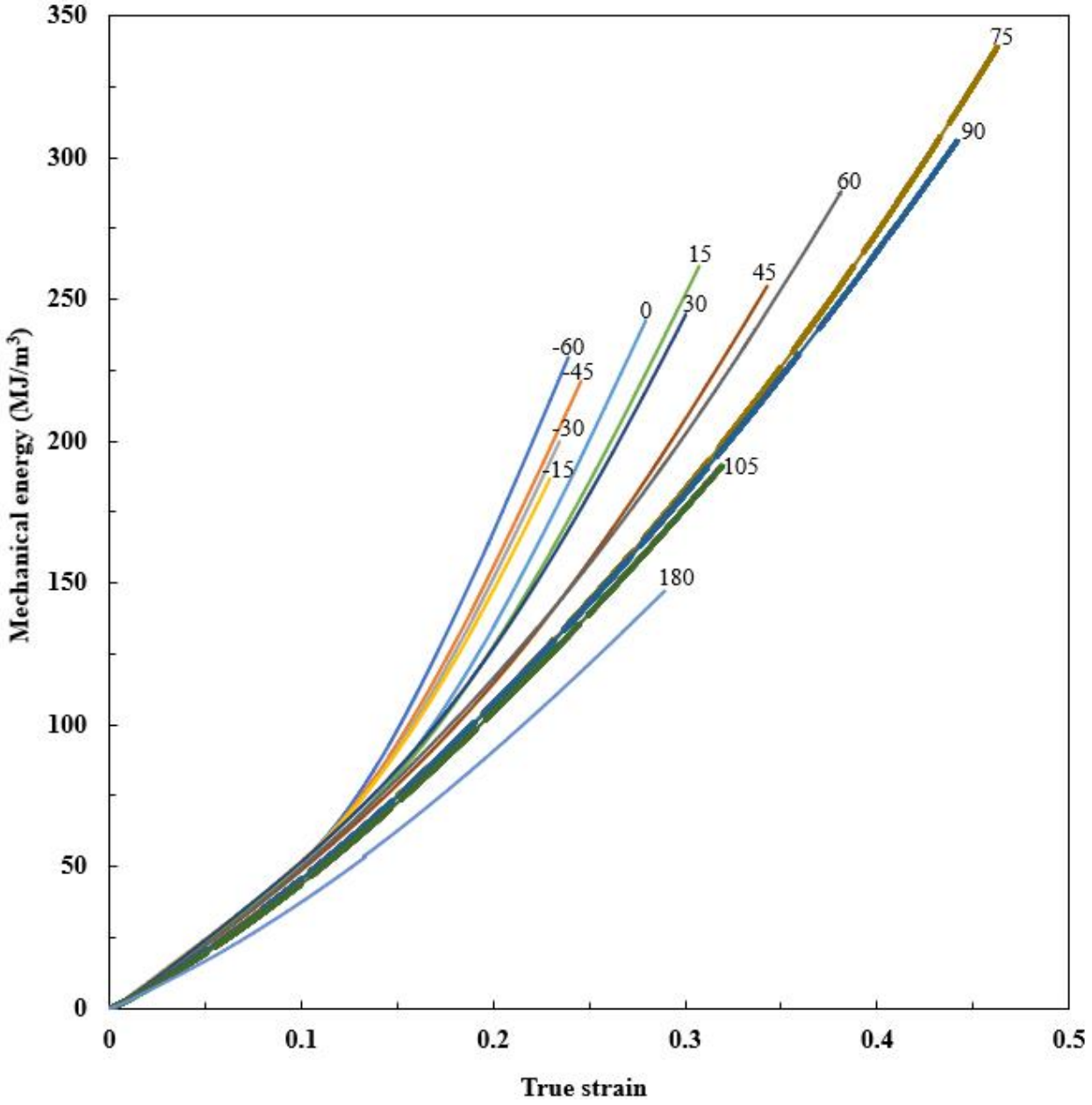


**Figure 4.27: Cumulative mechanical energy absorbed by the steel as a function of strain and temperature during tensile testing for alloy A tested at an initial strain rate of 6.67 x $10^{-4}$ $s^{-1}$**

### 4.1.4 Microstructural analysis

Microstructural analysis was done on two samples which were deformed at 30 °C and 105 °C in tension for alloy A. The aim was to ascertain the deformation mechanisms at two different temperatures which had shown extremely different martensitic transformation as a function of strain (see Figure 4.2) and strain hardening behaviour (see Figure 4.17). This was done by revealing the stacking faults, deformation twins, ε-martensite, α′-martensite and

dislocation substructure development at different deformation temperatures. Figure 4.28 (a) shows that in the early stages of deformation (true strain of less than 0.072), the microstructure is already dominated by the shear bands, whereas at higher temperature of 105 °C, Figure 4.29 shows weak traces of slip bands extending through the austenite phase with tangled dislocations at a higher strain level of 0.375. Stacking faults were observed at lower temperatures and lower strain, whereas at higher temperature at 105 °C, close to the "absolute" $M_d$ temperature of the alloy A tested (approximated as 117 °C, see Figure 4.7), twinning was observed.

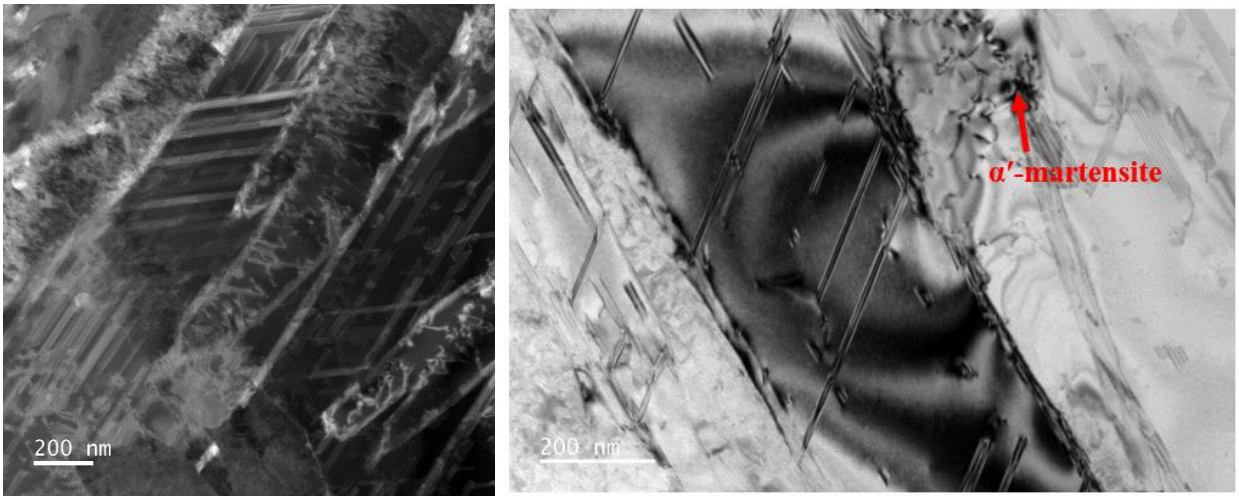


**(a)** **(b)**

**Figure 4.28: Microstructural analysis showing shear bands and stacking faults after straining to true strain of 0.072 at 30 °C for alloy A tested at an initial strain rate of 6.67 x $10^{-4}$ $s^{-1}$**

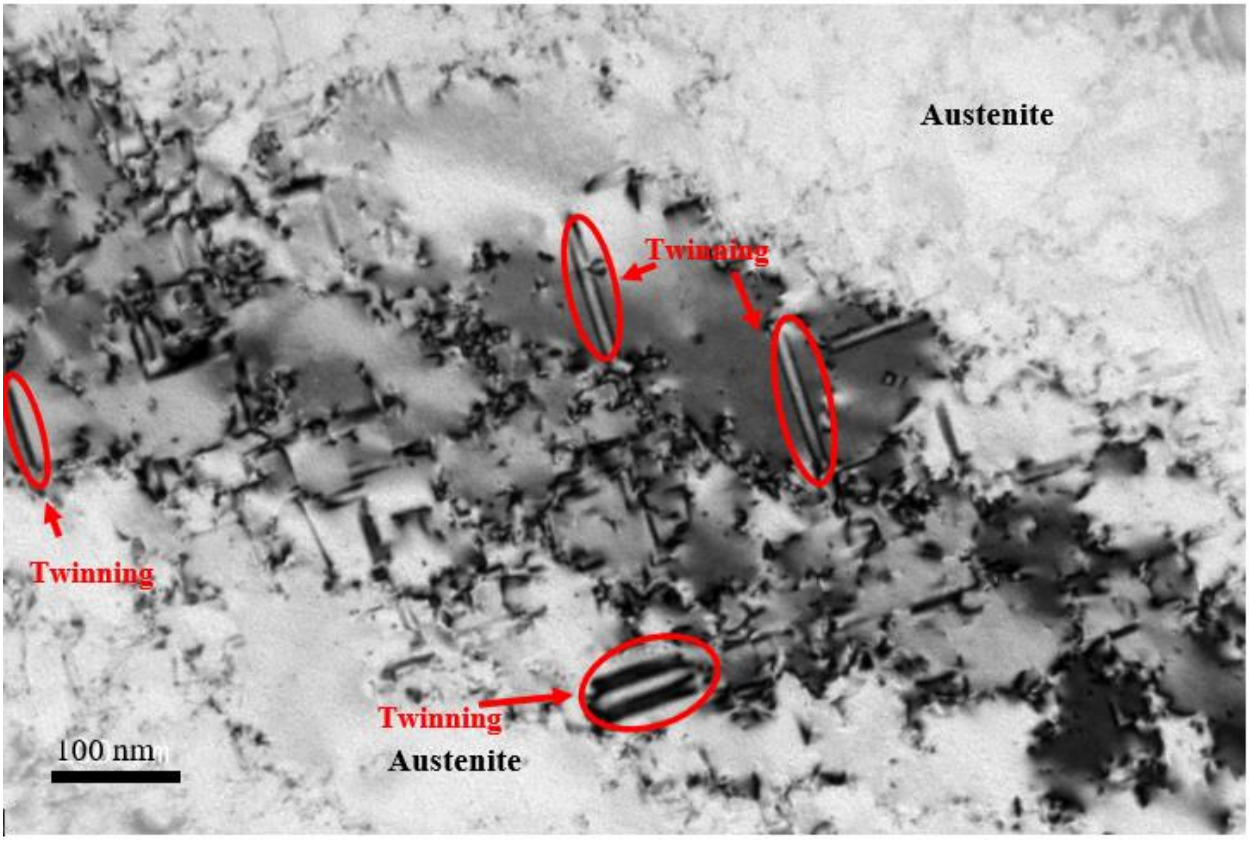


**Figure 4.29: Microstructural analysis showing twinning with small islands of strain-induced martensite after strained to true strain of 0.375 at 105 °C for alloy A tested at an initial strain rate of 6.67 x $10^{-4}$ $s^{-1}$.**

Figure 4.30 (a) shows an EBSD image with a corresponding EBSD Kikuchi pattern quality map in Figure 4.30 (b) of the sample deformed at 30 ℃ at a true strain of 0.072 showing the formation of strain-induced martensite. The two figures clearly show that the formation of martensite occur where there are dense small thin lines which indicate shear bands, stacking faults and ε-martensite. The observations were in accordance with literature that martensite nucleation occurs at the intersection shear bands which are the overlapping stacking faults and ε-martensite [46], [82]. Figure 4.31 (a) shows an EBSD image with a EBSD Kikuchi pattern quality map in Figure 4.31 (b) of the sample strained to a true strain of 0.375 and tested at 105 °C confirming the formation of twins with small islands of strain-induced martensite. The EBSD image shows a larger area as compared to TEM. Formation of martensite from twinning could be confirmed but in small amounts. This is in good agreement with literature that martensite nucleation occur at the intersection of shear bands and ε-martensite at lower strains and lower temperatures, and can occur at the intersection of mechanical twins at higher strains

and higher deformation temperatures [52], [27], [164]. The onset of the martensitic transformation has been induced by high concentration of localized twins. The volume fraction of martensite will be expected to increase as the volume fraction of twins increases as a function of strain. As the deformation temperature increases the formation of stacking faults is suppressed as twinning is promoted and the chemical driving force for SIMT decreases.

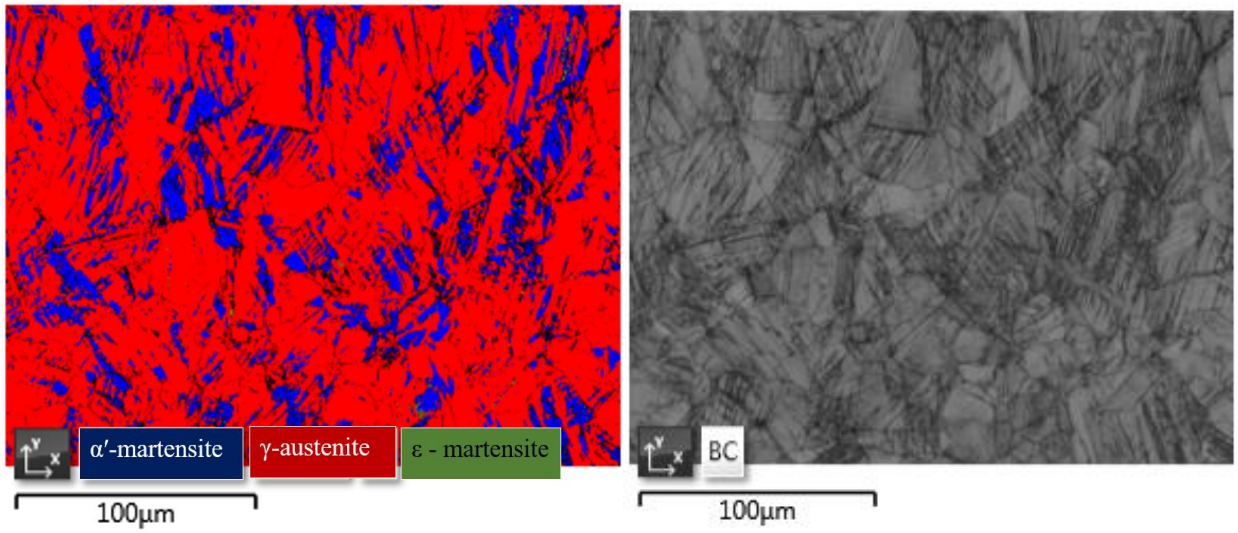


**(a)** **(b)**

**Figure 4.30: Microstructural analysis (a) EBSD image (b) corresponding EBSD Kikuchi pattern quality map, showing strain-induced martensitic transformation (blue-coloured phase) and ε-martensite (lime-green coloured phase) in an austenite matrix (red-coloured phase) at true strain of 0.072 at 30 °C for alloy A tested at an initial strain rate of 6.67 x $10^{-4}$ $s^{-1}$.**

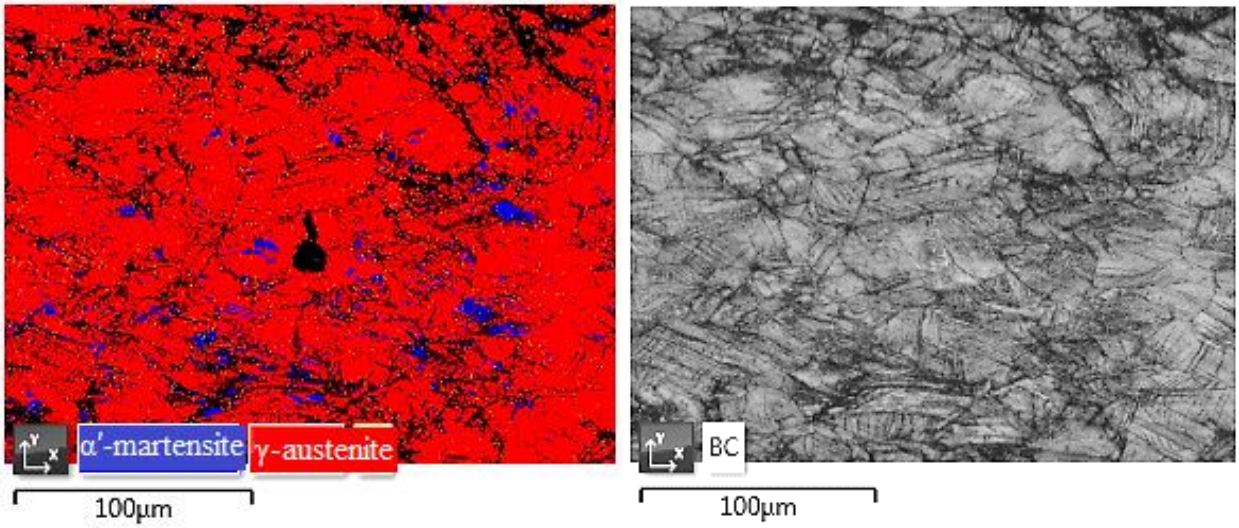


**(a)** **(b)**

**Figure 4.31: Microstructural analysis (a) EBSD image (b) corresponding EBSD Kikuchi pattern quality map, showing twinning with small islands (blue-coloured phase) of strain-induced martensite in a retained austenite matrix (red-coloured phase) after strained to true strain of 0.375 at 105 °C for alloy A tested at an initial strain rate of 6.67 x $10^{-4}$ $s^{-1}$.**

## 4.2 Influence of the degree of prior cold rolling using alloy A

Cold rolling was done on annealed and pickled (as-received) AISI 301LN (alloy A) steel to different gauges from 5% - 70% at room temperature with an interpass cooling in water. The initial thickness of the steel sheets was 4.05 mm. Thickness reduction of ~ 0.8 % and less per interpass was used to avoid significant adiabatic heating during cold rolling. Tensile samples were then machined from as-cold rolled samples according to ASTM standards used.

### 4.2.1 Effect of prior cold rolling on martensitic transformation

The amount of martensitic transformation as a function of percentage of prior cold rolling is as shown in Figure 4.32. Neutron diffraction analyses was used to quantify the volume fractions of austenite, strain-induced α′- and ε- martensites. The ε - martensite increases to a maximum in the early stages of deformation and then decreases to zero indicating ε - martensite as an intermediate phase in the γ → α′ transformation with increasing deformation. In the latter stages of deformation, no ε - martensite was detected indicating a direct γ → α′ transformation without the intermediate phase in these cases. Ferritescope measurements were used as quick, non-destructive approach to quantify only the magnetic strain-induced α′-martensite as calibrated by the neutron diffraction techniques (refer to Figure 3.3). Seven readings were taken on each

sample at different points on the surface of cold rolled samples. The mean and standard deviations were calculated. A calibration factor of 1.62 was used to convert Ferritescope readings to actual martenstite content as described in Chapter 3.3. It is important to note that the calibration factor obtained during cold rolling of 1.62 is different from a calibration factor obtained during tensile deformation as explained in Chapter 3.3.

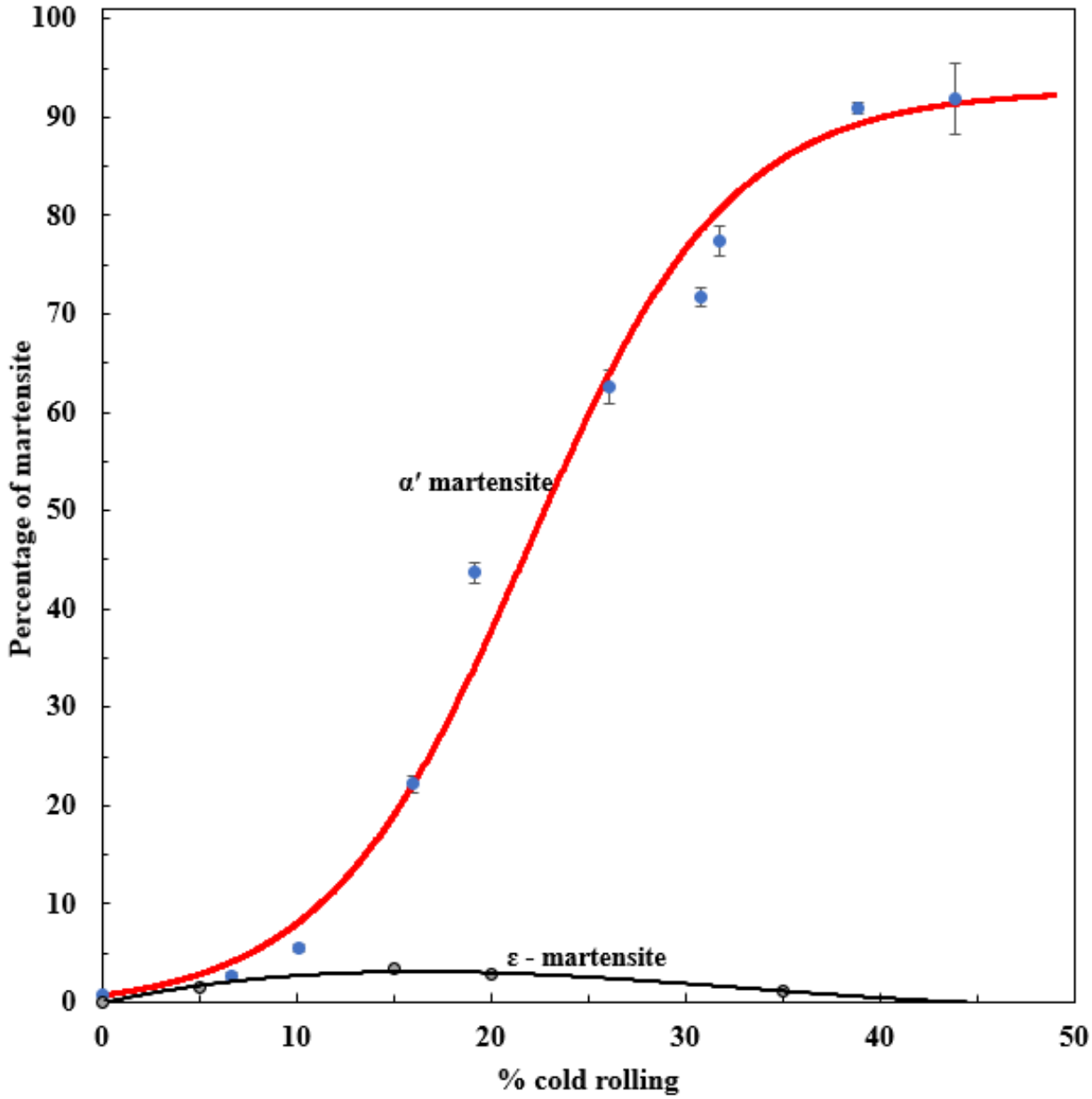


**Figure 4.32: The variation of percentage of martensite induced as a function of percentage of cold rolling at room temperature for alloy A**

Figure 4.33 denotes the slope of the curve in Figure 4.32 as a function of cold rolling percentage. Figure 4.33 shows the rate of $\gamma \rightarrow \alpha'$ strain–induced martensitic transformation as a function of cold rolling percentage as determined by the instantaneous gradient of the curve of the percentage of strain induced martensite as a function of prior cold rolling. The instantaneous gradient increased to a maximum and thereafter decreases to zero martensitic transformation, as martensitic transformation reaches a saturation level.

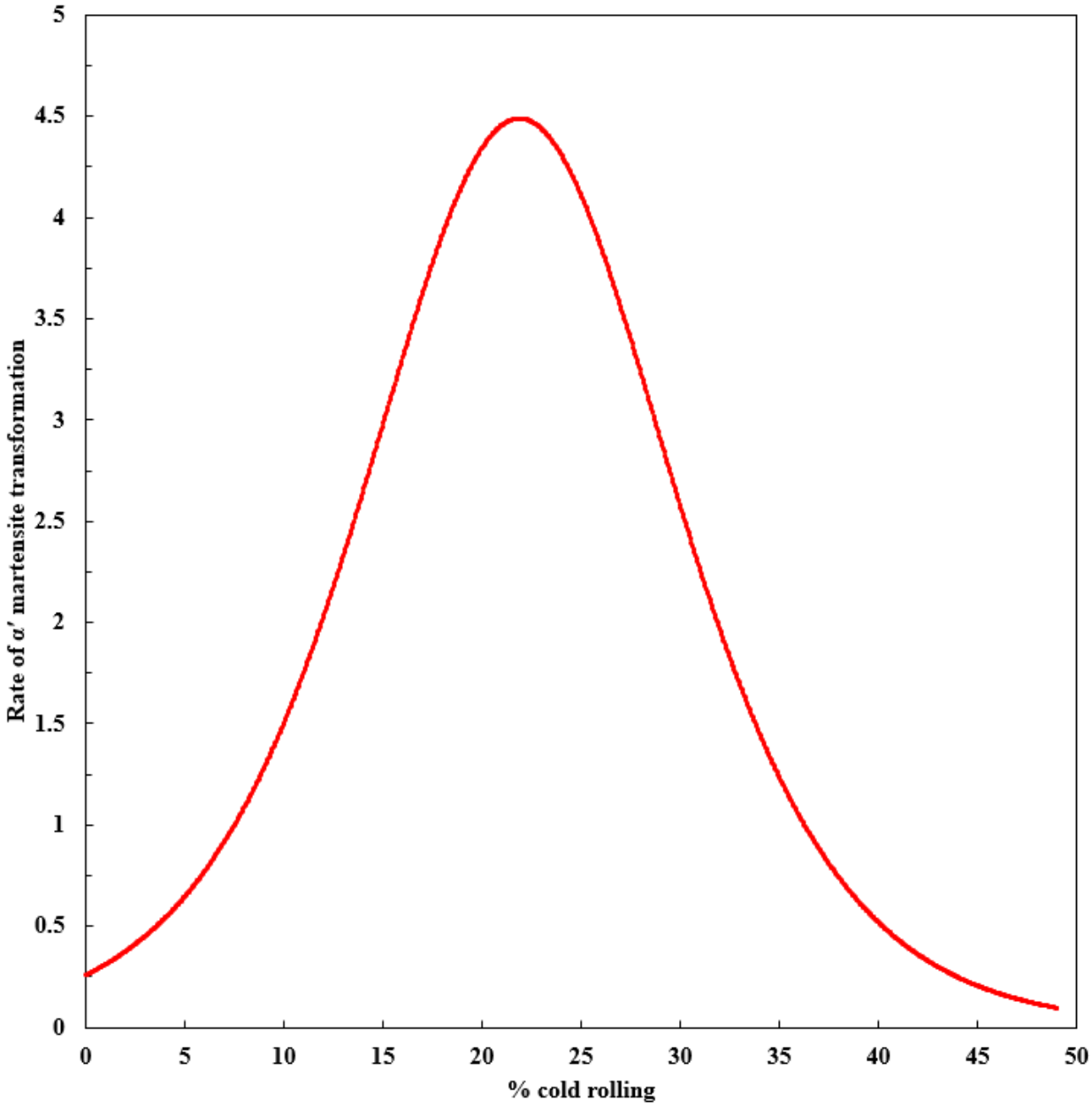


**Figure 4.33: The variation of rate of α′ martensite transformation as a function of percentage of cold rolling at room temperature for alloy A**

Figure 4.34 shows the percentage of α′-martensite induced as a function of strain during tensile deformation after various degree of prior cold rolling at 30 °C. Interruption was done at 5% engineering strain intervals allowing Ferritescope measurements to be taken to quantify the magnetic strain-induced α′-martensite. Seven readings were taken on each sample at different points within the gauge length on the surface. The mean and standard deviations were calculated. A calibration factor of 1.7 was used to convert Ferritescope readings to actual martenstite content as described in Chapter 3.3. The Ferritescope readings were taken under unloaded (unstressed) conditions. The same form of sigmoidal function describing the kinetics of martensitic transformation with no prior cold rolling is the same function describing the kinetics of martensitic transformation with prior cold rolling but shifted to lower strain values. Therefore, the sigmoidal curve fitted, for prior cold rolling at all true strain levels could be accurately described by sigmoidal equation 4.1 with $R^2 \geq 0.996$, at lower levels of prior cold rolling tested. However, a transition from sigmoidal curve after low degrees of prior cold rolling to smooth (parabolic) curve after high degree of cold rolling taking the shape of the upper part of the sigmoidal curve was observed. The sigmoidal curve fitted, for samples which had shown significant plastic deformation, at all true strain levels could be accurately described by the same equation (4.1) described before.

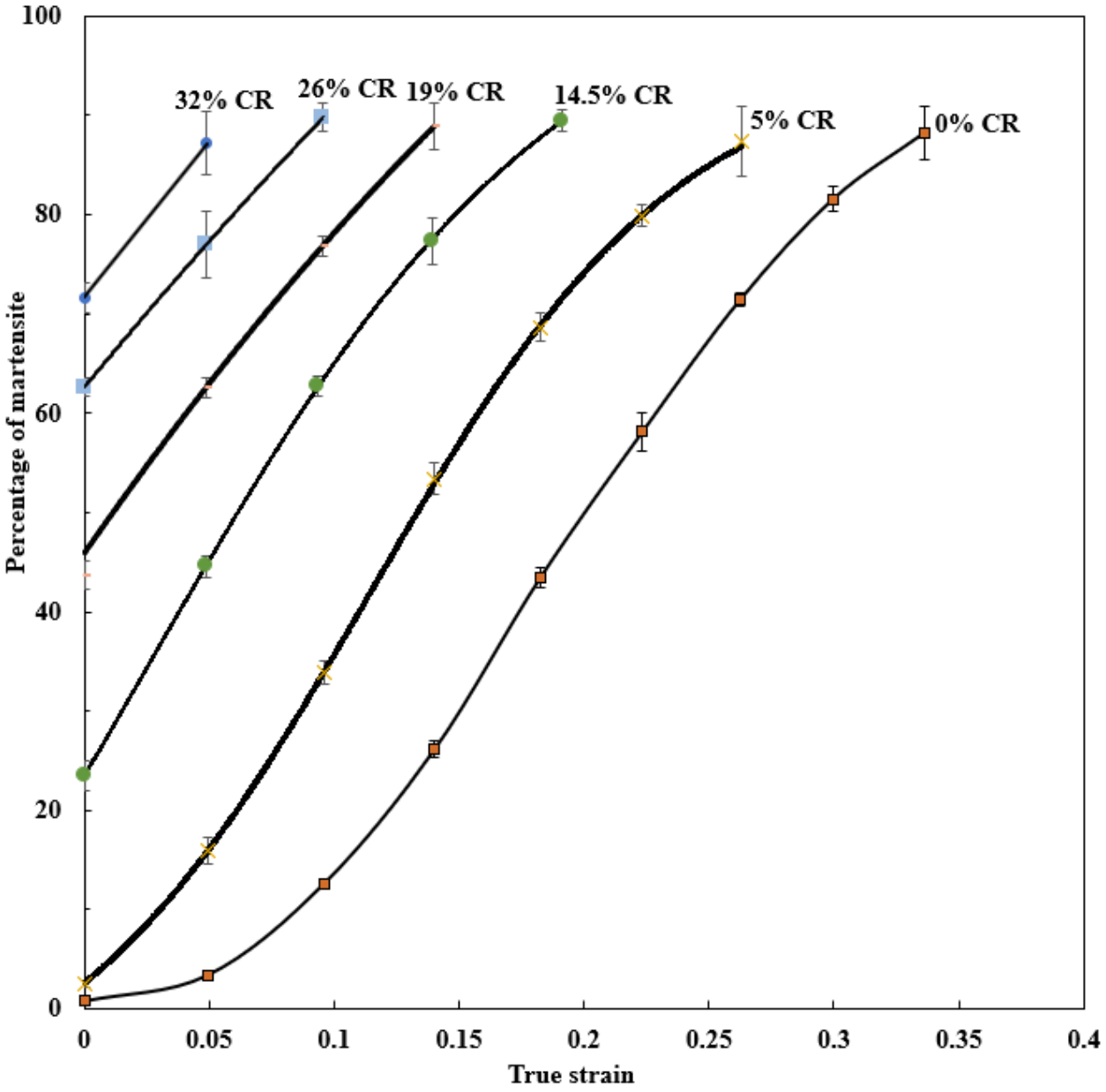


**Figure 4.34: Percentage of α′-martensite induced as a function of strain after various degree of prior cold rolling at 30 °C for alloy A tested at an initial strain rate of 6.67 x $10^{-4}$ $s^{-1}$ (fitted shifted sigmoidal curves)**

Figure 4.35 shows the rate of γ → α′ strain–induced martensitic transformation per unit strain (dVα′/dε). These values denote the slopes of the curves in Figure 4.34 as a function of strain. The instantaneous gradient increased to a maximum and thereafter decreases to zero martensitic transformation. Prior cold rolling had shifted the curves in Figure 4.35 to lower strain values, that is, to the left in a similar fashion as in Figure 4.34.

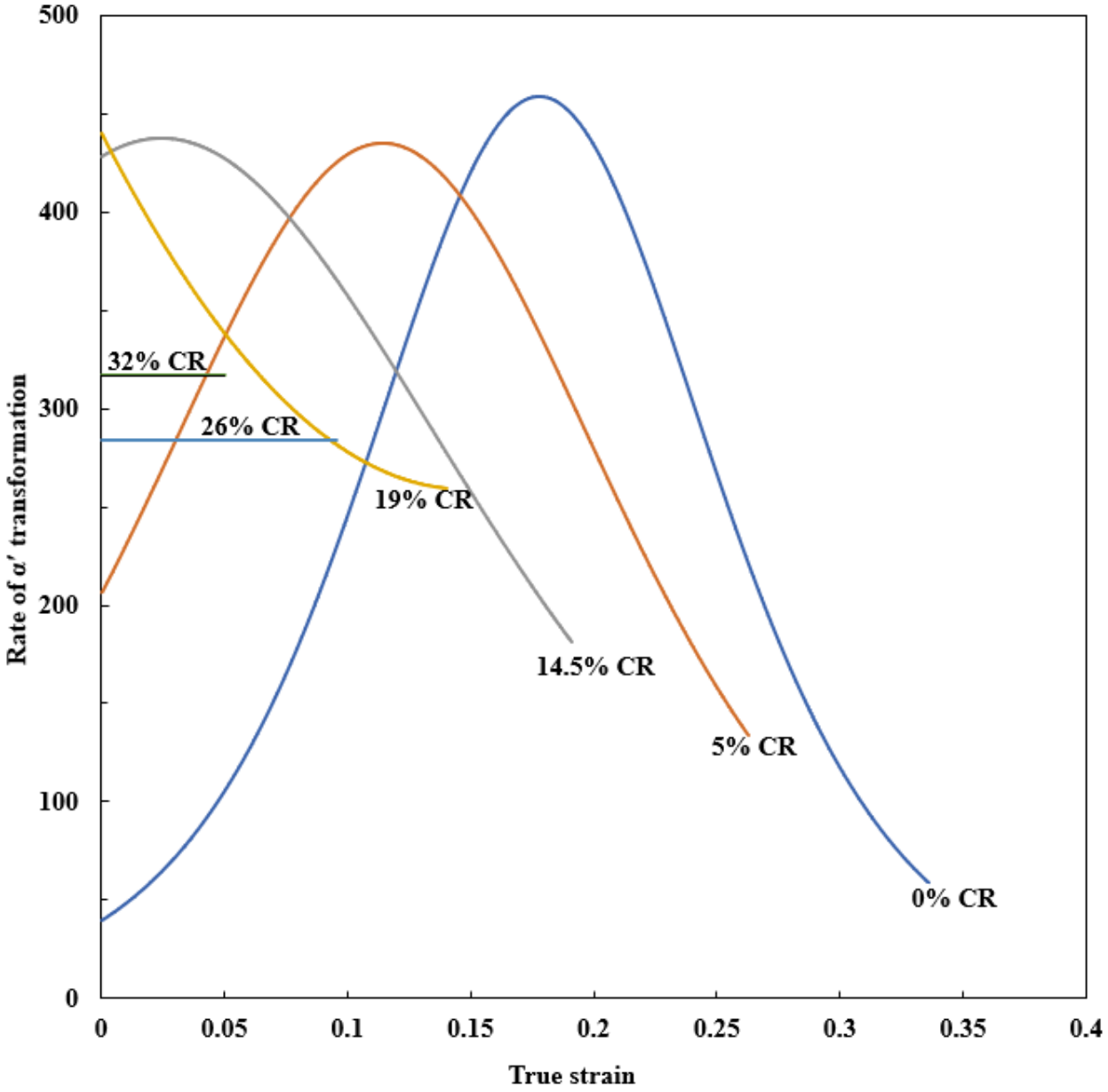


**Figure 4.35: Rate of α′-Martensite transformation as a function of strain after various degree of prior cold rolling at 30 °C for alloy A tested at an initial strain rate of 6.67 x $10^{-4}$ $s^{-1}$**

### 4.2.2 Effect of prior cold rolling on tensile behavior

Figure 4.36 and Figure 4.37 show the engineering stress-strain and true stress-strain curves, respectively, after a certain degree of cold rolling at room temperature, (25 °C). Plastic deformation decreases as the degree of prior cold rolling increases. The yield point elongation plateau disappears as the amount of prior cold rolling increases and the shape of all true stress – strain curves at higher strains appear to be shifted to lower strains taking the same trend as

observed in Figure 4.34. This clearly show the effect of martensitic transformation on the true stress – strain curves of the material.

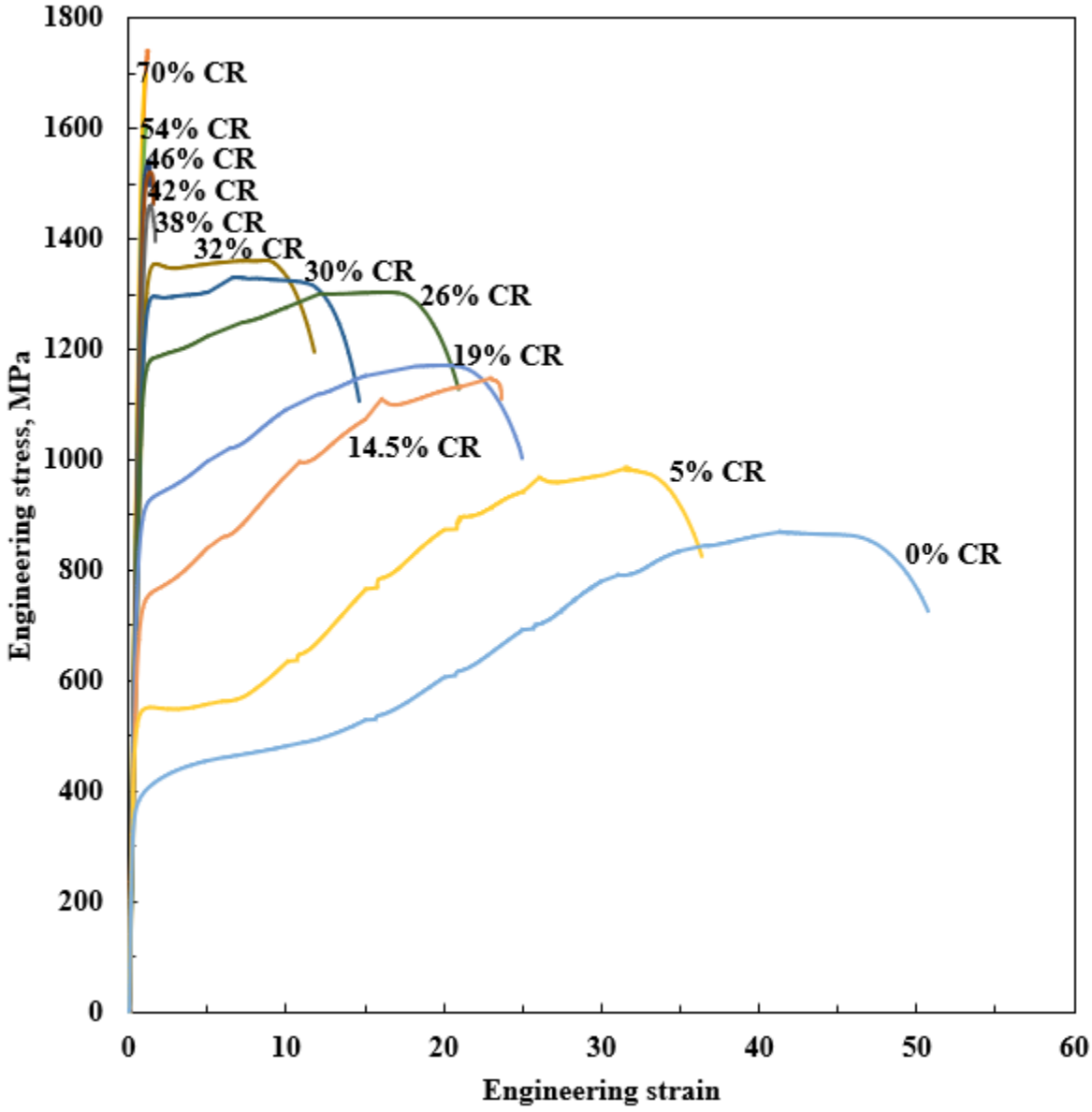


**Figure 4.36: The Engineering stress – strain curves of previously cold rolled samples. Tensile testing performed at room temperature, (25 °C) for alloy A tested at an initial strain rate of 6.67 x $10^{-4}$ $s^{-1}$**

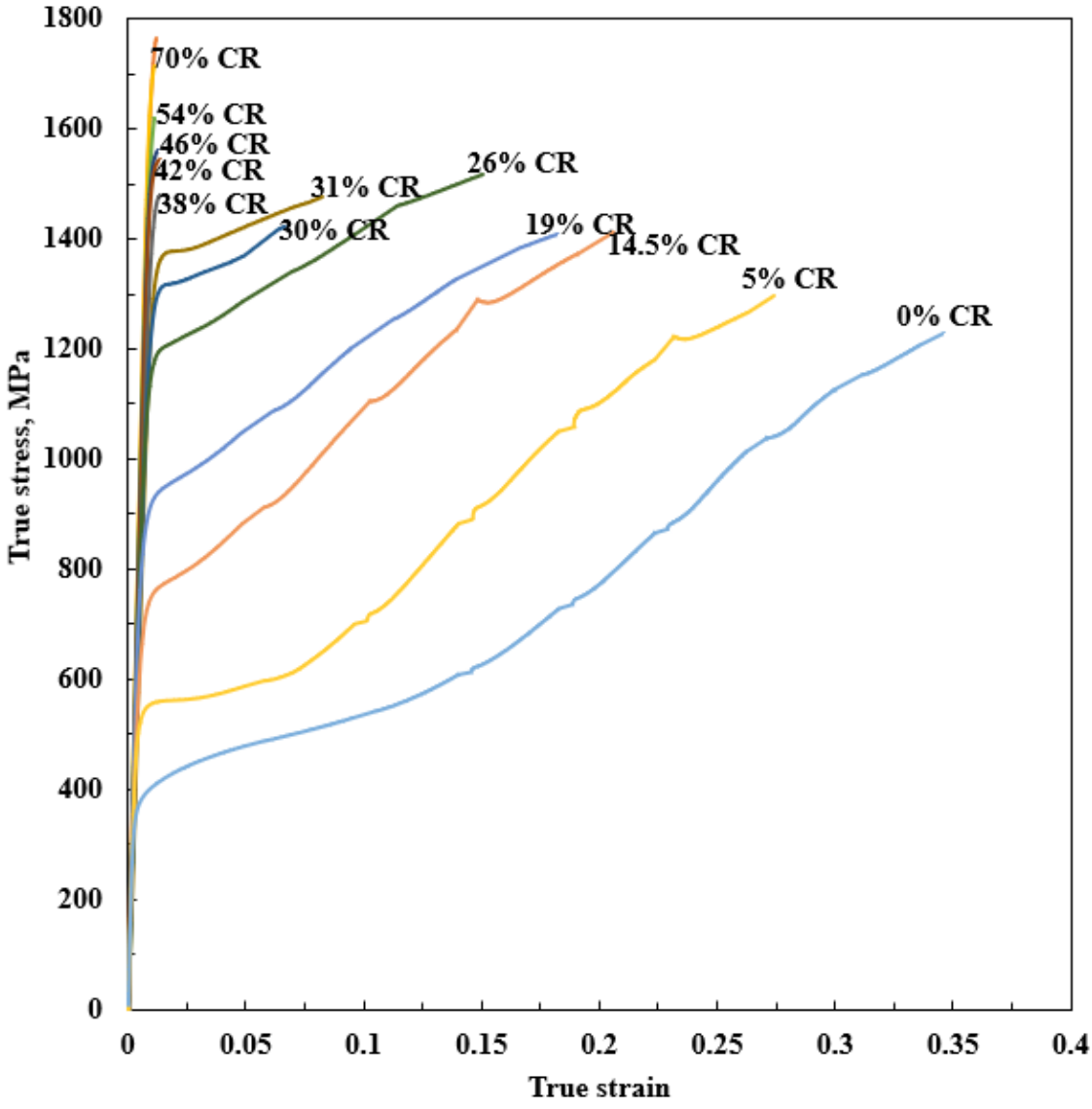


**Figure 4.37: The True stress – strain curves of previously cold rolled samples. Tensile testing performed at room temperature, (25 °C) for alloy A tested at an initial strain rate of 6.67 x $10^{-4}$ $s^{-1}$**

There is a significant increase in the yield strength and tensile strength with increase in percentage of prior cold rolling as shown in Figure 4.38. This is attributed to the increasing amount of martensite induced during prior cold rolling which is conformed with Figure 4.39. The increase in yield strength is attributed to increased dislocation density and strain-induced martensite formed during cold rolling. There is severe impairing of the ductility as a function of thickness reduction due to higher SIMT during cold rolling as indicated by decrease in uniform and total elongation to fracture as a function of both percentage of prior cold rolling (see Figure 4.38) and initial amount of martensite (see Figure 4.39).

A 50% prior cold rolling has resulted in martensitic saturation of the sample. However, the tensile strength was observed to continuously increase with further increase in prior cold rolling as shown in Figure 4.38.

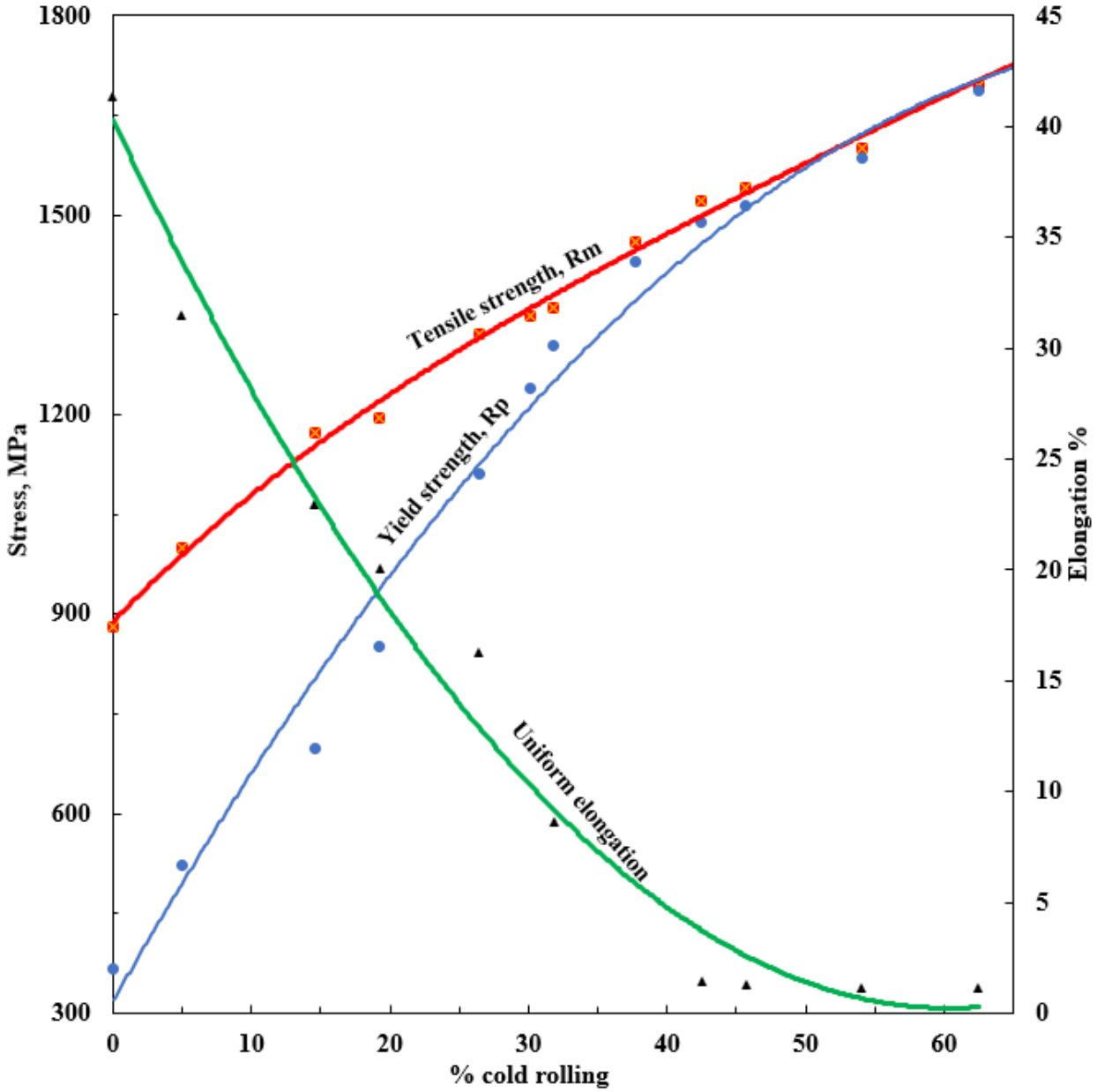


**Figure 4.38: The variation of yield strength ($R_{p0.2}$), tensile strength ($R_m$) and uniform elongation as a function of percentage of cold rolling at room temperature for alloy A tested at an initial strain rate of 6.67 x $10^{-4}$ $s^{-1}$**

Table 4.5 shows a comparison of the mechanical properties for the cold rolled alloy A vs the mechanical properties obtained for AISI 301 as reported by Southern African Stainless Steel

Development Association (SASSDA) [165], the Nickel Distribution Institute (NDI) [166], and advertised in a data sheet by AK Steel [167]. The comparison demonstrates that the strength properties of the lean alloyed AISI 301LN compares well with that of the higher alloyed AISI 301 steels. The SASSDA and AK steel publications did not provide specific chemistries, but the NDI examples provides a chemistry of C 0.10%; Ni 7.13% and Cr 17.57%.

**Table 4.5: Comparison of the effects of cold work on the mechanical properties for the tested alloy A vs published data on 301 alloy by SASSDA, NDI and AK Steel**

| **% CR** | **0** | | | | **10** | | | |
|---|---|---|---|---|---|---|---|---|
| Type of steel | Sassda 301 | NDI 301 | AKS 301 | Tested alloy A | Sassda 301 | NDI 301 | AKS 301 | Tested alloy A |
| Yield strength | 275 | 276 | 296 | 368 | 585 | 600 | 655 | 661 |
| Tensile strength | 755 | 827 | 896 | 880 | 1035 | 1034 | 1138 | 1069 |
| Rp/Rm | 0.36 | 0.33 | 0.33 | 0.42 | 0.57 | 0.58 | 0.58 | 0.62 |
| **% CR** | **20** | | | | **30** | | | |
| Type of steel | Sassda 301 | NDI 301 | AKS 301 | Tested alloy A | Sassda 301 | NDI 301 | AKS 301 | Tested alloy A |
| Yield strength | 1035 | 827 | 965 | 958 | 1310 | 1034 | 1172 | 1239 |
| Tensile strength | 1275 | 1172 | 1241 | 1220 | 1445 | 1276 | 1379 | 1356 |
| Rp/Rm | 0.81 | 0.71 | 0.78 | 0.79 | 0.91 | 0.81 | 0.85 | 0.91 |

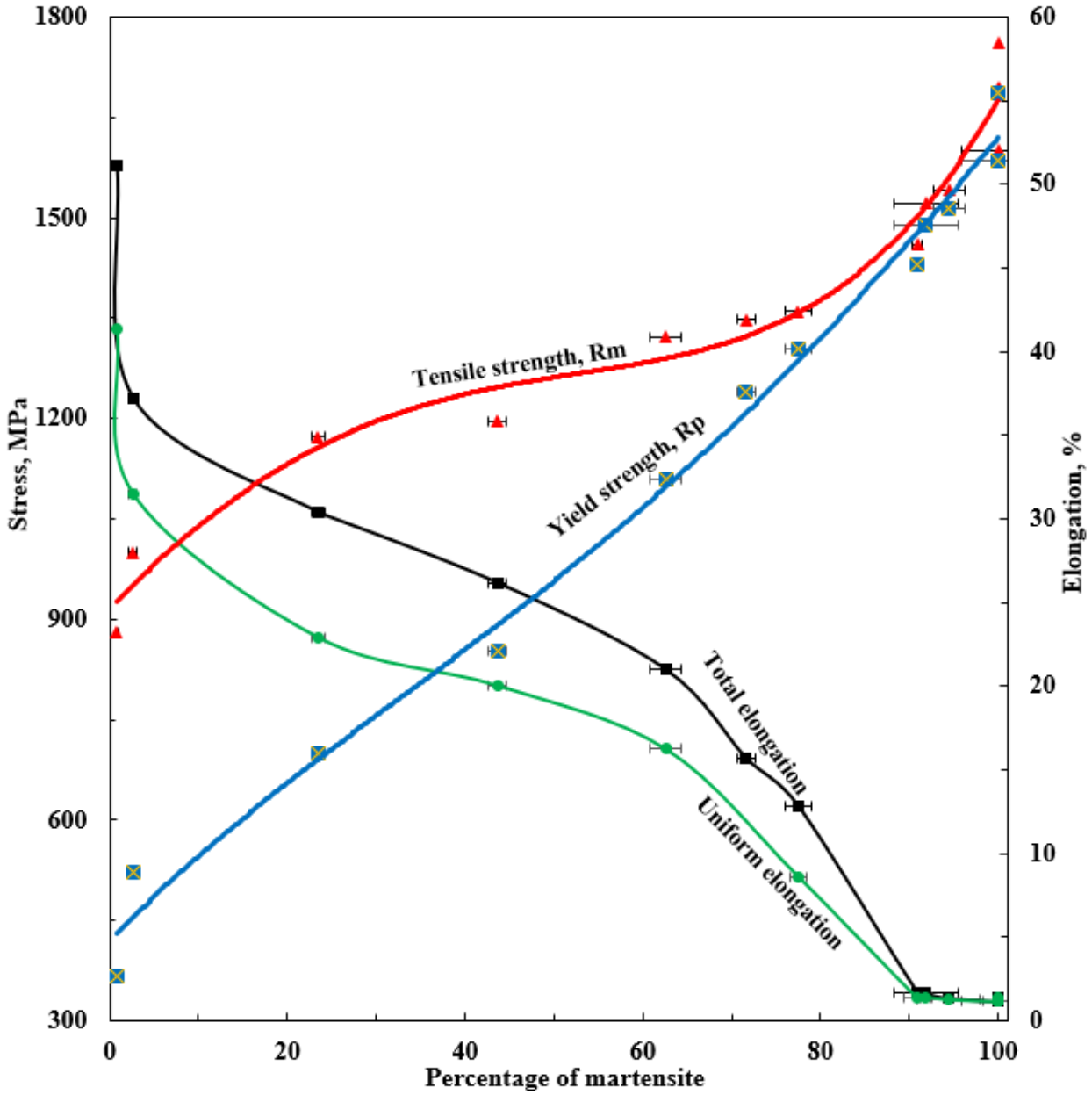


**Figure 4.39: The variation of yield strength ($R_{p0.2}$), tensile strength ($R_m$), uniform and total elongation to fracture as a function of initial amount of martensite after cold rolling at room temperature for alloy A tested at an initial strain rate of 6.67 x $10^{-4}$ $s^{-1}$**

Figure 4.40 shows the variation of product of strength and uniform elongation as a function of percentage of cold rolling at room temperature. The stipulated values of tensile strength required is in the range (1000 ~ 1150 MPa) and uniform strain of at least 22%, indicates a minimum value of the product of strength and elongation of 22 Gpa. This makes ~ 17.5% as the maximum temper cold rolling that could be applied to achieve this specific property.

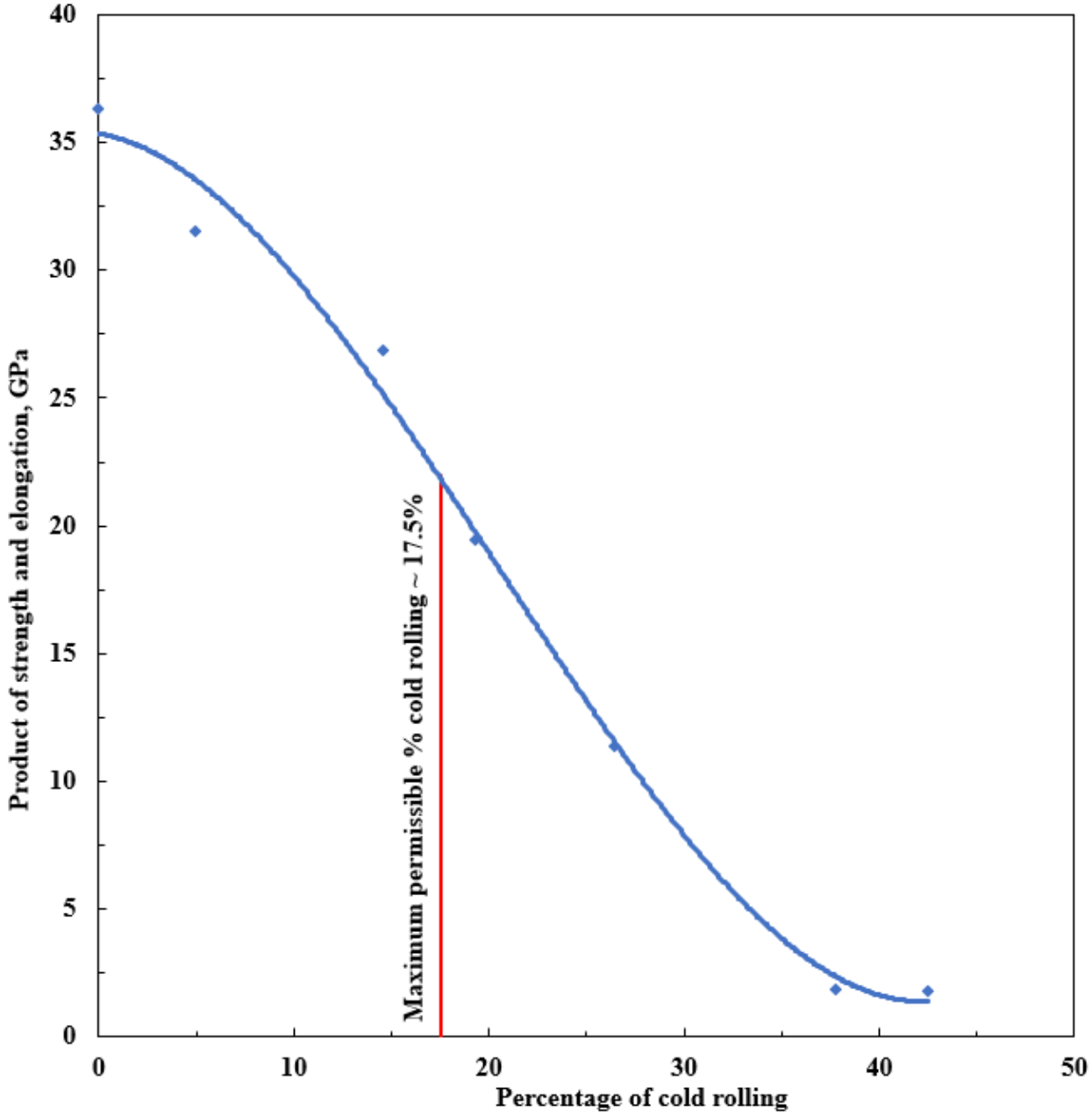


**Figure 4.40: The variation of product of strength and uniform elongation as a function of percentage of cold rolling at room temperature for alloy A tested at an initial strain rate of 6.67 x $10^{-4}$ $s^{-1}$**

The ratio of $R_p/R_m$ is important for formability purposes. A stipulated limit of less than 0.8 has been classified in the design manuals for structural stainless steels for metro coach manufacturing. Figure 4.41 shows the ratio of $R_p/R_m$ as a function of initial amount of martensite after cold rolling at room temperature. Figure 4.41 clearly show that the initial amount of martensite should be below 58 % for the $R_p/R_m$ to meet the criterion of less than 0.8. Figure 4.42

shows the variation of ratio of $R_p/R_m$ as a function of percentage of cold rolling at room temperature. Maximum temper rolling required to achieve this property is 24 % as shown in the Figure 4.42 as equated to the amount of martensite of 58 % in Figure 4.32.

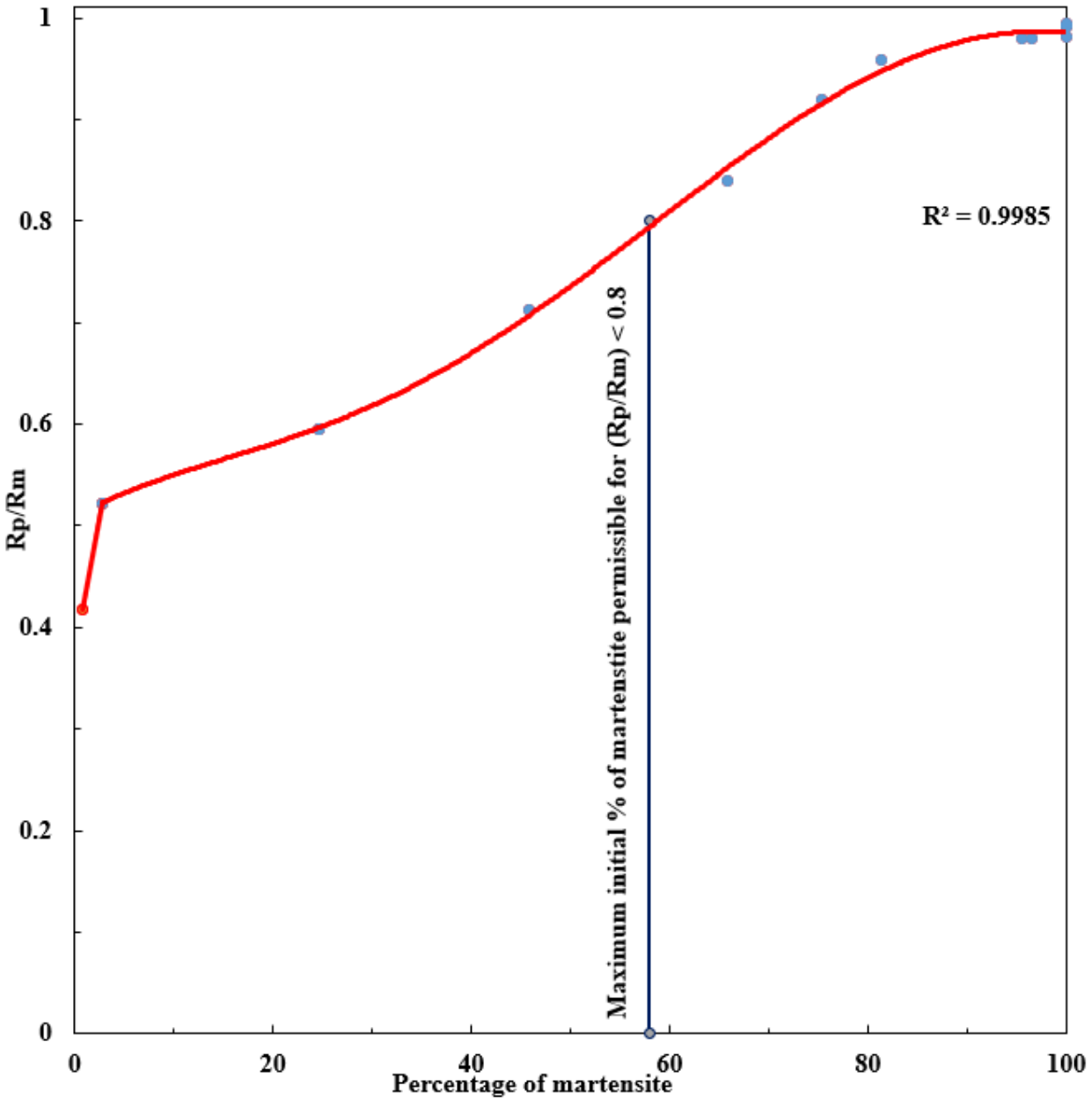


**Figure 4.41: The variation of ratio of ($R_{p(0.2)}/R_m$) as a function of initial amount of martensite after prior cold rolling at room temperature for alloy A tested at an initial strain rate of 6.67 x $10^{-4}$ $s^{-1}$**

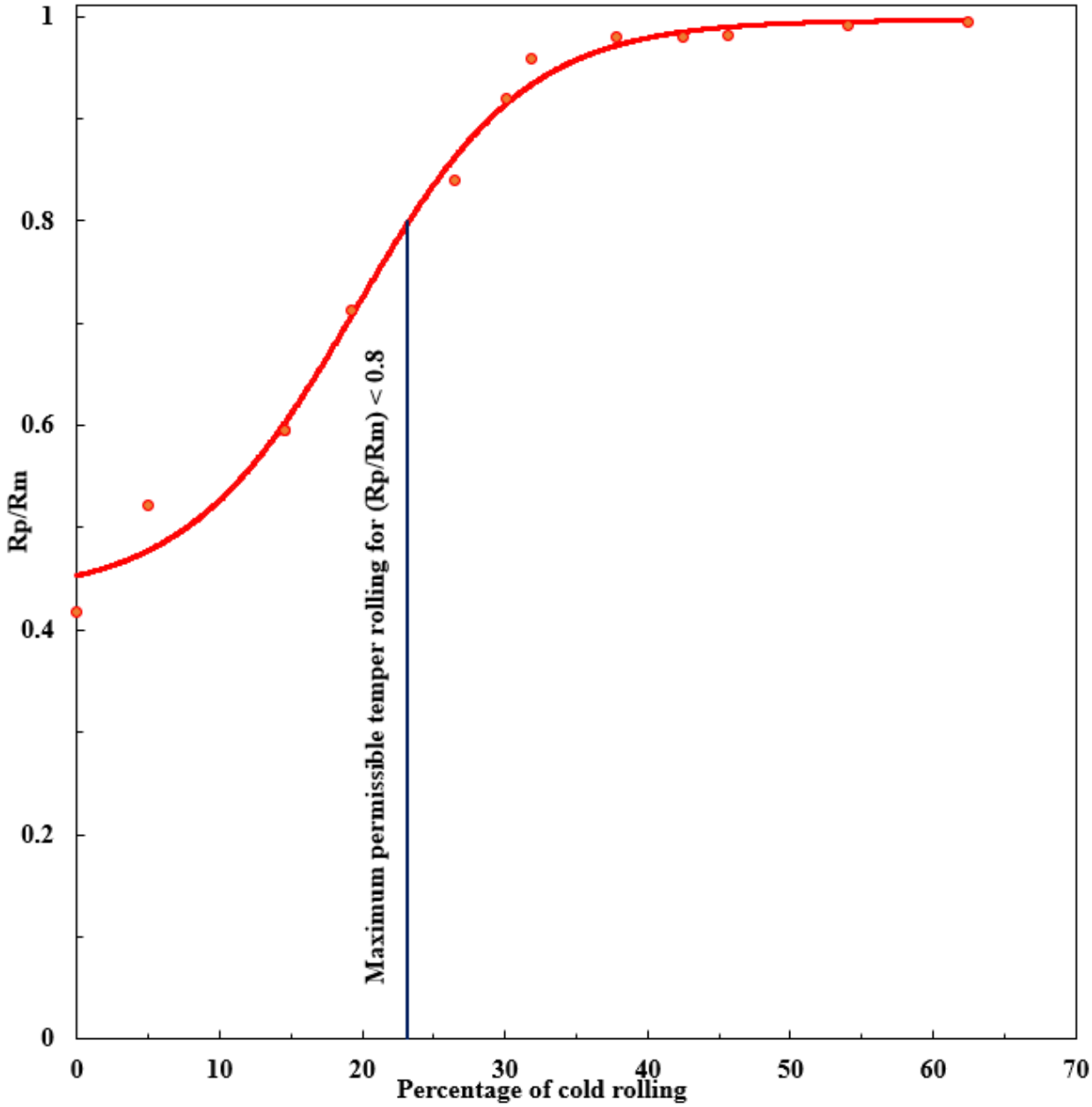


**Figure 4.42: The variation of ratio of ($R_{p(0.2)}/R_m$) as a function of percentage of cold rolling at room temperature for alloy A tested at an initial strain rate of 6.67 x $10^{-4}$ $s^{-1}$**

Figure 4.43 shows the variation of macro Vickers hardness ($Hv_{10}$) and tensile strength ($R_m$) as a function of percentage of cold rolling at room temperature for alloy A tested at an initial strain rate of 6.67 x $10^{-4}$ $s^{-1}$.

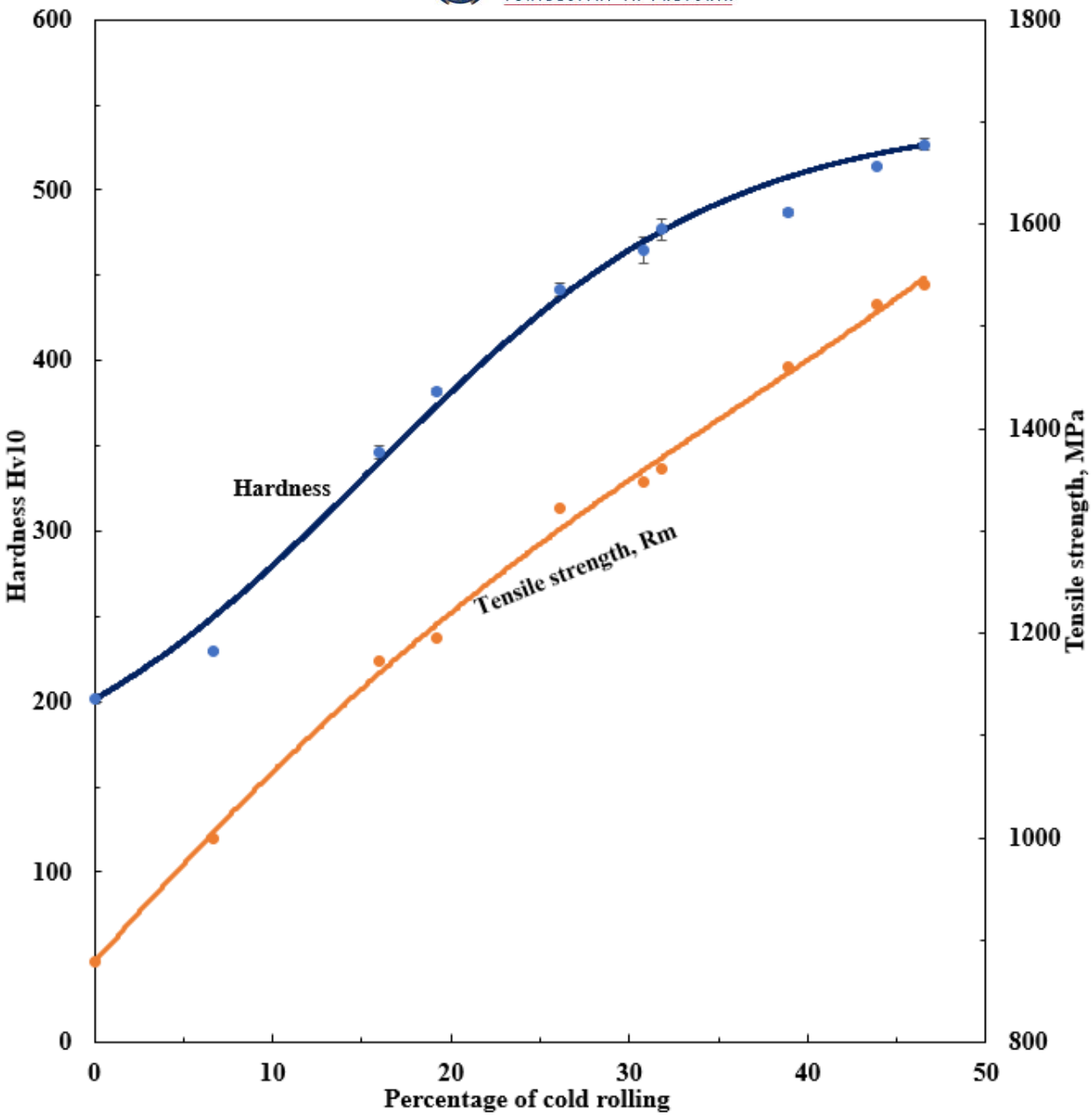


**Figure 4.43: The variation of macro Vickers hardness ($Hv_{10}$) and tensile strength ($R_m$) as a function of percentage of cold rolling at room temperature for alloy A tested at an initial strain rate of 6.67 x $10^{-4}$ $s^{-1}$**

It could be seen that there is a good correspondence between the tensile strength and hardness after 20% of cold rolling. Figure 4.44 shows the variation of tensile strength ($R_m$) as a function of macro Vickers hardness ($H_{v10}$) after cold rolling at room temperature for alloy A tested at an initial strain rate of 6.67 x $10^{-4}$ $s^{-1}$.

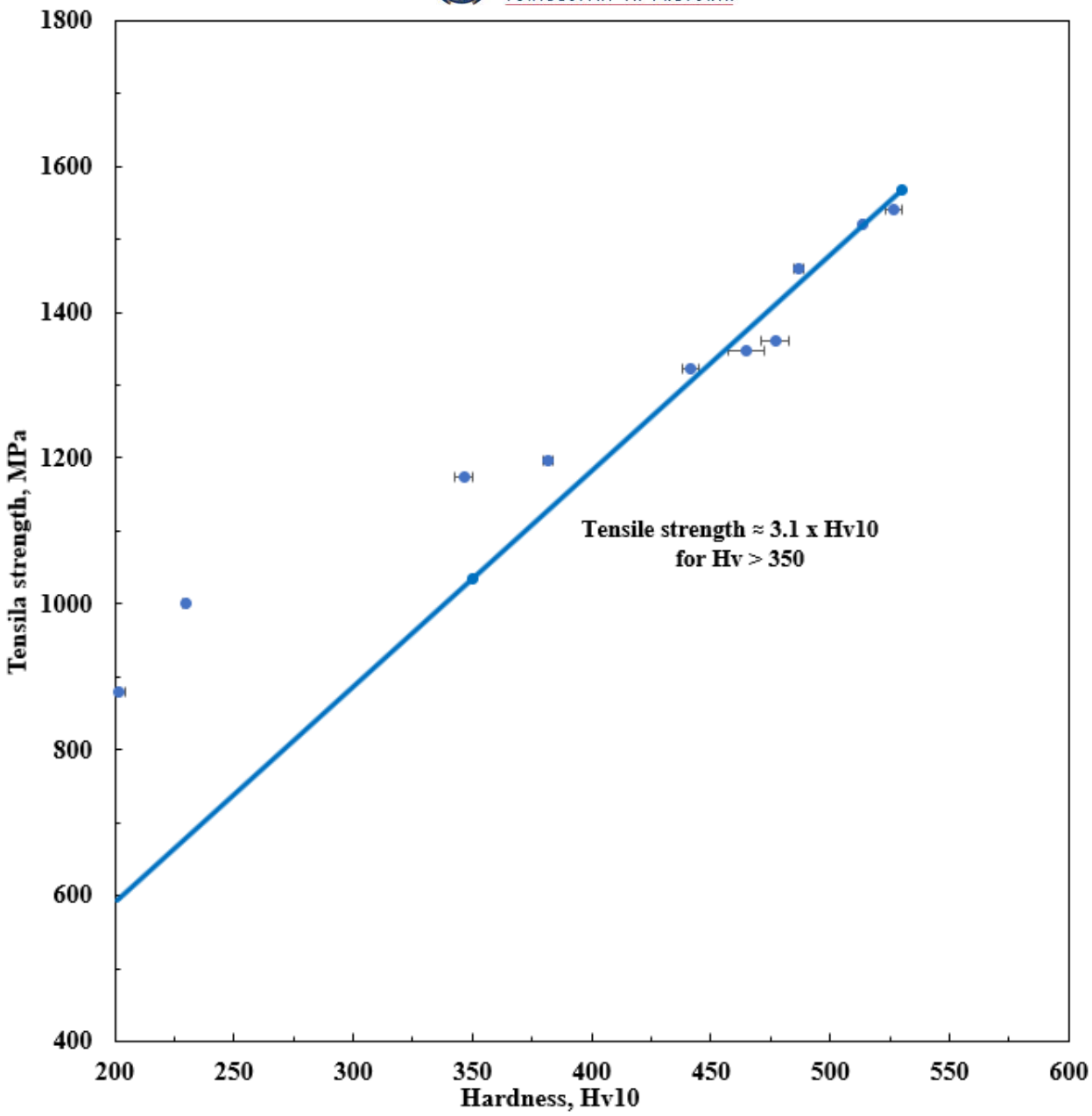


**Figure 4.44: The variation of tensile strength ($R_m$) as a function of macro Vickers hardness ($Hv_{10}$) after cold rolling at room temperature for alloy A tested at an initial strain rate of 6.67 x $10^{-4}$ $s^{-1}$**

The ratio was calculated to be approximately 3.1 as shown in Figure 4.44, for values of Hv > 350. At lower levels of deformation, the ratio of tensile strength to hardness was found to be as high as 4.0, as could be seen by direct division of tensile strength and hardness in Figure 4.43. The hardness indentation is typically related to flow stress at 8% tensile strain [168]. A rapid martensitic transformation during tensile deformation was observed for materials deformed below 20 % cold rolling with uniform strain approximating as high as 40%. This means the

measurement of tensile strength at high strain (with higher percentage of martensite) and hardness determination at low strain, indentation strain of as low as 8% and hence lower amount of martensite would give a huge deviation from a ratio of 3.1 for the tested metastable austenitic steel. The ratio of tensile strength to Vickers hardness is higher than 3 in the early stages of deformation due to large difference of percentage of martensite induced between 8% tensile strain corresponding to Vickers hardness indentation and maximum uniform strain corresponding to tensile strength. The maximum uniform strain decreases from 40% (as-received sample) to below 10% (for samples cold rolled to at least 30%) as shown in Figure 4.38. This suggests that the flow stress caused by tensile strain due to hardness indentation approximates a third of ultimate tensile strength that could be obtained during tensile deformation.

The stipulated hardness requirement of 36 $HR_C$ is equivalent to 342 $H_v$ for comparison purposes. For hardness not to exceed 342 $H_v$, the limiting final temper rolling at 30 °C to avoid exceeding the maximum hardness was established as 17.5%.

Figure 4.45 shows the variation of macro Vickers hardness ($Hv_{10}$) and tensile strength ($R_m$) as a function of percentage of strain induced martensite at room temperature for alloy A tested at an initial strain rate of $6.67 \times 10^{-4}$ $s^{-1}$. The increase in hardness is attributed to the increase in strain induced martensite with plastic deformation.

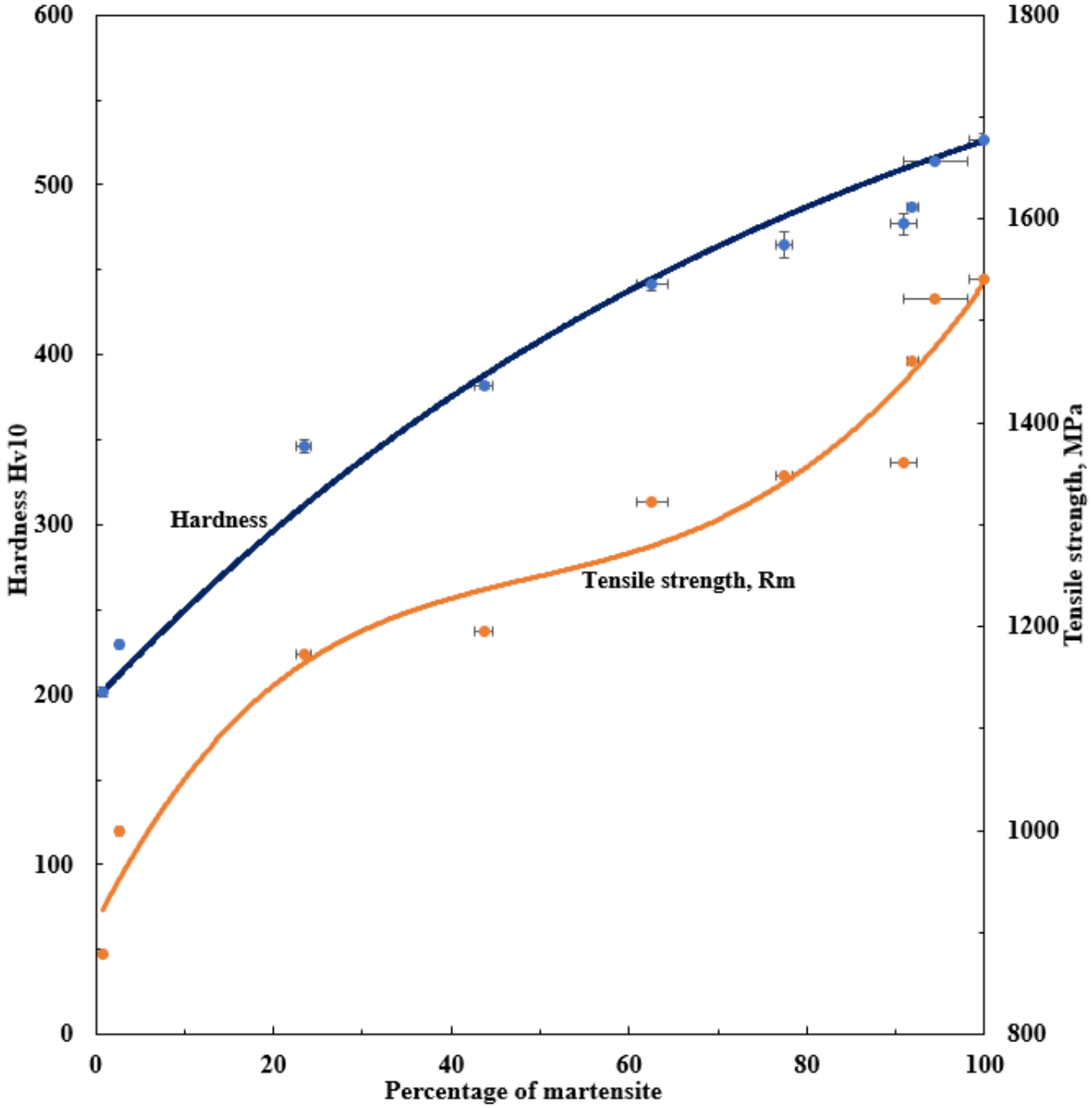


**Figure 4.45: The variation of macro Vickers hardness ($Hv_{10}$) and tensile strength ($R_m$) as a function of percentage of martensite at room temperature for alloy A tested at an initial strain rate of 6.67 x $10^{-4}$ $s^{-1}$.**

The different degree of prior cold rolling had resulted in different amounts of strain induced α′-martensite contents. The percentage of prior cold rolling at room temperature indicates the initial amount of strain-induced α′-martensite contents, with the higher the percentage of prior cold rolling the higher the initial amount of strain induced α′-martensite as shown in Figure 4.32. Figure 4.46 shows the hardening sigmoidal curves as a function of

percentage of prior cold rolling. The Figure 4.46 shows the result of sigmoidal fits to the experimental tensile data obtained in Figure 4.37 on a log-log plot of true stress-strain, for true strain values corresponding to plastic deformation.

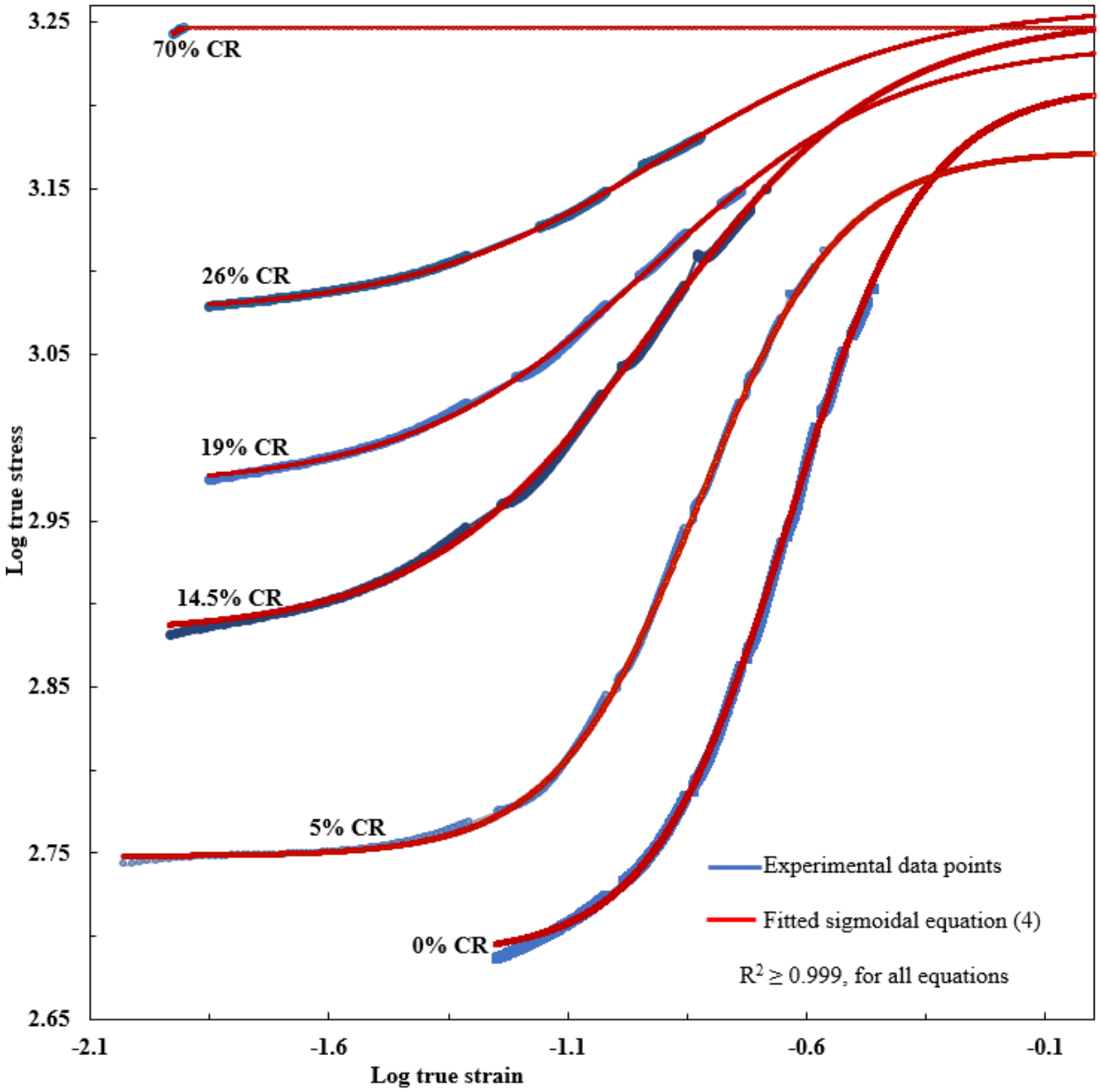


**Figure 4.46: The log-log plot of the tensile true stress-strain curves at 30 °C, after various amounts of prior cold rolling showing sigmoidal flow stress behavior for alloy A tested at an initial strain rate of 6.67 x $10^{-4}$ $s^{-1}$**

Similar to that done in Figure 4.17, fitted sigmoidal curves through the experimental data were extended up to the true strain levels of 1.0, to arrive at estimates of the strength coefficient,

K. The strength coefficient, K was found to be in the range of 1500 MPa ~ 1780 MPa, as calculated from the convergence of sigmoidal hardening curves at log stress of ~ 3.25 (at log true strain of 0). The tensile testing was done with interruption at every 5% engineering strain to allow Ferritescope measurements to be taken as well as to prevent the adiabatic heating so as the deformation temperature remains close to 30 °C. A small portion of the data which corresponds to unloading (removal of stress) and loading to the new yield point were removed on each interruption cycle during tensile deformation to develop a smooth curve in order to derive a continuous constitutive equation. The range of strength coefficients determined in this fashion was found to be in agreement with the true strength coefficient (value of 1715 MPa) determined by cold rolling to 63.2% (which is equivalent to the compressive true strain of 1 ≡ log true strain of 0) and tensile testing thereafter.

Figure 4.47 shows the variation of the instantaneous strain hardening exponent, $n_i$ determined in tension as a function of true strain (in the sigmoidal behaviour region, shown in Figure 4.46) and percentage of prior cold rolling. The instantaneous strain hardening exponent, $n_i$ was calculated by the instantaneous derivative of the log-log plot of equation (4.8), which was used to describe the mathematical relationship of the data shown in Figure 4.46.

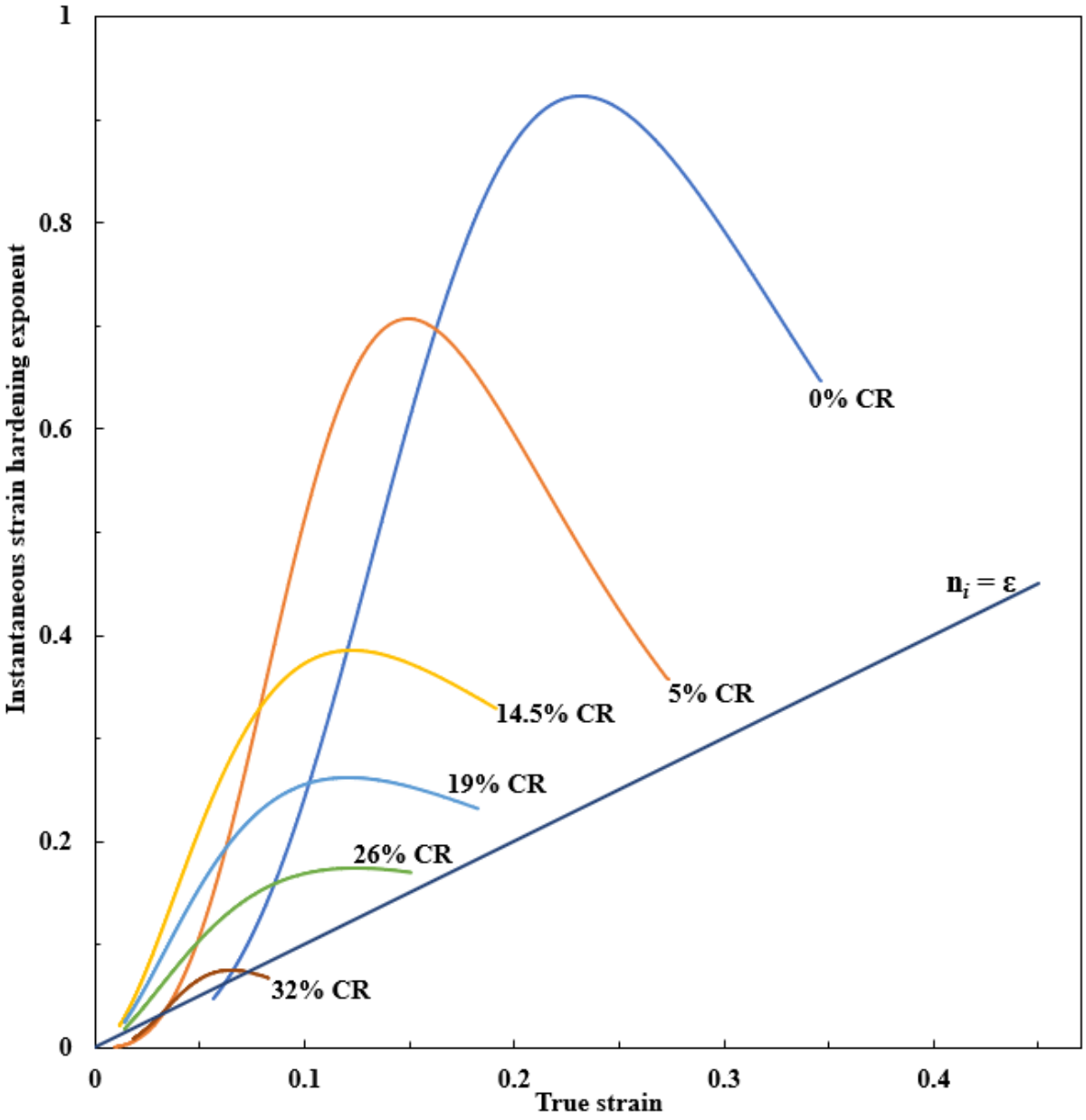


**Figure 4.47: Variation of instantaneous strain hardening exponent, $n_i$ as a function of thickness reduction at room temperature for alloy A tested at an initial strain rate of 6.67 x $10^{-4}$ $s^{-1}$**

At low levels of applied strain the instantaneous strain hardening exponent increases rapidly with increasing strain up to a peak value, after which it again decreases rapidly, in a fashion similar to the instantaneous gradient of martensitic transformation as a function of strain ($dV\alpha'/d\varepsilon$) (see Figure 4.35), which increased to a maximum rapidly and thereafter decreases to zero martensitic transformation. The rapid decrease in strain hardening rate after reaching a peak is attributed to suppressed martensitic transformation as the saturation value of martensite

content is approached during deformation. Comparing Figure 4.35 and Figure 4.47, the peak value for martensitic transformation was reached at lower strains than the peak values of the instantaneous work hardening rate, for samples with prior cold rolling. The results clearly indicate that the work hardening behaviour of AISI 301LN steel is controlled by the formation of strain induced α′-martensite [128]. It is evident that martensitic transformation controls the hardening rate as was observed before. Figure 4.48 shows the interaction of the work hardening rate (dσ/dε) as a function of strain after various levels of prior cold rolling. The curves were obtained by differentiating the flow stress-strain curves shown in Figure 4.46.

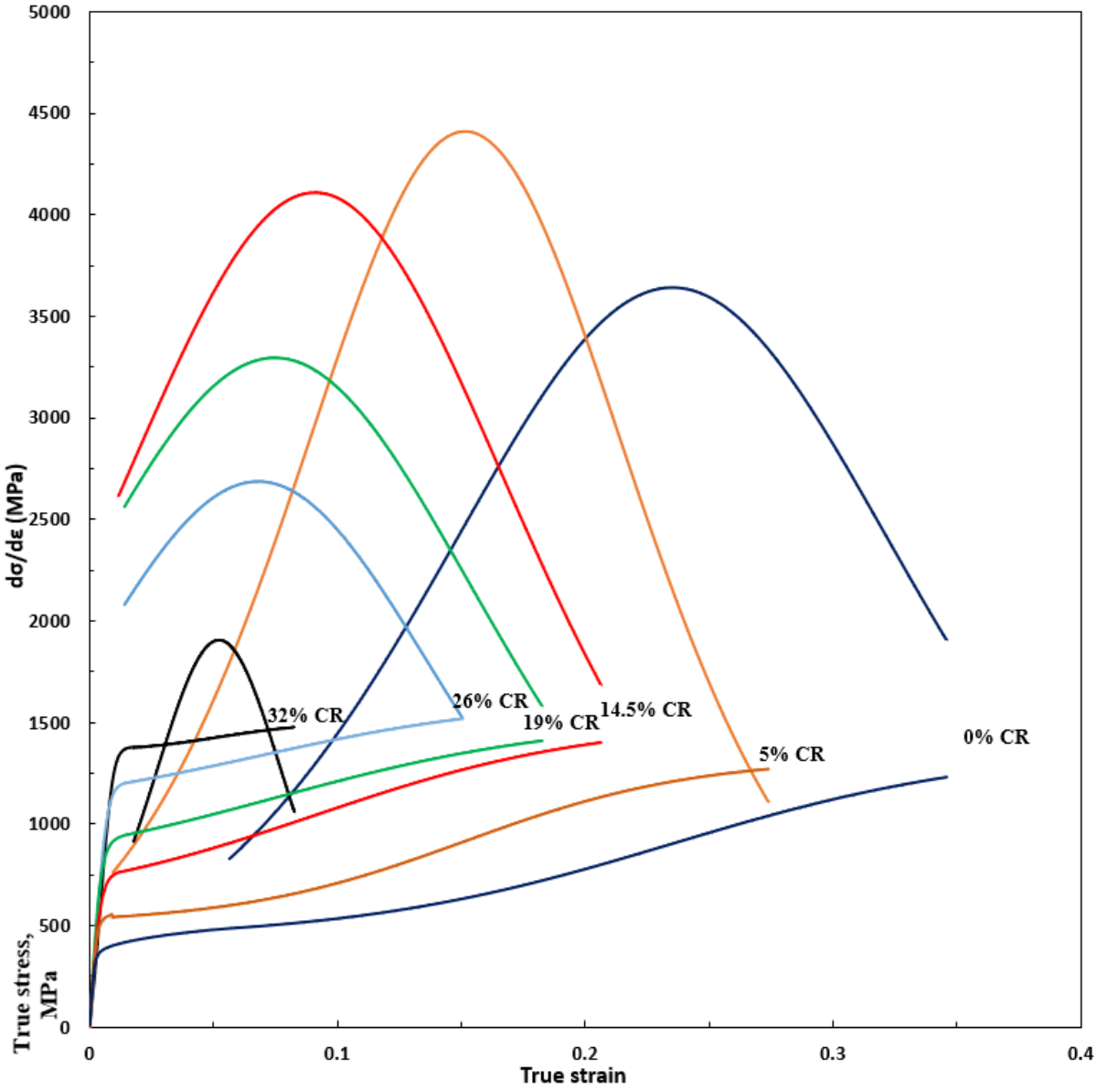


**Figure 4.48: True stress and work hardening rate as a function of true strain after different levels of prior cold rolling**

Distinct peaks of the work hardening rate curves correspond to the strain at which the maximum instantaneous work hardening rate occurs. The peak work hardening rate values decreases continually as a function of prior cold rolling, beyond 5 %. This is attributed to the decrease in α′-martensitic transformation rate at higher percentage of prior cold rolling as explained before. At higher percentage of prior cold rolling, the distinct decreased α′-martensitic transformation peaks were shifted to the lower strain values and becomes smaller until they eventually disappear with increasing percentage of prior cold rolling. Figure 4.49 shows the work hardening curves as a function of true stress obtained under uniaxial tensile tests after various levels of prior cold rolling.

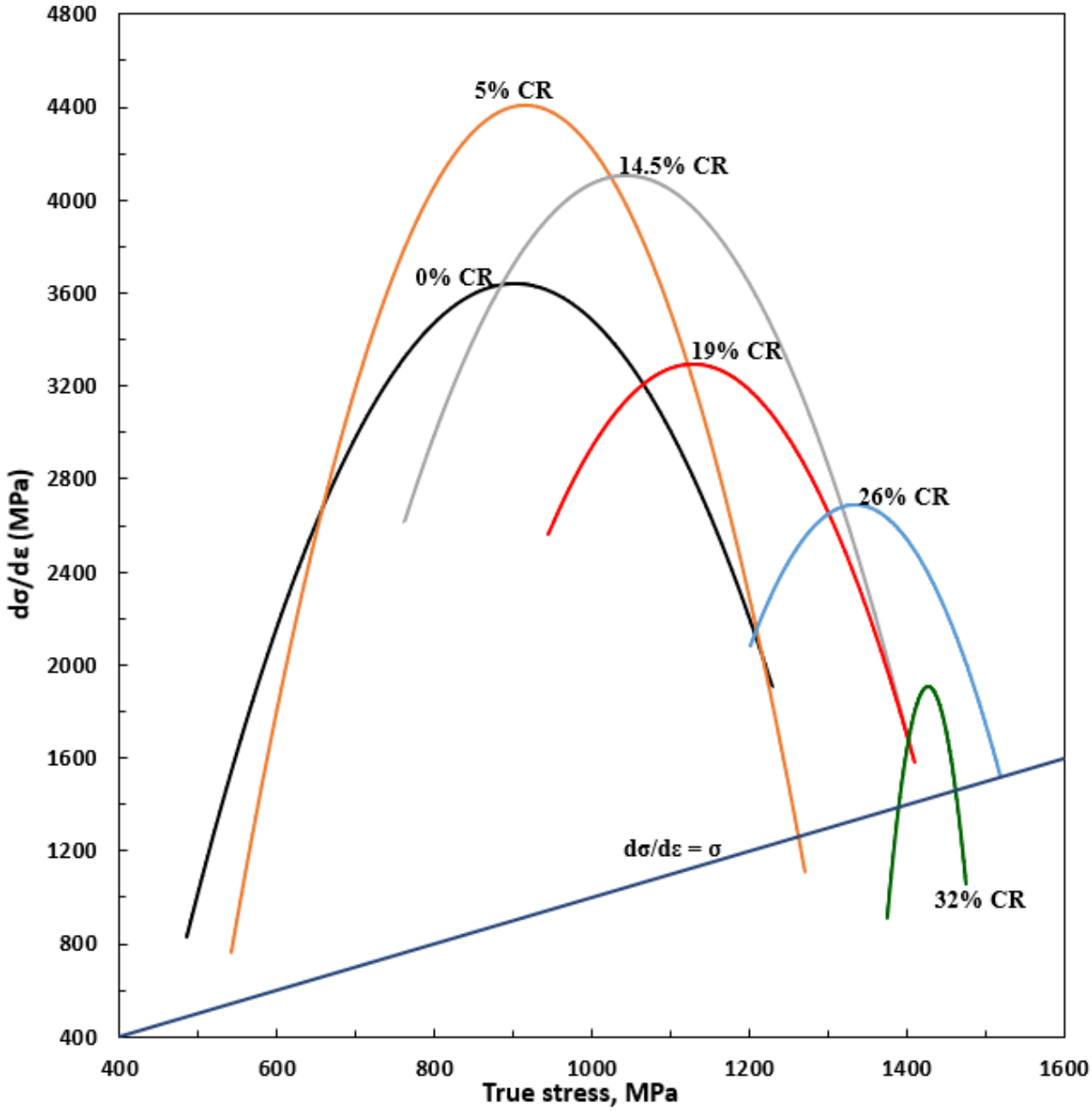


**Figure 4.49: True stress and work hardening rate as a function of true stress after different levels of prior cold rolling**

The straight line $(\partial\sigma/\partial\varepsilon) \leq \sigma$, which corresponds to the Considère criterion was drawn in Figure 4.49 showing the point of instability. Considère's plastic criterion is fulfilled when necking occurs where $(\partial\sigma/\partial\varepsilon) \leq \sigma$ after neglecting the elastic region. Regardless of the degree of prior cold rolling, the Considère's criterion of plastic instability was successfully observed during tensile deformation. Figure 4.50 shows the variation of peak instantaneous strain hardening exponent as a function of initial amount of strain induced α′-martensite, showing a rapid decrease in strain hardening response as the initial amount of martensite increases.

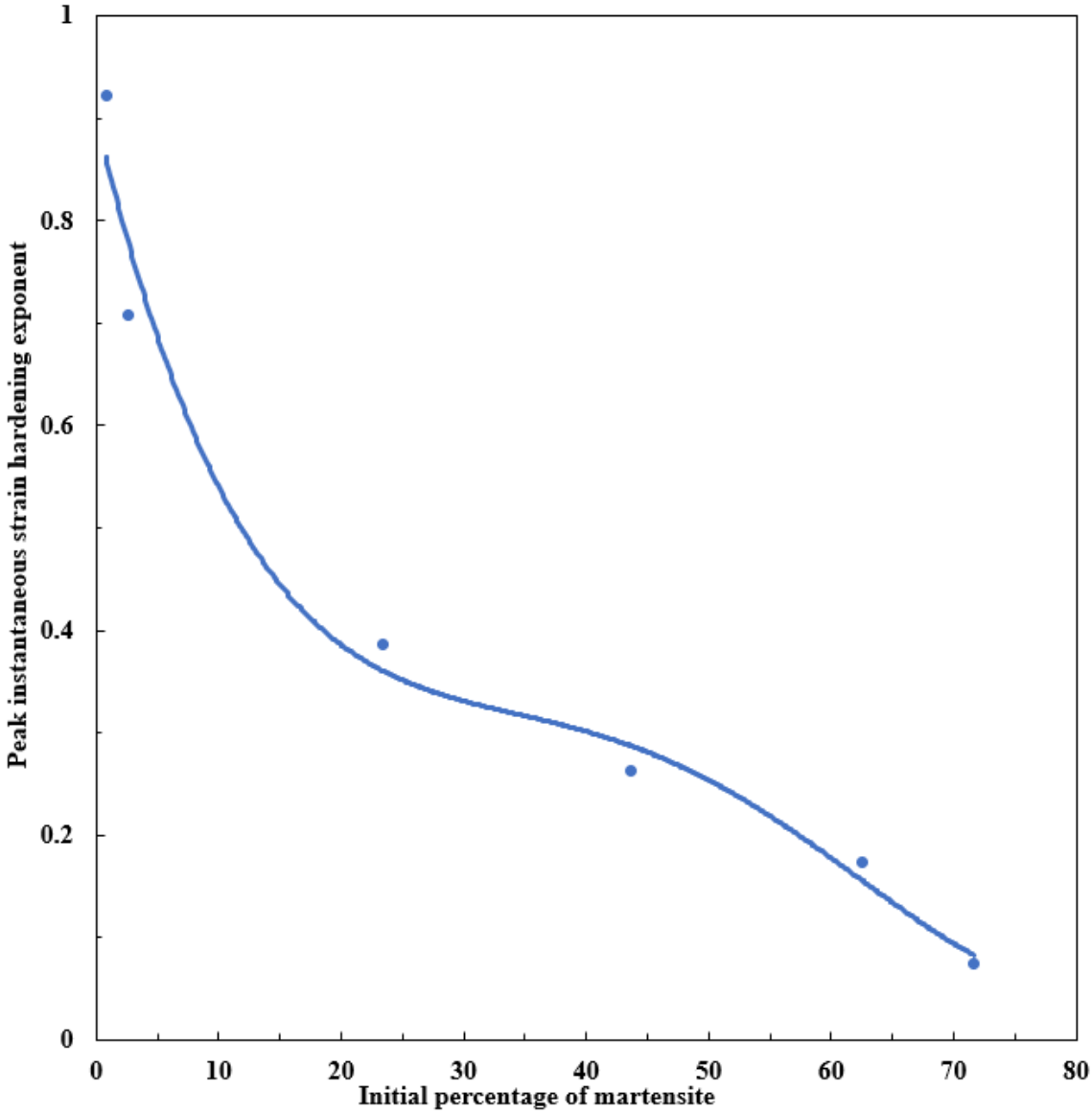


**Figure 4.50: Peak instantaneous strain hardening exponent ($n_i$) as a function of initial percentage of strain induced α′-martensite for alloy A tested at an initial strain rate of 6.67 x $10^{-4}$ $s^{-1}$**

The high strain hardening observed is due to high amounts of austenite and high strain hardening is associated with high ductility. Martensite phase is critical for strength and is required in stringent range as it has adverse impact on ductility. The volume fraction of austenite could be estimated using the equation, $V_\gamma + V_{\alpha'} = 1$. The lower the value of initial amount of austenite, after high degree of cold rolling, the lower the strain hardening response of the material. This is shown by lower peak values of instantaneous strain hardening exponent, $n_i$. Conversely, the material with higher initial amount of austenite (low percentage of initial strain-

induced martensite) exhibited higher peak values of instantaneous strain hardening exponent, $n_i$, indicating the higher strain hardening response of austenite.

### 4.2.3 Modification of developed constitutive equation for prior cold rolled samples

The developed sigmoidal equation 4.8 can be modified to describe the strain hardening behavior for materials which had undergone prior cold rolling. This is in the same way as Swift model which has an additional term, $\varepsilon_o$, which accounts for pre-strain as explained in 2.8.3 Swift model section. However, unlike Swift model, prior cold rolling in this material introduces a varied yield strength, hence the B term in the equation, which is the minimum log of true stress ($\log \sigma_{min}$) at the beginning of the sigmoidal curve varies due to prior significant martensitic transformation. Figure 4.51 shows the variation of the B term, shown in the sigmoidal equation (4.8) as a function of pre-strain by compression.

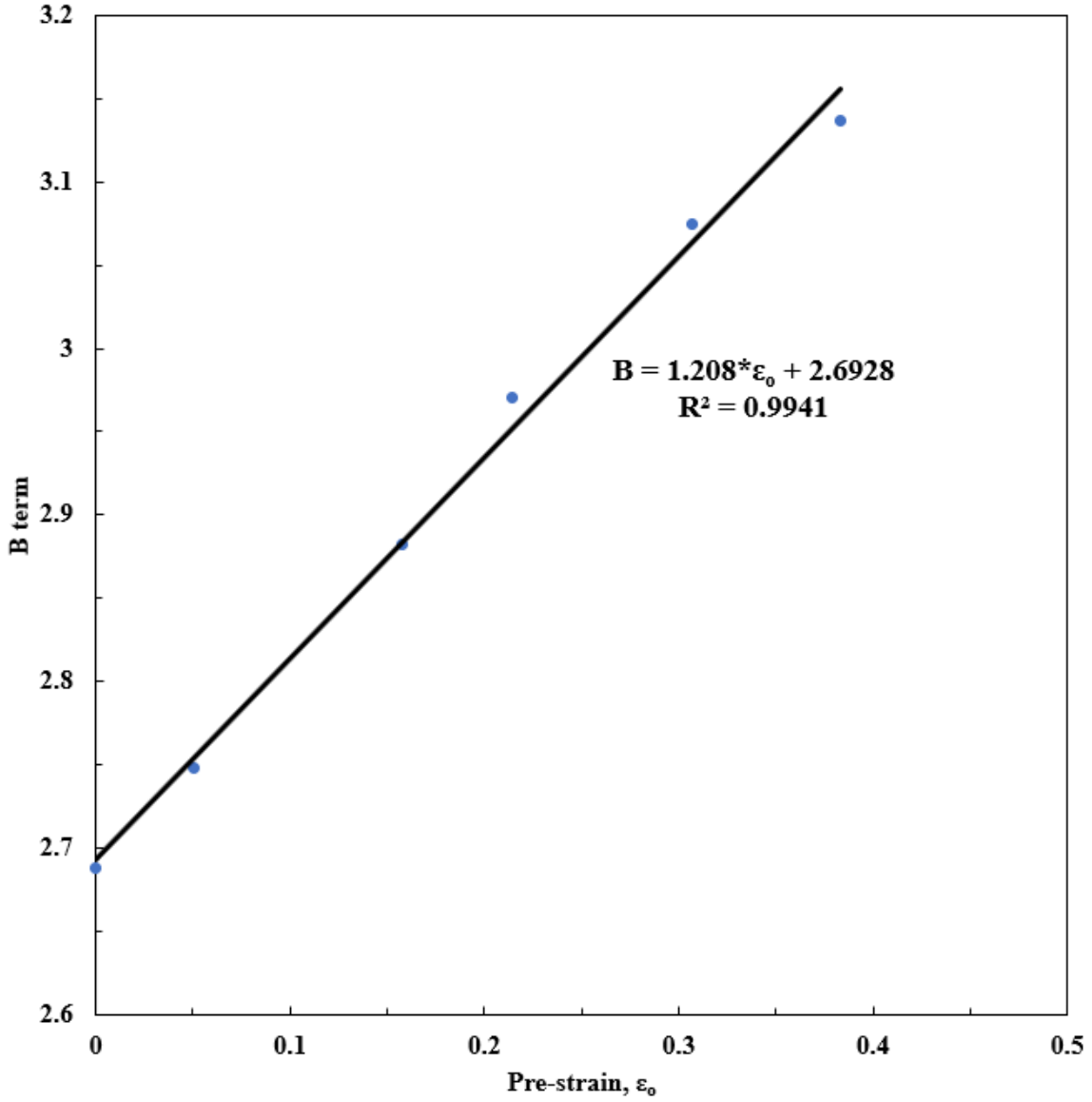


**Figure 4.51: The variation of B term in sigmoidal equation (4.8) as a function of pre-straining for alloy A tested at an initial strain rate of 6.67 x $10^{-4}$ $s^{-1}$**

Pre-strain by compression results in increase in varied yield strength, as shown in Figure 4.37. The values of the B term were determined from individual sigmoidal equations used in fitting the log-log plots of the tensile true stress-strain curves at 30 °C, after various amounts of prior cold rolling shown in Figure 4.46. The variation of the B term as a function of pre-strain was found to be linear. The A term in the sigmoidal equation (4.8) which was the maximum log of true stress (log $\sigma_{max}$) when the sigmoidal function levels off after the martensitic transformation reaches saturation point is considered 3.25. It was found that the sigmoidal hardening curves converge at approximately log stress of 3.25 (corresponding to log true strain

of 0) which corresponds to strength coefficient, K of 1766 MPa after deformation at 30 °C (refer to Figure 4.46). The $\alpha_s$ term in the sigmoidal equation 4.8 is the log strain value where there is a maximum slope of the log-log plot of the true stress-true strain curve, that is, the true strain corresponding to the maximum instantaneous strain hardening exponent. Figure 4.52 shows the variation of the true strain for maximum slope as a function of pre-strain. The true strain for maximum slope eventually becomes zero indicating no strain hardening behaviour thereafter. Maximum strain sensitivity, $\alpha_s$, corresponds to the log true strain value where there is a maximum slope of the log-log plot of the true stress-true strain curve of Figure 4.46. The variation of true strain corresponding to maximum instantaneous strain hardening exponent, ($10^{\alpha}$) as a function of pre-straining can be represented by the following equation (valid up to pre-strain, $\varepsilon_o$, of 0.46):

**True strain corresponding to maximum slope = $-404*\varepsilon_o^5 + 393*\varepsilon_o^4 - 149*\varepsilon_o^3 + 28*\varepsilon_o^2 - 2.70*\varepsilon_o +$ 0.231 …..... Equation 4.15**

with $R^2 = 1.00$.

Where:

$\varepsilon_o$ is the pre-strain introduced with prior cold rolling.

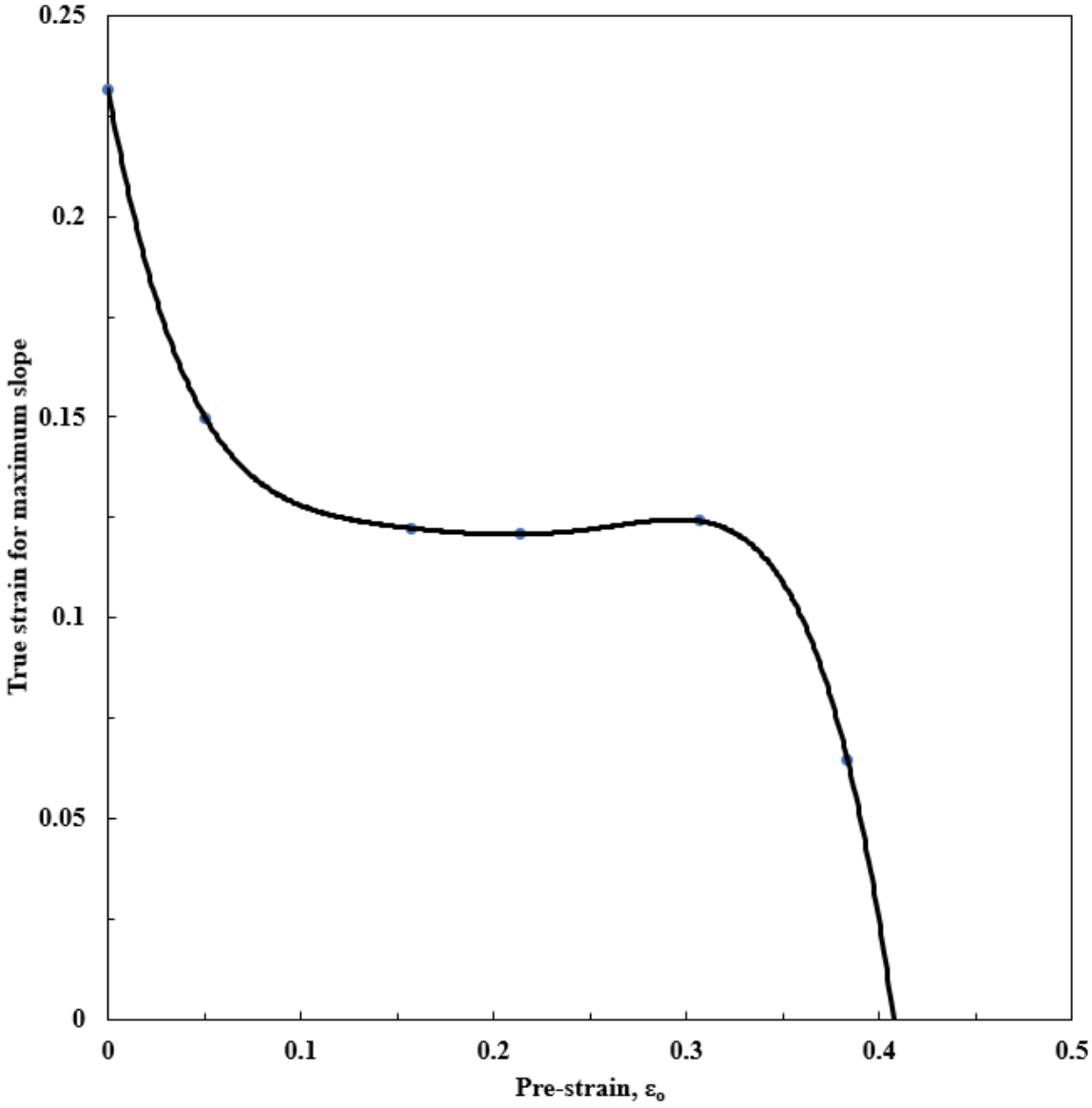


**Figure 4.52: The variation of true strain corresponding to maximum instantaneous strain hardening exponent as a function of pre-straining for alloy A tested at an initial strain rate of 6.67 x $10^{-4}$ $s^{-1}$**

Figure 4.53 shows the variation of $\beta_s$ as a function of pre-strain. $\beta_s$ is a constant derived from the nature of the log-log plots of the true stress-strain curves in Figure 4.46. The numerical value is given by, $\beta = (A - B)(4 \times n_{ipeak})^{-1}$, where $n_{ipeak}$ is the peak instantaneous strain hardening exponent, which is the instantaneous derivative of the sigmoidal function as given in equation (4.8). The $\beta_s$ constant as a function of pre-straining can be represented by the following equation (valid up to pre-strain, $\varepsilon_o$, of 0.46):

$$\beta_s = -739.72*\varepsilon_o^5 + 691.87*\varepsilon_o^4 - 235.99*\varepsilon_o^3 + 33.202*\varepsilon_o^2 - 0.9981*\varepsilon_o + 0.1418 \ldots\ldots \text{Equation 4.16}$$

with $R^2 = 1$.

Where:

$\varepsilon_o$ is the pre-strain introduced with prior cold rolling.

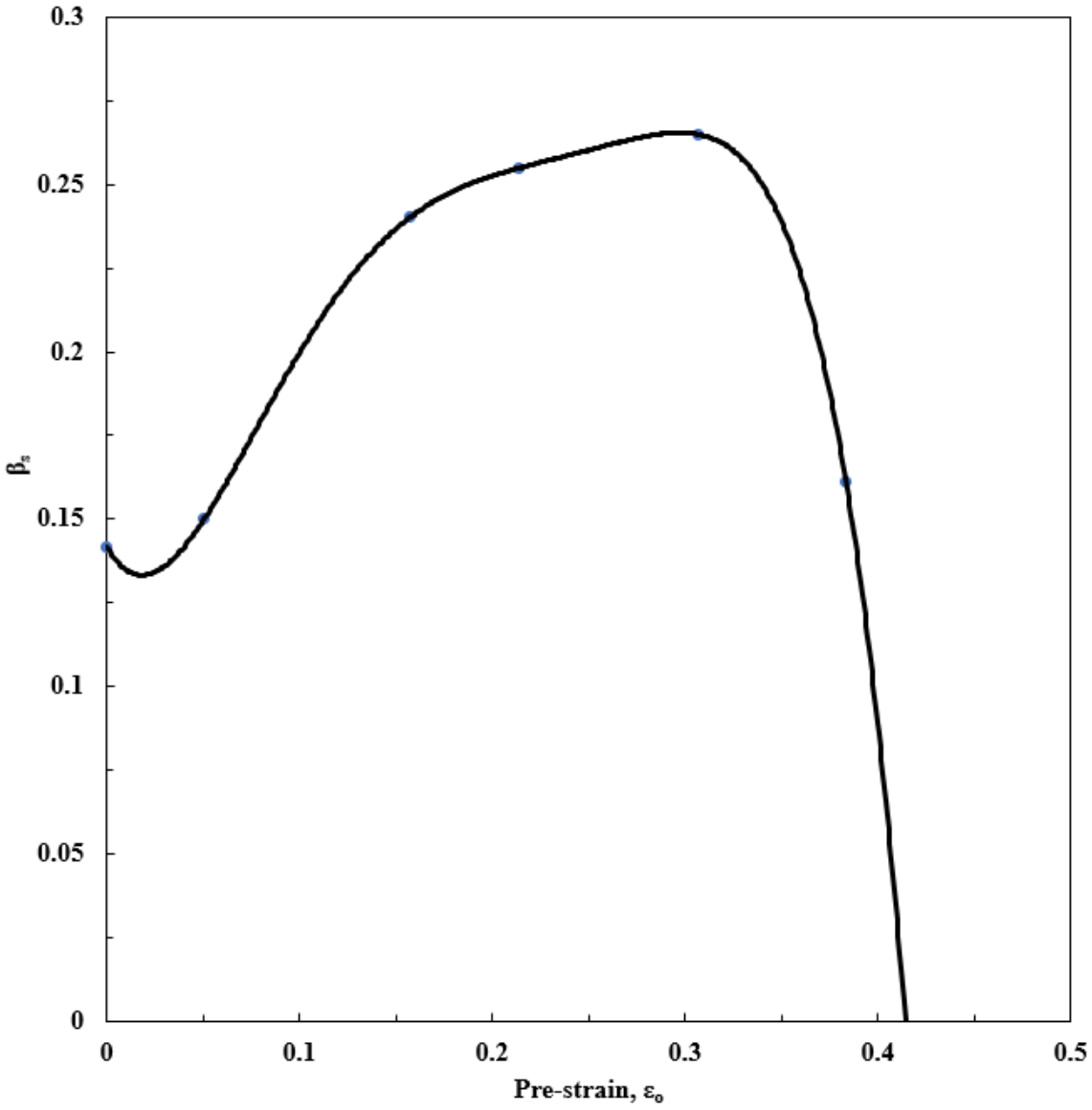


**Figure 4.53: The variation of $\beta_s$ as a function of pre-straining for alloy A tested at an initial strain rate of 6.67 x $10^{-4}$ $s^{-1}$**

The experimental strain hardening curves, with pre-straining term considered, could be accurately described by the following single modified sigmoidal equation of 4.1:

$$\log \sigma = 3.25 + (1.21*\varepsilon_o - 0.554)[1 + \exp(\log \varepsilon - \alpha_s)(\beta_s)^{-1}]]^{-1} \text{ ……..... Equation 4.17}$$

with $R^2 \geq 0.999$, for pre-strains tested.

Where:

$\sigma$ is the true stress in MPa,

$\varepsilon_o$ is the pre-strain introduced with prior cold rolling.

$\varepsilon$ is the true strain.

$\alpha_s$ is the maximum strain sensitivity which corresponds to the log true strain value where there is a maximum slope of the log-log plot of the true stress-true strain curve.

$\beta_s$ is a constant derived from the nature of the log-log plots of the true stress-strain curves. The numerical value is given by, $\beta = (3.25 - B)(4 \times n_{ipeak})^{-1}$, where $n_{ipeak}$ is the peak instantaneous strain hardening exponent, which is the instantaneous derivative of the sigmoidal function).

From equation 4.17, for the term $1.21*\varepsilon_o - 0.554$ to be equal to zero, pre-strain, $\varepsilon_o$ should be 0.46. Sigmoidal equation 4.17 then reduces to $\log \sigma = 3.25$, showing no strain hardening. This is because the value of B term would be equal to the value of A (= 3.25), which is the maximum log of true stress ($\log \sigma_{max}$) when the sigmoidal function levels off after the martensitic transformation reaches saturation point, estimated as 87% in this case at 30 °C. Therefore, the sigmoidal equation (4.17) is only valid up to pre-strain of ~ 0.46.

**Table 4.6: Constants B, $\alpha_s$ and $\beta_s$ in equation (4.17) as a function of pre-strain in the AISI 301LN steel**

| Pre-strain | | B | $\alpha_s$ | True strain | $n_{ipeak}$ | $\beta_s$ | $R^2$ |
|---|---|---|---|---|---|---|---|
| %CR | $\varepsilon_o$ | | | $10^{\alpha}$ | | | |
| 0 | 0 | 2.69 | -0.636 | 0.231 | 0.92 | 0.142 | 0.999 |
| 5 | 0.05 | 2.75 | -0.825 | 0.150 | 0.71 | 0.150 | 1.00 |
| 14.5 | 0.16 | 2.88 | -0.913 | 0.122 | 0.39 | 0.240 | 0.999 |
| 19 | 0.21 | 2.97 | -0.918 | 0.121 | 0.2 | 0.255 | 0.999 |
| 26 | 0.31 | 3.08 | -0.906 | 0.124 | 0.17 | 0.265 | 0.999 |
| 32 | 0.38 | 3.14 | -1.19 | 0.065 | 0.07 | 0.161 | 0.999 |

*%CR is the percentage of prior cold rolling.

### 4.2.4 Mechanical energy required to induce martensitic transformation in prior cold rolled samples

The mechanical energy values associated with the strain hardening of prior cold rolled samples were calculated by establishing the area below the tensile true stress-strain curves (shown in Figure 4.37, all true stress-strain curves). Figure 4.54 shows the energy absorption of the AISI 301LN prior cold rolled steel after various degree of prior cold rolling.

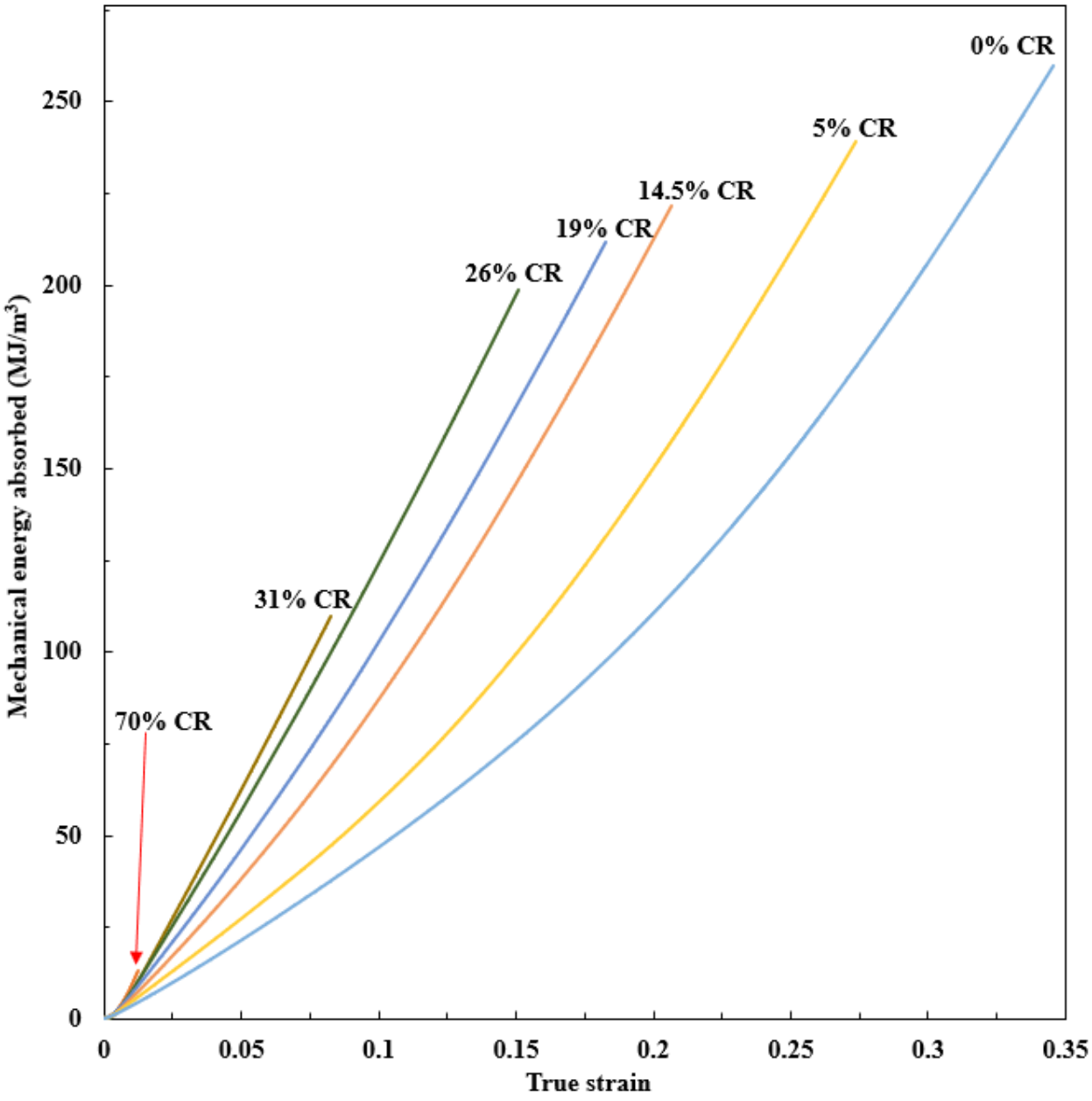


**Figure 4.54: The mechanical energy absorbed as a function of strain on prior cold rolled samples for alloy A tested at an initial strain rate of 6.67 x $10^{-4}$ $s^{-1}$**

Figure 4.54 shows a proportional relationship between the applied strain and the mechanical energy absorbed during tensile deformation at 30 °C as a function of strain. As the level of cold rolling increases, the toughness decreases to less than 10 MJ/m$^3$ (at above 70% cold rolling) due to significantly impaired strain to fracture. The reduced amount of mechanical energy that can be absorbed by the material after heavily cold deformed makes it inferior in terms of crashworthiness as the material needs to absorb significant amount of energy in the event of a collision. Figure 4.55 shows the maximum cumulative mechanical energy that can be absorbed after a certain degree of cold rolling.

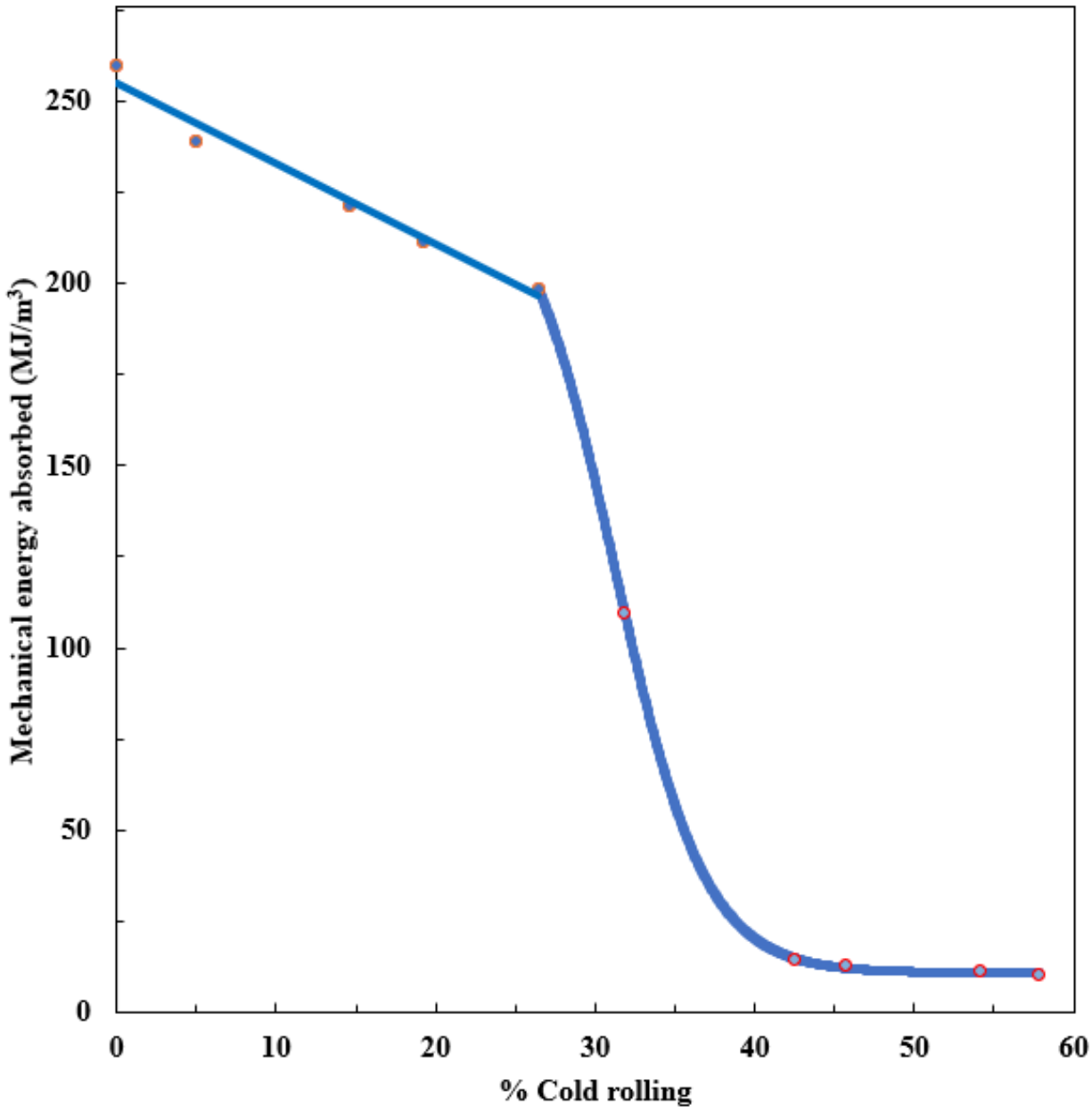


**Figure 4.55: The total mechanical energy as a function of percentage of cold rolling for alloy A**

The material with no prior cold rolling absorbs the maximum mechanical energy during tensile deformation. As the percentage of prior cold rolling increases, a decrease in mechanical energy that was absorbed by the materials was observed. This decrease in mechanical energy corresponds to the amount of energy absorbed during prior cold rolling. Therefore, the mechanical energy as a function of prior cold rolling was calculated as the difference between the mechanical energy absorbed by a material after a given degree of prior cold rolling and the mechanical energy by a material with no prior cold rolling.

There is an abrupt decrease in uniform strain after 30 % prior cold rolling (see Figure 4.38), which resulted in abrupt decrease in mechanical energy absorbed as shown in Figure 4.55. The significantly very low uniform strain after high degree of prior cold rolling, greater than 30 % had resulted in limited amount of energy absorption capability of a material. The amount of energy that the material can absorb if used in the making of crash-relevant structures of a vehicle using the ideal yield strength (750 ~ 920 MPa), tensile strength (1000 ~ 1150 MPa) and uniform strain of at least 22%, the minimum mechanical energy that the material must be able to absorb has been calculated as 193 MJ/m$^3$. This makes cold rolling of 27%, the maximum possible final temper rolling that can be applied to this material. However, other required mechanical properties such as yield strength, tensile strength, hardness, elongation to fracture may limit the range of percentage of final temper rolling that can be applied to this material as will be discussed latter in this thesis.

### 4.2.5 Microstructural analyses using cold rolled samples

Microstructural analysis was done on two samples which were cold rolled at room temperature to 10% and 20% for alloy A. The aim was to ascertain the deformation mechanisms for martensitic transformation during cold rolling. Figure 4.56 shows longitudinal cross-sectional EBSD images of samples cold rolled to (a) 10% and (b) 20% at a magnification of 1000×. The images were magnified to show some regions with ε-martensite (lime green coloured-phase) between the α′-martensite (blue coloured-phase) and austenite (red coloured-phase): The ε-martensite phase appears to be an intermediate phase during the transformation of austenite to α′-martensite as it can be seen on the edges of the α′-martensite. This could mean that the ε-martensite is first formed but soon quickly transforms to α′-martensite during further cold rolling. This is in good agreement with the results presented earlier in this work where volume fraction of ε-martensite increased to a maximum during cold rolling and then decreases as the volume

fraction of strain-induced α′-martensite reaches saturation value (refer to Figure 4.32). This makes ε-martensite as the most potent nucleation site for α′-martensite [46], [82].

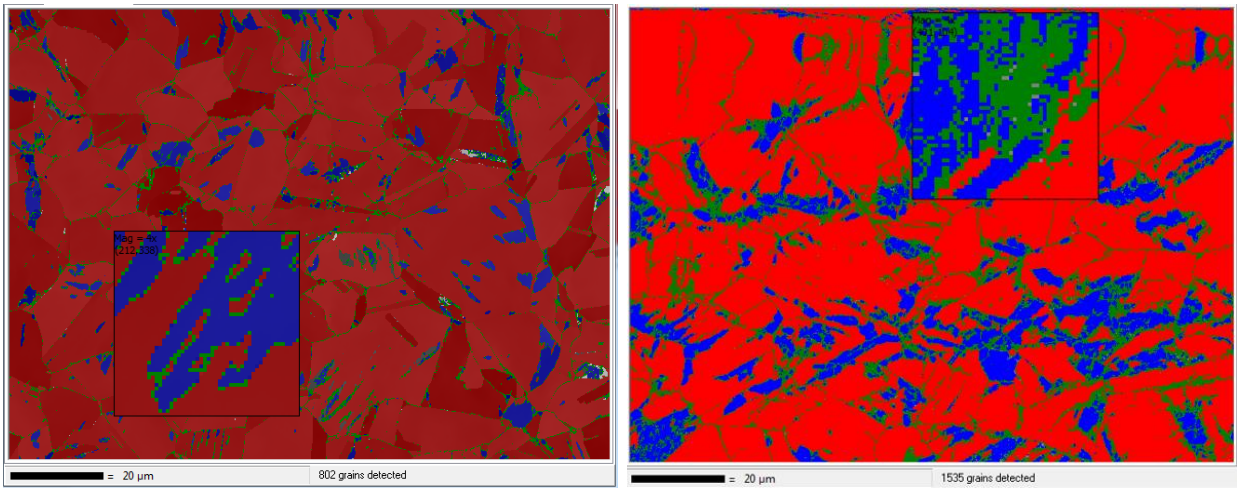


**(a)** **(b)**

**Figure 4.56: Longitudinal cross-sectional EBSD images of samples cold rolled to (a) 10% and (b) 20%. The lime green coloured-phase is ε-martensite between the blue coloured-phase (α′-martensite) and red coloured-phase (austenite)**

### 4.2.6 Uniaxial tensile deformation vs cold rolling at 30 °C

Figure 4.57 shows the variation of percentage of martensite induced as a function of true strain during uniaxial tensile deformation and cold rolling at 30 °C for alloy A. It can be shown that higher amount of strain-induced martensite at a given strain was obtained through tensile deformation than cold rolling at the same deformation temperature. During tensile deformation, strain is uniformly distributed whilst during cold rolling there is friction-induced redundant strain near the surfaces. The redundant strain causes variability of the amount of strain-induced martensite within the sample. Due to high penetration of Ferritescope instrument, the overall percentage of martensite determined during tensile deformation is higher than the overall percentage of martensite determined during cold rolling. The friction-induced redundant strain near the surface gives rise to the nucleation of martensite which then propagates towards the centre during further cold rolling.

The austenite to martensite transformation involves a change in volume, if the hydrostatic stress is compressive, transformation is retarded as volume expansion is inhibited, and transformation is enhanced if it is tensile. Adiabatic heating is higher during cold rolling as compared to tensile deformation due to friction and redundant strain which further retards the

martensitic transformation at a given deformation temperature. The deformation behavior during cold rolling results in texture differences between surface and bulk material. Due to friction near the surface, the texture is best described as a shear deformation whilst in the bulk material, the texture is better described by a uniaxial compression.

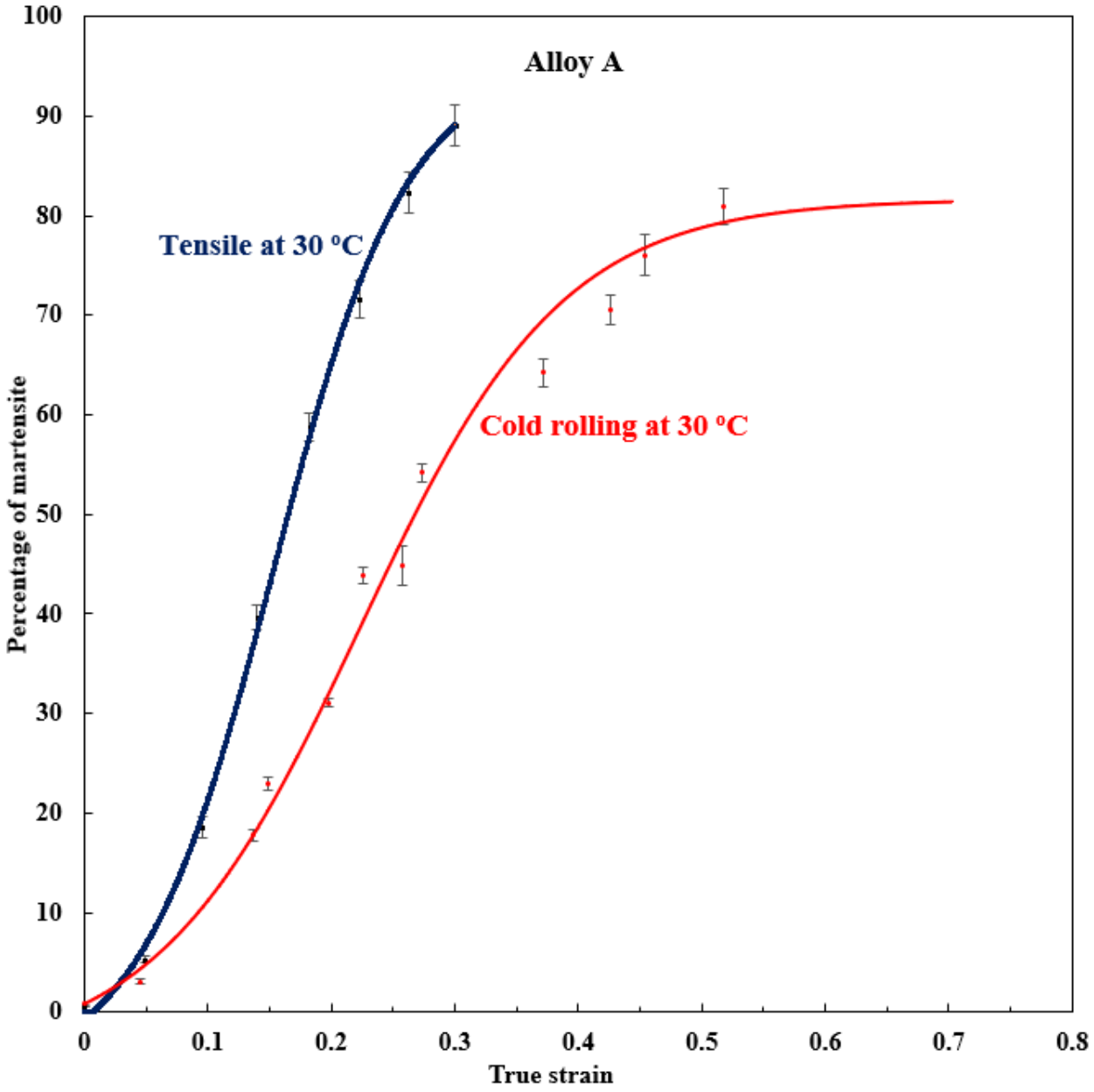


**Figure 4.57: The variation of percentage of martensite induced as a function of true strain, for cold rolling and tensile deformation at 30 °C for alloy A**

Figure 4.58 shows the corresponding rate of α′-martensitic transformation as a function of true strain during uniaxial tensile deformation and cold rolling at 30 °C for alloy A. The rate of

α′-martensitic transformation is higher during uniaxial tensile deformation than cold rolling. The saturated maximum percentage of martensite which can be induced at 30 °C was found to be the same during uniaxial tensile deformation and cold rolling. This explains that the maximum percentage of martensite which can be induced is dependent on deformation temperature.

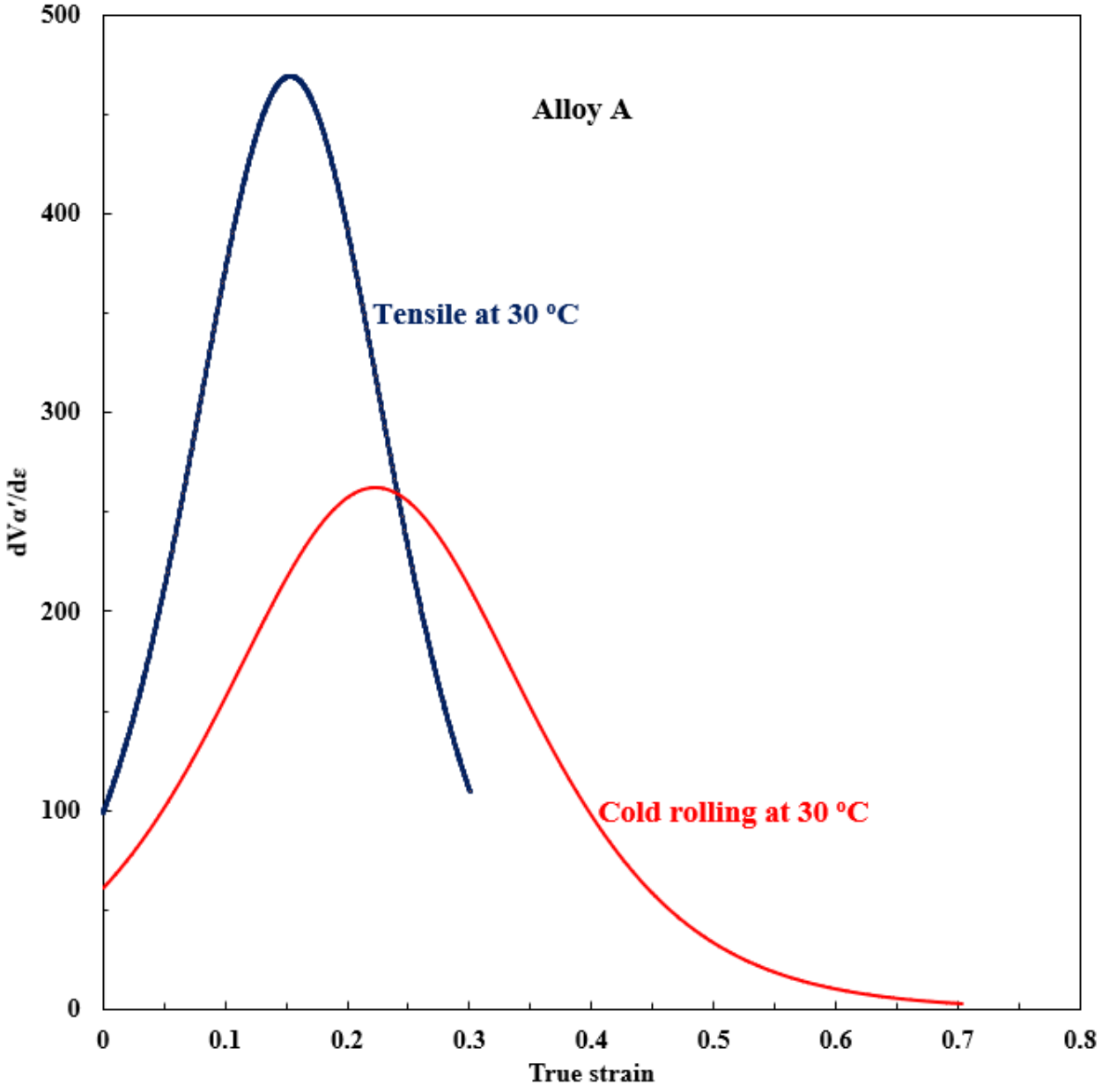


**Figure 4.58: The variation of rate of α′-Martensite transformation, as a function of true strain, for cold rolling and tensile deformation at 30 °C for alloy A**

The whole analysis in Figure 4.57 and Figure 4.58 for alloy A was repeated using alloy B and the results are as shown in Figure 4.59 and Figure 4.60.

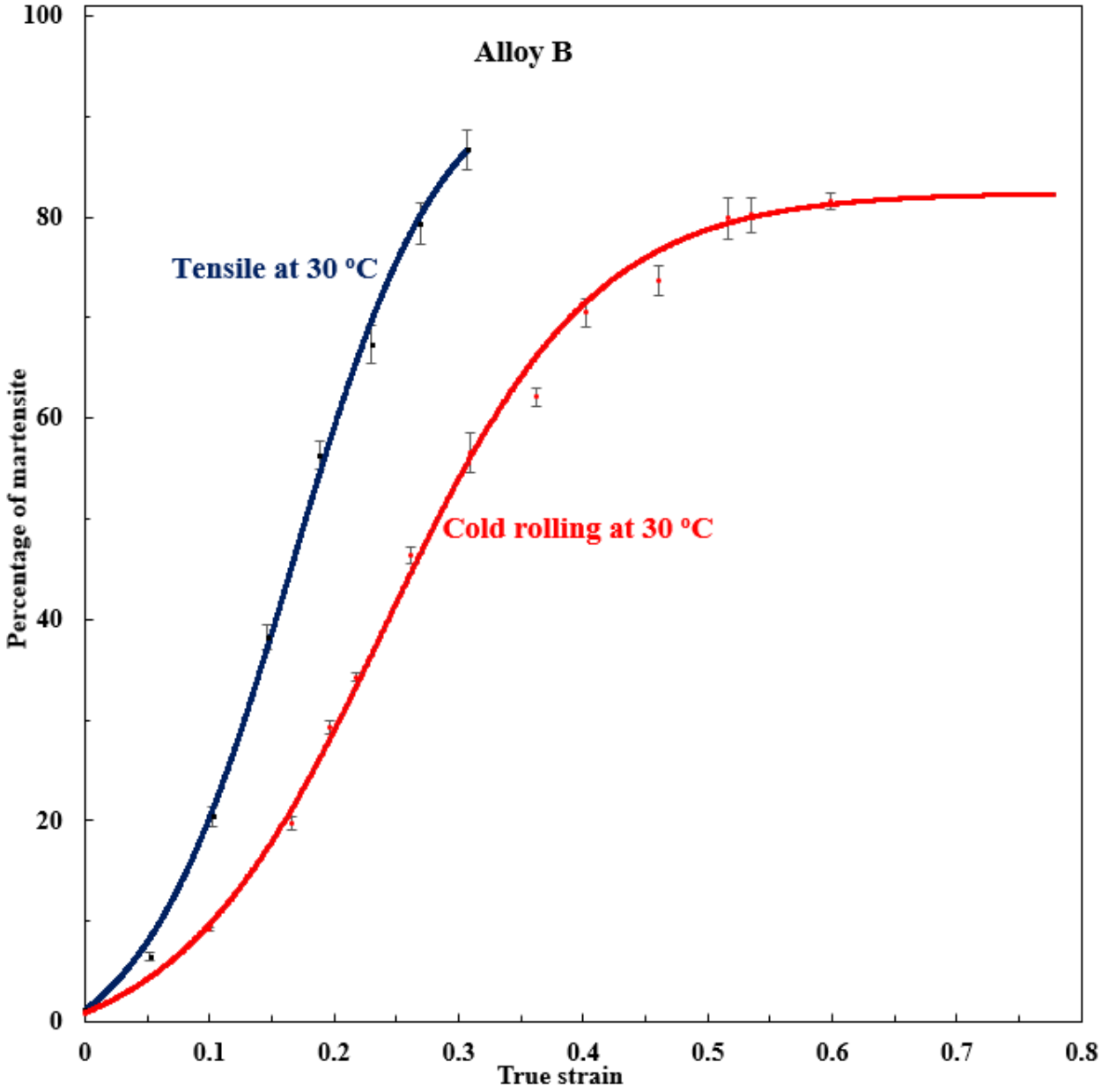


**Figure 4.59: The variation of percentage of martensite induced as a function of true strain, for cold rolling and tensile deformation at 30 °C for alloy B**

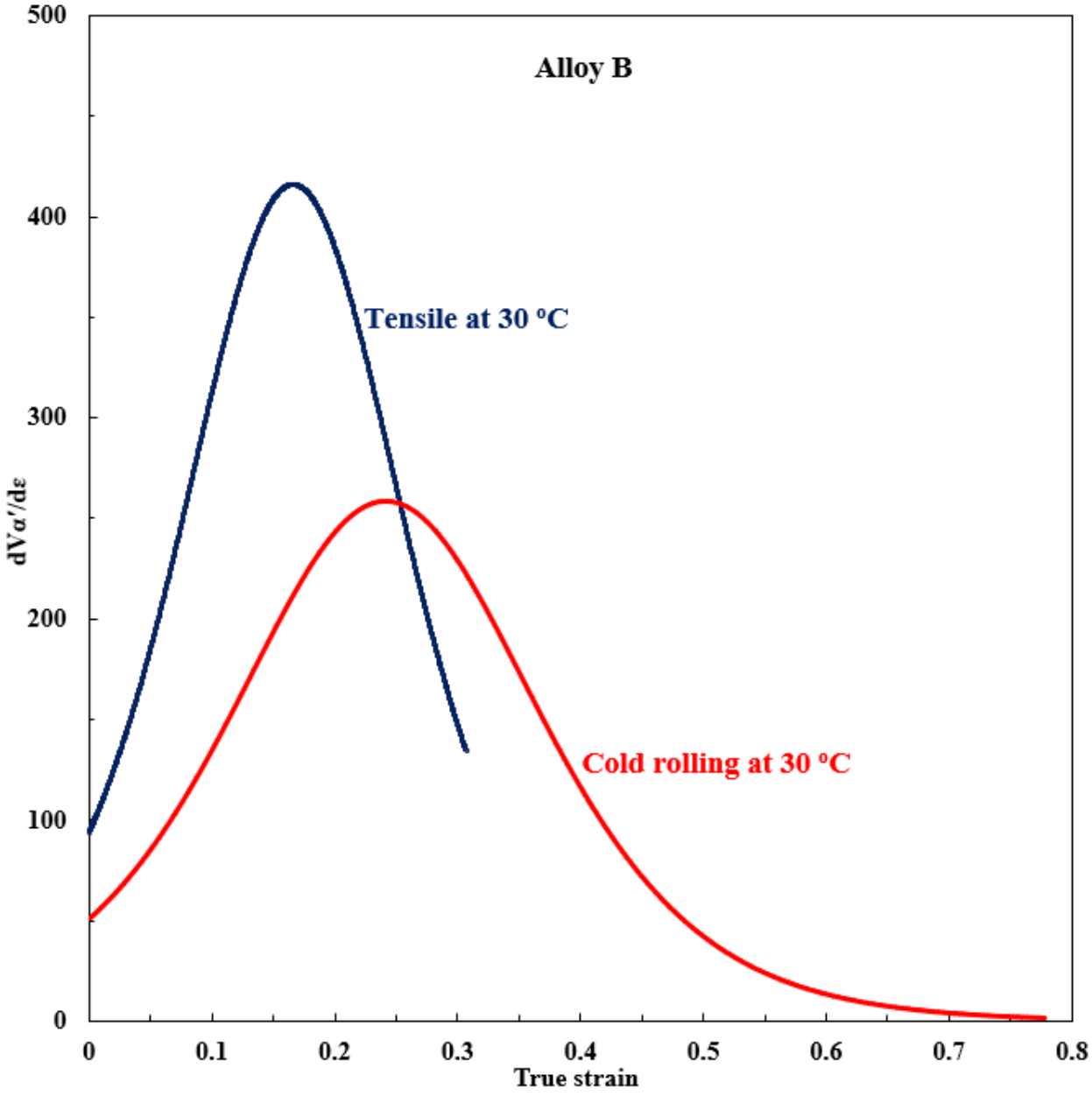


**Figure 4.60: The variation of percentage of rate of α′-Martensite transformation, as a function of true strain, for cold rolling and tensile deformation at 30 °C for alloy B**

### 4.3 Strain rate

The influence of strain rate on the martensitic transformation was investigated using Gleeble 1500 Thermomechanical Simulator. A series of interrupted tensile tests were done in the Gleeble 1500 Thermomechanical Simulator at a fixed initial temperature of 30 °C at varying strain rates from 1.67 x $10^{-3}$ $s^{-1}$ to 1.7 $s^{-1}$. Engineering strain was calculated by dividing the crosshead displacement by the original length of the sample whereas engineering stress was

determined by dividing the force by the cross-sectional area. Engineering strain was converted to true strain as before. Figure 4.61 shows the percentage of α′-martensite induced as a function of strain at various strain rates at 30 °C during tensile deformation using Gleeble 1500 Thermomechanical Simulator. Interruption was done at 5% strain intervals allowing an indication of the percentage of magnetic strain-induced α′-martensite was determined using a Ferritescope instrument (Helmut Fisher GmbH, model MP3B) at 5% strain intervals and corrected to actual α′-martensite content by the previously determined correlation factor of 1.7 as described in Chapter 3. Seven readings were taken on each sample at different points within the gauge length on the surface. The magnetic measurements on the specimens were taken at different strains under unloaded conditions. The mean and standard deviations were calculated. A thermocouple was attached to the sample within the gauge length to measure the temperature increase as a result of cold work performed and a temperature increase of ~ 10 °C was observed within the uniform strain at all strain rates tested. After each interruption, enough time was given for the material to stabilize at 30 °C before another 5% strain applied.

The same form of sigmoidal function (sigmoidal equation 4.1) was used to describe the martensitic transformation as a function of strain. Figure 4.61 shows that high strain rates do not have much effect on the volume fraction and rate of α′-martensite transformation if there is control on temperature increase due to adiabatic heating. The indirect effect of high strain rates is the increase in temperature due to adiabatic heating. It has been shown that a temperature increase can result in reduction in chemical driving force for martensitic transformation [126].

Figure 4.62 shows the rate of $\gamma \rightarrow \alpha'$ strain–induced martensitic transformation as a function of strain, $(dV\alpha'/d\varepsilon)$ at various strain rates tested at 30 °C. These values denote the slopes of the curves in Figure 4.61 as a function of strain. The instantaneous gradient increased to a maximum and thereafter decreases to zero martensitic transformation. The strain at which the peak martensitic transformation occurs appears to be varying slightly in the strain rates range tested as shown in Figure 4.62.

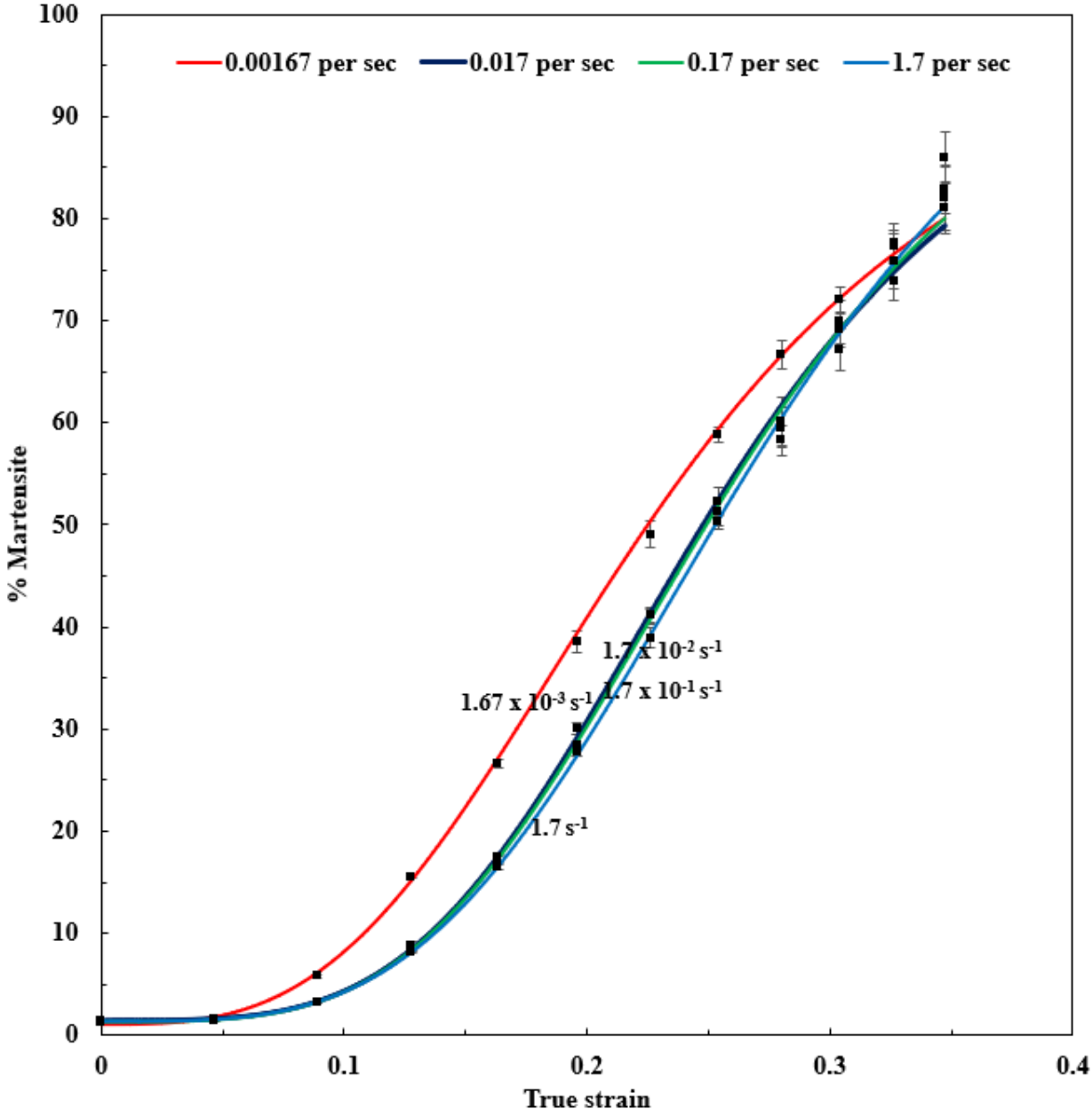


**Figure 4.61: Percentage of α′-martensite induced as a function of strain for alloy A at various strain rates at 30 °C**

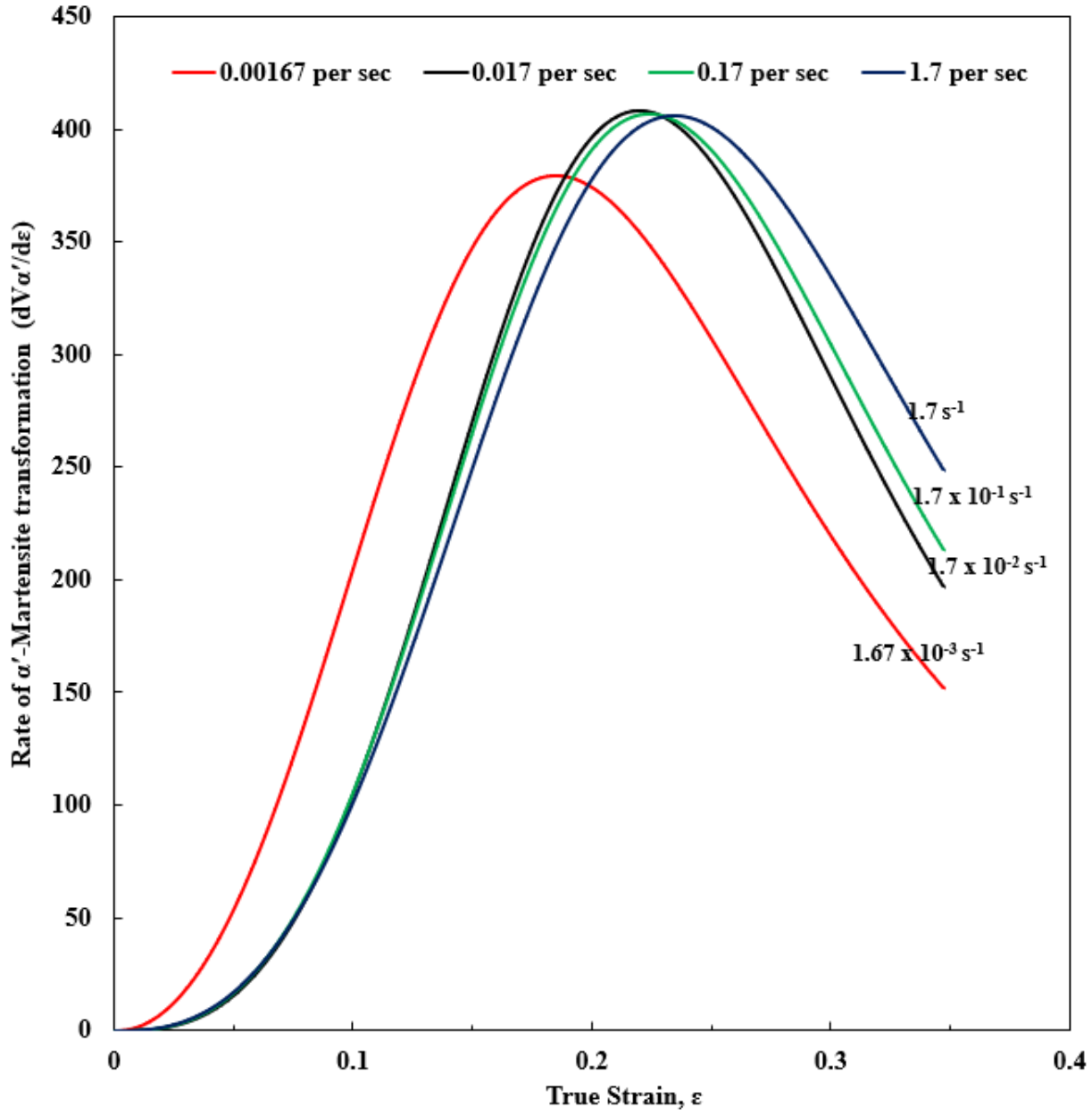


**Figure 4.62: Rate of α′-Martensite transformation as a function of strain for alloy A at various strain rates at 30 °C**

## 4.4 Alloy chemistry

### 4.4.1 Comparison using cold rolling techniques

Three different industrially produced heats (Alloy A, Alloy B and Alloy C) were cold rolled at room temperature. The slightly varied chemistry in these alloys within AISI 301LN was not by design one might be wondering why a systematic alloying was not done but rather as produced by the stainless-steel company. An investigation on whether slight variation of

chemistry within the AISI 301LN grade has varied effect on the martensitic transformation as a function of percentage of cold rolling was investigated using cold rolling techniques. There was a need to investigate whether slight variation of chemistry within the same AISI 301LN grade has a major effect on the martensitic transformation during cold working due to inconsistency mechanical properties. Figure 4.63 shows the percentage of α′-martensite induced as a function of cold rolling at room temperature. An indication of the percentage of magnetic strain-induced α′-martensite was determined using a Ferritescope instrument (Helmut Fisher GmbH, model MP3B) after small thickness reduction intervals and corrected to actual α′-martensite content by the previously determined correlation factor of 1.62 as described in Chapter 3.3. Seven readings were taken on each sample at different points on the surface. The mean and standard deviations were calculated. Samples were water cooled after each interpass. The same form of sigmoidal function (sigmoidal equation 4.1) was used to describe the martensitic transformation as a function of percentage of cold rolling with $R^2 \geq 0.994$. Figure 4.64 shows the corresponding rate of $\gamma \rightarrow \alpha'$ strain–induced martensitic transformation as a function of thickness reduction for the three different heats of AISI 301LN. The instantaneous gradient increased to a maximum and thereafter decreases to zero martensitic transformation.

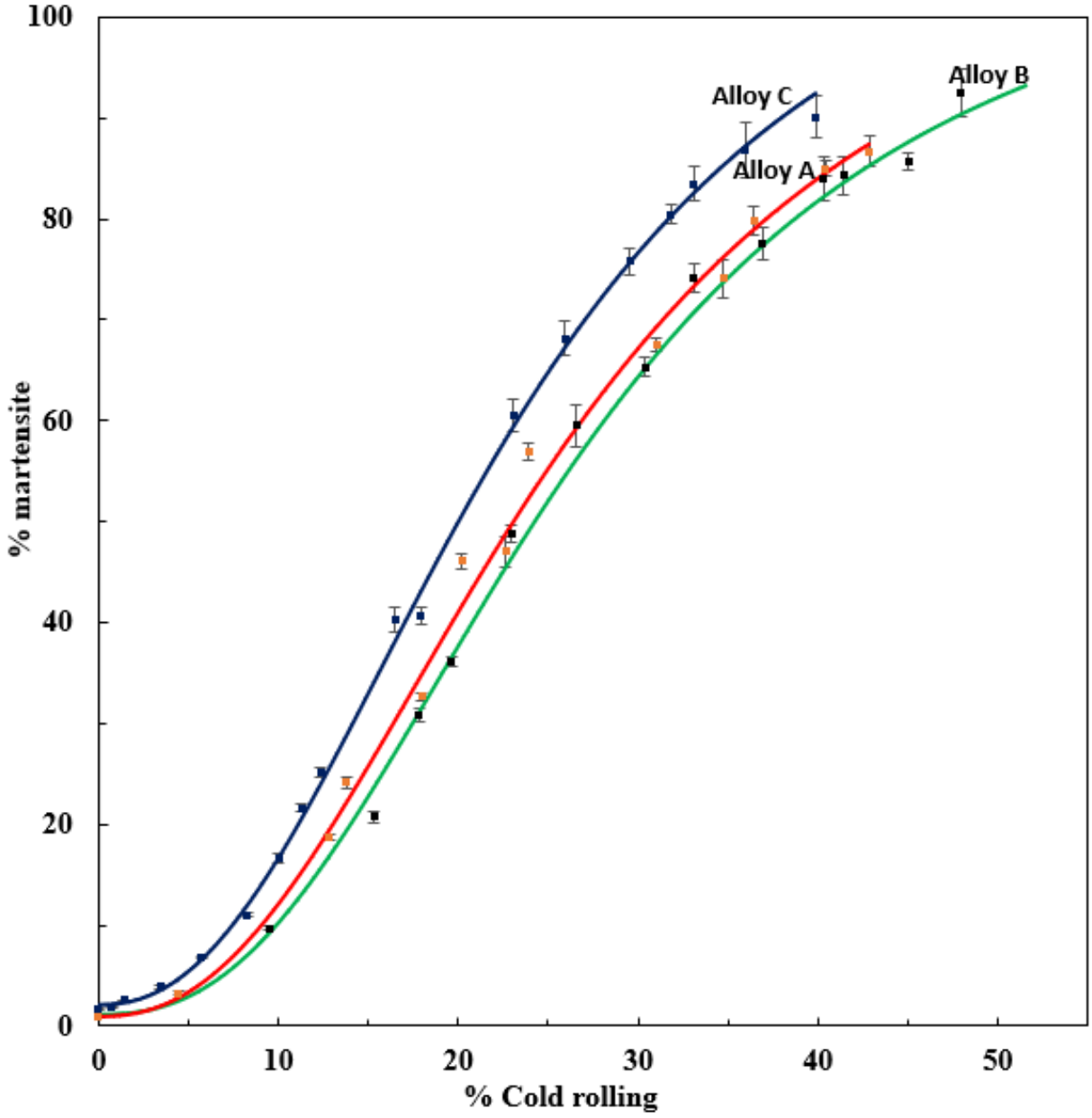


**Figure 4.63: Percentage of α′-martensite induced as a function of thickness reduction at room temperature for all alloys tested**

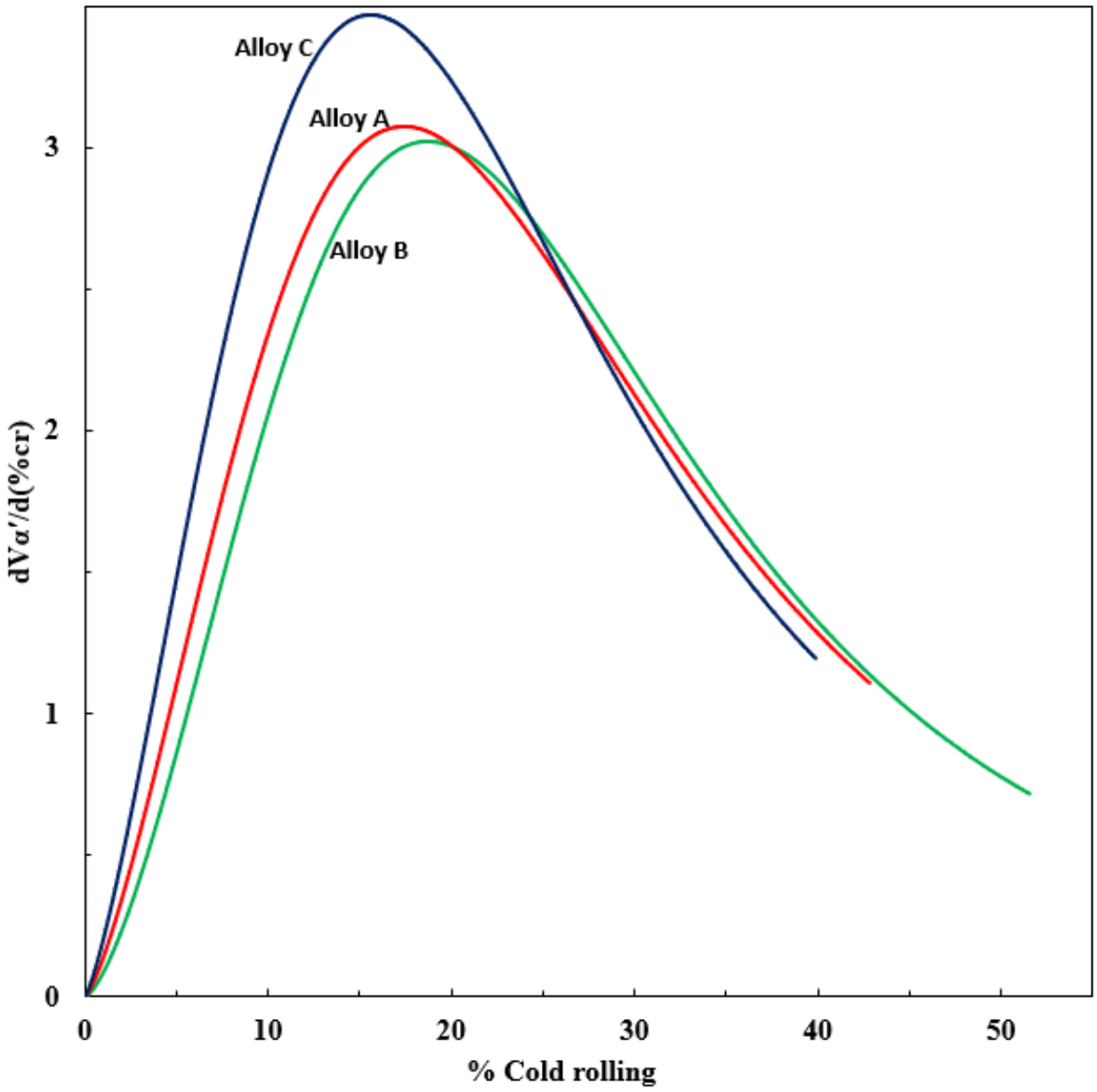


**Figure 4.64: Rate of α′-Martensite transformation as a function of thickness reduction at room temperature for all alloys tested**

### 4.4.2 Comparison using tensile testing techniques

Interrupted tensile deformation was done on two different industrially produced heats (Alloy A and Alloy B) within a temperature range of 30 °C to 60 °C. Due to limited number of samples, only alloy A and alloy B were tested at varying temperatures. An investigation on whether slight variation of chemistry within the AISI 301LN grade has varied effect on the martensitic transformation as a function of strain and $M_d$ (30/50) temperature was investigated

using tensile deformation techniques. Figure 4.65 shows the α′-martensite transformation as a function of temperature and strain for the two alloys (A and B). Interruption was done at 5% engineering strain intervals allowing Ferritescope measurements to be taken. An indication of the percentage of magnetic strain-induced α′-martensite was determined using a Ferritescope instrument (Helmut Fisher GmbH, model MP3B). Seven readings were taken on each sample at different points within the gauge length on the surface. The mean and standard deviations were calculated. A calibration factor of 1.7 was used to convert Ferritescope readings to actual martenstite content as described in Chapter 3.3 for samples deformed using tensile forces. The Ferritescope readings were taken under unloaded (unstressed) conditions.

Figure 4.65 shows that alloy A is more metastable as compared to alloy B with slightly higher percentage of strain-induced martensite at a given strain and deformation temperature. The experimentally determined $M_d$ (30/50) temperature for alloy A has been found to be approximately 61 °C and 55 °C for alloy B. The same form of sigmoidal function (sigmoidal equation 4.1) was used to describe the martensitic transformation as a function of percentage of cold rolling.

Figure 4.66 shows the corresponding rate of $\gamma \rightarrow \alpha'$ strain–induced martensitic transformation as a function of true strain for the two different heats of AISI 301LN through tensile for alloy A and B. The instantaneous gradient increased to a maximum and thereafter decreases to zero martensitic transformation.

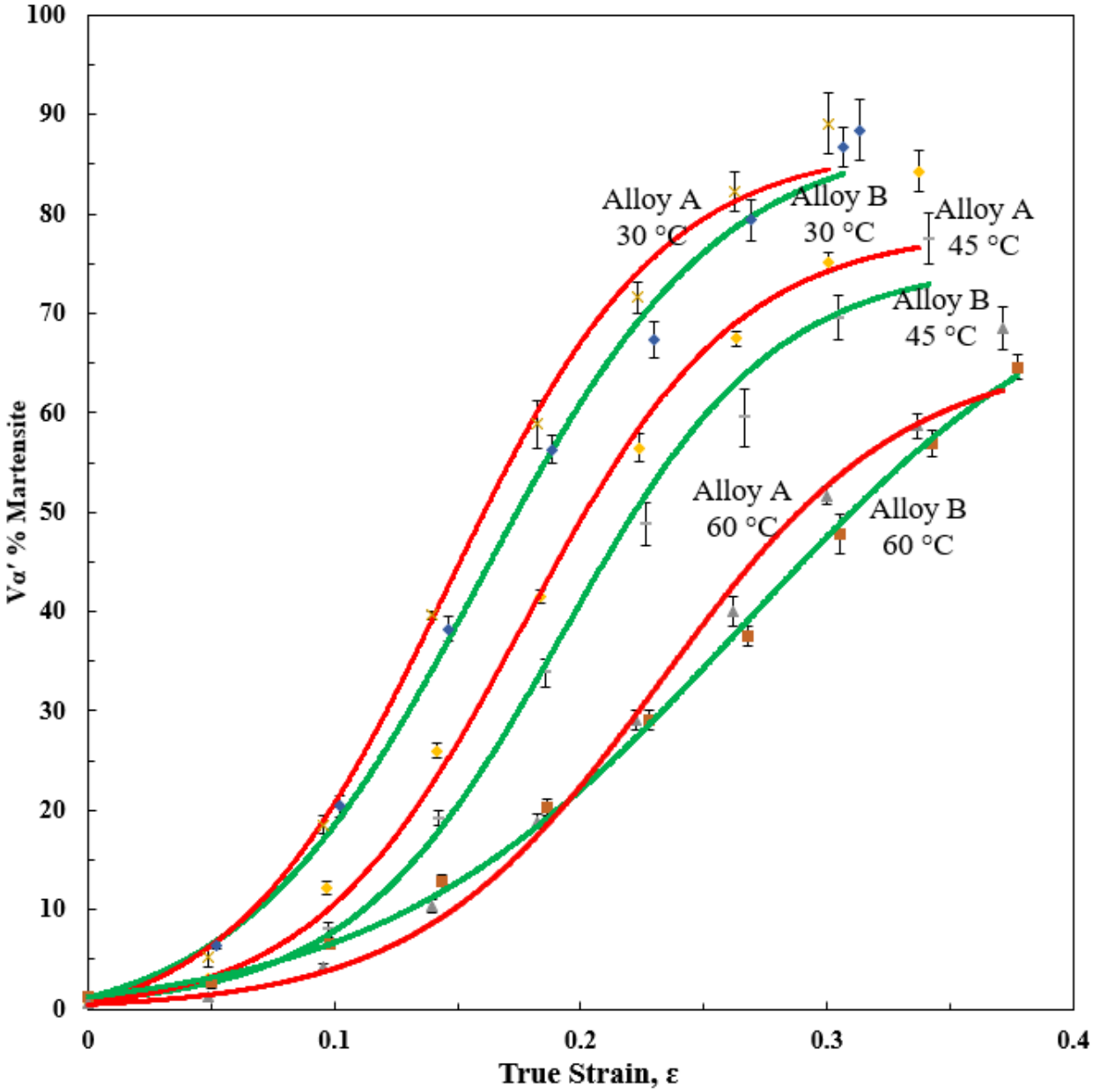


**Figure 4.65: Percentage of α′-martensite induced as a function of true strain at various deformation temperatures through tensile for alloy A and B tested at an initial strain rate of 6.67 x $10^{-4}$ $s^{-1}$**

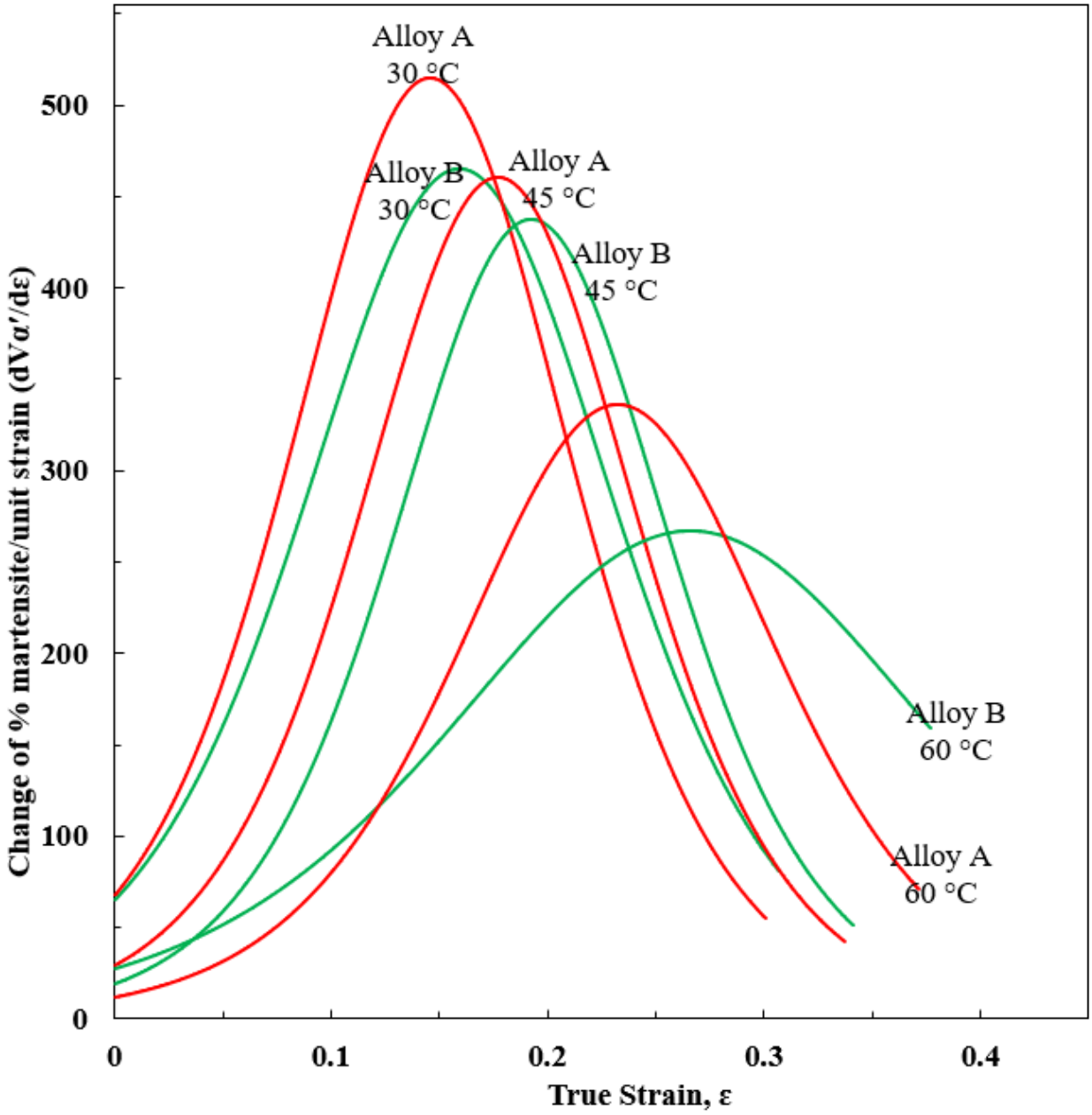


**Figure 4.66: Rate of α′-Martensite transformation as a function of true strain at various deformation temperatures through tensile for alloy A and B tested at an initial strain rate of 6.67 x $10^{-4}$ $s^{-1}$**

# Chapter 5: Discussion

The goal of this present study is to develop a set of constitutive equations that will describe the strain hardening behaviour and martensitic transformation kinetics as a function of applied strain and temperature, for the specific lean AISI 301 LN alloy (low carbon and nickel, medium - high nitrogen) in question. It is thought that these constitutive equations will facilitate the development of processes and products that can be regarded as pertaining to the "third generation AHSS" products.

The results presented in the preceding chapter will be discussed in this chapter, and the fundamentals underpinning the development of the equations will be explored. The question regarding whether the equations developed are likely to lead to the development of third generation AHSS steels and products, will also be discussed.

## 5.1 Influence of temperature and degree of tensile deformation

The influence of temperature on the tensile flow behavior of AISI 301LN was studied within a temperature range of -60 °C to 180 °C for alloy A. The strain hardening behaviour of AISI 301LN metastable austenitic stainless steel is a complex process which involves strain hardening related to the generation of a dislocation structure and a transformation and/or twinning related hardening depending on the deformation temperature. Strain hardening related to dislocation multiplication is common in all metals below the recrystallization temperature and can be modelled by a classical Hollomon equation. The second hardening phenomenon, which is caused by the strain-induced martensitic transformation (SIMT) and twinning, causes a deviation from a Hollomon parabolic curve and must be modelled using another strategy. The fact that the fraction of martensite formed in austenitic steels, as a function of applied strain and temperature, is known to be represented by a sigmoidal relationship, implies that the constitutive equations sought would probably include a contribution in terms of sigmoidal terms.

Figure 5.1 shows the deviation of the flow stress relationship from a classical Hollomon-type on a log-log plot of true stress-strain curve at 30 °C, (for clarity purposes). The secondary hardening phenomenon is observed to begin at $\approx \log \varepsilon = -1.0$ (true strain of 0.1). The generation of stacking faults, mechanical twins and α′-martensite in the early stages of deformation therefore hinders the dislocation movement resulting in the dispersion (boundary) strengthening. In the strain region beyond the critical strain for martensitic transformation, a very rapid sigmoidal strain hardening was observed at the lowest temperatures investigated. As the strain

hardening temperatures were increased, the sigmoidal strain hardening behaviour was less pronounced and at the highest temperatures evaluated (90 ~ 180 °C) the function describing the strain hardening behaviour of metastable austenitic AISI 301LN steel, changes to a polynomial function showing a significant decrease in deviation from the classical Hollomon type. The changes in sigmoidal strain hardening behaviour as a function of temperature, can best be appreciated by analysing the instantaneous strain hardening exponent, $n_i$, as a function of temperature, as presented in Figure 4.21 (for true strain greater than 5%). The plots of percentage of martensite as a function of true strain showed a similar full sigmoidal behaviour in the same temperature range of 75 °C and lower for the same alloy which reduced to a polynomial at higher deformation temperatures (see Figure 4.2).

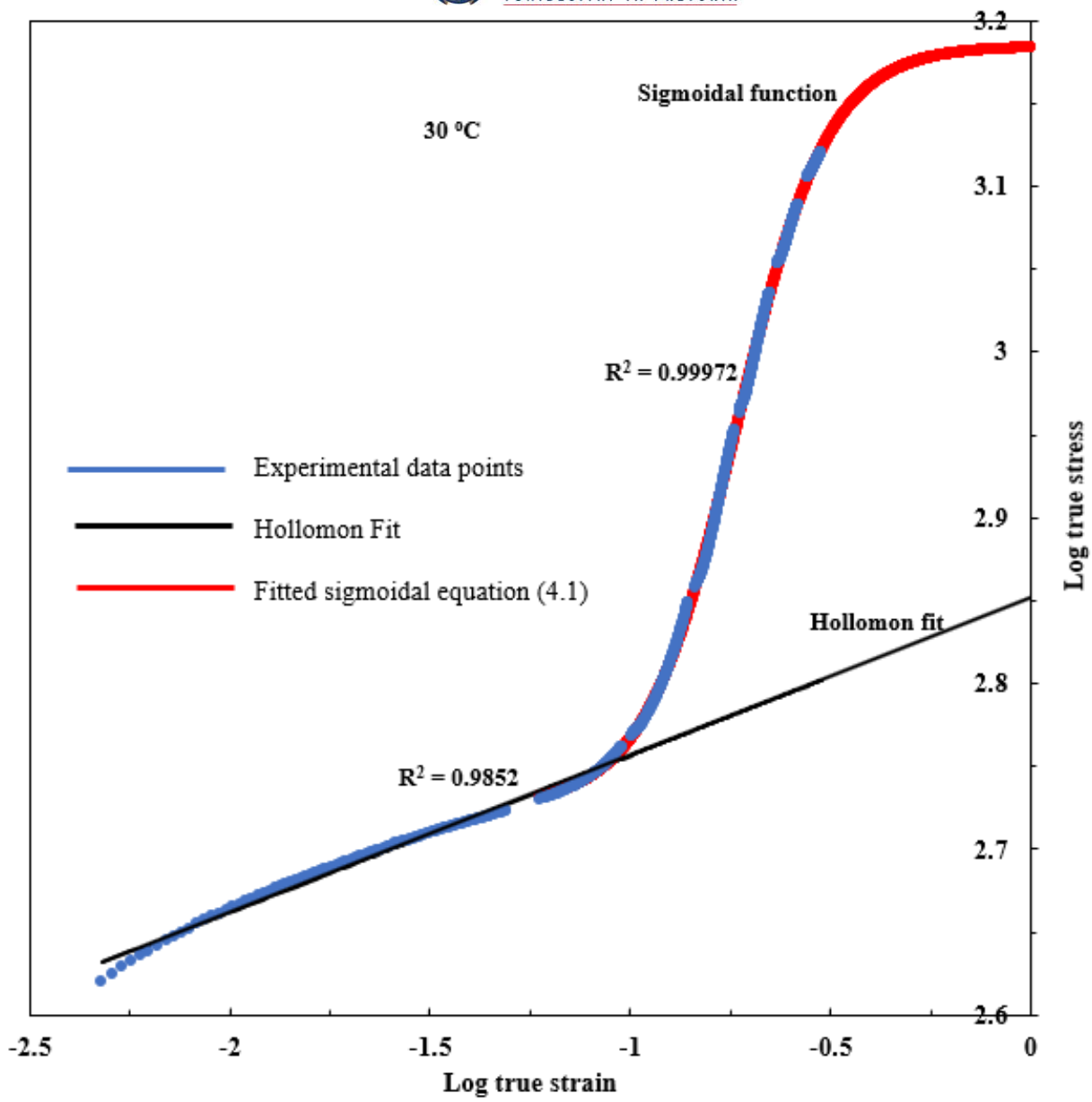


**Figure 5.1: The log-log plot of true stress-strain at 30 °C in tension, showing sigmoidal flow stress behavior and a linear Hollomon fit**

The combined effect of strain-induced martensitic transformation (SIMT) and strain hardening becomes stronger as deformation temperature decreases leading to a drastic increase in the flow stress. This indicates that there is strong temperature dependence of the austenitic stability during deformation. The volume fraction and the rate of strain-induced martensitic transformation decreases as the deformation temperature increases. This is due to the decrease in chemical driving force to induce strain-induced martensite as deformation temperature increases as explained in Figure 2.1, which shows Gibbs free energy diagram for martensite, annealed and

deformed austenite as a function of temperature. The decrease in the chemical driving force for transformation needs to be compensated by a higher mechanical energy contribution through plastic deformation at higher stress to induce the martensitic transformation [45]. Therefore, the onset of strain-induced martensitic transformation was delayed to higher strain levels with increasing deformation temperature.

Figure 5.2 shows a plot of variation of percentage of martensite and stress deviation from a Hollomon extrapolation as functions of true strain during tensile deformation at 30 °C.

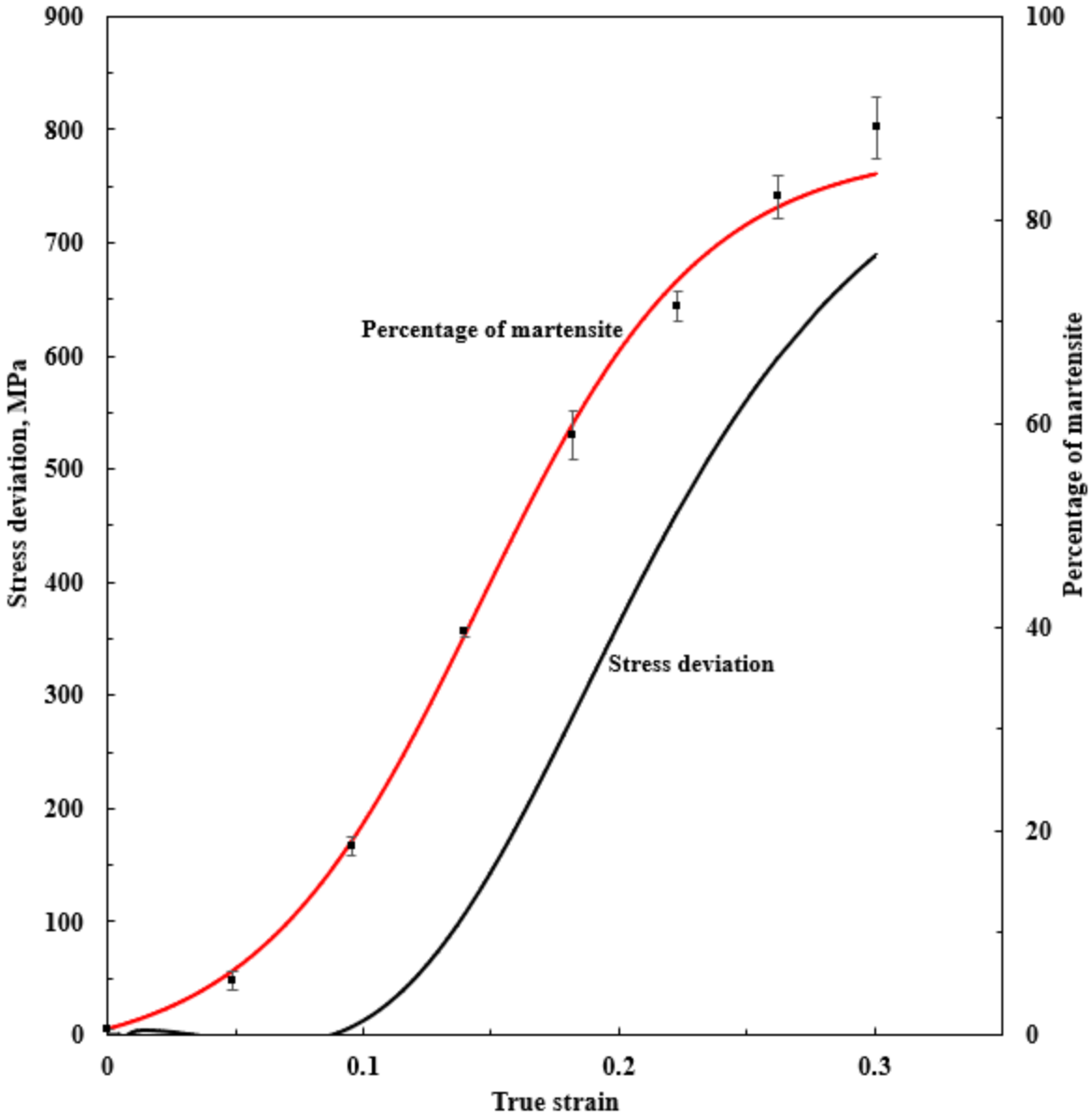


**Figure 5.2: The variation of percentage of martensite induced and stress deviation from linear Hollomon fit as a function of strain after tensile deformation at 30 °C, both showing sigmoidal behavior**

Both curves show a similar shape indicating that the strain hardening behaviour observed was controlled mainly by the formation of strain induced α′-martensite. Figure 5.3 shows a plot of true stress as a function of percentage of martensite during tensile deformation at 30 °C.

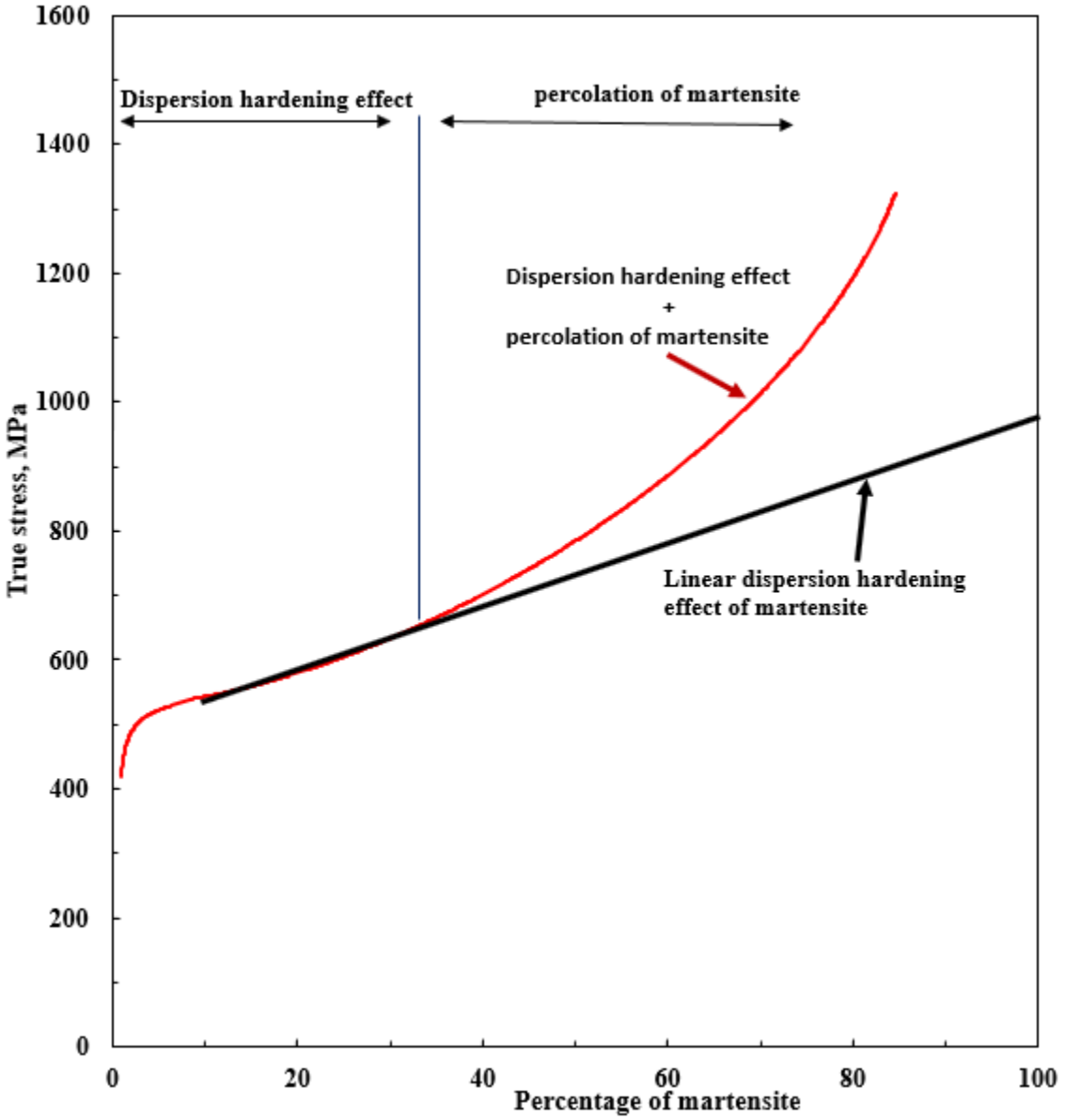


**Figure 5.3: True stress as a function of percentage of martensite during tensile deformation at 30 °C**

The increase in strength during tensile deformation as a function of strain induced martensite could be estimated as linear up to about 30 ~ 35% and then deviates. The linear variation could be explained by the dispersion hardening effect from the formation of strain-induced martensite in the austenitic matrix (in accordance with the results shown in Figure 2.9).

The increased deviation after 35% strain-induced martensite is believed to be due to the "percolation effect of martensite," where clusters of martensite forms a continuous network linking up in 3D adding more barriers to dislocation movement in the austenite phase. Percolation effect of martensite as defined by Talonen [128], is when martensite forms continuous network through the material making the flow of austenite phase more difficult. At percolation threshold of martensite, there is an interchange of roles of martensite and austenite, where martensite behaves as a matrix phase and austenite as dispersions embedded in the martensite phase. This effect results in higher strength as more stress is required to move the dislocations past the percolated martensite barriers. The percolation effect in α′-martensite reduces the plasticity of the austenite. Percolation of strain-induced martensite causes an abrupt change in the relationship between stress and martensite content from linear as observed in Figure 5.3. It has been found out in this work that percolation effect of martensite sets in when the percentage of martensite is in the range of 30 ~ 45% (see Figure 4.2). This is the percentage of martensite present when the rate of martensitic transformation reaches maximum (refer to Figure 4.26). The percentage of martensite present after deformation to the strain values corresponding to $\alpha_m$, remain fairly constant in the range of 30 ~ 45%.

Figure 5.4 was plotted to show the variation of true stress as a function of strain – induced martensite at deformation temperatures of 45 °C and above. The figures are separated for clarity.

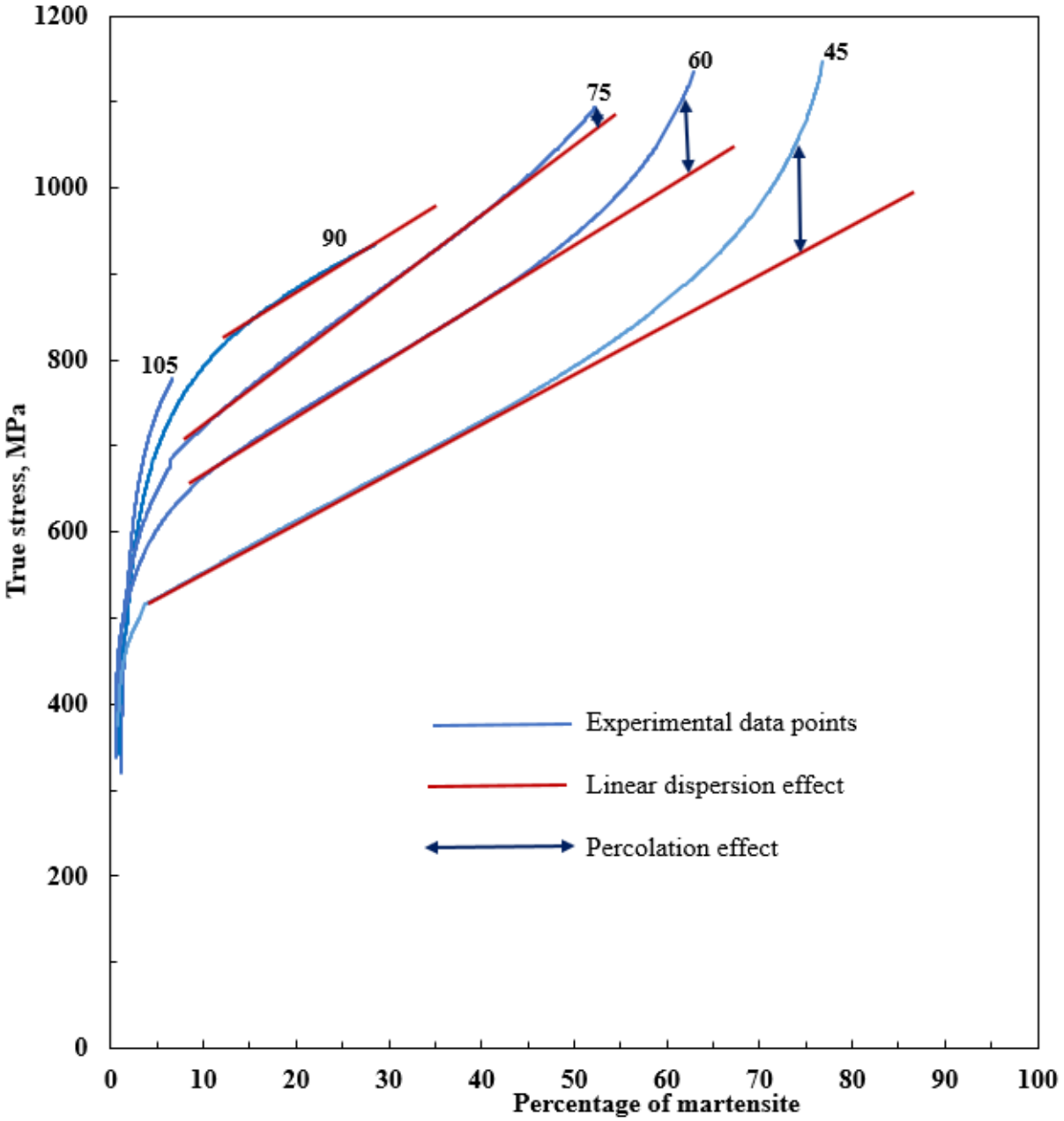


**Figure 5.4: Linear dispersion effect and martensite percolation effect of strain-induced martensite in austenite matrix after tensile deformation at temperatures of 45 °C and above**

The curves do not lie one on top of the other indicating another mechanism other than only flow stress to have an effect on the martensitic transformation. The same effects of linear dispersion followed by percolation effect of martensite were observed throughout the deformation temperatures. The observed strengthening mechanism is largely due to dispersed martensite in the austenite matrix with a deviation to a positive parabolic polynomial after ~ 45% strain-induced martensite at all temperatures shown. This further supports that percolation effect

of martensite after ~ 45% strain-induced martensite had caused an increase in strength contribution. The true strain corresponding to ~ 45% strain-induced martensite, (refer to Figure 4.2), is again observed to be the true strain where maximum rate of strain-induced martensitic transformation occurs (refer to Figure 4.3).

The increased stress levels in the martensitic phase at higher percentages of martensite is believed to be due to the percolation effect of the SIMT martensite. Moreover, the critical amount of stress required for the onset of α′-martensite transformation could be observed in the graphs showing stress as a function of α′-martensite content. The linear variation could be observed from when the percentage of martensite reaches 5 ~ 10% in all the curves. The amount of stress required to induce for instance 10% of martensite increases with increase in deformation temperature. Therefore, Figure 5.4 shows that higher stress is required to initiate α′-martensite transformation and the associated dispersion hardening at higher deformation temperatures due to increased austenitic stabilization at elevated temperatures. As deformation temperature decreases, lower amount of stress is required to induce 5 ~ 10% of α′-martensite. The temperature at which no stress is required to induce α′-martensitic transformation is known as martensite start temperature, $M_s$.

Figure 5.5 shows stress-strain curves for Sandvik Nanoflex, a precipitation hardening, metastable austenitic stainless steel at various deformation temperatures. A careful study of the stress-strain curves at low temperature by Datta K et al. [72], shows that the material goes through an initial softening plateau and then increases.

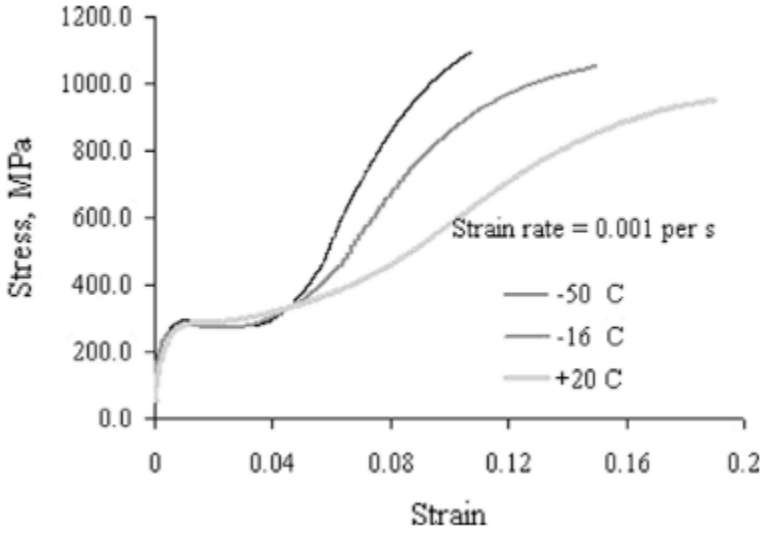


**Figure 5.5: Stress-strain curves for Sandvik Nanoflex steel at various deformation temperatures [72].**

As deformation temperature increases, this plateau disappears indicating that it is linked to SFE which is temperature dependence. Datta K et al. performed X-ray characterization on tensile deformed samples interrupted at very low strains around the plateau at -50 °C. Figure 5.6 shows a magnified section of the total XRD scan of the Sandvik Nanoflex steel tested at -50 °C showing austenite, α′- and ε-martensite peaks tested after interrupting at low strains around the plateau.

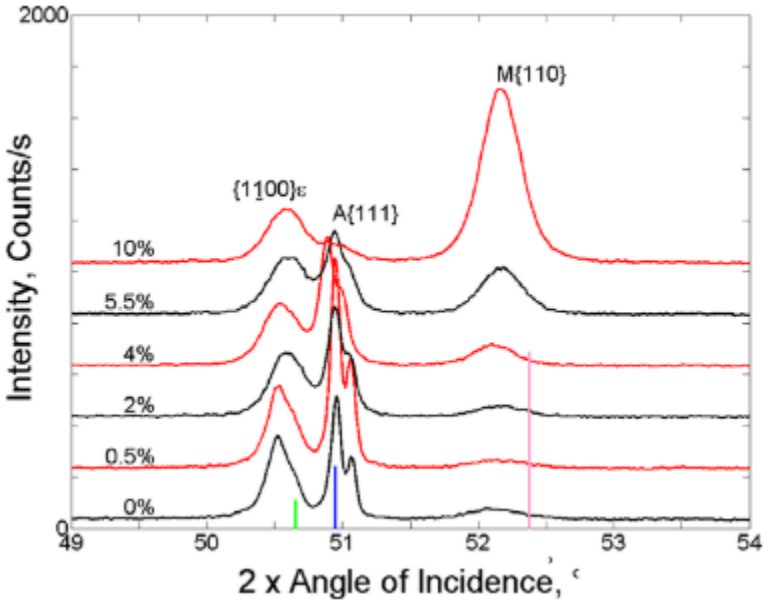


**Figure 5.6: A magnified section of the total scan of the Sandvik Nanoflex® steel tested at -50 °C showing austenite, α′- and ε-martensite peaks [72].**

It is clear from their work that softening plateau is caused by the ε-martensitic transformation as there was no significant α′-martensite formed up to 5.5% strain. In fact, the plateau in Figure 5.5 quickly disappears soon after applied strain of at least 5.5% and intensity of α′-martensite peaks on XRD scan shown in Figure 5.6 could be seen increasing thereafter. Negative strain hardening was observed in the early stages of deformation at low temperatures in Figure 4.22 corroborates that the plateau is caused by formation of strain-induced ε-martensite causing strain softening.

At sub-ambient temperatures, martensite softening effect was observed as well as percolation effect of martensite as the variation of true stress does not vary linearly with the percentage of martensite. For instance, at -60 °C the onset of the percolation effect corresponds with a true strain of 0.09 (refer to Figure 4.2). It is again observed that when the percolation

effect of martensite sets in, it brings about the maximum rate of strain-induced martensitic transformation and the maximum instantaneous strain hardening exponent (refer to Figure 4.3). Figure 5.7 shows the martensite softening effect and percolation effect at -60 °C. For clarity purposes, the true stress vs martensite at -60 °C only was shown.

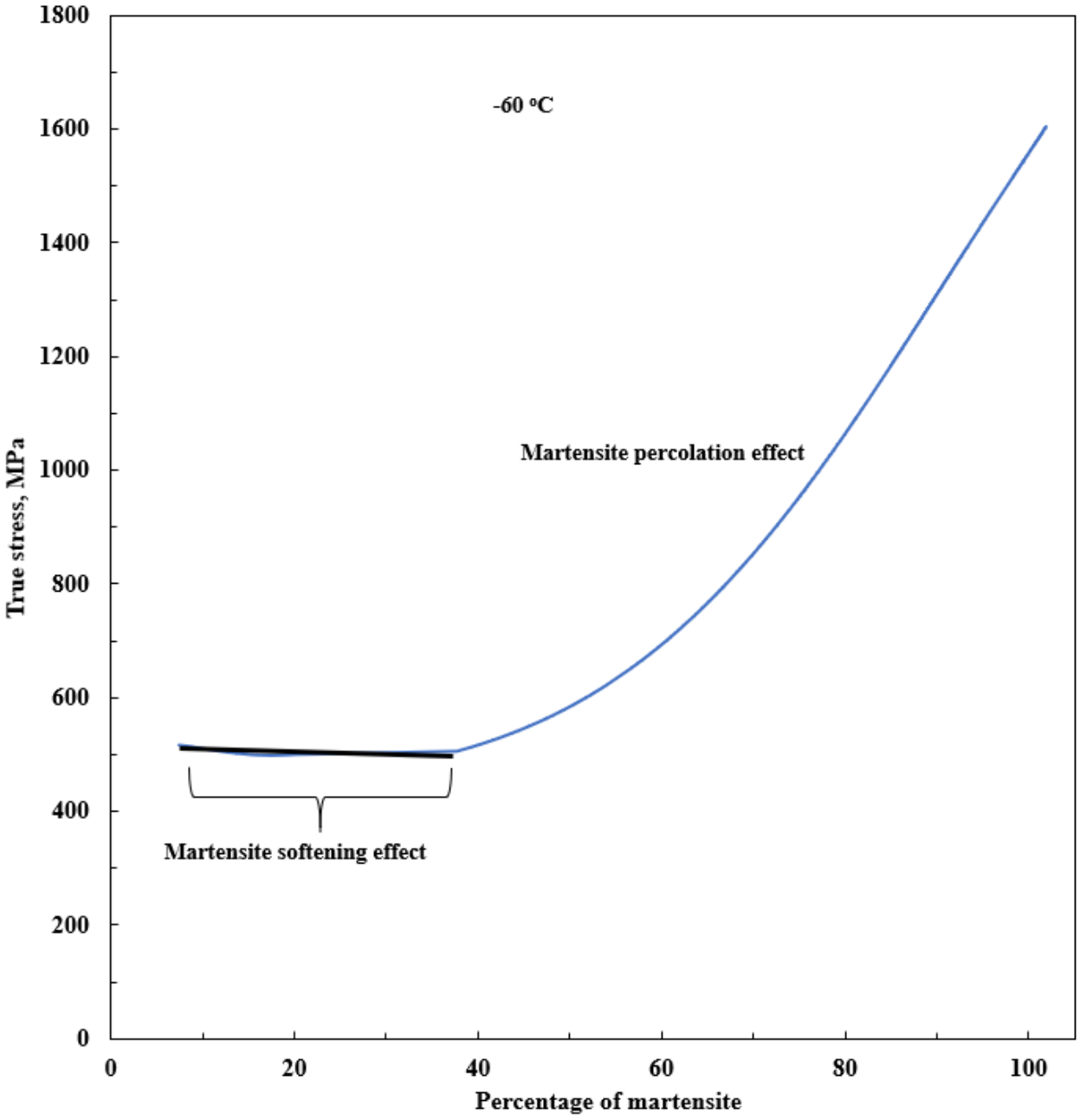


**Figure 5.7: Martensite softening effect and martensite percolation effect of strain-induced martensite in austenite matrix after tensile deformation at temperatures of -60 °C**

The plateau on the stress-strain curve was observed up to higher strain values with decreasing deformation temperatures. As deformation temperature increases, the yield point elongation plateau decreases until it disappears above 30 °C (refer to Figure 4.9), indicating only strain-induced transformation. Figure 5.8 shows the martensite softening effect and percolation effect at 15 °C showing a much reduced yield point elongation plateau as compared to that shown in Figure 5.7 at -60 °C.

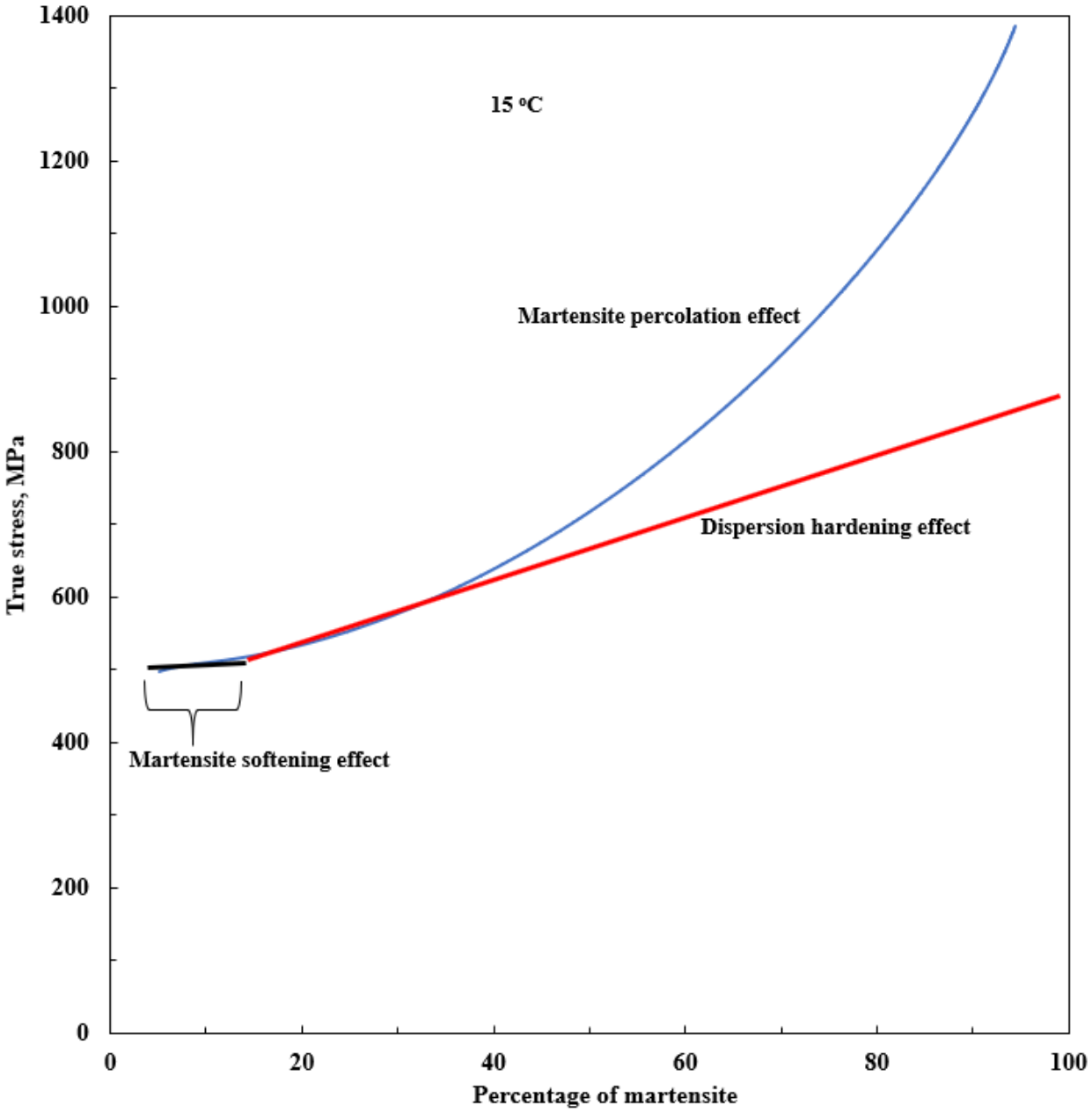


**Figure 5.8: Martensite softening effect and martensite percolation effect of strain-induced martensite in austenite matrix after tensile deformation at temperatures of 15 °C**

The dispersed strain-induced martensite strengthening mechanism in the austenite matrix was observed in Figure 5.8 by a linear fit followed by a deviation to a positive parabolic polynomial after ~ 35% strain-induced martensite. This was again believed to be due to the percolation effect of martensite resulting in increased strength contribution as previously explained. The true strain corresponding to ~ 35% strain-induced martensite, (refer to Figure 4.2), is again observed to be approximately equal to the percentage of martensite present when maximum rate of strain-induced martensitic transformation occurs for the deformation temperature analysed (refer to Figure 4.3).

As the deformation temperatures were increased, the sigmoidal strain hardening behaviour was less pronounced and at temperatures evaluated above 90 °C, the function describing the strain hardening behaviour of metastable austenitic AISI 301LN steel, changes to a linear (Hollomon-type) function on a log-log plot of true stress-strain curve. These changes in sigmoidal strain hardening behaviour as a function of temperature, can be best appreciated by analysing the instantaneous strain hardening exponent, $n_i$, as a function of temperature (Figure 4.21). The strain hardening behaviour shown in Figure 4.21 was analysed by taking instantaneous derivative of the curves and plotting it against the strain, to arrive at Figure 4.17. In the temperature range where SIMT is intense, the peak instantaneous strain hardening exponent was found to decrease from a value of 1.69 at a strain of 0.12 at -60 °C to 0.68 at 75 °C (see Figure 4.25). For the lower temperatures, however, the $n_i$-values rapidly increases with increasing strain, up to a peak $n_i$-value. As the strain corresponding to the peak $n_i$-value is exceeded, the $n_i$-values decrease sharply. The observed value is to be expected where sigmoidal behaviour is observed, as dictated by the mathematics inherent to equation (4.8). Accordingly, it has been observed that the strain hardening behaviour can be grouped into three temperature regions, which are: i) -60 °C ≤ T ≤ 0 °C, ii) 0 °C < T ≤ 75 °C and iii) 75 °C < T ≤ 105 °C, as shown in Figure 4.25.

In the case of the first group (-60 °C ≤ T ≤ 0 °C), strong sigmoidal strain hardening behaviour is observed, that is, the instantaneous strain hardening exponent $n_i$ is very low at low strains, increasing rapidly to a high peak value and thereafter decreasing again. For this group, martensite formation starts at relatively low strains of $\varepsilon < 0.05$, Figure 4.2), and the strain required for peak work hardening was 0.16 or below. The peak strain hardening exponent values in this region are extremely high in the order of 1.3 and above. The volume fraction of martensite

formed at these relatively low values of applied strain required for peak work hardening is in the order of 70 % and is relatively constant.

For the second temperature region, 0 °C < T ≤ 75 °C, the peak strain hardening exponent values steadily decline with increasing deformation temperature, reaching values of 0.7 at the upper temperatures in this range. Similarly, the required applied strain for achieving the peak instantaneous strain hardening exponent, $n_i$, increases steadily with increasing temperature up to values in the order of 0.4 at the upper temperatures. The percentage martensite associated with the peak strain hardening exponent also steadily decreases with increasing temperature, reaching a value of 42% at 75 °C.

For the third temperature range, (90 °C ~ 105 °C), peak values of the instantaneous strain hardening exponents ($n_i$) are not observed since sigmoidal behaviour strain hardening is absent. The linear (Hollomon) behaviour on a log-log plot of true stress-strain curve observed results in constant strain hardening exponents seen throughout the strain range, with strain hardening exponents ranging from 0.38 at 90 °C to 0.32 at 105 °C. The extent of martensite formation is limited, with the maximum martensite formed at 105 °C being 7 %. This is believed to be due to increased stability of austenite from metastable to stable austenite at these elevated temperatures. The increased stability of austenite is believed to be due to increased SFE which resulted in the strain hardening mechanism changing from a TRIP effect to mixed forms of strain hardening of TRIP and TWIP effects. Mechanical twinning in the austenite phase with small islands of strain-induced martensite was observed using EBSD after true strain values of 0.375 at 105 °C as shown in Figure 4.31 This confirms the mixed deformation forms of TRIP and TWIP effects. The fundamentals of strain-induced martensitic transformation thermodynamics can be explained in terms of Gibbs free energy and SFE as below:

1. The critical Gibbs free energy for strain-induced martensitic transformation is known to be temperature dependent (Figure 2.1). As the deformation temperature increases higher mechanical energy need to be supplied to achieve strain-induced martensitic transformation as shown in Figure 2.1. As the deformation temperature increases the chemical energy component decreases till the summation of chemical and mechanical energy components become less than the critical Gibbs free energy for martensitic transformation. The corresponding temperature is the $M_d$ temperature, beyond which no martensitic transformation occurs and behaves like a stable austenitic stainless steel. For the AISI 301LN alloy investigated, the $M_d$ temperature was found to be quite high, ~ 117 °C. This finding

indicates that the Gibbs free energy for this alloy (alloy A), in the annealed austenitic state, is quite high.

2. The strain hardening mechanism is mainly controlled by the stacking fault energy (SFE) which is compositional and temperature dependence. The tested AISI 301LN alloy has a very low calculated stacking fault energy of 15.3 $mJm^{-2}$ at room temperature (calculated using a composition-based Brofman and Ansell equation [101]). The value was found to be very close to the experimentally determined SFE of AISI 301LN using X-ray diffraction [39], of approximately 14.7 ± 0.8 $mJ/m^2$. The theoretical temperature dependence of SFE ($\gamma_{SFE}$), $d\gamma/dT$ for Fe-18Cr-7Ni-0.18C, for an alloy similar in composition to the one tested, has been approximated as 0.1 $mJm^{-2}K^{-1}$ for 20 °C ~ 327 °C temperature range and 0.06 $mJm^{-2}K^{-1}$ for temperatures below 30°C [92], [93]. At 90 °C and above, the SFE could be then estimated as being above 20 $mJm^{-2}$ which falls in the region where TWIP strain hardening mechanism is expected to become more dominant [88]. The high SFE results in reduction in the formation of shear bands which are essential nucleation sites for strain-induced martensitic transformation. Furthermore, the reduced number of shear bands results in the decrease in rate of transformation. With increased SFE, the strain hardening mechanism therefore changes from a pure TRIP effect (below 12 $mJ/m^2$) to a mixture of TRIP and TWIP effects and then, at the highest temperatures, to TWIP effects only (above 20 $mJ/m^2$). At temperatures below the $M_d$ (30/50), experimentally determined to be 60 °C [158], the low stacking fault energy makes the material metastable and amenable to SIMT leading to a strong increase in strain hardening with increased applied strain.
3. A continual increase of $\alpha_m$, and $\alpha_s$ as deformation temperature (refer to Figure 4.4 and Figure 4.18, respectively) increases suggests that the parameters are also dependence of SFE ($\gamma_{SFE}$). The variation of such parameters with SFE has been reported in literature [121], [169].
4. The maximum elongation temperature (M.E.T) as was defined by Livitsanos and Thompson [155], was suggested to be dependent on the formation of ε-martensite and SFE. In this work and many other research work [73], proposes that a distinctive peak of elongation is due to formation of ε-martensite. The maximum SFE for which formation of ε-martensite is possible had been reported in literature as approximately 20 $mJm^{-2}$ [83], [84], making it the characteristic SFE for maximum elongation.

No observation of any martensite peaks observed even after cooling to temperatures approaching absolute zero Kelvin (-273 °C) as shown in Figure 4.1 despite being lower than the predicted calculated $M_s$ temperature (-240 °C) using the Eichelman and Hull equation [106]. The $M_d$ (30/50) as extrapolated in Figure 4.7 was found to be 61 °C which is 32 °C higher than the calculated $M_d$ (30/50) value of 29 °C, according to the Angel equation [27]. Possible reasons for discrepancy in both cases could be attributed to the fact that both Eichelman and Hull equation and the Angel's equation to calculate the $M_s$ and $M_d$ (30/50) temperatures, respectively for 18-8 stainless steel uses the same constant for both the carbon and nitrogen content. More recent work has however shown that nitrogen is much more potent than carbon in terms of the thermal stabilization of austenite [107], [108]. It was therefore deemed that both Eichelman and Hull equation and Angel's equation might not be accurate in predicting $M_s$ and $M_d$ (30/50) temperatures of the alloy studied, respectively. However, the calculated values of $M_s$ and $M_d$ (30/50) temperatures were used for comparison of austenite stabilities of the tested alloy in reference to the minimum and maximum AISI 301LN specification as shown Table 4.1.

Figure 5.9 shows the calculated vs actual true stress – strain graphs for validation of equation (4.8) in predicting tensile flow stress behavior of AISI 301LN metastable austenitic stainless steel. The calculated true stress – strain curves are shown from a true strain of 0.05 where sigmoidal equations were shown to be valid.

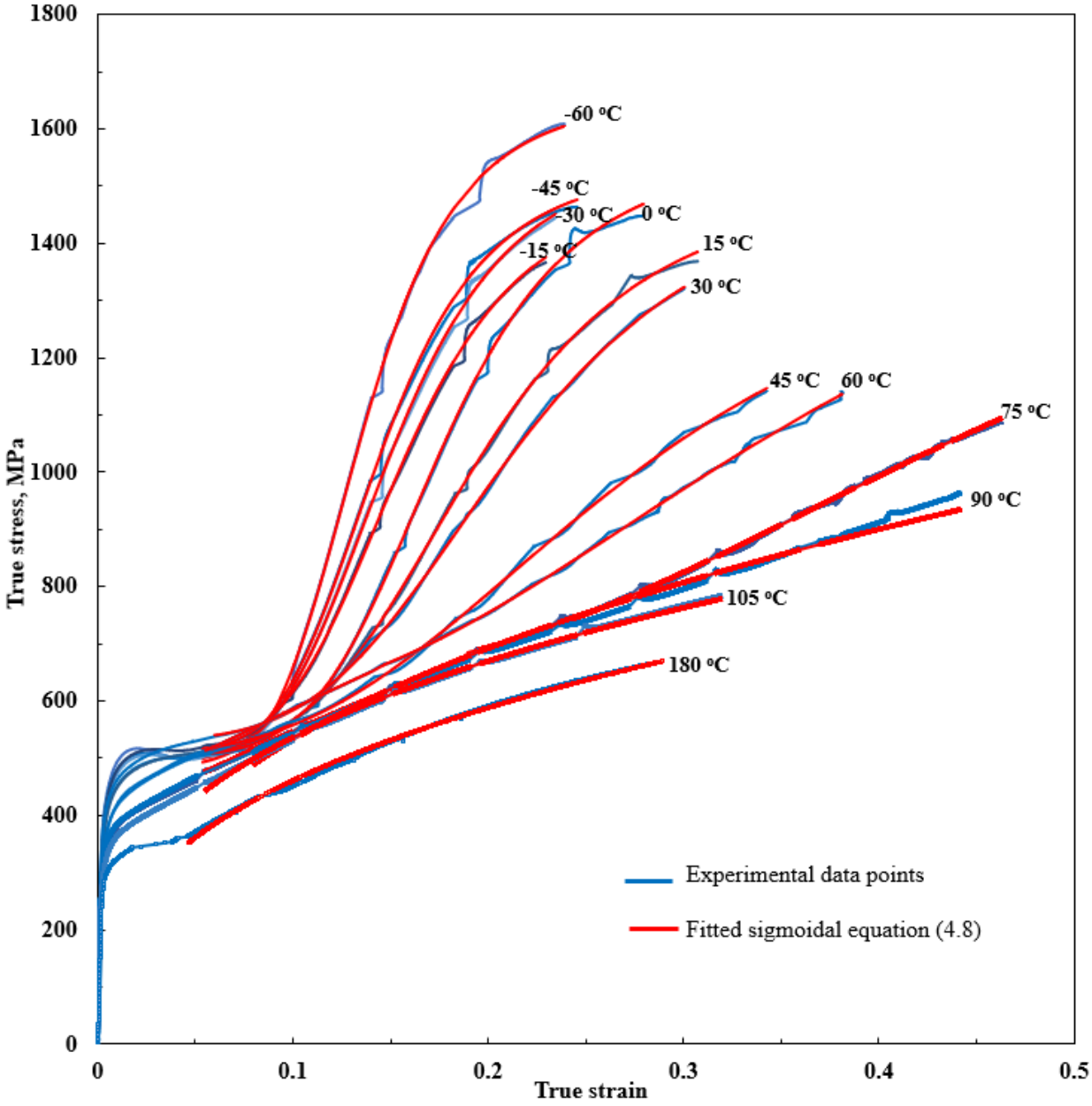


**Figure 5.9: Calculated vs actual true stress – strain graphs for validation of equation (4.8).**

The α′-martensite transformation as a function of mechanical energy absorbed and temperature was analysed to correlate to cold rolling practice. There is uniform distribution of strain during tensile deformation and hence no redundant strain, unlike cold rolling which makes use of compressive forces. In the latter case, there is greater deformation near the surface than the centre of the material due to friction-induced redundant strain during cold rolling practice. In an industrial application, curves and relationships correlating thickness reduction to mechanical

properties and the α′-martensite transformation as a function of temperature will however be more useful rather similar relationship as a function of tensile strain.

### 5.2 Influence of the degree of prior cold rolling

The volume fraction of ε-martensite was observed increasing to a maximum in the early stages of deformation and then decreases to zero around 30% cold rolling. This is in accordance with the literature where it was reported that ε-martensite is an intermediate phase for α′-martensite. At higher deformation, austenite transforms directly to α′-martensite without the formation of ε-martensite. Friction-induced redundant strain during cold rolling results in more deformation near the surface than the centre. This causes in textural differences between surface and bulk material during cold rolling results. The deformation mode is best described as a shear deformation near the surface due to friction, whilst in the bulk material, the deformation mode is better described as a uniaxial compression. Shear deformation causes slightly higher amounts of α′ martensite near the surface in the early stages of deformation. Adiabatic heating is higher during cold rolling as compared to tensile deformation due to friction and redundant strain which further retards the martensitic transformation at a given deformation temperature.

Prior cold rolling was found to have influence on both strain hardening and mechanical properties. The flow strength values increase as the percentage of prior cold rolling increases. This is attributed to SIMT and increase in dislocation density. An increase in SIMT has therefore led to an increase in yield strength and ultimate tensile strength and decrease in uniform elongation. The amount of strain-induced martensite as determined by the amount of prior cold rolling in Figure 4.46 had shown that the strain hardening response is proportional to the amount of austenite. The convergence of sigmoidal hardening curves at a log stress value of 3.25 (at log true strain of 0) indicates the maximum strength coefficient, K attainable in this alloy in the deformation temperature range tested. The strength coefficient, K has been found to be ~ 1780 MPa, and is in good agreement with the tensile strength of samples cold rolled to above 63.2% (which is equivalent to the compressive true strain of 1 ≡ log true strain of 0) of 1715 MPa.

Figure 5.10 shows the calculated true stress – strain curve vs actual true stress – strain curve to validate sigmoidal equation (4.8) for different levels of prior cold rolling of AISI 301LN metastable austenitic stainless steel in the plastic region. Figure 5.11 shows the calculated true stress – strain curve vs actual true stress – strain curve to validate the modified sigmoidal

equation (4.17) for AISI 301LN metastable austenitic stainless steel pre-strained in compression in the plastic region.

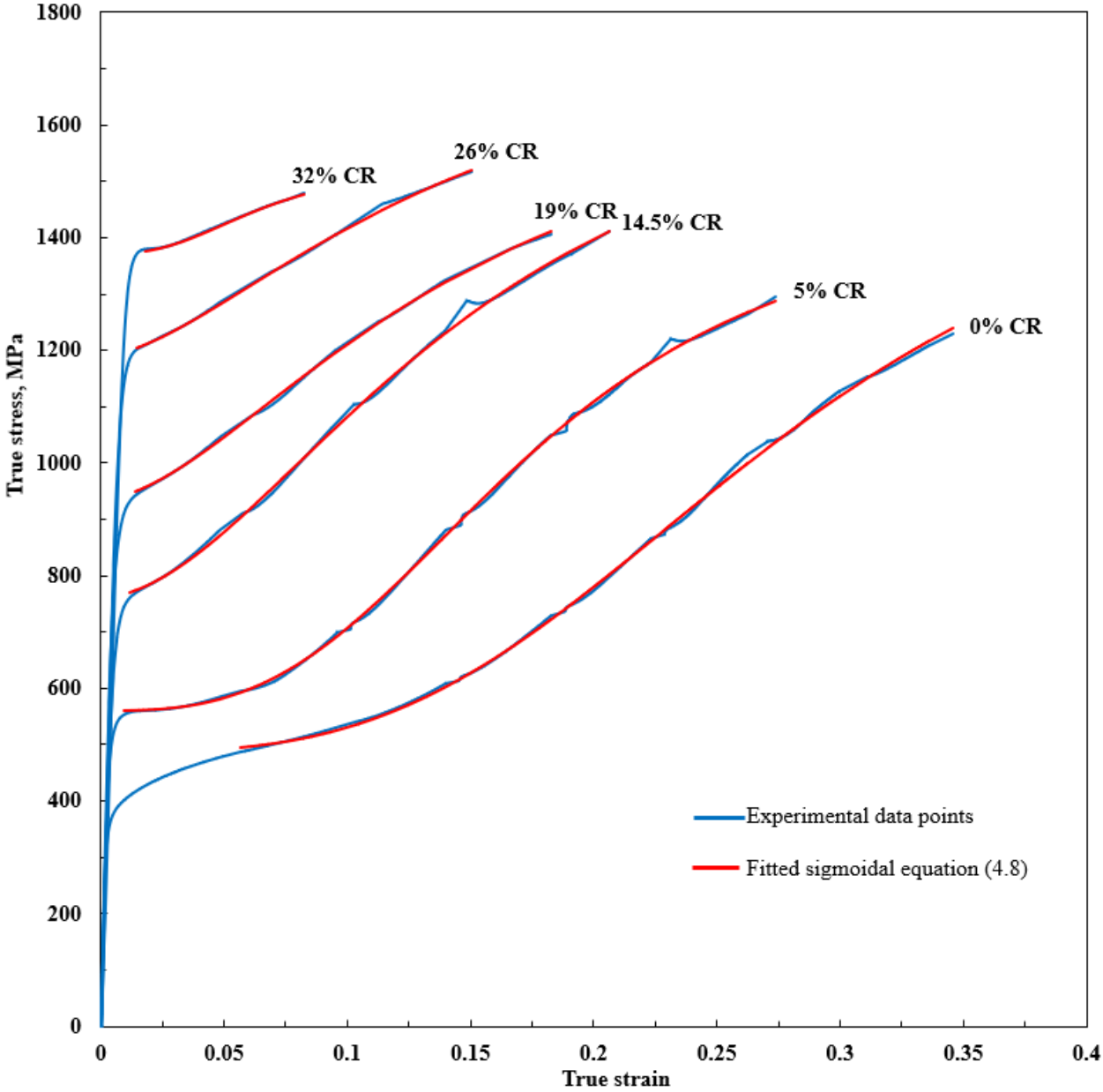


**Figure 5.10: Calculated vs actual true stress – strain graphs for validation of equation (4.8) for prior cold rolled samples.**

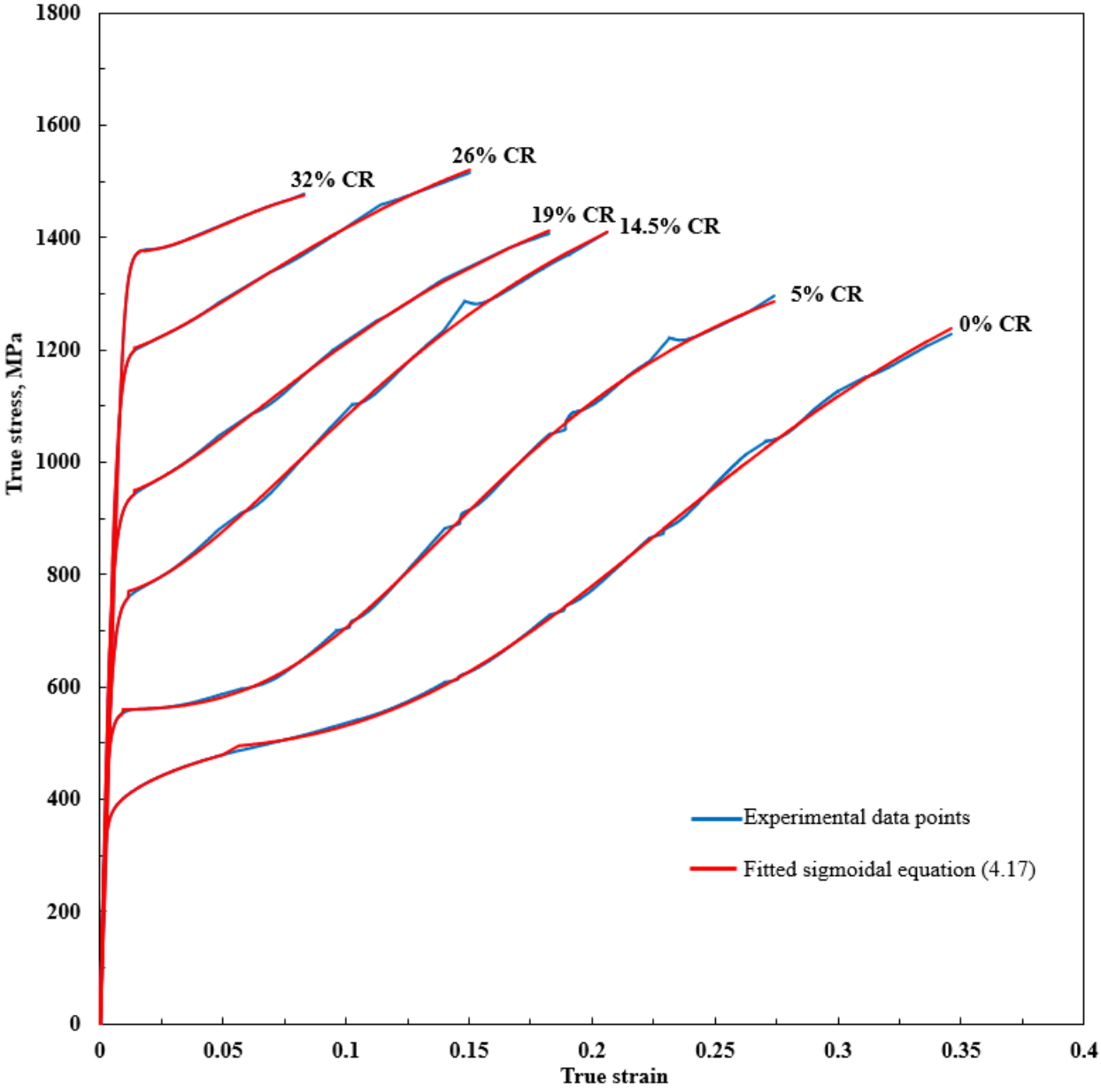


**Figure 5.11: Calculated vs actual true stress – strain graphs for validation of equation (4.17).**

Both Figure 5.10 and Figure 5.11 show that as prior cold rolling increases, the plateau diminishes. If the plateau is associated with formation of ε-martensite as described in Figure 5.5 and Figure 5.6 earlier, then it shows no formation of ε-martensite during tensile deformation for samples received a higher percentage of prior cold rolling. The formation of ε-martensite is linked to the SFE of the alloy. Mahato et al. [94] reported that SFE increases with increasing strain and had shown an increase in SFE from 19.9 mJ/m$^2$ at 2% strain, 23.4 mJ/m$^2$ at 5% strain

to over 40 mJ/m$^2$ at 46%. Figure 5.12 shows the variation of true stress as a function of α′-martensite induced for prior cold rolled AISI 301LN.

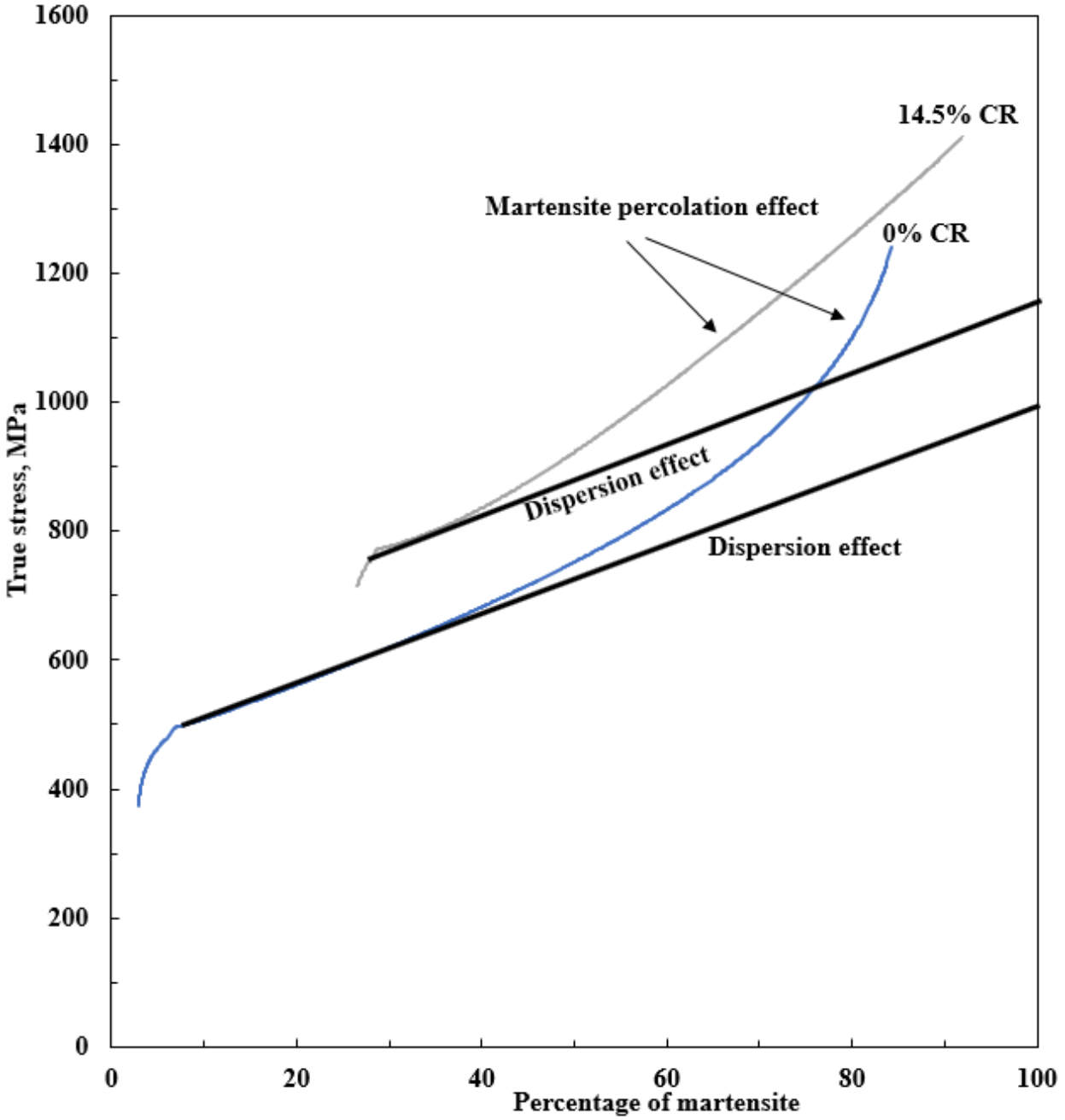


**Figure 5.12: Dispersion hardening effect and martensite percolation effect in austenite matrix after prior cold rolling**

An abrupt change in the relationship between stress and martensite content was observed Figure 5.12 due to percolation effect of martensite. Percolation effect was observed in the same range of percentage of martensite 30 ~ 45% as before in materials which had received prior cold

rolling of 14.5% with an initial percentage of strain – induced martensite of 45% (see Figure 4.34). An initial percentage of strain – induced martensite of above 45% would be beyond the observation of percolation effect of martensite on a true stress vs α′-martensite plot during tensile deformation. As explained before, the percentage of martensite present when the rate of martensitic transformation reaches maximum correspond to the critical amount of martensite for percolation effect (refer to Figure 4.35 for the true strain corresponding to the maximum rate of martensitic transformation and Figure 4.34 for the corresponding percentage of martensite present). The percentage of martensite present at maximum rate of martensitic transformation was found to be fairly constant in the same range of 30 ~ 45%, as determined before. The curves do not lie one on top of the other but however, appear to be converging at higher percentage pf martensite.

### 5.3 Strain rates using tensile tests

The secondary effect of higher strain rates results in adiabatic heating during deformation causing a temperature increase. As a result, an effect of increasing strain rates will be equivalent to the influence of temperature on the flow curves. High strain rates without temperature increase has little influence on the martensitic transformation for AISI 301LN. This is in accordance with what has been reported in literature for metastable AISI 300 series as compared to AISI 200 series [96]. The adiabatic heating from high strain rates lowers the chemical driving force for the strain-induced martensitic transformation and increase the SFE. This thereby decreases the transformation rate since the α′-martensite nucleation would have occurred in the early stages of deformation when SFE would have been still relatively constant. In the current work, tensile testing was interrupted at 5% strain intervals giving the material enough time for cooling. Therefore, there was not much influence of adiabatic heating on chemical driving force and SFE as a function of strain rate. It is believed that the strain-induced martensitic transformation is inhibited only when heating increases due to increased plastic deformation.

### 5.4 Summary of the results and achievement of properties representing a third generation of AHSS products

Properties of cold rolled AISI 301LN, depending with the degree of prior cold rolling were plotted on Figure 1.1 (shown before) to give Figure 5.13. The position of metastable AISI 301LN in a strength-formability relationship can be varied within a wide range of work

hardening. It could be seen that this material can be placed well above the first-generation steels in Figure 1.1.

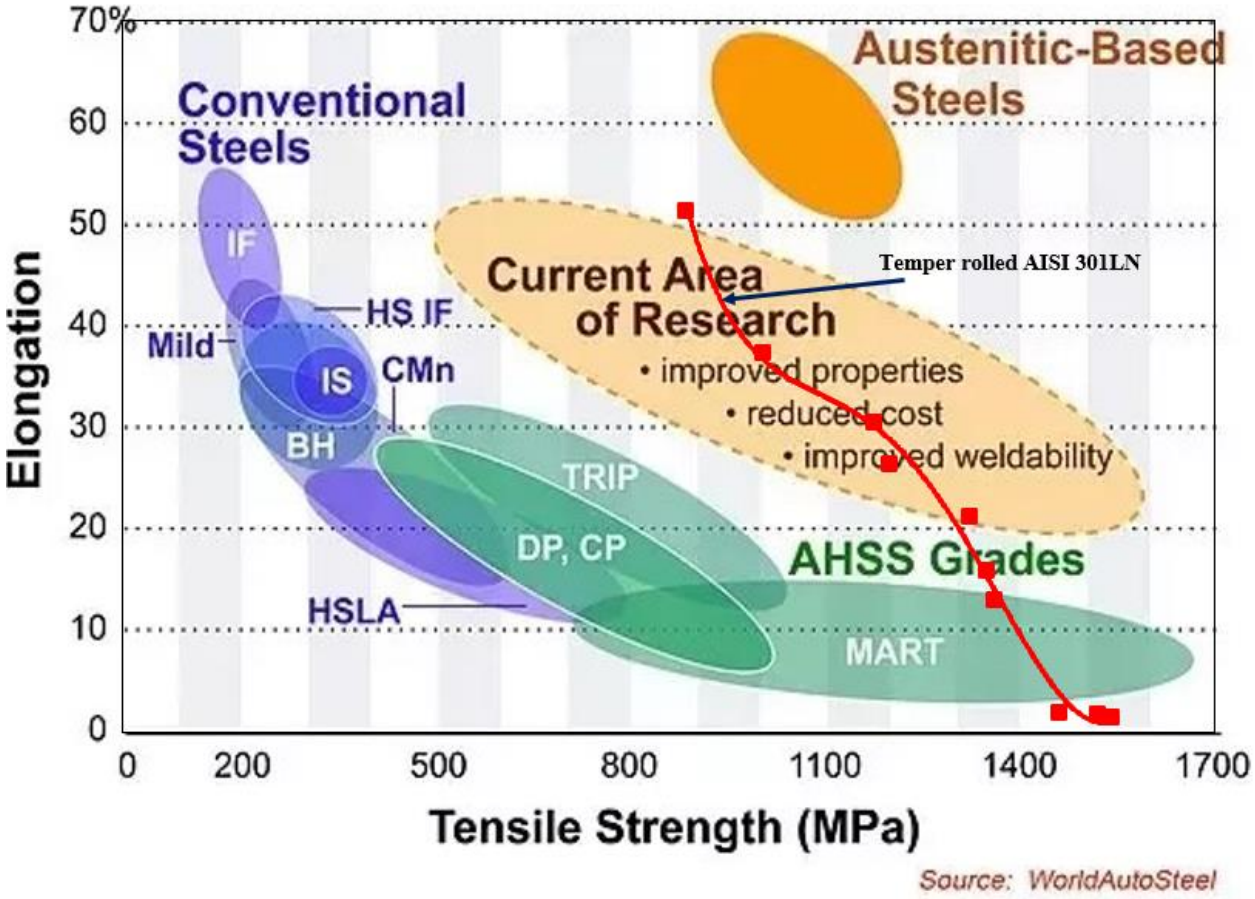


**Figure 5.13: The strength-ductility relationship of metastable AISI 301LN cold rolled at room temperature overlaid on Figure 1.1 (shown before)**

To achieve the required mechanical properties as stated in Table 1.1, the percentage temper rolling needed for each mechanical property identified, are summarized in Table 5.1, where final temper rolling should be between 13 % and 14.5 % at 30 °C. The final product should therefore have 13 ~ 17.5 % martensite to achieve the stipulated mechanical properties.

**Table 5.1: Final temper rolling required to achieve the stipulated limits of mechanical properties required for crash resistant AISI 301LN steel**

| Mechanical property | Final temper rolling required (%CR) | |
|---|---|---|
| | Minimum | Maximum |
| 1. Yield strength, $R_p(0.2)$ | 13 | 19 |
| 2. Tensile strength, $R_m$ | 5.5 | 14.5 |
| 3. Elongation to fracture, $A_{50}$ | 0 | 24 |
| 4. Hardness ($H_{RC}$) | 12.5 | 17.5 |
| 5. Ratio ($R_p(0.2)/R_m$) | 0 | 24 |

The range of true strain required to achieve the target mechanical properties can be equated to the amount of α′-martensite required. With the amount of α′-martensite required, the range of true strain can then be determined over a wide range of deformation temperature as shown in Figure 5.14. Therefore, the final temper rolling can be applied taking into consideration the final gauge thickness required. A higher deformation temperature can be chosen where a higher temper rolling is required thereby avoiding unwanted high amount of strain induced martensite at ambient temperatures. There is need of control of amount of strain induced martensite to achieve stipulated mechanical properties. The 13% and 14.5% range of percentage of cold rolling obtained in Table 5.1 correspond to 13.5 % and 18 % strain induced martensite, respectively. Figure 5.14 shows the minimum and maximum final temper rolling required to achieve the stipulated mechanical properties over a wide range of deformation temperature. The closeness of the minimum and maximum strain required achieve the stipulated mechanical properties at a given deformation temperature indicates a narrow window of opportunity. It should be noted that higher temper rolling at higher temperatures might impair the final strain to fracture, $A_{50}$.

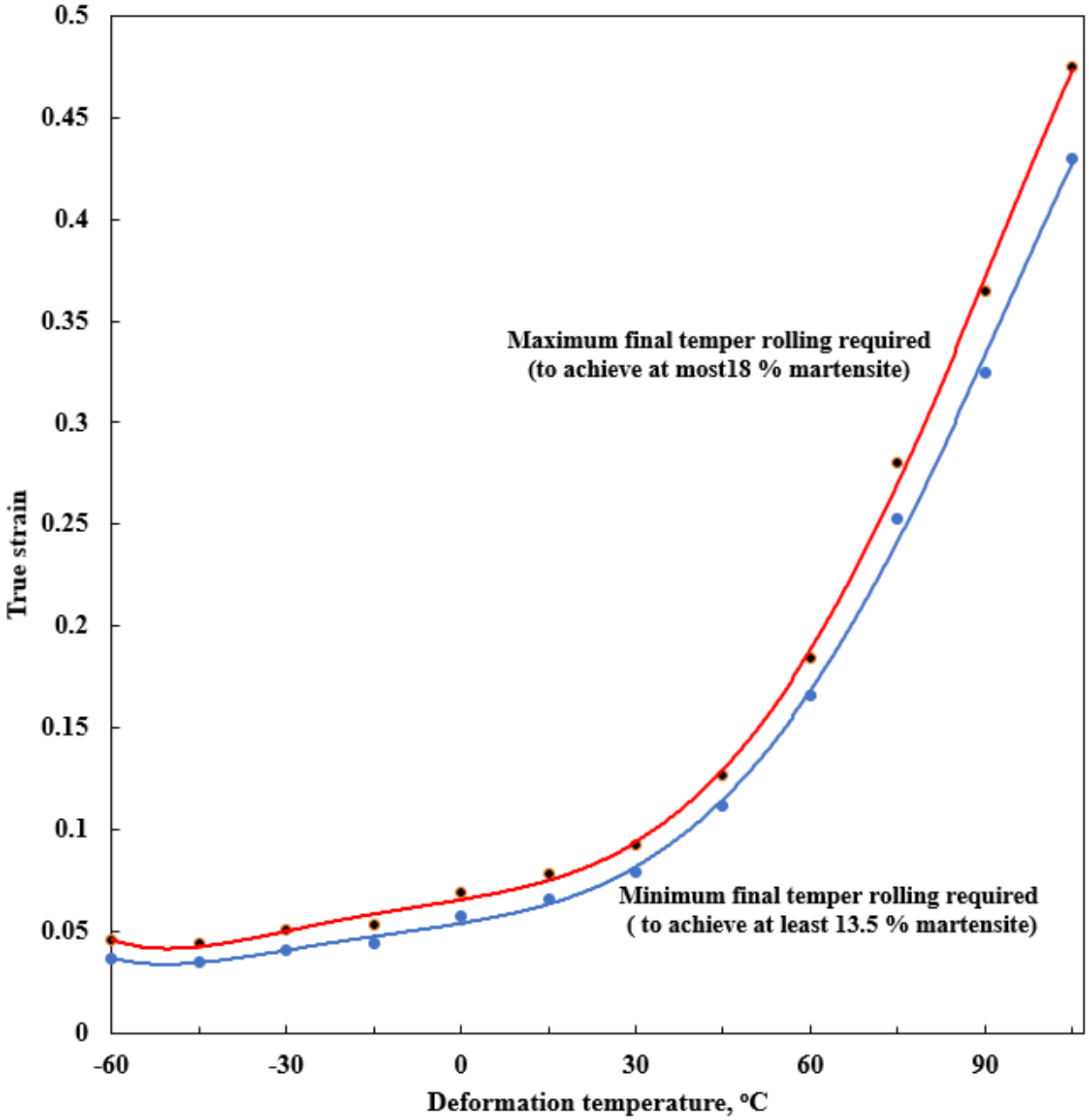


**Figure 5.14: Contour lines of amount of α′-martensite as a function of strain in cold rolling and deformation temperature**

# Chapter 6: Conclusions and Recommendations

This chapter focusses on conclusions and recommendations made after a well-detailed analysis of the experimental results in relation to the afore-mentioned research aims and objectives.

## 6.1 Conclusions

The quantification of the influence of a number of variables on the mechanical properties and microstructural evolution during plastic deformation of lean-alloyed AISI 301LN metastable austenitic stainless steel was studied. A strong correlation between the development of microstructures and the flow behavior at various temperatures was observed. Based on the results and analysis, the following conclusions have been drawn:

1. A set of constitutive equations that describe the strain hardening behaviour and martensitic transformation kinetics as a function of applied strain and temperature, for a specific lean AISI 301 LN alloy (low carbon and nickel, medium -high nitrogen), was developed and was shown to be accurate for both tensile and compressive straining applications.
2. A sigmoidal equation was found to be the only mathematical relationship to adequately describe the tensile strain hardening behaviour of the lean alloyed AISI 301LN steel studied, above true strain levels of 0.05 and for temperatures of 75 °C and below. The sigmoidal nature of the strain hardening relationships was shown to be due to strain-induced martensitic transformation, which was found to also follow sigmoidal relationships when expressed as a function of applied true tensile strain. The same forms of mathematical equations were found to adequately describe both the strain hardening behaviour and strain-induced martensitic transformation for prior cold rolled samples as well.
3. At temperatures of 90 °C and above, linear log-log equations (Hollomon equations) were found to adequately describe the strain hardening behaviour of this steel. This change in sigmoidal to linear strain hardening at elevated temperatures was also observed in equations that describe the volume fraction of martensite formed as a consequence of applied strain at these temperatures, for the strain-induced transformation of austenite to $\alpha'$-martensite.
4. The change of strain hardening behaviour that sets in at 90 °C, was found to be due to lower amounts of martensitic transformation at the higher temperatures because of

increased stabilization of the austenitic phase (as indicated by the increase in the derived SFE values). At lower temperatures, the formation of strain-induced martensite and twinning has led to the deviation of work-hardening from classical Hollomon behaviour to sigmoidal relationships.

5. Relatively low values of instantaneous strain hardening exponents were found at high temperatures which resulted in insignificant contributions to strength by strain hardening at those temperatures. At lower temperatures, however, very high instantaneous strain hardening exponents have been found, in the order of 1.3 and above. The strong instantaneous strain hardening at lower temperatures lead to high strength coefficients for the AISI 301LN steel (above 1500 MPa for temperatures below 45 °C). The accuracy of estimations of strength coefficients were verified by cold rolling testing at high strains validating the derived sigmoidal equations.
6. In addition to chemical composition, temperature of deformation dominates the austenite stability through its influence on the SFE. Deformation at a temperature of 75 °C and above coincides with SFE values above 20 $mJ/m^2$, leading to a dominant TWIP deformation mechanism at these temperatures.
7. Compared to other austenitic grades, it was found that the lean alloyed AISI 301LN alloy investigated displayed superior energy absorption. characteristics. Enhanced work hardening due to martensitic transformation results in high uniform elongation leading to higher amounts of mechanical energy that can be absorbed before fracture (toughness) thereby enhancing crashworthiness.
8. The percentage of prior cold rolling of metastable austenitic stainless steels reduces the subsequent tensile strain hardening response due to reduced austenite content after cold rolling. The amount of mechanical energy that the material can absorb therefore also decreases with increasing cold rolling and so does the uniform elongation resulting in reduced crashworthiness.
9. The absolute $M_d$ temperature for this steel was found to be around ~117 °C from the extrapolation of the sigmoidal relationship to zero percentage of α′-martensite induced. The $M_d$ (30/50) temperature was found to be 61 °C, which is significantly higher than that calculated from chemistry using empirical equations being 29 °C. No $M_s$ temperature was found to exist, even upon cooling to 3 K.

10. For the alloy investigated a small window of opportunity to obtain all the mechanical properties for good crashworthiness was observed to exist. The percentage of strain-induced martensite matters more than the degree of temper rolling. The percentage of strain-induced martensite can be equated to the degree of temper rolling. For final gauge control, the temperature of final temper rolling is therefore important. At ambient temperature, final temper rolling should be between 13 % and 14.5 %. which equates to 13.5 % to 18 % strain induced martensite.
11. The dispersion hardening strengthening mechanism was observed to occur below a "percolation" threshold value of 30 to 45% α′-martensite where an interchange of roles of martensite and austenite occurs. This behaviour is attributed to strain-induced martensite behaving as a matrix phase (after forming a continuous network linking up in 3D) and austenite as dispersions embedded in the martensite phase. Above the threshold martensite value mentioned, increased strain hardening and strength are observed as more stress is required to move the dislocations past the percolated martensite barriers with a reduction in the plasticity of the austenite resulting.

## 6.2 Recommendations

- Deformation temperature (including adiabatic heating) must be below 117 °C for the TRIP effect to occur. The TRIP effect is more effective in grain size refinement for improvement of mechanical properties without much sacrifice in ductility.
- Plant trials are recommended during which recording of rolling load and temperatures must be performed as this will be used in the calculation of mechanical energy absorbed by the material per pass. The determination of the percentage of martensite as a function of strain/thickness reduction recorded per pass must be performed, including determination of the increase in temperature during deformation due to adiabatic heating.
- For the lean-alloyed AISI 301 LN alloy investigated here, the influence of initial austenitic grain size on strain-induced martensite and $M_d$ temperature needs to be further investigated.
- The discrepancies regarding actual vs empirically calculated martensite start temperatures, observed in this work, both for athermal and deformation-induced transformation, warrants further investigation.

- The reasons for the formation of the percolation threshold in terms of volume fraction of martensite formed, prior to significant strain hardening setting in, needs to be investigated microstructurally.

**References:**

[1] R. Eckner, L. Krüger, M. Motylenko, A. S. Savinykh, S. V Razorenov, and G. V Garkushin, "Deformation mechanisms and microplasticity of austenitic TRIP / TWIP steel under flyer plate impact," *EPJ Web of Conferences 183*, vol. 03007, pp. 1–6, 2018.

[2] G. Fargas, A. Zapata, J. J. Roa, I. Sapezanskaia, and A. Mateo, "Correlation Between Microstructure and Mechanical Properties Before and After Reversion of Metastable Austenitic Stainless Steels," *Metallurgical and Materials Transactions A*, vol. 46, no. 12, pp. 5697–5707, 2015.

[3] A. Mateo, A. Zapata, and G. Fargas, "Improvement of mechanical properties on metastable stainless steels by reversion heat treatments Improvement of mechanical properties on metastable stainless steels by reversion heat treatments," *IOP Conference Series: Materials Science and Engineering*, vol. 48, p. 012001, 2013.

[4] Z. C. Li, R. D. K. Misra, H. Ding, H. P. Li, and Z. H. Cai, "The significant impact of pre-strain on the structure-mechanical properties relationship in cold-rolled medium manganese TRIP steel," *Materials Science & Engineering A*, vol. 712, pp. 206–213, 2018.

[5] S. Curtze, V. Kuokkala, M. Hokka, and P. Peura, "Deformation behavior of TRIP and DP steels in tension at different temperatures over a wide range of strain rates," *Materials Science and Engineering A*, vol. 507, pp. 124–131, 2009.

[6] M. De Cosmo, L. M. Galantucci, and L. Tricarico, "Design of process parameters for dual phase steel production with strip rolling using the finite-element method," *Journal of Materials Processing Technology*, vol. 92–93, no. January, pp. 486–493, 1999.

[7] L. P. Karjalainen, T. Taulavuori, M. Sellman, and a Kyröläinen, "Some Strengthening Methods for Austenitic Stainless Steels," *Steel Research International*, vol. 79, no. 6, pp. 404–412, 2008.

[8] M. C. Somani, P. Juntunen, L. P. Karjalainen, and R. D. K. Misra, "Enhanced Mechanical Properties through Reversion in Metastable Austenitic Stainless Steels," *Metallurgical and Materials Transactions A*, vol. 40, pp. 729–744, 2009.

[9] A. S. Hamada, A. P. Kisko, P. Sahu, and L. P. Karjalainen, "Enhancement of mechanical properties of a TRIP-aided austenitic stainless steel by controlled reversion annealing," *Materials Science & Engineering A*, vol. 628, pp. 154–159, 2015.

[10] C. M. Tamarelli, "AHSS 101: the evolving use of advanced high strength steels for automotive applications," 2000.

[11] S. Srikanth *et al.*, "Property Enhancement in Metastable 301LN Austenitic Stainless Steel through Strain-Induced Martensitic Transformation and its Reversion ( SIMTR ) for Metro Coach Manufacture," *International Journal of Metallurgical Engineering*, vol. 2, no. 2, pp. 203–213, 2013.

[12] A. Kisko, A. S. Hamada, J. Talonen, D. Porter, and L. P. Karjalainen, "Effects of reversion and recrystallization on microstructure and mechanical properties of Nb-alloyed low-Ni high-Mn austenitic stainless steels," *Materials Science & Engineering A*, vol. 657, pp. 359–370, 2016.

[13] A. F. Padilha, R. L. Plaut, and P. R. Rios, "Annealing of Cold-worked Austenitic Stainless Steels.," *ISIJ International*, vol. 43, no. 2, pp. 135–143, 2003.

[14] M. Eskandari, A. Kermanpur, and A. Najafizadeh, "Formation of nano-grained structure in a 301 stainless steel using a repetitive thermo-mechanical treatment," *Materials Letters*, vol. 63, no. 16, pp. 1442–1444, 2009.

[15] M. Eskandari, A. Zarei-hanzaki, and H. R. Abedi, "An investigation into the room temperature mechanical properties of nanocrystalline austenitic stainless steels," *Materials & Design*, vol. 45, pp. 674–681, 2013.

[16] M. Calcagnotto, D. Ponge, Y. Adachi, and D. Raabe, "Effect of Grain Refinement on Strength and Ductility in Dual-Phase Steels," *Proceedings of the 2nd International Symposium on Steel Science*, no. Isss, pp. 1–4, 2009.

[17] P. Behjati, A. Kermanpur, A. Najafizadeh, and H. S. Baghbadorani, "Effect of annealing temperature on nano/ultrafine grain of Ni-free austenitic stainless steel," *Materials Science and Engineering A*, vol. 592, pp. 77–82, Jan. 2014.

[18] M. Calcagnotto, D. Ponge, E. Demir, and D. Raabe, "Orientation gradients and geometrically necessary dislocations in ultrafine grained dual-phase steels studied by 2D and 3D EBSD," *Materials Science and Engineering A*, vol. 527, no. 10–11, pp. 2738–2746, 2010.

[19] D. M. Xu *et al.*, "Deformation behavior of high yield strength – High ductility ultrafine-grained 316LN austenitic stainless steel," *Materials Science and Engineering: A*, vol. 688, no. February, pp. 407–415, 2017.

[20] A. . Järvenpää, M. . Jaskari, L. . Pentti Karjalainen, and M. . Hietala, "Enhancing mechanical properties and formability of AISI 301LN stainless steel sheet by local laser heat treatment," *Key Engineering Materials*, vol. 554–557, pp. 885–892, 2013.

[21] V. S. A. Challa, X. L. Wan, M. C. Somani, L. P. Karjalainen, and R. D. K. Misra, "Significance of interplay between austenite stability and deformation mechanisms in governing three-stage work hardening behavior of phase-reversion induced nanograined/ultrafine-grained (NG/UFG) stainless steels with high strength-high ductility combinat," *Scripta Materialia*, vol. 86, pp. 60–63, 2014.

[22] R. Alturk, W. E. Luecke, S. Mates, A. Araujo, K. S. Raghavan, and F. Abu-Farha, "Rate effects on transformation kinetics in a metastable a ustenitic stainless steel," *Procedia Engineering*, vol. 207, pp. 2006–2011, 2017.

[23] A. Das, S. Tarafder, and P. Chandra, "Estimation of deformation induced martensite in austenitic stainless steels," *Materials Science and Engineering A*, vol. 529, pp. 9–20, 2011.

[24] H. K. Yeddu, "Martensitic Transformations in Steels: A 3D Phase-field Study," Doctoral Dissertation, KTH Royal Institute of Technology, 2012.

[25] Outokumpu, "Handbook of Stainless Steel," *Sandvikens Tryckeri*, pp. 1–89, 2013.

[26] S. Abbasi, A. Shokuhfar, and N. Ehsani, "Improvement of mechanical properties by optimization of Cr and Mo contents in xCr-yMo-9Ni-2Cu-1Ti-1V steel," *Metalurgija*, 2008.

[27] T. Angel, "Formation of Martensite," *Journal of the Iron and Steel Institute*, vol. 177, pp. 165–174, 1954.

[28] P. Santacreu, J. Glez, G. Chinouilh, and T. Frohlich, "Behaviour model of austenitic stainless steels for automotive structural parts," *Steel Research International*, vol. 77, no. 9–10, pp. 686–691, 2006.

[29] P.-O. Santacreu, J. C. Glez, N. Roulet, T. Fröhlich, and Y. Grosbety, "Austenitic stainless steels for automotive structural parts," *SAE Transactions*, pp. 805–810, 2006.

[30] J. W. Simmons, "Strain hardening and plastic flow properties of nitrogen-alloyed Fe-17Cr-(8-10)Mn-5Ni austenitic stainless steels," *Acta Materialia*, vol. 45, no. 6, pp. 2467–2475, 1997.

[31] P. Behjati, A. Kermanpur, and A. Najafizadeh, "Influence of nitrogen alloying on properties of Fe-18Cr-12Mn-XN austenitic stainless steels," *Materials Science & Engineering A*, vol. 588, pp. 43–48, 2013.

[32] A. Hedayati, A. Najafizadeh, A. Kermanpur, and F. Forouzan, "The effect of cold rolling regime on microstructure and mechanical properties of AISI 304L stainless steel," *Journal of Materials Processing Technology*, vol. 210, no. 8, pp. 1017–1022, 2010.

[33] M. Milad, N. Zreiba, F. Elhalouani, and C. Baradai, "The effect of cold work on structure and properties of AISI 304 stainless steel," *Journal of Materials Processing Technology*, vol. 203, no. 1–3, pp. 80–85, 2008.

[34] I. Shakhova, V. Dudko, A. Belyakov, K. Tsuzaki, and R. Kaibyshev, "Effect of large strain cold rolling and subsequent annealing on microstructure and mechanical properties of an austenitic stainless steel," vol. 545, pp. 176–186, 2012.

[35] L. E. Murr, K. P. Staudhammer, and S. S. Hecker, "Effects of Strain State and Strain Rate on Deformation-Induced Transformation in 304 Stainless Steel : Part I. Magnetic Measurements and Mechanical Behavior," *Metallurgical Transactions A*, vol. 13, pp. 627–635, 1982.

[36] E. Galindo-nava and P. Rivera-diaz-del-castillo, "Understanding martensite and twin formation in austenitic steels : A model describing TRIP and TWIP effects," *Acta Materialia*, vol. 128, pp. 120–134, 2017.

[37] J. Yoo, K. Choi, A. Zargaran, and N. J. Kim, "Effect of stacking faults on the ductility of Fe-18Mn-1 . 5Al-0 . 6C twinning-induced plasticity steel at low temperatures," *Scripta Materialia*, vol. 137, pp. 18–21, 2017.

[38] X. X. Wu, X. Y. San, X. G. Liang, Y. L. Gong, and X. K. Zhu, "Effect of stacking fault energy on mechanical behavior of cold-forging Cu and Cu alloys," *Materials and Design*, vol. 47, pp. 372–376, 2013.

[39] J. Talonen and H. Hänninen, "Formation of shear bands and strain-induced martensite during plastic deformation of metastable austenitic stainless steels," *Acta Materialia*, vol. 55, pp. 6108–6118, 2007.

[40] S. Rajasekhara, L. P. Karjalainen, A. Kyröläinen, and P. J. Ferreira, "Microstructure evolution in nano/submicron grained AISI 301LN stainless steel," *Materials Science and Engineering A*, vol. 527, no. 7–8, pp. 1986–1996, 2010.

[41] R. Mittal, "Strengthening Mechanism of Metals," in *Metallurgy & Materials Engineering*, 2009.

[42] G. E. Dieter and D. J. Bacon, *Mechanical metallurgy*, vol. 3. New York: McGraw-hill, 1986.

[43] R. Zaera, J. A. Rodríguez-martínez, A. Casado, J. Fernández-sáez, A. Rusinek, and R. Pesci, "A constitutive model for analyzing martensite formation in austenitic steels deforming at high strain rates," *International Journal of Plasticity*, vol. 29, pp. 77–101,

2012.

[44] T. Shintani and Y. Murata, “Evaluation of the dislocation density and dislocation character in cold rolled Type 304 steel determined by profile analysis of X-ray diffraction,” *Acta Materialia*, vol. 59, pp. 4314–4322, 2011.

[45] M. Hauser, M. Wendler, A. Wei, O. Volkova, and J. Mola, “On the Critical Driving Force for Deformation-Induced α 0 -Martensite Formation in Austenitic Cr – Mn – Ni Steels,” *Advanced Engineering Materials*, vol. 21, no. 5, pp. 1–6, 2019.

[46] A. Rezaee, A. Kermanpur, A. Najafizadeh, M. Moallemi, and H. Samaei Baghbadorani, “Investigation of cold rolling variables on the formation of strain-induced martensite in 201L stainless steel,” *Materials and Design*, vol. 46, pp. 49–53, 2013.

[47] H. F. G. De Abreu, M. J. G. Da Silva, L. F. G. Herculano, and H. Bhadeshia, “Texture analysis of deformation induced martensite in an AISI 301L stainless steel: microtexture and macrotexture aspects,” *Materials Research*, vol. 12, no. 3, pp. 291–297, 2009.

[48] D. Maréchal, C. W. Sinclair, P. Dufour, P. J. Jacques, and J. Mithieux, “In-Situ Measurements of Load Partitioning in a Metastable Austenitic Stainless Steel : Neutron and Magnetomechanical Measurements,” *Metallurgical and Materials Transactions A*, vol. 43, no. 12, pp. 4601–4609, 2011.

[49] P. Mayer, R. Skorupski, M. Smaga, D. Eifler, and J. C. Aurich, “Deformation induced surface hardening when turning metastable austenitic steel AISI 347 with different cryogenic cooling strategies,” *Procedia CIRP*, vol. 14, pp. 101–106, 2014.

[50] D. T. Llewellyn, “Work hardening effects in austenitic stainless steels,” *Materials Science and Technology*, vol. 13, no. 5, pp. 389–400, 1997.

[51] T. W. Mukarati, R. J. Mostert, and C. W. Siyasiya, “The sigmoidal strain hardening behaviour of a metastable AISI 301LN austenitic stainless steel as a function of temperature,” *Materials Science & Engineering A*, vol. 792, p. 139741, 2020.

[52] J. Choi and W. Jin, “Strain induced martensite formation and its effect on strain hardening behavior in the cold drawn 304 austenitic stainless steels,” *Scripta Materialia*, vol. 36, no. 1, pp. 99–104, 1997.

[53] Y. Jung, Y. Lee, D. K. Matlock, and M. C. Mataya, “Effect of grain size on strain-induced martensitic transformation start temperature in an ultrafine grained metastable austenitic steel,” *Metals and Materials International*, vol. 17, no. 4, p. 553, 2011.

[54] H. W. King and D. C. Larbalestier, “Austenitic stainless steels at cryogenic temperatures :

The compositional dependence of the Ms," *Cryogenics (Guildf).*, vol. 1667, pp. 521–524, 1981.

[55] H. Mirzadeh and A. Najafizadeh, "Correlation between processing parameters and strain-induced martensitic transformation in cold worked AISI 301 stainless steel," *Materials Characterization*, vol. 59, no. 11, pp. 1650–1654, 2008.

[56] L. Remy and A. Pineau, "Twinning and Strain-Induced F.C.C. → H.C.P. Transformation on the Mechanical Properties of C o-N i-C r-M o Alloys," *Materials Science and Engineering*, vol. 26, pp. 123–132, 1976.

[57] H. F. G. De Abreu *et al.*, "Deformation induced martensite in an AISI 301LN stainless steel: characterization and influence on pitting corrosion resistance," *Materials Research*, vol. 10, no. 4, pp. 359–366, 2007.

[58] L. Mosecker *et al.*, "Temperature effect on deformation mechanisms and mechanical properties of a high manganese C + N alloyed austenitic stainless steel," *Materials Science & Engineering A*, vol. 642, pp. 71–83, 2015.

[59] P. Parnian and M. H. Parsa, "The Effect of Strain Rate on Ultra-Fine Grained Structure of Cold Drawn 304L Stainless Steel Wires," *Procedia Materials Science*, vol. 11, pp. 24–31, 2015.

[60] P. Sahu, A. S. Hamada, T. Sahu, J. Puustinen, T. Oittinen, and L. P. Karjalainen, "Martensitic transformation during cold rolling deformation of an austenitic Fe-26Mn-0.14C alloy," *Metallurgical and Materials Transactions A: Physical Metallurgy and Materials Science*, vol. 43, no. 1, pp. 47–55, 2012.

[61] W. Barclay, "The Mechanisms of Deformation and Work Hardening in AISI Type 301 Stainless Steel," *Advances in the Technology of Stainless Steels and Related Alloys. ASTM International*, pp. 26–29, 1965.

[62] X. Yang, S. Sun, and T. Zhang, "The mechanism of bcc α′ nucleation in single hcp ε laths in the fcc γ→ hcp ε→ bcc α′ martensitic phase transformation," *Acta Materialia*, vol. 95, pp. 264–273, 2015.

[63] M. Smaga and I. Kube, "Effect of metallurgical variables on the austenite stability in fatigued AISI 304 type steels," *Engineering Fracture Mechanics*, vol. 185, pp. 139–159, 2017.

[64] E. Dryzek, M. Sarnek, and M. Wróbel, "Reverse transformation of deformation-induced martensite in austenitic stainless steel studied by positron annihilation," *Journal of*

*Materials Science*, vol. 49, no. 24, pp. 8449–8458, 2014.

[65] M. Shirdel, H. Mirzadeh, and M. H. Parsa, "Nano/ultra fine grained austenitic stainless steel through the formation and reversion of deformation-induced martensite : Mechanisms , microstructures , mechanical properties , and TRIP effect," *Materials Characterization*, vol. 103, pp. 150–161, 2015.

[66] J. Kim and B. C. De Cooman, "Stacking fault energy and deformation mechanisms in Fe-xMn-0.6C-yAl TWIP steel," *Materials Science & Engineering A*, vol. 676, pp. 216–231, 2016.

[67] H. Wang, X. Sun, P. Yang, W. Mao, and L. Meng, "Analysis of the Transformation-induced Plasticity Effect during the Dynamic Deformation of High-manganese Steel," *Journal of Materials Science & Technology*, vol. 31, no. 2, pp. 191–198, 2015.

[68] G. N. Haidemenopoulos, N. Aravas, and I. Bellas, "Kinetics of strain-induced transformation of dispersed austenite in low-alloy TRIP steels," *Materials Science & Engineering A*, vol. 615, pp. 416–423, 2014.

[69] K. Spencer, M. Véron, K. Yu-Zhang, and J. D. Embury, "The strain induced martensite transformation in austenitic stainless steels : Part 1 – Influence of temperature and strain history The strain induced martensite transformation in austenitic stainless steels Part 1 – Influence of temperature and strain his," *Materials Science and Technology*, vol. 25, no. 1, pp. 7–17, 2009.

[70] H. Ding, H. Ding, D. Song, Z. Tang, and P. Yang, "Strain hardening behavior of a TRIP / TWIP steel with 18 . 8 % Mn," *Materials Science and Engineering A*, vol. 528, pp. 868–873, 2011.

[71] N. Solomon and I. Solomon, "Phase transformatio influence on corrosion resistance of AISI 316 austenitic stainless steel," *University Politehnica of Bucharest Scientific Bulletin - Series B*, vol. 72, no. 4, 2010.

[72] K. Datta, R. Delhez, P. M. Bronsveld, J. Beyer, H. J. M. Geijselaers, and J. Post, "A low-temperature study to examine the role of ε-martensite during strain-induced transformations in metastable austenitic stainless steels," *Acta Materialia*, vol. 57, pp. 3321–3326, 2009.

[73] S. Martin, S. Wolf, U. Martin, and L. Kru, "Deformation Mechanisms in Austenitic TRIP / TWIP Steel as a Function of Temperature," *Metallurgical and Materials Transactions A*, vol. 47, no. 1, pp. 49–58, 2016.

[74] M. Moallemi, A. Najafizadeh, A. Kermanpur, and A. Rezaee, "Effect of reversion annealing on the formation of nano / ultrafine grained structure in 201 austenitic stainless steel," *Materials Science and Engineering A*, vol. 530, pp. 378–381, 2011.

[75] J. Lu *et al.*, "Stacking fault energies in austenitic stainless steels," *Acta Materialia*, vol. 111, pp. 39–46, 2016.

[76] S. K. Ghosh, P. Mallick, and P. P. Chattopadhyay, "Effect of Cold Deformation on Phase Evolution and Mechanical Properties in an Austenitic Stainless Steel for Structural and Safety Applications," *Journal of Iron and Steel Research, International*, vol. 19, no. 4, pp. 63–68, 2012.

[77] S. Lu, Q. Hu, B. Johansson, and L. Vitos, "Stacking fault energies of Mn , Co and Nb alloyed austenitic stainless steels," *Acta Materialia*, vol. 59, no. 14, pp. 5728–5734, 2011.

[78] N. Solomon and I. Solomon, "Deformation induced martensite in AISI 316 stainless steel," *Revista de Metalurgia*, vol. 46, no. 2, pp. 121–128, 2010.

[79] H. Christ, A. Grigorescu, and C. Müller-bollenhagen, "Metastable Austenitic Stainless Steels and the Effect of Deformation-Induced Phase Transformation on the Fatigue Properties," 2001.

[80] T. W. Mukarati, R. J. Mostert, and C. W. Siyasiya, "Effect of heavy temper rolling on the mechanical properties of AISI 301 stainless steel," *Proceedings of the AMI Precious Metals 2017 (THE PRECIOUS METALS DEVELOPMENT NETWORK (PMDN), Polokwane, South Africa*, vol. S94, pp. 93–103, 2017.

[81] S. Curtze and V. Kuokkala, "Dependence of tensile deformation behavior of TWIP steels on stacking fault energy , temperature and strain rate," *Acta Materialia*, vol. 58, pp. 5129–5141, 2010.

[82] S. K. Ghosh, P. Mallick, and P. P. Chattopadhyay, "Effect of Cold Deformation on Phase Evolution and Mechanical Properties in an Austenitic Stainless Steel for Structural and Safety Applications," *Journal of Iron and Steel Research International*, vol. 19, no. 4, pp. 63–68, 2012.

[83] X. Wan, J. Yu, G. Xu, and G. Li, "Effect of strain rate on microstructures and mechanical properties of Fe – 18Cr – 8Ni steel," *Materials Science and Technology*, vol. 35, no. 2, pp. 195–203, 2019.

[84] A. Kisko, R. D. K. Misra, J. Talonen, and L. P. Karjalainen, "The influence of grain size on the strain-induced martensite formation in tensile straining of an austenitic 15Cr – 9Mn

– Ni – Cu stainless steel," *Materials Science & Engineering A*, vol. 578, pp. 408–416, 2013.

[85] M. El-tahawy, Y. Huang, H. Choi, H. Choe, J. L. Lábár, and T. G. Langdon, "Microstructure, phase composition and hardness evolution in 316L stainless steel processed by high-pressure torsion," *Materials Science & Engineering A*, vol. 657, pp. 215–223, 2016.

[86] M. Moallemi, A. Kermanpur, A. Najafizadeh, A. Rezaee, H. S. Baghbadorani, and P. D. Nezhadfar, "Deformation-induced martensitic transformation in a 201 austenitic steel : The synergy of stacking fault energy and chemical driving force," *Materials Science & Engineering A*, vol. 653, pp. 147–152, 2016.

[87] T. Yonezawa, K. E. N. Suzuki, S. Ooki, and A. Hashimoto, "The Effect of Chemical Composition and Heat Treatment Conditions on Stacking Fault Energy for Fe-Cr-Ni Austenitic Stainless Steel," *Metallurgical and Materials Transactions A*, vol. 44, no. 13, pp. 5884–5896, 2013.

[88] T. H. Lee, E. Shin, C. S. Oh, H. Y. Ha, and S. J. Kim, "Correlation between stacking fault energy and deformation microstructure in high-interstitial-alloyed austenitic steels," *Acta Materialia*, vol. 58, no. 8, pp. 3173–3186, 2010.

[89] G. B. Olson, "A mechanism for the strain-induced martensitic transformations* nucleation of," *Journal of the Less-Common Metals*, vol. 28, no. 1, pp. 107–118, 1972.

[90] V. S. A. Challa, X. L. Wan, M. C. Somani, L. P. Karjalainen, and R. D. K. Misra, "Strain hardening behaviour of phase reversion-induced nanograined/ultrafine-grained (NG/UFG) austenitic stainless steel and relationship with grain size and deformation mechanism," *Materials Science and Engineering A*, vol. 613, pp. 60–70, 2014.

[91] X. Li, L. Chen, Y. Zhao, X. Yuan, R. Devesh, and K. Misra, "Influence of original austenite grain size on tensile properties of a high-manganese transformation-induced plasticity ( TRIP ) steel," *Materials Science & Engineering A*, vol. 715, pp. 257–265, 2018.

[92] L. Rémy, A. Pineau, and B. Thomas, "Temperature Dependence of Stacking Fault Energy in Close-Packed Metals and Alloys," *Materials Science and Engineering*, vol. 36, pp. 47–63, 1978.

[93] W. A. N. Jianfeng, C. Shipu, and X. U. Zuyao, "The influence of temperature on stacking fault energy in Fe-based alloys," *Science in China*, vol. 44, no. 4, pp. 345–352, 2001.

[94] B. Mahato *et al.*, "An effective stacking fault energy viewpoint on the formation of

extended defects and their contribution to strain hardening in a Fe – Mn – Si – Al twinning-induced plasticity steel," *Acta Materialia*, vol. 86, pp. 69–79, 2015.

[95] G. M. De Bellefon, C. Domain, J. C. Van Duysen, and K. Sridharan, "Composition-dependence of stacking fault energy in austenitic stainless steels through linear regression with random intercepts," *Journal of Nuclear Materials*, vol. 492, pp. 227–230, 2017.

[96] J. Talonen, "Effect of strain-induced α'-martensite transformation on mechanical properties of metastable austenitic stainless steels. PhD diss.," Helsinki University of Technology, 2007.

[97] L. Vitos, J. . Nilsson, and B. Johansson, "Alloying effects on the stacking fault energy in austenitic stainless steels from first-principles theory," *Acta Materialia*, vol. 54, no. 14, pp. 3821–3826, 2006.

[98] R. E. Schramn and R. P. Reed, "Stacking Fault Energies of Seven Commercial Austenitic Stainless Steels," *Metallurgical Transactions A*, vol. 6, no. 7, p. 1345, 1975.

[99] J. Huang, X. Ye, J. Gu, X. Chen, and Z. Xu, "Enhanced mechanical properties of type AISI301LN austenitic stainless steel through advanced thermo mechanical process," *Materials Science & Engineering A*, vol. 532, pp. 190–195, 2012.

[100] A. Poulon-quintin, S. Brochet, J. Vogt, J. Glez, and J. Mithieux, "Fine Grained Austenitic Stainless Steels : The Role of Strain Induced α′ Martensite and the Reversion Mechanism Limitations," *ISIJ International*, vol. 49, no. 2, pp. 293–301, 2009.

[101] P. Brofman and G. Ansell, "On the Effect of Carbon on the Stacking Fault Energy of Austenitic Stainless Steels," *Metallurgical Transactions A*, vol. 9, pp. 879–880, 1978.

[102] C. G. Rhodes and A. W. Thompson, "The Composition Dependence of Stacking Fault Energy in Austenitic Stainless Steels," *Metallurgical Transactions A*, vol. 8, no. 12, pp. 1901–1906, 1977.

[103] D. Rafaja, C. Krbetschek, C. Ullrich, and S. Martin, "Stacking fault energy in austenitic steels determined by using in situ X-ray diffraction during bending research papers," *Journal of Applied Crystallography*, vol. 47, no. 3, pp. 936–947, 2014.

[104] D. Qi-Xun, A.-D. Wang, X.-N. Cheng, and X.-M. Luo, "Stacking fault energy of cryogenic austenitic steels," *Chinese Physics*, vol. 11, no. 06, pp. 596–600, 2002.

[105] M. Ojima *et al.*, "Weak Beam TEM Study on Stacking Fault Energy of High Nitrogen Steels," *Journal of Iron and Steel Research International*, vol. 80, no. 7, pp. 477–481, 2009.

[106] A. A. Gorni, "Steel forming and heat treating handbook," *São Vicente, Brazil*, p. 48, 2015.

[107] T. Masumura, N. Nakada, T. Tsuchiyama, S. Takaki, T. Koyano, and K. Adachi, "The difference in thermal and mechanical stabilities of austenite between carbon- and nitrogen-added metastable austenitic stainless steels," *Acta Materialia*, vol. 84, pp. 330–338, 2015.

[108] T. Masumura, T. Tsuchiyama, S. Takaki, T. Koyano, and K. Adachi, "Difference between carbon and nitrogen in thermal stability of metastable 18 % Cr-8 % Ni austenite," *Scripta Materialia*, vol. 154, pp. 8–11, 2018.

[109] W. Ozgowicz and A. Kurc, "The effect of the cold rolling on the structure and mechanical properties in austenitic stainless steels type 18-8," *International Scientific Journal*, vol. 38, no. 1, pp. 26–33, 2009.

[110] K. Nohara, Y. Ono, and N. Ohashi., "Composition and grain size dependencies of strain-induced martensitic transformation in metastable austenitic stainless steels," *Tetsu-to-Hagané*, vol. 63, no. 5, pp. 772–782, 1977.

[111] A. Macadre, K. Tsuboi, N. Nakada, and T. Tsuchiyama, "Ultra-grain refinement effect on tensile and phase transformation behaviour in a metastable austenitic steel charged in hydrogen gas," *Procedia Materials Science*, vol. 3, pp. 350–356, 2014.

[112] M. Roberto, C. Augusto, and S. De Oliveira, "Evaluation of the martensitic transformations in austenitic stainless steels," *Materials Science and Engineering A*, vol. 517, pp. 281–285, 2009.

[113] F. Hahnenberger, M. Smaga, and D. Eifler, "Microstructural investigation of the fatigue behavior and phase transformation in metastable austenitic steels at ambient and lower temperatures," *International Journal of Fatigue*, vol. 69, pp. 36–48, 2014.

[114] A. M. Beese and D. Mohr, "Experimental Quantification of Phase Transformation in Austenitic Stainless Steel," *Proc. SEM Annu. Conf. June 1-4, 2009 Albuquerque New Mex. USA ©2009 Soc. Exp. Mech. Inc.*, pp. 1–7, 2009.

[115] S. Martin, C. Ullrich, and D. Rafaja, "Deformation of austenitic CrMnNi TRIP / TWIP steels : Nature and role of the ε-martensite," *Materials Today: Proceedings*, vol. 2, pp. S643–S646, 2015.

[116] G. Cios *et al.*, "The Investigation of Strain-Induced Martensite Reverse Transformation in AISI 304 Austenitic Stainless Steel," *Metallurgical and Materials Transactions A*, vol. 48, no. 10, pp. 4999–5008, 2017.

[117] C. Gauss, I. R. S. Filho, M. J. R. Sandim, P. A. Suzuki, A. J. Ramirez, and H. R. Z. Sandim, "In situ synchrotron X-ray evaluation of strain-induced martensite in AISI 201 austenitic stainless steel during tensile testing," *Materials Science & Engineering A*, vol. 651, pp. 507–516, 2016.

[118] G. Zietek and Z. Mroz, "A constitutive hardening model of coupled plastic deformation and martensitic transformation in steels," *Mechanics of Materials*, vol. 100, pp. 154–166, 2016.

[119] D. Maréchal, "Linkage between mechanical properties and phase transformations in a 301LN austenitic stainless steel, Doctoral dissertation, University of British Columbia," 2011.

[120] Y. Tian, A. Borgenstam, and P. Hedström, "A Microstructural Investigation of Athermal and Deformation-induced Martensite in Fe-Cr-Ni Alloys," *Materials Today: Proceedings*, vol. 2, pp. S687–S690, 2015.

[121] M. Cohen and G. B. Olson, "Kinetics of Strain-Induced Martensitic Nucleation," *Metallurgical Transactions A*, vol. 6A, pp. 791–795, 1975.

[122] S. Martin, C. Ullrich, D. Imek, U. Martin, and D. Rafaja, "Stacking fault model of-martensite and its DIFFaX implementation," *Journal of Applied Crystallography*, vol. 44, no. 4, pp. 779–787, 2011.

[123] H. Hotz, B. Kirsch, S. Becker, E. von Harbou, R. Muller, and J. C. Aurich, "Improving the surface surface morphology of metastable austenitic steel AISI 347 in a two-step turning process," *Procedia CIRP*, vol. 71, pp. 160–165, 2018.

[124] R. F. Kubler, M. Berveiller, and P. Buessler, "Semi phenomenological modelling of the behavior of TRIP steels," *International Journal of Plasticity*, vol. 27, pp. 299–327, 2011.

[125] Y. Tian, U. Lienert, A. Borgenstam, T. Fischer, and P. Hedström, "Martensite formation during incremental cooling of Fe-Cr-Ni alloys : An in-situ bulk X- ray study of the grain-averaged and ...," *Scripta Materialia*, vol. 136, pp. 124–127, 2017.

[126] X. Li, J. Chen, L. Ye, W. Ding, and P. Song, "Influence of strain rate on tensile characteristics of SUS304 metastable austenitic stainless steel," *Acta Metallurgica Sinica (English Letters)*, vol. 26, no. 6, pp. 657–662, 2013.

[127] M. Hadji and R. Badji, "Microstructure and Mechanical Properties of Austenitic Stainless Steels After Cold Rolling," *Journal of Materials and Performance*, vol. 11, pp. 145–151, 2002.

[128] J. Talonen, P. Nenonen, G. Pape, and H. Hänninen, "Effect of strain rate on the strain-induced γ → α′-martensite transformation and mechanical properties of austenitic stainless steels," *Metallurgical and Materials Transactions A*, vol. 36A, no. 2, pp. 421–432, 2005.

[129] S. L. Wong, M. Madivala, U. Prahl, F. Roters, and D. Raabe, "A crystal plasticity model for twinning- and transformation-induced plasticity," *Acta Materialia*, vol. 118, pp. 140–151, 2016.

[130] E. I. Samuel, B. K. Choudhary, and K. B. S. Rao, "Influence of temperature and strain rate on tensile work hardening behaviour of type 316 LN austenitic stainless steel," *Scripta Materialia*, vol. 46, pp. 507–512, 2002.

[131] B. K. Choudhary and D. P. R. Palaparti, "Comparative tensile flow and work hardening behaviour of thin section and forged thick section 9Cr – 1Mo ferritic steel in the framework of Voce equation and Kocks – Mecking approach," *Journal of Nuclear Materials*, vol. 430, pp. 72–81, 2012.

[132] B. L. Ennis, E. Jimenez-melero, E. H. Atzema, and M. Krugla, "Metastable austenite driven work-hardening behaviour in a TRIP-assisted dual phase steel," *International Journal of Plasticity*, vol. 88, pp. 126–139, 2017.

[133] Y. Tomita and T. Iwamoto, "Constitutive modeling of TRIP steel and its application to the improvement of mechanical properties," *International Journal of Mechanical Sciences*, vol. 37, no. 12, pp. 1295–1305, 1995.

[134] X. Tian and Y. Zhang, "Mathematical description for flow curves of some stable austenitic steels," *Materials Science and Engineering*, vol. A174, pp. L1–L3, 1994.

[135] T. W. Mukarati, R. J. Mostert, and C. W. Siyasiya, "Development of a mathematical equation describing the strain hardening behaviour of metastable AISI 301 austenitic stainless steel," *IOP Conference Series: Materials Science and Engineering*, vol. 655, no. 1, p. 012008, 2019.

[136] D. P. R. Palaparti, B. K. Choudhary, E. I. Samuel, V. S. Srinivasan, and M. D. Mathew, "Influence of strain rate and temperature on tensile stress – strain and work hardening behaviour of 9Cr – 1Mo ferritic steel," *Materials Science and Engineering A*, vol. 538, pp. 110–117, 2012.

[137] E. I. Samuel and B. K. Choudhary, "Universal scaling of work hardening parameters in type 316L (N) stainless steel," *Materials Science and Engineering*, vol. 527, pp. 7457–7460, 2010.

[138] K. G. Samuel, S. L. Mannan, and V. M. Radhakrishnan, "The Influence of Temperature and Prior Cold Work on the Strain-Hardening Parameters of a Type 316 LN Stainless Steel," *International Journal of Pressure Vessels & Piping*, vol. 52, pp. 151–157, 1992.

[139] A. Soussan, S. Degallaix, and T. Magnin, "Work-hardening behaviour of nitrogen-alloyed austenitic stainless steels," *Materials Science & Engineering A*, vol. 142, pp. 169–176, 1991.

[140] P. M. Ahmedabadi, V. Kain, and A. Agrawal, "Modelling kinetics of strain-induced martensite transformation during plastic deformation of austenitic stainless steel," *Materials and Design*, vol. 109, pp. 466–475, 2016.

[141] N. Tsuchida, Y. Yamaguchi, Y. Morimoto, T. Tonan, Y. Takagi, and R. Ueji, "Effects of Temperature and Strain Rate on TRIP Effect in SUS301L Metastable Austenitic Stainless Steel," *ISIJ International*, vol. 53, no. 10, pp. 1881–1887, 2013.

[142] N. Tsuchida, T. Kawahata, E. Ishimaru, and A. Takahashi, "Effects of Temperature and Strain Rate on Tensile Properties of a Lean Duplex Stainless Steel," *ISIJ International*, vol. 54, no. 8, pp. 1971–1977, 2014.

[143] H. long YI, L. x. DU, G. dong WANG, and X. h. LIU, "Development of Nb-V-Ti Hot-Rolled High Strength Steel With Fine Ferrite and Precipitation Strengthening," *Journal of Iron and Steel Research International*, vol. 16, no. 4, pp. 72–77, 2009.

[144] K. Mumtaz *et al.*, "Magnetic measurements of martensitic transformation in austenitic stainless steel after room temperature rolling," *Materials Science*, vol. 39, no. 1, pp. 85–97, 2004.

[145] R. Surkialiabad, A. Hedayati, and A. S. Alam, "Monitoring of Martensitic Transformation in Cold-Rolled 304L Austenitic Stainless Steel by Eddy Current Method," *Transformation*, vol. 2, no. 10, p. 11, 2013.

[146] M. Shirdel, H. Mirzadeh, and M. H. Parsa, "Estimation of the kinetics of martensitic transformation in austenitic stainless steels by conventional and novel approaches," *Materials Science & Engineering A*, vol. 624, pp. 256–260, 2015.

[147] J. Talonen, P. Aspegren, and H. Hänninen, "Comparison of different methods for measuring strain induced α-martensite content in austenitic steels," *Materials Science and Technology*, vol. 20, no. 12, pp. 1506–1512, 2004.

[148] M. Smaga, A. Boemke, T. Daniel, and M. W. Klein, "Metastability and fatigue behavior of austenitic stainless steels," *MATEC Web of Conferences*, vol. 165, p. 040108, 2018.

[149] P. Haušild, V. Davydov, J. Drahokoupil, M. Landa, and P. Pilvin, "Characterization of strain-induced martensitic transformation in a metastable austenitic stainless steel," *Materials and Design*, vol. 31, no. 4, pp. 1821–1827, 2010.

[150] I. R. S. Filho *et al.*, "Effects of strain-induced martensite and its reversion on the magnetic properties of AISI 201 austenitic stainless steel," *Journal of Magnetism and Magnetic Materials*, vol. 419, pp. 156–165, 2016.

[151] S. S. M. Tavares, J. M. Pardal, M. J. Gomes, H. F. G. Abreu, and M. R. Silva, "Deformation induced martensitic transformation in a 201 modified austenitic stainless steel," *Materials Characterization*, vol. 60, pp. 907–911, 2009.

[152] R. Lawrence, "The Effect of Phase Morphology and Volume Fraction of Retained Austenite on the Formability of Transformation Induced Plasticity Steels. Masters diss., Queen's University," 2010.

[153] D. Ryoo, N. Kang, and C. Kang, "Effect of Ni content on the tensile properties and strain-induced martensite transformation for 304 stainless steel," *Materials Science and Engineering A*, vol. 528, pp. 2277–2281, 2011.

[154] M. C. Ruch *et al.*, "Characterization of Cold Rolling-Induced Martensite in Austenitic Stainless Steels," *Proceedings of the 19th World Conference on Non-Destructive Testing*, pp. 13–17, 2016.

[155] C. P. Livitsanos and P. F. Thomson, "The effect of temperature and deformation rate on transformation-dependent ductility of a metastable austenitic stainless steel," *Materials Science and Engineering*, vol. 30, no. 2, pp. 93–98, 1977.

[156] A. M. Beese and D. Mohr, "Identification of the Direction-Dependency of the Martensitic Transformation in Stainless Steel Using In Situ Magnetic Permeability Measurements," *Experimental Mechanics*, vol. 51, no. 5, pp. 667–676, 2011.

[157] X. Fang, Z. Fan, B. Ralph, P. Evans, and R. Underhill, "Effect of temper rolling on tensile properties of C-Mn steels," *Materials Science and Technology*, vol. 18, no. 3, pp. 285–288, 2002.

[158] T. W. Mukarati, R. J. Mostert, and C. W. Siyasiya, "Effect of temperature and strain on austenite to martensite transformation in AISI 301LN metastable austenitic stainless steel," *Submitted for publication*, 2020.

[159] A666-15, *"666: Standard Specification for Annealed or Cold-Worked Austenitic Stainless Steel Sheet."* 2015, pp. 1–8.

[160] A. Järvenpää, M. Jaskari, J. Man, and L. P. Karjalainen, "Austenite stability in reversion-treated structures of a 301LN steel under tensile loading," *Materials Characterization*, vol. 127, pp. 12–26, 2017.

[161] Y. S. Han and S. H. Hong, "The effect of Al on mechanical properties and microstructures of cryogenic alloys," *Materials Science and Engineering*, vol. A222, pp. 76–83, 1997.

[162] G. C. Soares, M. R. M. Carla, and L. D. A. Santos, "Influence of Temperature on Mechanical Properties , Fracture Morphology and Strain Hardening Behavior of a 304 Stainless Steel," *Materials Research*, 2017.

[163] J. A. Munoz, A. Komissarov, M. Avalos, and R. E. Bolmaro, "Mechanical and microstructural behavior of a heterogeneous austenitic stainless steel processed by Equal Channel Angular Sheet Extrusion (ECASE) _ Elsevier Enhanced Reader.pdf," *Materials Science & Engineering A*, vol. 792, 2020.

[164] Y. F. Shen, X. X. Li, X. Sun, Y. D. Wang, and L. Zuo, "Twinning and martensite in a 304 austenitic stainless steel," *Materials Science and Engineering: A*, vol. 552, pp. 514–522, 2012.

[165] D. P. Rowlands, "The Mechanical Properties of Stainless Steel: How these are determined, and the factors which influence their values," *Stainless Steel Information Series 3, SASSDA*, 2014.

[166] Nickel Development Institute, "Mechanical and physical properties of austenitic chromium-nickel stainless steels at ambient temperatures," 1968.

[167] AK Steel Corporation, "Product data bulletin: 301 STAINLESS STEEL," *accessed online 2020*.

[168] X. Zhao, Y. Shen, L. Qiu, Y. Liu, X. Sun, and L. Zuo, "Effects of intercritical annealing temperature on mechanical properties of Fe-7.9Mn-0.14Si-0.05Al-0.07C steel," *Materials*, vol. 7, no. 12, pp. 7891–7906, 2014.

[169] M. Naghizadeh and H. Mirzadeh, "Modeling the kinetics of deformation-induced martensitic transformation in AISI 316 metastable austenitic stainless steel," *Vacuum*, vol. 157, pp. 243–248, 2018.